Kinetic and Mechanistic Studies in Atmospheric Chemistry Using Photoionization Mass Spectrometry

Neil Uist Macdonald Howes

Submitted in accordance with the requirements for the degree of Doctor of Philosophy

The University of Leeds

School of Chemistry

July 2016

The candidate confirms that the work submitted is his own. Where work which has formed part of a jointly-authored publication has been included, the contribution of this candidate to this work has been explicitly indicated overleaf. The candidate confirms that appropriate credit has been given where reference has been made to the work of others.

Acknowledgements

Firstly, I would like to thank my supervisor, Professor Paul Seakins, for giving me the opportunity to study at Leeds, and for all of his help and advice over the past 4 years. A big thank you must also be given to Dr. Mark Blitz whose experimental expertise has helped me greatly throughout my PhD. I would also like to thank all of my past and present colleagues in both B36 and the Dainton Lab, particularly Dr. Dan Stone whose knowledge of the Criegee intermediates has proved invaluable. I must also thank both Dr. Robin Shannon and Diogo De Jesus Medeiros whose MESMER calculations have been used to support the experimental work presented.

I first started my undergraduate degree in Leeds in 2007, since then I have made countless friends, to who I am very grateful for their companionship over the years. As there are so many, I won't mention individual names, but a huge thanks to every one of you!

A special thank you must also go to my family, as without their love, support and guidance, I am sure I would not be here. More specifically, I would like to thank: my sister, Catriona, who I have always looked up to and who was a great role model to me when I was young; my Dad who not only instilled in me a passion for science at a young age, but also for the enthusiasm he still has shown in my work today; and my Mum for the encouragement and kindness she has always shown me in all walks of life.

Finally, and most importantly, I must thank my girlfriend (and best friend), Steph. It's hard to put into words how much your love and kindness has helped over the past few years. You always to put my needs first, sometimes even to your own detriment, without you by my side I would not have got to this point. Thank you.

Abstract

The aim of this thesis is to provide updated, accurate kinetic (and where possible mechanistic) information regarding the oxidation pathways of various volatile organic compounds (VOCs) and trace gas species within the troposphere.

The vast majority of the experiments discussed were conducted using a pulsed laser photolysis, photoionization mass spectrometry (PLP-PIMS) set-up, which operated at low pressures (p = 2 Torr). PLP-PIMS is a time-resolved technique can be used to directly monitor multiple species simultaneously and with time; details of this method are found in Chapter II. Initially, one shortcoming of the PLP-PIMS technique was that it could not detect OH radicals (due to the ionization potential of OH). However, in Chapter III a 1 + 1' multiphoton ionization (MPI) scheme was implemented, making OH detection possible.

In Chapter IV, kinetic and mechanistic information regarding the oxidation of acetaldehyde, CH_3CHO, by OH is reported. From this study a rate coefficient of $k_{OH} = (1.6 \pm 0.2) \times 10^{-11}$ cm^3 $molecule^{-1}$ s^{-1} was measured, this is in good agreement with other literature values. Additionally, it was observed that a small yield of methyl radicals ($Y_{CH3} \approx 15\%$) was also produced. Methyl radicals were an unexpected product from this reaction and it is hypothesised that they are formed from the dissociation of nascent, chemically activated acetyl radicals. Notably, the yield of methyl radicals observed is significantly lower than would be expected from a statistical distribution of the energy between the products. Therefore, a post-reaction complex is proposed to allow for the redistribution of energy.

In Chapters VI, reactions of the C_1 and C_2 Criegee intermediates (CH_2OO and CH_3CHOO, respectively) with SO_2 and NO_2 are reported. For the C_1 Criegee intermediate (CI), rate coefficients of $k_{C1SO2} = (3.8 \pm 0.3) \times 10^{-11}$ cm^3 $molecule^{-1}$ s^{-1} and $k_{C1NO2} = (1.2 \pm 0.3) \times 10^{-12}$ cm^3 $molecule^{-1}$ s^{-1} are reported for the reactions with SO_2 and NO_2 respectively. For the C_2 CI, rate coefficients of $k_{C2SO2} = (1.8 \pm 0.3) \times 10^{-11}$ cm^3 $molecule^{-1}$ s^{-1} and $k_{C2NO2} = (7.0 \pm 1.6) \times 10^{-13}$ cm^3 $molecule^{-1}$ s^{-1} were measured. Moreover, in the C_2 CI + SO_2 reaction, acetaldehyde was positively identified as a product from this reaction at low pressures.

Finally, in Chapter VII the reactivity of Criegee intermediates towards different organic species was investigated. From these experiments it was observed that the C_1 CI had significant rate coefficients with carboxylic acids, and rate coefficients of $k_{C1FA} = (3.7 \pm 0.6) \times 10^{-11}$ cm^3 $molecule^{-1}$ s^{-1} and $k_{C1AA} = (7.1 \pm 1.1) \times 10^{-11}$ cm^3 $molecule^{-1}$ s^{-1} measured for the reactions with formic and acetic acid, respectively. However, the reactivity of CIs towards alkenes is thought to be considerably slower with upper limits of $k_{C1ethene} < 2 \times 10^{-14}$ cm^3

molecule^{-1} s^{-1} and $k_{C1isoprene} < 3 \times 10^{-13}$ cm^3 molecule^{-1} s^{-1} measured for the reactions of the C_1 CI with ethene and isoprene.

Table of Contents

Table of Figures

Table of Tables

Chapter I:

Introduction

1. Introduction

The initial chapter of this thesis gives an introduction to Earth's atmosphere and highlights some of the negative impacts that both anthropogenic and biogenic activities have had. Additionally, this chapter aims to give a brief overview of the chemistry that occurs within the Earth's atmosphere, with a particular focus on the oxidation of organic species in the atmosphere. Lastly, an introduction to field of reaction kinetics is given, with the emphasis on gas-phase kinetics and the theoretical methods relevant to this thesis.

1.1 Climate Change

Climate change has become a major threat to prolonged life on Earth (Haines et al., 2006). Sadly, up until very recently, climate issues have been largely ignored on both a governmental level and by the general public; indeed according to a study conducted in 2010, under half (~47%) of the American population even believed that climate change was occurring (Leiserowitz et al., 2013). This may be partially due to a lack of understanding of what climate change actually means: "Climate change refers to a change in the state of the climate that can be identified (e.g. by using statistical tests) by changes in the mean and/or the variability of its properties, and that persists for an extended period, typically decades or longer" (Cubasch et al., 2013). Crucially, and possibly what is misunderstood, climate change is based upon observed, quantifiable, changes to climate; it is not merely hypothesis – it is known that climate change is occurring. It is also true that to fully appreciate the ramifications that human activity has had upon climate change, the intricacies of the Earth's climate, including the role of the atmosphere, must be well understood.

1.1.1 The Earth's Climate System

The atmosphere surrounding Earth is responsible for moderating its climate; the chief input of energy to this system is from solar radiation (Figure 1.1). Prior to the industrial revolution, the Earth's surface temperature had remained, relatively constant, since the end of the last glacial period, approximately 12,000 years ago (Severinghaus and Brook, 1999); suggesting that an equilibrium had been reached between the incoming radiation from the Sun and the outgoing radiation from the Earth and its atmosphere. The Earth receives (on average) approximately 1.74×10^{17} Joules of energy per second (i.e. 174 PW) from the Sun (Thorpe, 2011); just over a half is absorbed by the Earth's surface. Of the other half, approximately 30% is reflected back out of the Earth's atmosphere whilst the remaining 20% is absorbed by gas molecules within the atmosphere. For example, stratospheric ozone absorbs much (>97%) of the ultra-violet light at wavelengths between 200 nm > λ > 315 nm (Wayne, 1991).

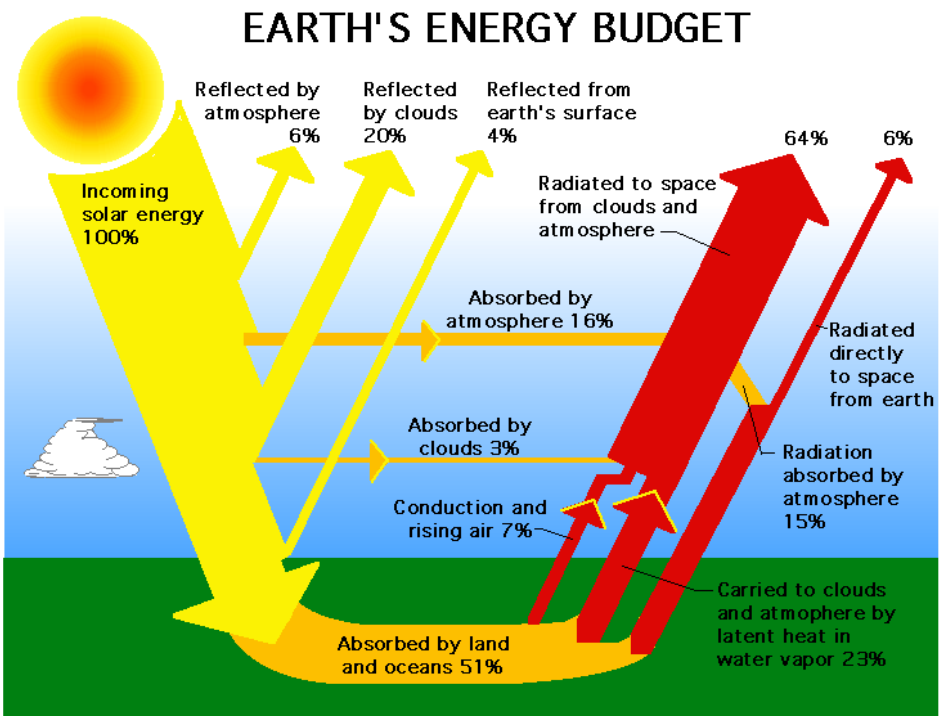

Figure 1.1: A schematic of the Earth's energy budget, Source: ERBE, Atmospheric Sciences Division, NASA LaRC.

The majority of the outgoing energy emitted from the Earth's surface is in the infra-red (IR) part of the electromagnetic spectrum (also known as longwave radiation). Although most of the IR emitted is radiated directly into space, some is absorbed by certain molecules within the Earth's atmosphere; water vapour, carbon dioxide, methane to name a few. Upon absorption these excited molecules either emit longwave radiation or transfer the surplus energy *via* collisions; a significant proportion of the emitted light is directed back down towards Earth, adding to the heat in the lower atmosphere and to the Earth's surface temperature: this phenomenon is commonly known as the greenhouse effect. The greenhouse effect is often thought as solely a negative; however, without it the average surface temperature of Earth would be -18 °C, too cold to sustain water-based life (Jacobson, 2002). Indeed the greenhouse effect is integral to the balance of incoming solar radiation and the outgoing longwave radiation, which supports life on Earth. Unfortunately, problems do arise when there are changes to this system.

1.1.2 Man's Influence on Climate Change

Between the years 1750 and 2011, fossil fuel combustion has led to the release of (1375 ± 110) Gigatonnes of CO_2 directly into the atmosphere (Cubasch et al., 2013). This rise in anthropogenic carbon-based emissions has had a marked environmental impact, altering the composition of the Earth's atmosphere and increasing CO_2 levels by 45%, from just under 280 ppm to 406.5 ppm (as of the 2nd of March 2016), since the industrial

revolution (McGee, 2016). This poses serious implications for the climate; the effects of global warming are becoming ever more apparent and over the last century the average surface temperature on Earth has increased by $0.85^{+0.21}_{-0.20}$ °C (IPCC, 2013). The observed increase in CO_2 is thought to be key to this warming as CO_2 has an associated radiative forcing (RF) value of +(1.82±0.19) W m^{-2} (Figure 1.2). Note: a positive RF value implies that respective component is contributing to global warming, whilst a negative RF suggest the component is causing a net cooling in the atmosphere.

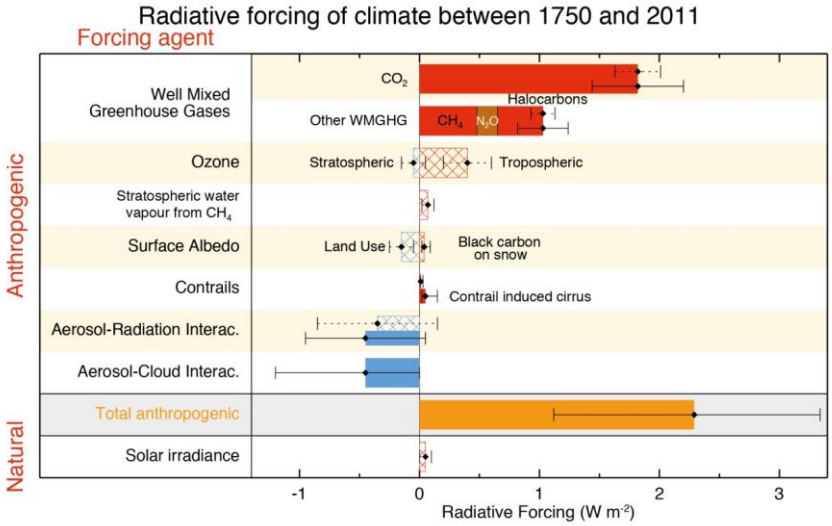

Figure 1.2: Radiative forcing diagram from the IPCC report 2013. The schematic indicates the most significant factors contributing to global warming (Hartmann et al., 2013).

There are many who deny man's influence on climate and insist that the observed increase in temperature is due to a combination of natural occurrences (such as El-Niño) and the Sun's solar cycle (Hegerl et al., 2007). However, in the past decade there have been a number of studies and reports, which have shown indisputably that anthropogenic sources are partially (if not predominantly) responsible for the observed global warming. Possibly the best example of the anthropogenic impact of global warming can be seen in Figure 1.3. In this study by Meehl et al. (2012) Community Climate System Models (CCSM4) were run to simulate the observed changes in the average global temperature. This model included all of the major components causing radiative forcing. From these simulations it was observed that neither the anthropogenic nor the natural components of the model could accurately describe the observed temperature variation; however, when both the anthropogenic and natural components were included in the model, the correlation to the temperature variation is much improved (Meehl et al., 2012).

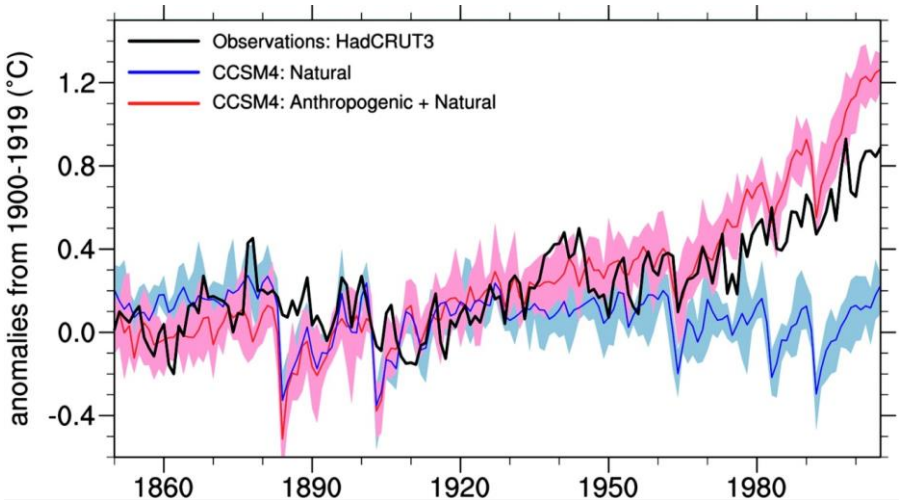

Figure 1.3: The black curve represents observations. The blue curve represents the result of a computer simulation that accounts for natural variations like volcanic eruptions and changes in the brightness of the Sun. The red curve includes all the natural variations in the blue curve, but adds human emissions like CO_2 and sulfate aerosols. The shaded blue/red areas represents the uncertainty of the simulations (Meehl et al., 2012).

In addition, due to society's current dependence on fossil fuels (a finite resource), it is almost certain there will be some sort of an energy crisis in the years to come, unless serious action is taken. It is currently estimated that the human race utilizes over 470 EJ of energy annually, 85% from fossil fuel combustion (Demirbas, 2009, Forinash, 2010). Approximately half of the energy is used by the billion people living in the most economically developed countries, conversely the one billion poorest account for only 4% of the annual primary energy use (Argiri et al., 2006). If nothing is done to reduce the need for fossil fuels it is forecast that over the next twenty years petroleum consumption may increase by up to 75%, due to greater demand in developing countries like India and China (Semelsberger et al., 2006). This will undoubtedly put considerable stress on what is a dwindling supply of energy and lead to larger annual emissions of CO_2 into the atmosphere.

It is clear that action must be taken now if we are to minimise the effects of global warming (Cubasch et al., 2013). Fortunately, with the negotiation of the Paris Agreement at the UN's COP 21 meeting in December of last year, it seems that governments around the world are starting to take climate change (and particularly man's influence upon it) seriously. However, if the reductions in greenhouse gas emissions targeted by the Paris Agreement are to be met, it is clear that a complete appreciation of the Earth's atmosphere, and in particular the reactions occurring within it, must be accurately understood; this field of research is known as atmospheric chemistry.

1.2 The Earth's Atmosphere

Although often taken for granted, the atmosphere surrounding our planet is of vital importance to sustaining life on Earth as we know it. Held close by gravitational interactions with Earth, the atmosphere is constantly changing, due to both dynamic processes and chemical reactions. The Earth's atmosphere is often classified into different layers (Figure 1.4); these layers can be described by their characteristic vertical temperature gradients (Finlayson-Pitts and Pitts Jr., 1999). The lowest level of the atmosphere is known as the troposphere; it contains between 85-90% of the atmosphere's mass and stretches out from the Earth's surface to an altitude of approximately 7 km at the poles and to 15 km at the equator. The main feature of the temperature profile in the troposphere is that the temperature decreases with increasing altitude; this is because the primary source of heating in the troposphere is due to energy transfer from the Earth's surface (Park, 1997). This negative temperature gradient leads to rapid vertical movement of gases by convection and means all species are well mixed in this region.

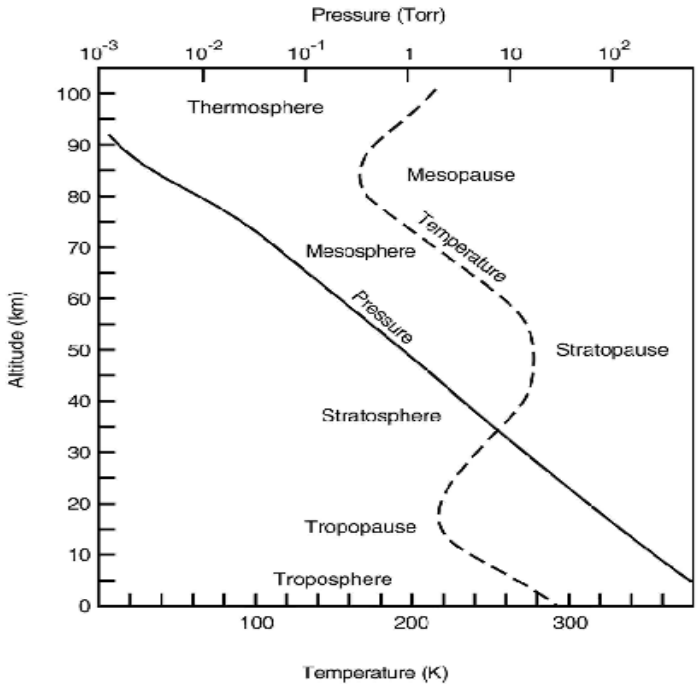

Figure 1.4: Vertical temperature profile of attitudes from 0-100 km. Taken from Finlayson-Pitts and Pitts, (2000).

Located directly above the troposphere is the stratosphere; approximately 40 km thick, it contains the vast majority of atmospheric ozone which absorbs UV light and causes the positive temperature gradient in this region (Hansen et al., 2011). In the mesosphere (~50 – 90 km in altitude) the temperature cools to less than 200 K and this region also experiences rapid mixing. Above the mesosphere comes the thermosphere and exosphere, the upper

most regions of the atmosphere. The temperature in the thermosphere is reliant or the solar activity and increases with altitude. It should be noted that the majority of the information described in the next section will concern the chemistry of the lowest part of the troposphere, also known as the boundary layer, as it is in this region of the atmosphere that the chemistry described in Chapters IV - VII predominantly occurs.

1.3 The Chemistry of the Earth's Atmosphere

In the following section of this chapter will be divided into three parts, this first being a detailed description of the basic gas-phase reactions, which control much of the chemistry in clean, remote environments. Next will be a discussion of the 'extra' chemistry introduced by anthropogenic emissions in polluted environments. Finally, the impact of biogenic emissions will be reported.

1.3.1 Atmospheric Chemistry of Remote Environments

The composition of the Earth's atmosphere, reported in Table 1.1, is primarily composed of nitrogen (78%), oxygen (21%) and argon (0.9%). However, it is the traces species which dictate much of atmospheric chemistry and have major implication for climate change, as can be seen in Figure 1.2.

Table 1.1: Chemical Composition of the Atmosphere, adapted from Brasseur et al., 1999.

Constituent	Chemical Formula	Volume Mixing Ratio (Dry Air†)	Major Sources
Nitrogen	N_2	78.084%	Biological
Oxygen	O_2	20.948%	Biological
Argon	Ar	0.943%	Inert
Carbon Dioxide	CO_2	360 ppmv *	Combustion
Neon	Ne	18.18 ppmv	Inert
Helium	He	5.24 ppmv	Inert
Methane	CH_4	1.7 ppmv	Biogenic and anthropogenic
Nitrous Oxide	N_2O	0.31 ppmv	Biogenic and anthropogenic
Carbon Monoxide	CO	50-200 ppbv	Photochemical and anthropogenic
Ozone (troposphere)	O_3	10-500 ppbv	Photochemical
Volatile Organic Compounds	RH	5-20 ppbv	Anthropogenic and biogenic
Ammonia	NH_3	10 pptv - 1 ppbv	Biogenic
Hydroxyl	OH	0.1-10 pptv	Photochemical
Hydroperoxyl	HO_2	0.1-10 pptv	Photochemical

†Excludes Water Vapour.

***Note the value quoted in Table 1.1 is from 1999, and is significantly lower than the current atmospheric concentration of CO_2, which is 406.5 ppmv (as of the 2nd of March 2016).**

One such trace species is the hydroxyl radical, OH, which, although only present in small concentrations in the atmosphere, controls much of its oxidative chemistry (Atkinson, 2000). The average lifetime of an OH radical is extremely short (τ < 1 s) as it reacts rapidly, playing a central role in the chemistry of many of the most environmentally relevant species in the atmosphere, including greenhouse gases such as ozone and methane (Smith et al., 2006). The hydroxyl radical is principally formed in the troposphere from the short wave UV photolysis of O_3 (λ < 340 nm).

$$O_3 + h\nu\ (\lambda < 340\ \text{nm}) \rightarrow O(^1D) + O_2 \quad \text{(R1.1)}$$

$$O(^1D) + H_2O \rightarrow 2\ OH \quad \text{(R1.2)}$$

Such is the oxidizing capacity of the OH radical that the atmospheric lifetimes of many trace gas species are entirely dependent on their reactivity towards OH (E1.1).

$$\tau_X = \frac{1}{k_{OH}[OH]} \quad \text{(E1.1)}$$

In equation E1.1: τ_X refers to the lifetime of species X; k_{OH} is the bimolecular rate coefficient of species X with OH; and [OH] is the atmospheric concentration of hydroxyl radicals.

Given E1.1, it is clearly of the utmost importance that both global and local concentrations of OH are accurately known (Stone et al., 2012). It should also be noted that many of the rate coefficients, k_{OH}, determined are strongly temperature dependent, meaning that their rates will vary greatly throughout the troposphere (Kurylo and Orkin, 2003). A major sink for OH in 'clean' (i.e. low NO_x) environments is reaction with CO; this reaction leads to the formation of HO_2, another important reactant within the troposphere (Stone et al., 2012).

$$OH + CO \rightarrow CO_2 + H \quad \text{(R1.3)}$$

$$H + O_2 + M \rightarrow HO_2 + M \quad \text{(R1.4)}$$

The hydroperoxyl radical (HO_2) is coupled closely to OH and is converted back to it *via* its reaction with ozone (R1.5).

$$HO_2 + O_3 \rightarrow OH + 2O_2 \quad \text{(R1.5)}$$

From reactions R1.3-1.5, it is clear that OH and HO_2 radicals are closely related and are commonly referred to as HO_x radicals. It should be noted that as these species are so closely linked, and that the main OH production pathway is *via* photolysis, that both these species exhibit a diurnal variation in concentration.

Together the HO_x radicals are responsible for the oxidation of the majority of volatile organic compounds (VOCs) present in the troposphere (Jacob, 1999). It is therefore unsurprising that the OH radical is key in the tropospheric oxidation of hydrocarbons; indeed OH is directly involved in the initiation of methane oxidation (Wayne, 1991).

$$OH + CH_4 \rightarrow CH_3 + H_2O \quad \text{(R1.6)}$$

The next step of oxidation process involves reaction with O_2 forming the methylperoxy radical, CH_3O_2; this family of radicals are commonly referred to as RO_2 species (Finlayson-Pitts and Pitts Jr., 1999).

$$CH_3 + O_2 + M \rightarrow CH_3O_2 + M \quad \text{(R1.7)}$$

It should be noted that this is not the end of the oxidation process for methane and it will eventually be converted into CO_2 in the atmosphere (the oxidation total process can take many years). In R1.7, M is a third body species, which in the atmosphere is typically N_2 or O_2.

Significantly, both HO_2 and RO_2 radicals play an important role in the destruction of tropospheric HO_x radicals in 'clean' environments (Whalley et al., 2010).

$$HO_2 + HO_2 \rightarrow H_2O_2 + O_2 \quad \text{(R1.8)}$$

$$HO_2 + RO_2 \rightarrow ROOH + O_2 \quad \text{(R1.9)}$$

Summarized above (R1.1-1.9) are some of the most important reactions in unpolluted environments. Notably, this mechanism is simplified and many other reactions and species are involved. However, these reactions do seem to control much of the chemistry in clean environments and there has generally been good agreement between field measurements and atmospheric models in unpolluted regions (Heard and Pilling, 2003).

1.3.2 Chemistry of Polluted Environments

In polluted environments, much of the chemistry is surprisingly similar; of course the composition of VOCs is different, as the local sources will be anthropogenic, rather than from natural sources; however the oxidation paths of these differing VOCs does not cause major changes in the generic chemistry of the troposphere (Finlayson-Pitts and Pitts Jr., 1999). The most notable difference between clean and polluted environments is that the concentrations of the nitrogen oxides, NO and NO_2 (collectively known as NO_x), are significantly higher in polluted environments. The major source of NO_x is automotive emissions, a process that was highlighted last year by the Volkswagen emission scandal, where it was observed that several different diesel models were producing NO_x levels up to

40 times the legislated maximum set by the US Environmental Protection Agency (EPA). It was later discovered that Volkswagen were aware of this problem and had falsified the test results to meet the required standards (Schiermeier, 2015). NO_x is formed when combustion takes place in the presence of nitrogen; as a by-product of combustion, NO_x levels are generally elevated in urban areas, where traffic congestion is higher. Within the atmosphere, NO and NO_2 rapidly interconvert, significantly this cycle also produces tropospheric ozone (Brasseur et al., 1999).

$$NO_2 + h\nu\ (\lambda < 430\ nm) \rightarrow NO + O(^3P) \quad \text{(R1.10)}$$

$$O(^3P) + O_2 + M \rightarrow O_3 + M \quad \text{(R1.11)}$$

$$NO + O_3 \rightarrow NO_2 + O_2 \quad \text{(R1.12)}$$

As reactions R1.10-1.12 are all fast the following steady state for O_3 can be determined:

$$[O_3] = \frac{J_{10}[NO_2]}{k_{12}[NO]} \quad \text{(E1.2)}$$

In equation E1.2: J_{10} is the rate coefficient for the photolysis of R1.10; and k_{12} is the rate coefficient for reaction R1.12. The full derivation of this steady state approximation for ozone can be found in Appendix A.

Although stratospheric ozone plays a vital role in protecting life from harmful shortwave UV radiation, the formation of tropospheric ozone is largely detrimental. The formation of tropospheric ozone is predicted to enhance global warming, as it has a positive radiative forcing value of $+0.4\ W\ m^{-2}$ (Myhre et al., 2013). Furthermore, tropospheric ozone is a major component of photochemical smog, a mixture of several pollutants, which include: ozone; particulate matter; peroxyacetyl nitrate (PAN); and NO_x. Photochemical smog typically forms above large conurbations; particularly in areas where traffic congestion is high. Additionally, photochemical smog has adverse health effects on human life, causing eye irritation and respiratory problems (Elsom, 2013). The formation of tropospheric ozone is also important as the reaction between ozone and alkenes is thought to be a key source of night-time OH (Emmerson et al., 2005). Specifically, OH is formed from the decomposition of Criegee intermediates; note that, Criegee intermediates will be discussed in greater detail in the following section.

Both NO and NO_2 are involved are several key reactions within the troposphere; indeed, NO is an important reducing agent for both HO_2 and RO_2 in polluted environments (R1.13-1.14); both of these reactions are closely linked to the HO_x cycle.

$$HO_2 + NO \rightarrow OH + NO_2 \quad \text{(R1.13)}$$

$$RO_2 + NO \rightarrow RO + NO_2 \quad \text{(R1.14)}$$

where RO ≡ R(O·)H

$$R(O\cdot)H + O_2 \rightarrow RC{=}O + HO_2 \quad \text{(R1.15)}$$

It should be noted that in polluted environments reaction R1.14 dominates over reactions R1.9; this amplifies the net ozone production (Hanst, 1971), because R1.14 simultaneously increases the formation of NO_2 and decrease [NO] (see E1.2).

NO_2 is also involved in other important atmospheric reactions. In particular, NO_2 plays a crucial role in the formation of the molecule PAN, another major component of photochemical smog.

$$CH_3CO + O_2 + M \rightarrow CH_3C(O)O_2 + M \quad \text{(R1.16)}$$

$$CH_3C(O)O_2 + NO_2 \rightleftharpoons CH_3C(O)O_2NO_2 \quad \text{(R1.17)}$$

As well as being a component of photochemical smog, PAN is also a known reservoir for NO_x radicals, as PAN eventually decomposes to form NO_2 (R1.17). Moreover, as PAN decomposition is a relatively slow process, therefore PAN can travel long distances before decomposing; thus PAN facilitates the transport of NO_x away from polluted regions to remote environments (Fischer et al., 2014).

However, PAN cannot be formed without acetyl (CH_3CO) radicals (R1.16); the main pathway to acetyl radical formation in the troposphere is primarily from the hydrogen abstraction of acetaldehyde by OH (R1.18).

$$CH_3CHO + OH \rightarrow CH_3CO + H_2O \quad \text{(R1.18)}$$

From reaction R1.18 it can be seen that acetaldehyde (CH_3CHO) is the other key precursor to PAN formation; acetaldehyde is both a primary and secondary pollutant in the atmosphere. Note that primary pollutants are emitted directly into the atmosphere, whereas secondary pollutants are formed within the atmosphere itself. For example, acetaldehyde is formed during combustion; in particular, it is a major product of bioethanol combustion and enhanced acetaldehyde concentrations have been observed in Sao Paulo, where bioethanol is commonly used as fuel (Corrêa et al., 2003). Additionally, acetaldehyde can also be formed within the atmosphere and is a product from the oxidation of both ethane and ethanol (Singh and Hanst, 1981, Calvert, 2011).

It should be highlighted that R1.18 is the focal reaction of Chapter IV of this thesis. It is clear that in order to fully understand the formation, concentration and overall impact of

PAN in the troposphere, an accurate understanding of the precursors to PAN formation (such as the chemistry of acetyl radicals) must be appreciated. In particular, the investigation in Chapter IV focuses on an additional reaction channel: the chemically activated decomposition of acetyl radicals (R1.19).

$$CH_3CHO + OH \rightarrow CH_3CO^* + H_2O \quad \text{(R1.18a)}$$

$$CH_3CO^* \rightarrow CH_3 + CO \quad \text{(R1.19)}$$

1.3.3 Chemistry of Remote Forested Regions

It is currently estimated that biogenic volatile organic compounds (BVOCs) emissions may be responsible for the release of 1150 Tg of carbon per year (Guenther et al., 1995), although this value is subject to a considerable uncertainty, dependent on many variables, such as; temperature, solar radiation and plant type (Guenther, 2006). Unsurprisingly, this leads to significant ambiguity on the total mass of BVOCs released into the atmosphere (Laothawornkitkul et al., 2009). These biological emissions are primarily produced by plants, and are predominately members of the terpene family. By far the most abundant of these emissions is the hemiterpene, isoprene (C_5H_8), which is thought to be responsible for approximately ~45% of all BVOC emissions (Guenther et al., 1995).

Within the troposphere most BVOCs are oxidised, and hence removed, by the hydroxyl radical; these initial products then undergo further oxidation to form RO_2 (R1.20-1.21).

Where R′=R″ is a generic VOC:

$$OH + R'=R'' \rightarrow R \quad \text{(R1.20)}$$

and R arises from OH addition to the double bond

$$R + O_2 + M \rightarrow RO_2 + M \quad \text{(R1.21)}$$

In remote forested environments (low NO_x), the fate of the RO_2 formed is predominately dependent on both self-reaction (i.e. $RO_2 + RO_2$), or removal by HO_2 (Tyndall et al., 2001). The oxidation path described should lead to a net loss of both HO_x and O_3 in such environments. However, a number of recent studies have highlighted serious inadequacies in the BVOC oxidation process, where the models systematically underestimate the OH concentration, leading to the belief of a significant ‘missing’ source of OH (Lelieveld et al., 2008, Whalley et al., 2011). Thus far, the most plausible ‘missing’ sources of HO_x proposed are the RO_2 radicals formed from R1.21, which are highly oxygenated, due to the addition of OH across the double-bond. These oxygenated peroxy radicals may follow several different reaction pathways, some of which may recycle HO_x radical; for example the HO_x recycling pathways in the Leuven Isoprene Mechanism can yield up to a factor of four

increase in the modelled [OH], explaining the previous discrepancies between the measured and the modelled data (Peeters et al., 2009, Stavrakou et al., 2010).

Another important sink for unsaturated BVOCs is the reaction with ozone, which attacks across the carbon-carbon double bond forming an intermediary ozonide species, which rapidly decomposes leading to the formation of both a carbonyl species and a Criegee intermediate (CI). In recent years there has been significant interest in CIs as potential oxidants in forested areas. Indeed, a recent study from a boreal forest in Hyytiälä, Finland, suggests that CIs may have the capacity to oxidize sulphur dioxide, a reaction which has significant impact on both local sulphuric acid and sulphate aerosol concentrations (Mauldin et al., 2012). Moreover, the kinetics of both the C_1 and C_2 CIs (CH_2OO and CH_3CHOO respectively) have been directly measured for the first time and have been shown to react rapidly with both SO_2 and NO_2 (Welz et al., 2012, Taatjes, 2013); the results from these studies indicate that CIs could have a considerable impact on regional sulphuric acid concentrations (Percival et al., 2013). Notably, the reactivity of Criegee Intermediates with atmospheric trace gases was the topic of much of the research to be discussed in this thesis and further details can be found in Chapters V, VI and VII.

The impact of the chemistry of BVOCs on the climate is uncertain, largely due to the uncertainties in both the emission flux and the oxidation pathways, highlighted above. However, there are several ways in which these processes can change radiative forcing in remote forested environments. Firstly, like all organic compounds the eventual atmospheric fate of species is conversion to CO_2; therefore, BVOC emissions have a direct impact on the atmospheric CO_2 concentrations and hence will contribute to global warming. Additionally, some of the initial oxidants of BVOCs have low vapour pressures and hence enter the particle phase (solid or aerosol), leading to increased particulate matter and aerosols in these regions. Although uncertain, it is suspected that atmospheric aerosols will have a negative radiative forcing (Figure 1.2). So far, the potential climate impacts mentioned are speculative, however, what is known is that if global warming continues and the Earth's global average temperature continues to rise, the rate of BVOC emission will increase which will enhance all the chemistry described above (Peñuelas and Llusià, 2003). Clearly, then it is of the utmost importance that the chemistry of these regions is well understood, so that the future of these can be more accurately simulated. Note: the emission rate of isoprene starts to decrease above 40°C; therefore in tropical environments where temperatures are very high, further warming may actually lead to a decrease in BVOC emissions (Laothawornkitkul et al., 2009).

Having now briefly discussed the fundamental reactions controlling the chemistry of the troposphere, the focus of this chapter will be shifted. All of the worked discussed in this thesis is based around the field of reaction kinetics; therefore, the remainder of this chapter aims to give a brief outline of some of the theory behind reaction kinetics.

1.4 Theories of Chemical Reactions and Reaction Kinetics

1.4.1 An Introduction to Reaction Kinetics and the Rate Equation

Reaction kinetics is a branch of physical chemistry concerning the measurement of rates of reaction. Generically, chemistry could be described as the study of chemical reactions; therefore understanding the kinetics of a reaction is of fundamental importance in chemistry (Pilling and Seakins, 1995). Although, theoretical studies are becoming ever more important within the field, reaction kinetics is still driven, primarily, by experimental work. Up until the middle of the 20th century, the field of reaction kinetics was limited to the study of relatively slow reactions; however, the development of new techniques exploiting faster electronics, lasers and more sensitive detection techniques, have enabled the kinetics of increasingly reactive species to be probed. Indeed, the timescales upon which reactions can be probed has been reduced to the point where the reaction dynamics (i.e. the mechanisms by which the reactions take place) may now be probed. Note that, the timescale over which dynamics are measured is ~10^{-15} s; this can be achieved using a femtosecond laser.

The rate of reaction may be described as the rate of decrease of the reactant concentration (i.e. $-\frac{d[\mathrm{A}]}{dt}$, R1.22), or the rate of increase in the concentration of products (i.e. $\frac{d[\mathrm{C}]}{dt}$, R1.22).

$$\mathrm{A} + \mathrm{B} \rightarrow \mathrm{C} \qquad \text{(R1.22)}$$

For all chemical reactions a generic rate equation can be written. For the reaction shown above (R1.22) the rate equation is:

$$-\frac{d[\mathrm{A}]}{dt} = k[\mathrm{A}]^{\alpha}[\mathrm{B}]^{\beta} \qquad \text{(E1.3)}$$

In equation E1.3: $-\frac{d[\mathrm{A}]}{dt}$ is the rate of reaction; k is a constant of proportionality, termed the rate coefficient/constant (note: not actual constants of proportionality as values of k can vary with both temperature and pressure); [A] and [B] are the concentrations of A and B respectively; finally, α and β are the orders of the reaction, with respect to [A] and [B]. Crucially, the exponents α and β can only be determined experimentally; these exponents tell us how the rate of the reaction will vary with concentration of the associated reactant (Pilling and Seakins, 1995). Commonly, the orders with respect to the reactants will be; 0, 1, 2 (and very occasionally 3); furthermore the total order of the reaction is equal to α + β. It

should be noted that the rate equation of certain reactions can be predicted provided the reaction mechanism is understood. Species involved in (or prior to) the rate determining step (RDS) of the reaction will, generally, appear in the rate equation; conversely species involved after to the RDS do not appear in the rate equation (i.e. are 0th order). For elementary (one-step) reactions, around which this thesis is based, the molecularity (i.e. the number of molecules involved in the collision complex) is equivalent to the total order of the reaction. Indeed, the majority of the reactions studied for this thesis were bimolecular reactions (i.e. 2nd order). Furthermore, the rates of these reactions were all monitored using the pseudo first-order kinetics; a concept which will be discussed in detail in Section 1.5.

Although the field of reaction kinetics still does rely heavily upon experimental measurements to give insight into rate of chemical reactions, rate coefficients can also be determined theoretically; the theoretical approach has become more common in recent years, as advances in technology have made theoretical work quicker, cheaper and more accurate than in years past. In the subsequent sections of this chapter some fundamental theories used to determine rate coefficients for elementary reactions will be discussed: collision theory and transition state theory (TST).

1.4.2 Collision Theory

Collision theory is the simplest of the theories which can be used to calculate the rate coefficient for an elementary chemical reaction. In collision theory it is assumed that the species reacting behave as hard spheres, and that a reaction may only occur upon/during a collision (i.e. no interacting forces between the species). Using collision theory an estimation of the rate coefficient of the species A and B, of radii r_A and r_B respectively, can be made; however, the first step is to calculate the collision rate per unit volume, Z_{AB} (Pilling and Seakins, 1995).

$$Z_{AB} = \sigma_{AB} \times \left(\frac{8k_B T}{\pi\mu}\right)^{\frac{1}{2}} \times [A][B] \quad \text{(E1.4)}$$

where:

$$\sigma_{AB} = \pi \times (r_A + r_B)^2 \quad \text{(E1.5)}$$

In equations E1.4-1.5: σ_{AB} is the collision cross sectional area; the term $\left(\frac{8k_B T}{\pi\mu}\right)^{\frac{1}{2}}$ refers to the Maxwell distribution, which describes the speeds of the individual molecules; k_B is the Boltzmann constant; T is the temperature (K); μ is the reduced mass of A and B; and of [A] and [B] are the concentrations of A and B respectively.

There is a problem with E1.4 as a model of the reaction between A and B, and that is not all collisions lead to a chemical reaction. The primary reason for this is that not all collisions

have sufficient energy to exceed the activation barrier to the reaction. Again, if a Maxwell-Boltzmann distribution of energy is considered the fraction of collision with sufficient energy to react, f_E can be described by the following equation (E1.6).

$$f_E = e^{\left(-\frac{E_A}{RT}\right)} \tag{E1.6}$$

therefore:

$$\rho = \sigma_{AB} \times \left(\frac{8k_B T}{\pi\mu}\right)^{\frac{1}{2}} \times e^{\left(-\frac{E_A}{RT}\right)} \times [A][B] \tag{E1.7}$$

note that if: $k = \frac{\rho}{[A][B]}$ and $Z'_{AB} = \sigma_{AB} \times \left(\frac{8k_B T}{\pi\mu}\right)^{\frac{1}{2}}$

$$k = Z'_{AB} \times e^{\left(-\frac{E_A}{RT}\right)} \tag{E1.8}$$

In equations E1.6-1.8: E_A is the minimum energy required to surmount the activation barrier (i.e. the activation energy); R is the ideal gas constant; ρ is rate of reaction (taking concentrations of A and B into account); and k is the rate coefficient for the reaction between A and B.

One final amendment is needed before the equation for collision theory is complete. Notably, a reaction will not occur between species A and B unless they are oriented in the correct manner. However, thus far, no steric factor for the reaction has been applied to the collision theory model (E1.8). This is rectified in E1.9; where a steric factor, P_S, has been included:

$$k = Z'_{AB} \times P_S \times e^{\left(-\frac{E_A}{RT}\right)} \tag{E1.9}$$

Although a good starting point for the estimation of reaction rate coefficients, there are several major problems when using collision theory to calculate reaction rate coefficients. The first is the assumption that the reacting species are equivalent to hard spheres as it completely ignores the structure of the molecules/species in general, which can dictate how the species react. It should be noted that the steric factor does try to account for this, but it is not predictive. The second problem is that collision theory assumes the reaction between A and B occurs instantaneously upon impact, this assumption is again inaccurate. Indeed, not only do most reactions form a pre-reaction complex, but there are also often long-distance interactive forces occurring between the reacting species (i.e. permanent or temporary charges); clearly, the assumption that the reaction is instantaneous is a poor one (Pilling and Seakins, 1995).

To obtain more accurate theoretical estimations of rate coefficients a more sophisticated model is necessary, such as transition state theory (TST).

1.4.3 Transition State Theory

Unlike collision theory, transition state theory accounts for the formation of an activated complex species as an intermediary between the reactants and the products (Figure 1.5). Notably, the transition state ($AB^{\ddagger}$) is located at the highest energy point along the reaction coordinate. For reaction R1.22 the following differential rate equation is given:

$$\frac{d[\mathrm{C}]}{dt} = k[\mathrm{A}][\mathrm{B}] \qquad \text{(E1.10)}$$

where $\frac{d[\mathrm{C}]}{dt}$ is the rate of change of the concentration of the products, C, with time; k is the rate coefficient for the reaction; and [A] and [B] and the concentrations of A and B.

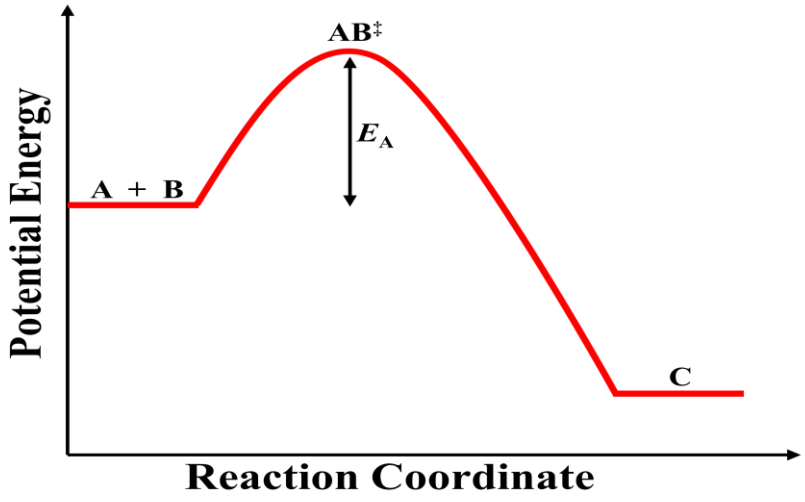

Figure 1.5: A schematic of a typical reaction profile, where $AB^{\ddagger}$ is the transition state species (or activated complex) and E_A is the energy required to surmount the activation barrier.

If we apply transition state theory to reaction R1.22, the following reactions can be used to fully describe the system:

$$\mathrm{A} + \mathrm{B} \rightleftharpoons \mathrm{AB}^{\ddagger} \qquad \text{(R1.23)}$$

$$\mathrm{AB}^{\ddagger} \rightarrow \mathrm{C} \qquad \text{(R1.24)}$$

Note that each of these reactions R1.23-1.24 have the following individual rate coefficients: the rate coefficient for the forward reaction of R1.23 is k_{A+B}; the reverse reaction of R1.23 is k_{-A+B}; and the rate coefficient for R1.24 is k_{AB}.

The following differential rate equation for the products of the reaction can be determined:

$$\frac{d[\mathrm{C}]}{dt} = k_{\mathrm{AB}}[\mathrm{AB}^{\ddagger}] \tag{E1.11}$$

Furthermore, transition state theory assumes that a quasi-equilibrium exists between the reactant and the intermediary species, $AB^{\ddagger}$:

$$K^{\ddagger} = \frac{[\mathrm{AB}^{\ddagger}]}{[\mathrm{A}][\mathrm{B}]} \tag{E1.12}$$

By combining equations E1.10-1.12 the following equations can be derived:

$$k[\mathrm{A}][\mathrm{B}] = k_{\mathrm{AB}}K^{\ddagger}[\mathrm{A}][\mathrm{B}] \tag{E1.13}$$

therefore:

$$k = k_{\mathrm{AB}}K^{\ddagger} \tag{E1.14}$$

However, before TST can be used to determine the rate coefficient of reaction R1.22, k; the rate coefficient, k_{AB}, and the equilibrium constant, $K^{\ddagger}$, must be defined. $K^{\ddagger}$ can be expressed as a product of an exponential function dependent upon the size of the activation barrier (denoted by $\Delta H^{\ddagger}$ in E1.15), and the molecular partition functions of species A, B and the activated complex $AB^{\ddagger}$; where the molecular partition functions are Q_{A}, Q_{B} and Q_{AB} respectively.

$$K^{\ddagger} = \left(\frac{Q_{\mathrm{AB}}}{Q_{\mathrm{A}}Q_{\mathrm{B}}}\right)e^{\left(-\frac{\Delta H^{\ddagger}}{RT}\right)} \tag{E1.15}$$

As the energy required to dissociate $AB^{\ddagger}$ is minimal, meaning that every time $AB^{\ddagger}$ stretches along the A-B bond, the transition state will fragment to either reactants or products (Engel and Reid, 2006). This means that k_{AB} is proportional the vibrational frequency, ν, coaxial to the A-B bond (E1.16). Note: k_{AB} is not equal to ν as a fraction of the vibrations along A-B also lead to the formation of the reactants A + B, and not the products C.

$$k_{\mathrm{AB}} = \kappa\nu \tag{E1.16}$$

In equation E1.16: ν is the vibrational frequency of the A-B bond; and κ is the proportionality constant for the fraction of ν which leads to formation of the product, C. Moreover, as this degree of freedom along the A-B bond corresponds to an easily dissociated vibrational stretch (leading to product formation), it can be described by a vibrational partition function, q_{AB}, where the vibrational frequency, ν, will tend towards zero (E1.17-1.18).

$$q_{\mathrm{AB}} = \frac{1}{1 - e^{\left(-\frac{h\nu}{k_{\mathrm{B}}T}\right)}} \tag{E1.17}$$

As $\nu \rightarrow 0$, and $h\nu << k_{\mathrm{B}}T$:

$$q_{\mathrm{AB}} \approx \frac{1}{1 - \left(1 - \frac{h\nu}{k_{\mathrm{B}}T}\right)} \approx \frac{1}{\left(\frac{h\nu}{k_{\mathrm{B}}T}\right)} \approx \frac{k_{\mathrm{B}}T}{h\nu} \tag{E1.18}$$

This adjustment to the partition function means that the equilibrium constant must be redefined. In equation E1.19: Q^{*}_{AB} is the molecular partition function for the transitory species, $\mathrm{AB}^{\ddagger}$, which excludes the contribution from the stretching mode that leads to dissociation.

$$K^{\ddagger} = q_{\mathrm{AB}} \left(\frac{Q^{*}_{\mathrm{AB}}}{Q_{\mathrm{A}}Q_{\mathrm{B}}}\right) e^{\left(-\frac{\Delta H^{\ddagger}}{RT}\right)} \tag{E1.19}$$

When all of these factors are taken into account, the overall rate coefficient, k, can be defined (E1.20).

$$k = \kappa \frac{k_{\mathrm{B}}T}{h} \left(\frac{Q^{*}_{\mathrm{AB}}}{Q_{\mathrm{A}}Q_{\mathrm{B}}}\right) e^{\left(-\frac{\Delta H^{\ddagger}}{RT}\right)} \tag{E1.20}$$

An advantage of TST over collision theory is that it inherently includes molecular complexity. However, what is also clear from E1.20 is that rate coefficients often exhibit temperature dependence; a dependence which is proportional to the activation barrier of the reaction (see Figure 1.5).

1.4.4 Temperature and Pressure Dependence

The majority of the experiments reported in this thesis were conducted at room temperature and at constant, but low, pressures (i.e. the temperature and pressure dependencies were not probed). However, the rate coefficients of many atmospheric (and combustion) reactions can vary greatly over quite a narrow range of temperatures and pressures (Seinfeld and Pandis, 2012). Moreover, both temperature and pressure within the Earth's atmosphere vary sufficiently to cause significant change to certain rate coefficients (Figure 1.4), it is important that the concepts behind temperature and pressure dependencies are understood. Indeed, in order to make the results from some of the reactions investigated for this thesis more relevant to the atmosphere, where the reactions in question take place, calculations (executed by R. Shannon) were employed to test the pressure dependence.

1.4.4.1 Temperature Dependence

Within the field of reaction kinetics the generic equation used to describe positive temperature dependencies is called the Arrhenius equation, E1.21. Moreover, both

equations E1.9 and E1.20 can be considered as variations upon the, aforementioned, Arrhenius equation.

$$k_{(T)} = A \times e^{\left(-\frac{E_A}{RT}\right)} \quad \text{(E1.21)}$$

In equation E.121: $k_{(T)}$ is the rate coefficient as a function of temperature; and A is a parameter known as the pre-exponential factor.

From equation E1.21 it can be seen that as the temperature is increased the exponential term, $e^{\left(-\frac{E_A}{RT}\right)}$, increases; therefore, for species which exhibit Arrhenius behaviour, the rate of reaction will increase as the temperature increases. This can be explained by returning to the potential energy surface in Figure 1.5., a schematic of reaction R1.22, which has an activation barrier of E_A. As the temperature increases the proportion of reactants with sufficient energy to overcome the activation barrier, E_A, will be larger; meaning the overall reaction rate will increase. Furthermore, at higher temperatures the reactants will also have more kinetic energy which will lead to an increase in the collision frequency of the interacting molecules (properties of the pre-exponential factor), which will again cause an increase in the reaction rate. Notably, by using transition state theory, there is the potential to predict the temperature dependencies of reactions which exhibit Arrhenius behaviour.

However, not all reactions behave in this manner; indeed, some reactions (such as barrierless reactions) exhibit negative temperature dependencies, meaning they occur faster at lower temperatures. For example, as barrierless reactions have negligible activation barriers (Figure 1.6), the exponential term in the Arrhenius equation, $e^{\left(-\frac{E_A}{RT}\right)}$, becomes equal to 1 at all temperatures, meaning increasing the temperature will not increase the reaction rate. Moreover, as temperature increases the energy of the reactants increases and hence the nascent energy of the formed complex (i.e. O_3* for the example in Figure 1.6), is also higher. This means that the re-dissociation back to reagents is faster as there is more vibrational energy stored in the products, O_3, hence it is more likely that sufficient energy is located in the bond, making dissociation more probable. Additionally as the O_3* is higher in energy more collisions are required to stabilize it, giving more time for re-dissociation.

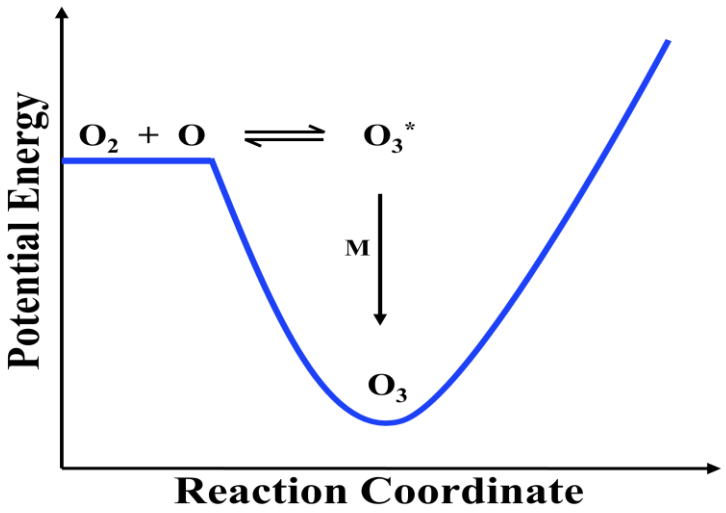

Figure 1.6: The potential energy surface for the barrierless reaction: $O_2 + O + M \rightarrow O_3 + M$.

Unfortunately, conventional TST does a poor job at determining the rate coefficients of barrierless reactions. Within TST there is a fundamental assumption that during the course of a reaction, the apex of the reaction coordinate (i.e. the saddle point) is not crossed more than once (Tromp and Miller, 1986). Although this assumption works well for reactions where the energy within the system is small in comparison to the activation barrier, it proves less accurate for reactions where the barriers to activation are insignificant. Moreover, for the second scenario described, rate coefficients tend to be overestimated as multiple recrossing over the saddle point can occur (Pritchard, 2005). However, the temperature dependence of such reactions (i.e. barrierless reactions) can be determined by using variational transition state theory (VTST) to locate the position of the transition state (where there is a minimum in the number of ro-vibrational states) on the potential energy surface (Truhlar and Garrett, 1984).

In order to interpolate between determinations of rate coefficients for barrierless processes or to extrapolate slightly beyond the measured range, the temperature dependencies can be parameterized using empirical descriptions of the reaction in the form:

$$k_{(T)} = A\left(\frac{T}{298\ K}\right)^{-n} \qquad \text{(E1.22)}$$

where *A* and n are determined through fitting to experimental observations.

Additionally, recent work at the University of Leeds has shown that even certain reactions with activation barriers demonstrate a strong negative temperature dependence at very low temperatures due to quantum mechanical tunnelling (QMT) through the activation barrier (Shannon et al., 2010, Shannon et al., 2014).

1.4.4.2 Pressure Dependence and Chemical Activation

Bond-forming reactions (such as association reactions) are characteristically exothermic by nature; additionally, these reactions can also be pressure dependent (Pilling and Seakins, 1995). For example, if we return to the association reaction of ozone (R1.25-1.26):

$$O_2 + O \rightleftharpoons O_3^* \quad \text{(R1.25)}$$

$$O_3^* + M \rightarrow O_3 + M \quad \text{(R1.26)}$$

The formation of a chemical bond is always accompanied by an energy release; as the newly formed product is more energetically stable than the reactants from which it is formed (Figure 1.6). As a consequence of this the nascent product formed has an excess of energy (denoted by '*' in R1.25-1.26); indeed, the internal energy stored within product (i.e. O_3^*) is sufficient to cause the nascent molecule to dissociate back to the reactants. However, if the excited molecule, O_3^*, is allowed to collide with a 'third body' species, M, some of the energy from the excited ozone radical can be transferred to this species, meaning the nascent O_3 species no longer has sufficient energy for dissociation (Hippler et al., 1990). This means at higher pressure where the concentration of M is greater, the stabilization reaction (R1.26) is more competitive with the dissociation reaction, and hence the rate of reaction is increased at higher pressures.

It should be noted that the most of the reactions discussed in the results section of this thesis are pressure independent; the reactions of the C_1 Criegee with SO_2 and NO_2 have be shown to be independent of pressure (Stone et al., 2014). Conversely, the alternative channel for the CH_3CHO + OH reaction discussed Chapter IV is predicted to exhibit a pressure dependence due to the formation of a chemically activated acetyl radicals. However, it should be highlighted that the pressure dependence determined by R. Shannon using master equation analysis was found to be minimal.

Notably, chemical activation occurs when a nascent and excited species has more than one possible exit channel, for example in the case of the acetaldehyde and OH reaction the nascent acetyl radicals can either be collisionally stabilized or they can decompose to produce CH_3 and CO radicals:

$$CH_3CHO + OH \rightarrow H_2O + CH_3CO^* \quad \text{(R1.18a)}$$

$$CH_3CO^* + M \rightarrow CH_3CO + M \quad \text{(R1.27a)}$$

$$CH_3CO^* \rightarrow CH_3 + CO \quad \text{(R1.27b)}$$

The process of chemical activation will be discussed further in Chapter IV.

1.5 Determination of Rate Coefficients: Experimental Methods

In Section 1.4, a brief introduction to the topic of reaction kinetics was given and within this the concept of the rate equation was presented. Within this section, Section 1.5, this theory will be expanded to include the integrated rate equation, which relates kinetic theory to experimental methods.

1.5.1 Integrated Rate Equations

From E1.3 it can be seen that the rate equation is a differential equation; therefore, to relate the concentration of the reactants directly with time, the rate equation must be integrated. Obviously, the generic integrated rate equations determined are dependent on the order of the reaction. The determination of the integrated rate equation for a generic (and elementary) first-order reaction (R1.29) will be shown below; note, further details for 0^{th} and 2^{nd} order processes can be found in Table 1.2 (Mortimer and Taylor, 2002).

$$\mathrm{A} \rightarrow \mathrm{B} \tag{R1.29}$$

R1.29 yields the following rate equation:

$$-\frac{d[\mathrm{A}]}{dt} = k[\mathrm{A}]^1 = k[\mathrm{A}] \tag{E1.23}$$

This can be rearranged to:

$$\frac{d[\mathrm{A}]}{[\mathrm{A}]} = -k\,dt \tag{E1.24}$$

Then integrated between: $[\mathrm{A}]_0$, $[\mathrm{A}]_t$ and 0, t

$$\int_{[A]_0}^{[A]_t} \frac{1}{[\mathrm{A}]} d[A] = \int_0^t -k\,dt \tag{E1.25}$$

$$\ln([\mathrm{A}]_\mathrm{t}) - \ln([A]_0) = \ln\left(\frac{[\mathrm{A}]_\mathrm{t}}{[\mathrm{A}]_0}\right) = -kt \tag{E1.26}$$

If the exponential of both sides is taken:

$$\frac{[\mathrm{A}]_\mathrm{t}}{[\mathrm{A}]_0} = e^{-kt} \tag{E1.27}$$

$$[\mathrm{A}]_\mathrm{t} = [\mathrm{A}]_0 e^{-kt} \tag{E1.28}$$

In equations E1.23-1.28: $[\mathrm{A}]_0$ is equivalent to the concentration of A at time = 0; similarly, $[\mathrm{A}]_t$ is equal to the concentration of A at time = t. From E1.27 it can be seen that first-order decay processes are exponential by nature. Furthermore, by rearranging E1.26, it can be seen that the rate coefficient, k, can be determined from a plot of ln([A]) vs. t.

E1.26 can also be rearranged into the form $y = mx + c$:

$$\ln([\mathrm{A}]_\mathrm{t}) = -kt + \ln([\mathrm{A}]_0) \tag{E1.29}$$

Using E1.29 it can be seen that the gradient of a ln([A]) vs. t plot will be equivalent to $-k$.

Table 1.2: Details of rate equations (Eqn) and integrated rate equations for 0th, 1st and 2nd order processes. Note: M is equivalent to mole dm^{-3} (or more commonly molecule cm^{-3} in gas kinetics).

Order	Rate Eqn	Integrated Rate Eqn	Characteristic Plot	Gradient of plot	Units of *k*
0th	$-\frac{d[\mathrm{A}]}{dt} = k$	$[\mathrm{A}]_t = [\mathrm{A}]_0 - kt$	[A] vs. *t*	-*k*	M s^{-1}
1st	$-\frac{d[\mathrm{A}]}{dt} = k[\mathrm{A}]$	$[\mathrm{A}]_t = [\mathrm{A}]_0 e^{-kt}$	ln([A]) vs. *t*	-*k*	s^{-1}
2nd	$-\frac{d[\mathrm{A}]}{dt} = k[\mathrm{A}]^2$	$\frac{1}{[\mathrm{A}]_t} = kt + \frac{1}{[\mathrm{A}]_0}$	1/[A] vs. *t*	*k*	M^{-1} s^{-1}

Table 1.2 yields vital information about the nature of 0th, 1st and 2nd order reactions respectively; crucially, this table provides an insight as to the method by which both the reaction order and rate coefficient can be determined experimentally. For example: if a reaction is thought to be second-order with respect to A (see R1.30), then a 1/[A] vs. *t* graph can be plotted. If this 1/[A] vs. *t* plot is linear with a positive gradient, then it is known the reaction is second-order with respect to A and the rate coefficient is equal to the gradient of the plot (Mortimer and Taylor, 2002).

$$\mathrm{A} + \mathrm{A} \rightarrow \mathrm{B} \qquad \text{(R1.30)}$$

Although it is important to understand the kinetics of the differing reactions described above, the majority of the reactions studied within this thesis were bimolecular processes involved two differing species (R1.22). To extract the kinetics from this sort of reaction requires a different methodology.

1.5.2 The Isolation Method: Pseudo First-Order Kinetics

As might be expected, when more than one reactant is involved in the integrated rate equation, understanding the kinetics with respect to the reactants becomes more complex; as the concentration of multiple, different species are all changing simultaneously. Commonly, the isolation method is used to simplify this type of reaction system.

The isolation method works by limiting the change in concentration of all the reagents involved in the reaction, bar one (the isolated species). This is done by maintaining the concentrations of all of the reactants in excess of the isolated species; traditionally the concentration of the isolated species should be at least an order of magnitude lower than the other reactants (Pilling and Seakins, 1995). Using this methodology the concentrations of the non-isolated species remain effectively constant throughout the reaction. Consequently, in the rate equation for the reaction the product of rate coefficient, *k*, and the concentration of non-isolated species, [B], also remains constant; this combined term is often referred to as the pseudo first-order rate coefficient, *k'*.

For R1.22 the following rate equation is determined:

$$-\frac{d[\mathrm{A}]}{dt} = k[\mathrm{A}][\mathrm{B}] \quad \text{(E1.30)}$$

If [B] ≈ 10×[A]:

$$k[\mathrm{A}][\mathrm{B}] = k'[\mathrm{A}] \quad \text{(E1.31)}$$

where

$$k' = k[\mathrm{B}] \quad \text{(E1.32)}$$

Notably, these pseudo first-order experiments yield exponential data, from which *k'* can be determined (E1.33).

$$[\mathrm{A}]_t = [\mathrm{A}]_0 e^{-k't} \quad \text{(E1.33)}$$

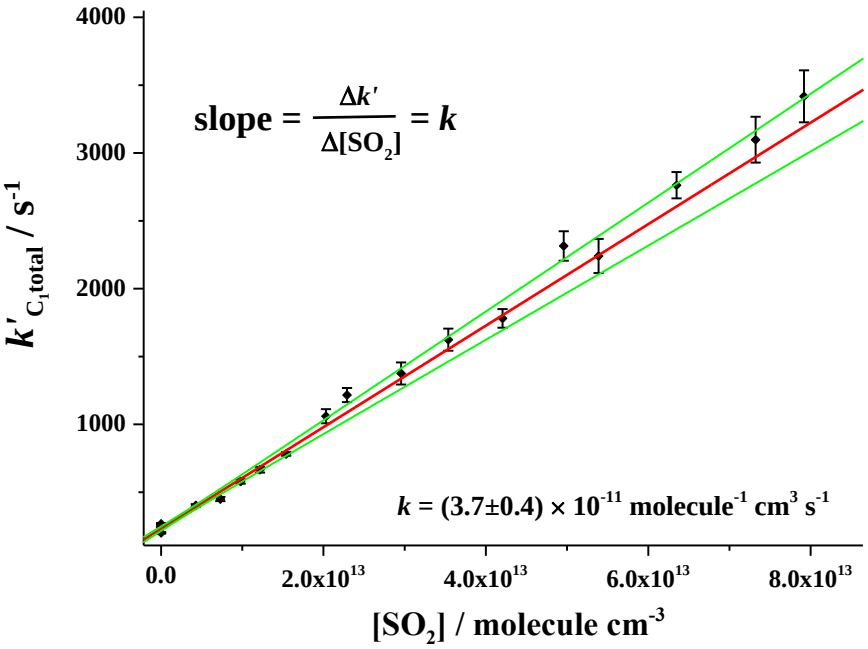

Figure 1.7: An example of a bimolecular plot of the reaction between the C_1 Criegee intermediate and SO_2 is shown (see Chapter VI for details). This figure also demonstrates how the bimolecular rate coefficient, *k*, is determined.

The bimolecular rate constant for the reaction may then be determined from the plot of *k'* vs. [B] (provided [B] is known); this type of graph is known as a bimolecular plot (Figure 1.7). It should be highlighted that this experimental methodology is a fundamental technique within the field of gas kinetics; indeed, all of the rate coefficients determined within this thesis were done using the isolation method.

Significantly, certain assumptions are made when using the isolation method; primarily that the concentration of the non-isolated species remains constant, which is not true. For example: if the initial concentration of the non-isolated species, $[B]_0$, was ten times the

initial concentration of the isolated species, $[A]_0$, the concentration of B after the completion of the reaction ($[B]_{end}$) will be 90% of $[B]_0$. Although, in this scenario the concentration of B remains almost constant during the course of a reaction ($[B]_{end} \approx 0.9\times[B]_0$), it does decrease. Moreover, the greater the difference in the initial concentrations of the reactants A and B, the smaller the change in the concentration of B during the reaction. This is why the concentration of the non-isolated species is usually kept at least order of magnitude higher. Note: if $[B]_0 < 10\times[A]_0$, the average concentration of B ($[B]_{av}$) will be lower than $[B]_0$, this may lead to underestimations of the bimolecular rate coefficients as the bimolecular plot analysis assumes the concentration of B remains constant (at $[B]_0$) throughout the reaction. Therefore, if $[B]_{av} < [B]_0$ all the points on the *x*-axis of the bimolecular should be shifted to the left, which will increase the gradient and hence the bimolecular rate coefficient.

It should be highlighted that at certain points in this thesis the experimental conditions used were estimated to by outside of the range optimal for the isolation method (i.e. $[B]_0 < 5\times[A]_0$). However, in both the experiments discussed in the Results section, Parts i and ii, the exact concentrations of the isolated species were unknown. The estimations given for the isolated species ([OH] and $[CH_2OO]$/$[CH_3CHOO]$ respectively) were conservative, meaning that they likely overestimate the concentration of the isolated species. Therefore, it is probable the difference in the concentrations of the isolated and non-isolated species is larger than presented. Moreover, for certain experiments, where pseudo first-order conditions were questioned, Kintecus models were run to assess the change in concentration of the non-isolated species and adjustments were made to account for this (see Chapter VI, Section 6.1.3).

1.6 Overview of Thesis

The final section of this introductory chapter will attempt to give a concise synopsis of the different chapters within this thesis. This thesis will focus principally on the kinetics of certain gas-phase reactions which are relevant to the Earth's atmosphere. Furthermore, the detection techniques used to monitor these aforementioned reactions will also be reviewed.

The majority of the experimental work described within this thesis was completed using pulsed laser photolysis – photoionization mass spectrometry (PLP-PIMS). The primary aim of Chapter II is to give a detailed explanation of this technique and the specific instrumentation used. Additionally, details about the experimental and analytical methods used are also given. Lastly, other common methods of monitoring gas phase kinetics are discussed.

Chapter III discusses some of the different configurations of the PIMS set-up tested during this PhD. The majority of the work discussed in this thesis is still in progress and further improvements are being made to increase the reliability of these techniques. Specifically, this chapter describes two separate reconfigurations of the PIMS system; the first being the utilization of multiphoton ionization scheme, which permits the detection of the hydroxyl radical, OH, which is an important atmospheric oxidant; the second a high pressure set-up, which would allow for experiments to be conducted at more atmospherically relevant conditions.

Chapter IV describes an investigation into the reaction between acetaldehyde (CH_3CHO) and the OH radical; in particular this chapter discusses the possibility of an alternate reaction pathway. Indeed, close investigation suggests that a small, but significant fraction of the nascent acetyl radicals (CH_3CO) have sufficient energy to decompose, forming CH_3 and CO radicals. Notably, the CH_3CHO + OH reaction has always been considered a simple abstraction reaction; this evidence suggests that even for reactions that are thought to be well understood, there is still much we do not know.

Chapters V-VII can be grouped together as all are centred on the reactivity of stabilized Criegee intermediates with various atmospheric trace gases. The primary objective from Chapter V is to give a detailed introduction the elusive Criegee biradicals, highlighting the common formation pathways in the lower atmosphere and subsequent reactions of the newly formed Criegee intermediates (CIs) within the troposphere. Chapter VI concentrates specifically on the reactivity of the stabilised C_1 and C_2 CIs with both SO_2 and NO_2 and the atmospheric implications of these reactions. Chapter VII discusses the reaction of the C_1 CI with selected atmospheric non-methane hydrocarbon and volatile organic compounds; ethene, isoprene, formic and acetic acid. Again, the atmospheric implications of these reactions are considered.

The final chapter, Chapter VIII, will give a summary of the key findings from the previous chapters and outline possible future work.

1.7 References

ARGIRI, M., COZZI, L., DOWLING, P., EMOTO, H., LYONS, L., MALYSHEV, T., T.MORGAN, O'GALLAGHER, T., OLEJARNIK, P., POCHETTINO, N., ROQUES, F., SCHIMPF, R., JONES, C., CAZZOLA, P., GIELEN, D., KIEFFER, G., WAIDE, P., GAGHEN, R., CUSTODIO, M., RAVERA, L. & SADIN, B. 2006. World energy outlook 2006. International Energy Agency.

ATKINSON, R. 2000. Atmospheric chemistry of VOCs and NO_x. *Atmospheric Environment,* 34**,** 2063-2101.

BRASSEUR, G. P., ORLANDO, J. J. & TYNDALL, G. S. 1999. *Atmospheric Chemistry and Global Change,* Oxford, Oxford University Press.

CALVERT, J. G. M., A; ORLANDO, J. J; PILLING, M. J AND WALLINGTON, T. J 2011. The Mechanisms of Atmospheric Oxidation of the Oxygenates. New York: Oxford University Press.

CORRÊA, S. M., MARTINS, E. M. & ARBILLA, G. 2003. Formaldehyde and acetaldehyde in a high traffic street of Rio de Janeiro, Brazil. *Atmospheric Environment,* 37**,** 23-29.

CUBASCH, U., WUEBBLES, D., CHEN, D., FACCHINI, M. C., FRAME, D., MAHOWALD, N. & WINTHER., J. G. 2013. Introduction. In: Climate Change 2013: The Physical Science Basis. Contribution of Working Group I to the Fifth Assessment Report of the Intergovernmental Panel on Climate Change. *In:* STOCKER, T. F., D. QIN, G.-K. PLATTNER, M. TIGNOR, S.K. ALLEN, J. BOSCHUNG, A. NAUELS, Y. XIA, V. BEX AND P.M. MIDGLEY (ed.). Cambridge, United Kingdom and New York, NY, USA.

DEMIRBAS, A. 2009. Biofuels: Securing the Planet's Future Energy Needs. London: Springer-Verlag.

ELSOM, D. 2013. Smog Alert: Managing Urban Air Quality. Abingdon: Earthscan.

EMMERSON, K. M., CARSLAW, N. & PILLING, M. J. 2005. Urban atmospheric chemistry during the PUMA campaign 2: Radical budgets for OH, HO_2 and RO_2. *Journal of Atmospheric Chemistry,* 52**,** 165-183.

ENGEL, T. & REID, P. 2006. *Physical Chemistry,* San Francisco, Pearson (Benjamin Cummings).

FINLAYSON-PITTS, B. J. & PITTS JR., J. N. 1999. *Chemistry of the upper and lower atmosphere: theory, experiments, and applications*, Academic press.

FISCHER, E. V., JACOB, D. J., YANTOSCA, R. M., SULPRIZIO, M. P., MILLET, D. B., MAO, J., PAULOT, F., SINGH, H. B., ROIGER, A., RIES, L., TALBOT, R. W., DZEPINA, K. & PANDEY DEOLAL, S. 2014. Atmospheric peroxyacetyl nitrate (PAN): a global budget and source attribution. *Atmos. Chem. Phys.,* 14**,** 2679-2698.

FORINASH, K. 2010. Foundations of Environmental Physics: Understanding Energy Use and Human Impacts. Washington: Island Press.

GUENTHER, A., HEWITT, C. N., ERICKSON, D., FALL, R., GERON, C., GRAEDEL, T., HARLEY, P., KLINGER, L., LERDAU, M., MCKAY, W. A., PIERCE, T., SCHOLES, B., STEINBRECHER, R., TALLAMRAJU, R., TAYLOR, J. & ZIMMERMAN, P. 1995. A global model of natural volatile organic compound emissions. *Journal of Geophysical Research: Atmospheres,* 100**,** 8873-8892.

GUENTHER, C. C. 2006. Estimates of global terrestrial isoprene emissions using MEGAN (Model of Emissions of Gases and Aerosols from Nature).

HAINES, A., KOVATS, R. S., CAMPBELL-LENDRUM, D. & CORVALAN, C. 2006. Climate change and human health: Impacts, vulnerability and public health. *Public Health,* 120**,** 585-596.

HANSEN, J., SATO, M., KHARECHA, P. & VON SCHUCKMANN, K. 2011. Earth's energy imbalance and implications. *Atmos. Chem. Phys. ,* 11**,** 13421–13449.

HANST, P. L. 1971. Mechanism of peroxyacetyl nitrate formation. *Journal of the Air Pollution Control Association,* 21**,** 269-271.

HARTMANN, D. L., A.M.G. KLEIN TANK, M. RUSTICUCCI, L.V. ALEXANDER, S. BRÖNNIMANN, Y. CHARABI, F.J. DENTENER, E.J. DLUGOKENCKY, D.R. EASTERLING, A. KAPLAN, B.J. SODEN, P.W. THORNE & ZHAI, M. W. A. P. M. 2013.

Observations: Atmosphere and Surface. In: Climate Change 2013: The Physical Science Basis. Contribution of Working Group I to the Fifth Assessment Report of the Intergovernmental Panel on Climate Change *In:* STOCKER, T. F., D. QIN, G.-K. PLATTNER, M. TIGNOR, S.K. ALLEN, J. BOSCHUNG, A. NAUELS, Y. XIA & MIDGLEY, V. B. A. P. M. (eds.). Cambridge, United Kingdom and New York, NY, USA.: Cambridge University.

HEARD, D. E. & PILLING, M. J. 2003. Measurement of OH and HO_2 in the troposphere. *Chemical reviews,* 103**,** 5163-5198.

HEGERL, G. C., F. W. ZWIERS, P. BRACONNOT, N.P. GILLETT, Y. LUO, J.A. MARENGO ORSINI, N. NICHOLLS & STOTT, J. E. P. A. P. A. 2007. Understanding and Attributing Climate Change. In: Climate Change 2007: The Physical Science Basis. Contribution of Working Group I to the Fourth Assessment Report of the Intergovernmental Panel on Climate Change. *In:* SOLOMON, S., D. QIN, M. MANNING, Z. CHEN, M. MARQUIS, K.B. AVERYT & MILLER, M. T. A. H. L. (eds.). Cambridge, United Kingdom and New York, NY, USA.

HIPPLER, H., RAHN, R. & TROE, J. 1990. Temperature and pressure dependence of ozone formation rates in the range 1–1000 bar and 90–370 K. *The Journal of Chemical Physics,* 93**,** 6560-6569.

IPCC 2013. Summary for Policymakers. In: Climate Change 2013: The Physical Science Basis. Contribution of Working Group I to the Fifth Assessment Report of the Intergovernmental Panel on Climate Change. *In:* STOCKER, T. F., QIN, D., PLATTNER, G.-K., TIGNOR, M., ALLEN, S. K., BOSCHUNG, J., NAUELS, A., XIA, Y., BEX, V. & MIDGLEY, P. M. (eds.). Cambridge, United Kingdom and New York, NY, USA: Cambridge University Press.

JACOB, D. 1999. Introduction to Atmospheric Chemistry. Princeton, New Jersey: Princeton University Press.

JACOBSON, M. Z. 2002. *Atmospheric Pollution: History, Science, and Regulation,* Cambridge, Cambridge Univerisity Press.

KURYLO, M. J. & ORKIN, V. L. 2003. Determination of atmospheric lifetimes via the measurement of OH radical kinetics. *Chemical reviews,* 103**,** 5049-5076.

LAOTHAWORNKITKUL, J., TAYLOR, J. E., PAUL, N. D. & HEWITT, C. N. 2009. Biogenic volatile organic compounds in the Earth system. *New Phytologist,* 183**,** 27-51.

LEISEROWITZ, A. A., MAIBACH, E. W., ROSER-RENOUF, C., SMITH, N. & DAWSON, E. 2013. Climategate, Public Opinion, and the Loss of Trust. *American Behavioral Scientist*.

LELIEVELD, J., BUTLER, T., CROWLEY, J., DILLON, T., FISCHER, H., GANZEVELD, L., HARDER, H., LAWRENCE, M., MARTINEZ, M. & TARABORRELLI, D. 2008. Atmospheric oxidation capacity sustained by a tropical forest. *Nature,* 452**,** 737-740.

MAULDIN, R. L., BERNDT, T., SIPILA, M., PAASONEN, P., PETAJA, T., KIM, S., KURTEN, T., STRATMANN, F., KERMINEN, V. M. & KULMALA, M. 2012. A new atmospherically relevant oxidant of sulphur dioxide. *Nature,* 488**,** 193-+.

MCGEE, M. 2016. *Weekly Data: Atmospheric CO_2* [Online]. British Columbia. Available: co2now.org [Accessed 02/03/16].

MEEHL, G. A., WASHINGTON, W. M., ARBLASTER, J. M., HU, A., TENG, H., TEBALDI, C., SANDERSON, B. N., LAMARQUE, J.-F., CONLEY, A., STRAND, W. G. & III, J. B. W. 2012. Climate System Response to External Forcings and Climate Change Projections in CCSM4. *Journal of Climate,* 25**,** 3661-3683.

MORTIMER, M. & TAYLOR, P. 2002. Chemical Kinetics and Mechanism. Cambridge, U.K.: Royal Society of Chemistry.

MYHRE, G., D. SHINDELL, F.-M. BRÉON, W. COLLINS, J. FUGLESTVEDT, J. HUANG, D. KOCH, J.-F. LAMARQUE, D. LEE, B. MENDOZA, T. NAKAJIMA, A. ROBOCK, G. STEPHENS & ZHANG, T. T. A. H. 2013. Anthropogenic and Natural Radiative Forcing. In: Climate Change 2013: The Physical Science Basis. Contribution of Working Group I to the Fifth Assessment Report of the Intergovernmental Panel on Climate Change. *In:* STOCKER, T. F., D. QIN, G.-K. PLATTNER, M. TIGNOR, S.K. ALLEN, J. BOSCHUNG, A. NAUELS, Y. XIA & MIDGLEY, V. B. A. P. M. (eds.). Cambridge, United Kingdom and New York, NY, USA.

PARK, C. 1997. The Environment: Principles and Applications. London: Routledge.

PEETERS, J., NGUYEN, T. L. & VEREECKEN, L. 2009. HO_x radical regeneration in the oxidation of isoprene. *Physical Chemistry Chemical Physics,* 11**,** 5935-5939.
PEÑUELAS, J. & LLUSIÀ, J. 2003. BVOCs: plant defense against climate warming? *Trends in Plant Science,* 8**,** 105-109.
PERCIVAL, C. J., WELZ, O., ESKOLA, A. J., SAVEE, J. D., OSBORN, D. L., TOPPING, D. O., LOWE, D., UTEMBE, S. R., BACAK, A., M C FIGGANS, G., COOKE, M. C., XIAO, P., ARCHIBALD, A. T., JENKIN, M. E., DERWENT, R. G., RIIPINEN, I., MOK, D. W. K., LEE, E. P. F., DYKE, J. M., TAATJES, C. A. & SHALLCROSS, D. E. 2013. Regional and global impacts of Criegee intermediates on atmospheric sulphuric acid concentrations and first steps of aerosol formation. *Faraday Discussions,* 165**,** 45-73.
PILLING, M. J. & SEAKINS, P. W. 1995. *Reaction Kinetics,* Oxford, Oxford University Press.
PRITCHARD, H. O. 2005. Recrossings and Transition-State Theory. *The Journal of Physical Chemistry A,* 109**,** 1400-1404.
SCHIERMEIER, Q. 2015. The science behind the Volkswagen emissions scandal. *Nature News,* 25.
SEINFELD, J. H. & PANDIS, S. N. 2012. *Atmospheric chemistry and physics: from air pollution to climate change,* John Wiley & Sons.
SEMELSBERGER, T. A., BORUP, R. L. & GREENE, H. L. 2006. Dimethyl ether (DME) as an alternative fuel. *Journal of Power Sources,* 156**,** 497-511.
SEVERINGHAUS, J. P. & BROOK, E. J. 1999. Abrupt Climate Change at the End of the Last Glacial Period Inferred from Trapped Air in Polar Ice. *Science,* 286**,** 930-934.
SHANNON, R. J., CARAVAN, R. L., BLITZ, M. & HEARD, D. E. 2014. A combined experimental and theoretical study of reactions between the hydroxyl radical and oxygenated hydrocarbons relevant to astrochemical environments. *Physical Chemistry Chemical Physics,* 16**,** 3466-3478.
SHANNON, R. J., TAYLOR, S., GODDARD, A., BLITZ, M. A. & HEARD, D. E. 2010. Observation of a large negative temperature dependence for rate coefficients of reactions of OH with oxygenated volatile organic compounds studied at 86-112 K. *Physical Chemistry Chemical Physics,* 12**,** 13511-13514.
SINGH, H. B. & HANST, P. L. 1981. Peroxyacetyl nitrate (PAN) in the unpolluted atmosphere: An important reservoir for nitrogen oxides. *Geophysical Research Letters,* 8**,** 941-944.
SMITH, S. C., LEE, J. D., BLOSS, W. J., JOHNSON, G. P., INGHAM, T. & HEARD, D. E. 2006. Concentrations of OH and HO_2 radicals during NAMBLEX: measurements and steady state analysis. *Atmospheric Chemistry and Physics,* 6.
STAVRAKOU, T., PEETERS, J. & MÜLLER, J. F. 2010. Improved global modelling of HO_x recycling in isoprene oxidation: evaluation against the GABRIEL and INTEX-A aircraft campaign measurements. *Atmos. Chem. Phys.,* 10**,** 9863-9878.
STONE, D., BLITZ, M., DAUBNEY, L., HOWES, N. U. M. & SEAKINS, P. 2014. Kinetics of CH_2OO reactions with SO_2, NO_2, NO, H_2O and CH_3CHO as a function of pressure. *Physical Chemistry Chemical Physics,* 16**,** 1139-1149.
STONE, D., WHALLEY, L. K. & HEARD, D. E. 2012. Tropospheric OH and HO_2 radicals: field measurements and model comparisons. *Chemical Society Reviews,* 41**,** 6348-6404.
TAATJES, C. W., O; ESKOLA, A; SAVEE, J; SCHEER, A; SHALLCROSS, D; ROTAVERA, B; LEE, E;DYKE, J; MOK, D; OSBORN, D AND PERCIVAL C 2013. Direct Measurements of Conformer-Dependent Reactivity of the Criegee Intermediate CH_3CHOO. *Science,* 340.
THORPE, D. 2011. *Solar Technology: The Earthscan Expert Guide to Using Solar Energy for Heating, Cooling and Electricity,* Abingdon, Earthscan.
TROMP, J. W. & MILLER, W. H. 1986. New approach to quantum mechanical transition-state theory. *The Journal of Physical Chemistry,* 90**,** 3482-3485.
TRUHLAR, D. G. & GARRETT, B. C. 1984. Variational transition state theory. *Annual Review of Physical Chemistry,* 35**,** 159-189.
TYNDALL, G., COX, R., GRANIER, C., LESCLAUX, R., MOORTGAT, G., PILLING, M., RAVISHANKARA, A. & WALLINGTON, T. 2001. Atmospheric chemistry of small organic peroxy radicals. *Journal of Geophysical Research: Atmospheres,* 106**,** 12157-12182.

WAYNE, R. 1991. *Chemistry of Atmospheres: An Introduction to the Chemistry of the Atmosphere of Earth, the Planets, and their Satellites,* Oxford, Oxford University Press.
WELZ, O., SAVEE, J. D., OSBORN, D. L., VASU, S. S., PERCIVAL, C. J., SHALLCROSS, D. E. & TAATJES, C. A. 2012. Direct Kinetic Measurements of Criegee Intermediate (CH_2OO) Formed by Reaction of CH_2I with O_2. *Science,* 335**,** 204-207.
WHALLEY, L., EDWARDS, P., FURNEAUX, K., GODDARD, A., INGHAM, T., EVANS, M., STONE, D., HOPKINS, J., JONES, C. E. & KARUNAHARAN, A. 2011. Quantifying the magnitude of a missing hydroxyl radical source in a tropical rainforest. *Atmospheric Chemistry and Physics,* 11**,** 7223-7233.
WHALLEY, L. K., FURNEAUX, K. L., GODDARD, A., LEE, J. D., MAHAJAN, A., OETJEN, H., READ, K. A., KAADEN, N., CARPENTER, L. J., LEWIS, A. C., PLANE, J. M. C., SALTZMAN, E. S., WIEDENSOHLER, A. & HEARD, D. E. 2010. The chemistry of OH and HO_2 radicals in the boundary layer over the tropical Atlantic Ocean. *Atmos. Chem. Phys.*, 10**,** 1555-1576.

Chapter II:

Experimental Methods

2. Experimental Methods

This chapter focuses on the pulsed laser photolysis, photoionization mass spectrometry technique (PLP-PIMS) used for the majority of the work described in this thesis. An introduction to the principles of laser action is given as both photolysis and photoionization steps utilize lasers. Following this is an overview of the experimental techniques commonly used in gas-phase kinetics and includes an in depth discussion of the time-of-flight mass spectrometry, the technique used for the majority of the experimental work reported in this thesis. The final section of this chapter provides details of the specific methodology used for data collection and analysis during this work.

2.1 Introduction to Experimental Techniques

Over recent years there has been significant progress in the measurement of gas-phase kinetics, particularly in the identification of product yields from multichannel reactions (Cathonnet, 1994, Seakins and Blitz, 2011, Fuentes et al., 2000, Baeza-Romero et al., 2012). This is of major importance as gas-phase reactions predominantly control both atmospheric and combustion processes (Atkinson, 2000, Zádor et al., 2011). A full understanding of such systems will shed light on the future of the Earth's atmosphere and the environment to be inhabited by the human race.

Advances in our understanding have been made possible, partially, by developments in computational work, in particular with both chemical modelling and *ab initio* calculations (Frisch et al., 2009, Jenkin et al., 1997). However, chemical models are only as good as the data input into them and *ab initio* calculations still require validation. Therefore, it is still of the utmost importance that accurate measurements are collected, from both *in situ* observations and laboratory studies, to support the computational work. Laboratory studies are particularly useful in providing information on the temperature and pressure dependence simple reactions. Moreover, with the development of laser flash photolysis, and the advancement in time-resolved detection techniques, short-lived radical reactions can be probed. Notably, radical species often dictate much of the chemistry in these gas-phase systems, hence identifying the kinetics of radical reactions is essential to the accuracy of the chemical models (Anderson, 1987). Even though the accuracy of simulations is generally improving, the systems still have many gas-phase reactions about which little is known. This means more experimental work needs to be done, particularly for studies that can yield quantitative information about complex reactions with multiple product channels; arguably mass spectrometry is the most valuable technique to provide such measurements (Blitz et al., 2007, Osborn et al., 2008, Welz et al., 2012).

Throughout this thesis, the vast majority of the work conducted has been completed by utilizing pulsed laser photolysis photoionization (time-of-flight) mass spectrometry, PLP-PIMS. Mass spectrometry is, in principle, a universal technique and can be used to detect numerous different species during the course of a reaction (Blitz et al., 2007). By using a time-of-flight mass spectrometer, it was possible for different species to be monitored simultaneously, which allowed both kinetic and mechanistic information to be acquired. This technique can often provide vital details about reaction mechanisms, hence improving our understanding of atmospheric and combustion systems in general (Baeza-Romero et al., 2012). An introduction to the PLP-PIMS system used during experimentation can be found in subsequent sections of this chapter.

2.2 An Introduction to Pulsed Laser Photolysis – Photoionization Mass Spectrometry

The pulsed laser photolysis - photoionization mass spectrometry (PLP-PIMS) system was designed and built by the University of Leeds in collaboration with Kore technology (Blitz et al., 2007). This system utilizes a time of flight mass spectrometer (ToF-MS). The major advantage of this technique is that it can theoretically be used to measure any species and monitor them simultaneously on a millisecond time scale (Blitz et al., 2007). A schematic representation of the PIMS system can be seen below (Figure 2.1). This system has been used to study the kinetics and mechanistics of a number of different gas-phase reactions, such as the reaction between OH and acetaldehyde and the reactions of Criegee intermediates with trace gases.

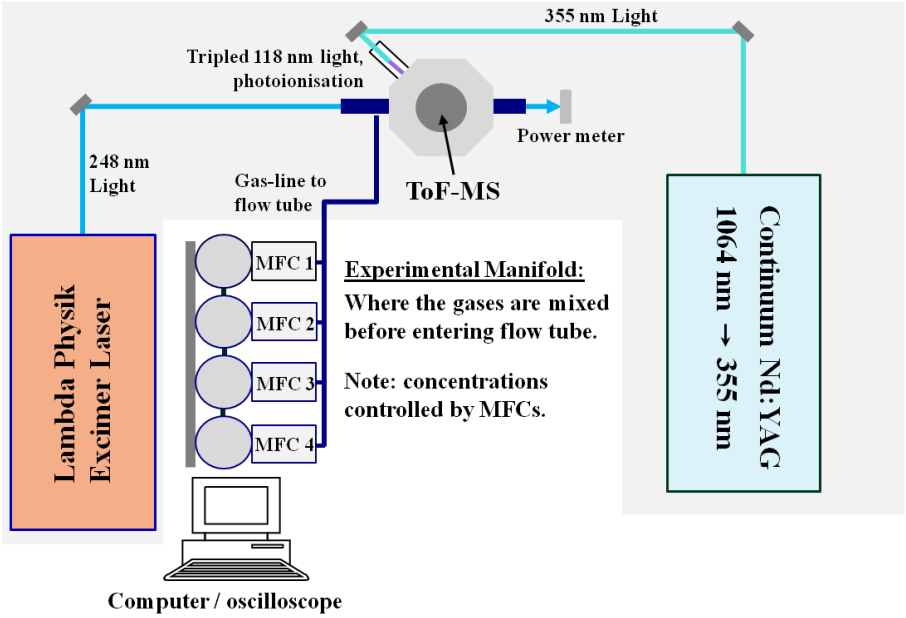

Figure 2.1: A schematic of the PLP-PIMS instrument at the University of Leeds.

The reactant gases were controlled using mass flow controllers and combined in a mixing manifold before entering a steel flow-tube (internal diameter of 10.5 mm and ~70 cm in length. Experiments were initiated by using a pulsed excimer laser (Lambda Physik, Compex 205) to photolyse the sample, generally at 248 nm. Excimer lasers can also produce light at other wavelengths, for example in Chapter IV photolysis of N_2O, using 193 nm excimer radiation, proved to be a useful precursor to OH in an oxygen-free environment. The irradiated reaction mixture was then sampled by the ToF-MS *via* a 1 mm pinhole located in the reaction tube directly below the mass spectrometer ion collection axis (Blitz et al., 2007). Before entering the mass spectrometer the sampled gas was ionized in a vacuum chamber using 118 nm (~10.5 eV) vacuum ultraviolet light (VUV). This photoionization light was directed orthogonally to the gas flow; this wavelength of light was produced by the frequency tripling of 355 nm radiation from a Continuum Nd:YAG laser (10-15 mJ/pulse). Xenon gas was utilised for frequency tripling. Turbo (Edwards, EXT 255H) and diffusion pumps (Varian, VHS-6) were used to keep the pressure low (10^{-5} Torr) in the vacuum chamber / mass spectrometer, to ensure optimal conditions for ToF-MS sampling (Baeza-Romero et al., 2012).

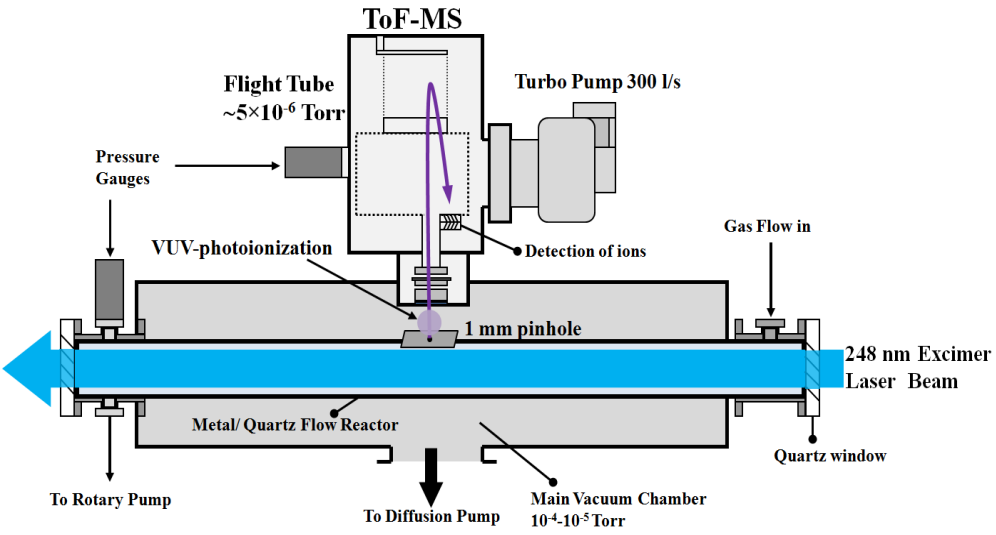

Figure 2.2: A schematic of the PIMS system, highlighting the flow-tube and mass spectrometer. Adapted from Blitz *et al.* (2007).

In comparison to other detection techniques used in experimental gas kinetics, the PLP-PIMS set-up is less sensitive towards its target species (see Section 2.4). For example, the PLP-LIF set-up described in Carr (2009) and Lockhart (2014) has a detection limit of approximately 10^8 molecule cm^{-3} for OH; notably, the limit of detection is significantly higher is the PLP-PIMS set-up and is estimated to be between 10^{10}-10^{11} molecules cm^{-3}, depending on the species.

This section aimed to give a brief outline of the basic configuration for the instrumentation used throughout this thesis. In the subsequent sections of this chapter a detailed description of the PLP-PIMS set up will be given; starting with the laser systems used for both pulsed laser photolysis and photoionization (Section 2.3). Following this the principle of mass spectrometry, particularly time-of-flight mass spectrometry, will be discussed (Section 2.4).

2.3 Laser Systems

The PLP-PIMS system utilises three different lasers: a Lambda Physik Compex 205 excimer laser, which was used to photolyse the sample and initiate chemistry. Secondly, there was a Continuum Powerlite 8010 Nd:YAG laser which produces 355 nm light which was frequency-tripled to form 118 nm light and was used to ionize the sample prior to detection. Both the excimer and the Nd:YAG lasers are pulsed, by pulsing the lasers it was possible to extract temporal information about the reaction on a microsecond timescale; pulsing can also be used to increase the laser energy output. It should be noted that a Sirah dye laser was also used to excite OH radicals so they can be subsequently ionized by 118 nm light (details of the technique can be in Chapter III).

2.3.1 The Principles behind Laser Systems

There are two criteria which must be met before lasing can commence: population inversion in the laser medium (a gas, liquid or solid where stimulated emission may take place) and an optical cavity, which allows for amplification in the light emitted (Andrews, 1997). However, to understand laser theory, one must first understand the principle of the absorption and emission of light. Quantum theory states that molecules, atoms and ions (Note: for the duration of this section on lasers these particles shall be collectively referred to as molecules) all possess sets of discrete energy levels. Under normal conditions the majority of the molecules will exist in the lowest of the electronic energy levels, known as the ground state. However, molecules can be excited, and electrons promoted to higher energy levels if the molecule receives a specific amount of energy equal in magnitude to the difference between two of the electronic states. This excitation most commonly occurs when a photon of light (a discrete energy 'packet' of light) is absorbed by the molecule. The energy of the photons is proportional to the frequency of the light. Max Planck proposed this equation in 1901, and in his honour it has been named the Planck's relation (Planck, 1901):

$$E = h.\nu \qquad \text{(E2.1)}$$

Equation E2.1 is commonly referred to as the Planck's relation, an equation which shows the energy (E) of a photon is directly proportional to the frequency of the photon (ν). The

constant of proportionality being Planck's constant, h, which is evaluated at 6.6261×10^{-34} J s.

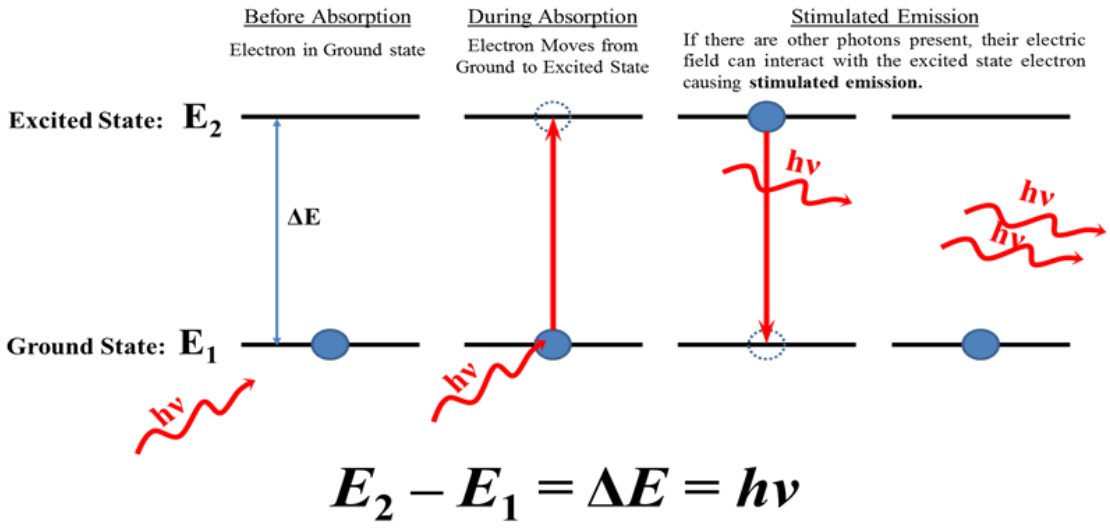

Figure 2.3: Diagram to explain the absorption and emission of light in Quantum theory. Adapted from a diagram in 'Lasers in Chemistry: Probing Matter.' 2008.

Conversely, electrons can also move from an excited state back to the ground state by either non-radiative or radiative processes, such as emitting a photon of light equal in energy to the difference between the electronic states - fluorescence (Figure 2.3). It should be noted that due to the relationship between the energy difference of electronic states and light frequency, the different photons of light that can be emitted by a molecule are individual to that molecule. Photons can be radiated in one of two ways: spontaneously or the emission of light can be stimulated (Andrews, 1997).

If there are no driving forces behind the radiation then emission will occur spontaneously, where the photon may be emitted in any direction; notably, the rate of spontaneous emission is proportional to the Einstein coefficient A_{21} (see Appendix B). However, if a light beam of monochromatic photons is directed into a system containing molecules which can absorb photons of this wavelength, thus causing excitation, the electron will likely relax back to the ground and emit a same wavelength of photon to that absorbed. Additionally, the probability of monochromatic emission increases if there are other photons of the same wavelength already present in the system – furthermore emission occurs preferentially in the direction of the applied light beam, thus increasing the light intensity in this orientation. This process is called stimulated emission (Andrews, 1997). Lasing will only commence if there is a sufficient net increase in photon density in a single orientation; this can be a challenge as the system reaches an equilibrium, where absorption and emission occur at the same rate. Equation E2.2 is a derivation of the Beer-Lambert law and can be used to

highlight the importance of population inversion to lasing (see Appendix B for more details).

$$I_t \propto I_0 e^{-(N_1 - N_2)} \quad \text{(E2.2)}$$

In equation E2.2: I_t represents the intensity of light transmitted through the sample; I_0 is the incident light intensity; N_1 is the population of the lower energy state; and N_2 is the population of the upper energy state. From E2.2 it can be seen that a net increase in light intensity (and hence lasing) will occur if the population in N_2 is greater the population in N_1. This phenomenon is known as population inversion.

2.3.1.1 Population Inversion

As alluded to above, population inversion is essential to laser systems. However, there is a problem in the two-level system: for lasing to occur the N_2 must be greater than N_1, but this is thermodynamically impossible according to the Boltzmann relation as it requires a negative absolute temperature (E2.3).

$$N_2/N_1 \propto e^{\frac{(E_1 - E_2)}{k_B T}} \quad \text{(E2.3)}$$

In equation E2.5: N_2/N_1 is the ratio of the number of species in the upper state compared to the lower state, E_1 is the energy of the lower level, and E_2 is the energy of the upper state, k_B is the Boltzmann constant and T in the absolute temperature in Kelvin.

As $E_1 < E_2$ only in a scenario where the absolute temperature is negative would the N_2/N_1 ratio be greater than 1, theoretically this is impossible (for continuous emission). That said, there are ways of maintaining population inversion in two-level laser systems, for example, by using pulsed excitation (or pumping) laser light; however, the population inversion will only be preserved if the rate of pumping is faster the rate of emission. Note that two-level laser systems do exist (i.e. an excimer laser), but, they are very rare and require specific conditions. In practise the most common method of maintaining a inverted population is by using 3- or 4- level laser systems.

In a 3-level laser system there is a further higher electronic state, E_3, using high energy optical pumping it is possible to excite ground state electrons into E_3, these excited electrons can then relax (non-radiatively) back down to the E_2 energy level (Lackner, 2008). Crucially, for the 3-level laser system to work the rate to the transition from E_3 to E_2 must be faster than the transition rate from E_2 to E_1, thus creating an inverted population between levels E_2 and E_1 (Figure 2.4). The E_2 energy level is often a metastable state as this allows the population of the E_2 level to increase so that the majority of electrons are located there. One problem with the 3-level laser system is that lasing repopulates the ground state; this

makes it difficult to sustain population inversion, this is the major advantage of the 4-level system (Andrews, 1997).

In the 4-level laser system, the lasing energy level (i.e. E_3, Figure 2.4 - Right-hand side) does not relax into the ground state, but into the E_2 level. For the 4-level laser system to function there must be a population inversion between the E_3 and E_2 energy states. Initially the intense pumping is required to excite molecules into the highest energy state, E_4, similarly to the 3-level system this state will relax non-radiatively to the E_3 state (note the rate that this occurs at must be greater than the rate of laser emission) and the population will build in this (metastable) state. In this system laser emission occurs between the E_3 and E_2 states, then relaxation from the E_2 state to the ground state by non-radiative methods. To maintain the population inversion between these levels the rate of relaxation from E_2 to E_1 must be faster than the rate of laser emission. Notably, both the Nd:YAG and dye lasers described in Sections 2.3.3 and 2.3.4 respectively operate using some variation of a 4-level laser system.

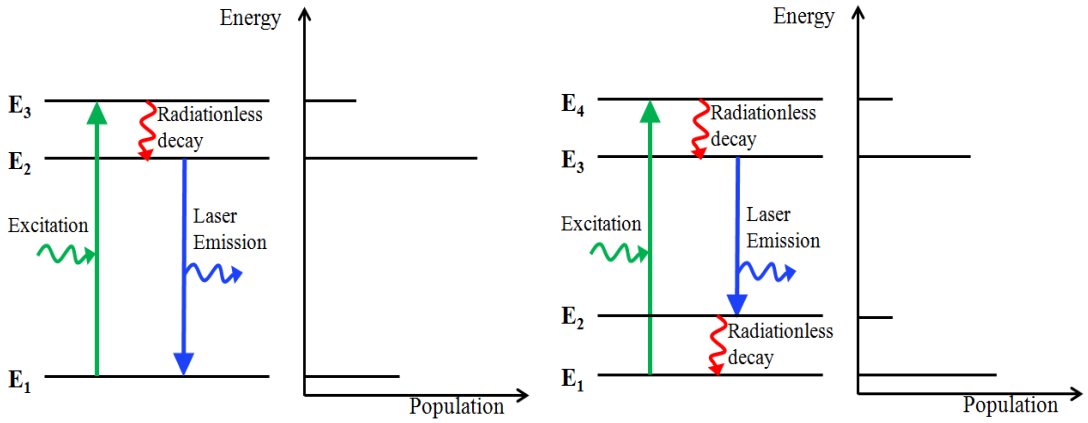

Figure 2.4: Diagram showing examples of a 3 and 4-level laser and the relative population of the energy levels. Adapted from Andrew, 1997.(Andrews, 1997)

2.3.1.2 The Optical Cavity

Often light amplification by population inversion is limited by kinetic losses of excited species or the process of absorption itself. To further increase the light amplification we can refer back to the Beer-Lambert law (E2.4) and see that the intensity of transmitted light in a laser system decreases exponentially with the path length. Therefore, one technique to increase the absorption of light (and hence stimulated emission) within the optical cavity is to increase the distance the light travels.

$$I_t = I_0 e^{-\sigma n l} \qquad \text{(E2.4)}$$

In the Beer-Lambert Law (E2.4): I_t represents the intensity of light transmitted through the sample; I_0 is the incident light intensity; σ is the cross section of the target species; n is the number density of the target species; and l is the optical path length through the sample.

The optical cavity is filled with a laser medium - a species which, when excited, will undergo stimulated emission as described above. In addition to this an external source of energy is also required to excite the laser medium, such as a flash lamp or an electrical discharge: note that both the laser medium and excitation source are necessary for lasing.

The final components of the cavity are two mirrors which are located at either side of the cavity; one of the mirrors fully reflective and one is partially transmissive (Figure 2.5). These mirrors cause the light to resonate within the cavity, which greatly increases the intensity the light with time, whilst simultaneously making the light highly directional. The directionality occurs as light will only resonate in one specific orientation efficiently and hence only the light in this direction will be amplified.

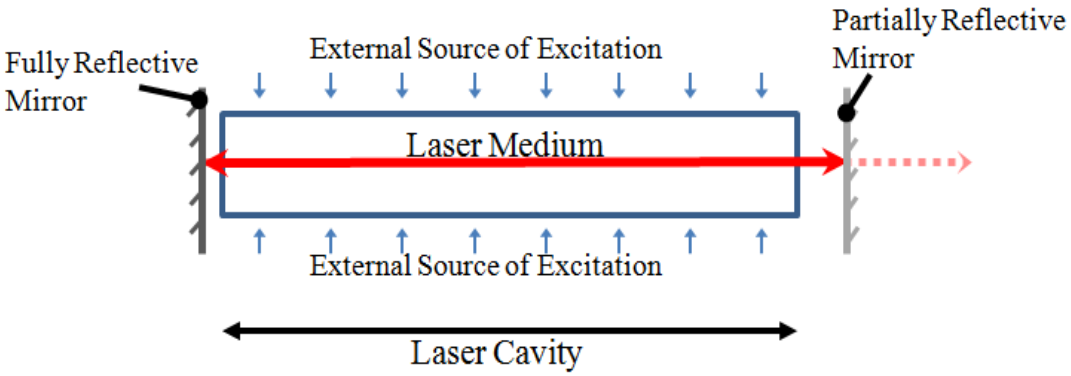

Figure 2.5: A schematic of the optical cavity, adapted from Andrews, (1997).

In the following sections of this chapter the various techniques within the PIMS set-up which utilize laser systems will be discussed, as will the different lasers used.

2.3.2 Pulsed Laser Photolysis

2.3.2.1 An Overview of Flash Photolysis

To initiate chemistry in the PIMS set-up pulsed laser photolysis (PLP), a form of flash photolysis, was utilised. Flash photolysis was first pioneered in 1949, and has since revolutionized gas-phase kinetics (Porter, 1950). What makes this method so valuable is that it has enabled the kinetics of short-lived species such as free radicals to be measured directly, this is of particular use in the field of gas kinetics which are predominantly controlled by short-lived species (Pilling and Seakins, 1995).

Flash photolysis uses a high-energy pulse of light (note that in PLP, the light source is a laser) to photolyse the chemical species and initiate chemistry. Photolysis is used to cleave covalent bonds and form radical species *in situ*. However, this statement is only true if a suitable reaction precursor is available. For example, in Chapter IV, acetyl chloride was utilised as a precursor for both acetyl and chlorine radicals (R2.1).

$$CH_3COCl + h\nu \rightarrow CH_3CO + Cl \qquad (R2.1)$$

Kinetic measurements can only be taken *via* flash photolysis provided that the length of light pulse used is significantly shorter than the lifetime of the reactive species (note a typical radical lifetime in the PIMS set-up would be between 1–10 ms). In early flash photolysis experiments flash lamps were employed to initiate chemistry (Nelson and Ramsay, 1956); however, it is now far more common for a laser to be used. There are several reasons for this shift in excitation sources; firstly lasers can be used to produce shorter light pulses of higher energy (an excimer laser will typically have a pulse duration of 20 ns, providing ~250 mJ pulse^{-1}) and hence can be used for pumping reactions on the microsecond timescale. In addition lasers, unlike flash lamps are highly directional, monochromatic, and do not suffer much from power degradation, so lower precursor concentrations may be used, hence minimising any unwanted reactions (Lackner, 2008).

2.3.2.2 Excimer Laser – Lambda Physik, Compex 205

The PLP-PIMS set-up utilises an excimer laser to photolytically initiate chemical reactions. Although often referred to as an excimer laser, this is a slight misnomer and the Lambda Physik Compex laser is in fact an example of an exciplex laser. Exciplex lasers are named after the active laser medium they form following stimulated absorption, excited diatomic complexes (Andrews, 1997). A high voltage electrical discharge is passed through a high pressure noble gas: halogen: buffer gas mixtures to initially excite the active medium. For the majority of the experiments detailed within this thesis a krypton/fluorine/helium gas mixture was utilised, which produces 248 nm light; however, there are a number of these mixtures which can used to produce various wavelengths of light (Table 2.1).

Table 2.1: A table of different exciplex laser mediums commonly used (2008).

Excimer	Wavelength	Pulse Energy / mJ
ArF	193 nm	200
KrCl	222 nm	35
KrF	248 nm	250
XeCl	308 nm	150
XeF	351 nm	80

Although highly unusual, excimer lasers use a two-level laser system to create population inversion. When the electrical discharge is passed through the active medium excited state krypton fluoride complex, KrF*, is formed (R2.2 – R2.4).

$$Kr + e^- \rightarrow Kr^+ + 2e^- \quad \text{(R2.2)}$$

$$F_2 + e^- \rightarrow F^- + F \quad \text{(R2.3)}$$

$$F^- + Kr^+ + He \rightarrow KrF^* + He \quad \text{(R2.4)}$$

Crucially the KrF* only forms a complex with a fully defined potential well when electronically excited, in the ground state no such complex exists (Figure 2.6). Lasing occurs between the excited KrF* state and the hypothetical KrF ground state; however, in the ground state the krypton and fluorine atoms are not bonded together and so dissociate very rapidly (much faster than the rate of stimulated emission). Consequently the ground state has only a very small population at any one time and so population inversion is created between higher bound state and the lower unbound state (Andrews, 1997).

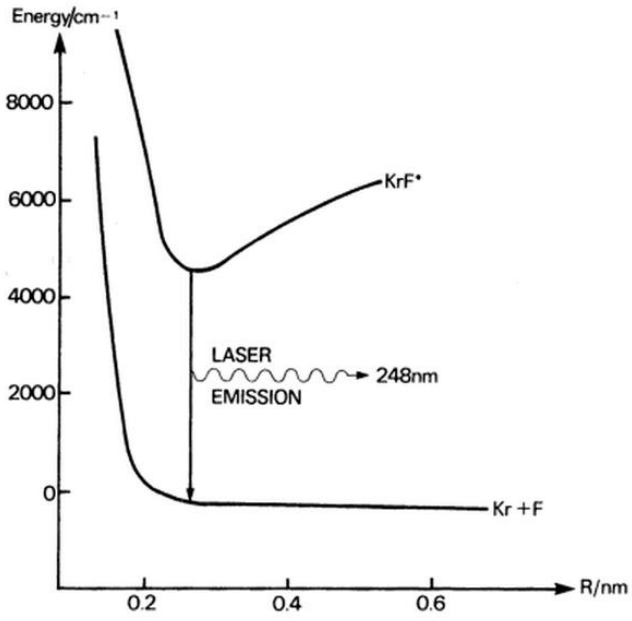

Figure 2.6: A schematic to describe the energetic of a KrF exciplex laser, Andrews (1997).

2.3.3 Photoionization

Although there are many different types of mass spectrometers they all share the same four basic steps: *ionization, acceleration, separation,* and *detection*. There are several different ways in way the gas sample could be ionized such as electron impact ionization or chemical ionization prior to detection (Harris, 2007). However, in the PIMS set-up a Nd:YAG (Continuum, Powerlite 8010) laser is used to photoionize the reaction mixture before they

enter the mass spectrometer (see Figure 2.1). Photoionization has a distinct advantage over other methods of ionization; the wavelength of light used in photoionization can be adjusted - this means that the energy used for ionization is tuneable for different compounds. So if, for example, the target molecule fragments severely upon ionization, a longer photoionization wavelength could be used to minimise fragmentation and yield a less complex spectrum. Conversely, if there are multiple species of the same mass, the input energy can be increased to amplify fragmentation: by increasing ion fragmentation it is often possible to distinguish between species of the same mass as they will, most likely, fragment differently.

2.3.3.1 Nd:YAG – Continuum, Powerlite 8010

The Continuum Powerlite 8010 laser utilises a crystalline lattice of neodymium-doped yttrium aluminium garnet; Nd:$Y_3Al_5O_{12}$ as a lasing medium; it is an example of a solid-state laser and is more commonly referred to as a Nd:YAG laser. Approximately 1% of the yttrium ions in the host yttrium aluminium garnet (YAG) lattice are replaced by Nd^{3+} ions. This is key as lasing occurs due to stimulated emission from electronically excited Nd^{3+} ions. In this laser a high power xenon flash lamp is used to excite ground state Nd^{3+} ions ($^4I_{9/2}$) into a high energy state which rapidly relaxes to the $^4F_{3/2}$ electronic state. Stimulated emission occurs between the $^4F_{3/2}$ state and the $^4I_{11/2}$ state, which rapidly relaxes back to the ground state of the Nd^{3+} ion – this is an example of a *four-level* laser system (Figure 2.4). The primary emission of a Nd:YAG laser is at 1064 nm, although different wavelengths of light can be produced from frequency mixing.

2.3.3.1.1 Q-switching

The Continuum Powerlite 8010 laser was operated in a pulsed mode. Moreover, in all the experiments described in this thesis the Nd:YAG laser was pulsed using Q-switching to optimise the output energy from the laser.

During the excitation (or pumping) of the active medium, the population inversion will slowly reach a steady-state; concurrently, the light intensity within the active medium is also amplified, but (due to spontaneous emissions) a saturation intensity is reached. In the case of the Nd:YAG laser, the time taken to attain the maximum population inversion is significantly greater than the time for the saturation intensity to be reached. To gain the maximum output from the laser these two events must be synchronised, allowing the active medium to reach a maximum level of population inversion before light saturation occurs; crucially, Q-switching enables this.

The Q-switch employs an electro-optical shutter, which when 'closed' limits the light intensity within the active medium, until the point of maximum population inversion is reached (~250 μs). At this instant, the Q-switch is 'opened', releasing the full power of the laser into the active medium, which allows stimulated emission to commence. As the active medium is already largely excited the intensity of light in the cavity builds up rapidly; this leads to the output of a short pulse of high energy photons (Koechner and Bass, 2003).

2.3.3.1.2 Non-linear Optics and Frequency Mixing

The fundamental wavelength of light output from the Nd:YAG is 1064 nm, however, as discussed above photoionization requires vacuum ultraviolet light (VUV); within this section the frequency conversion of the infrared light (λ = 1064 nm) to the VUV light (λ = 118 nm) will be reviewed.

Using non-linear optic techniques it was possible to modify the wavelength of light output. Within the Nd:YAG laser frequency-doubling crystals were utilised to produce the second (532 nm) and fourth harmonics (266 nm) of the 1064 nm output (Andrews, 1997). However, to produce the 355 nm light (which was used for frequency tripling to 118 nm) is more complex. This process is comparable to phase-matched frequency doubling; as multiple photons of light are combined to produce a single light beam of higher energy. In this case, two wavelengths of light (532 nm and 1064 nm) are added to produce 355 nm light. Notably, the 532 nm light has double the energy of the 1064 nm, meaning that the combined energy of these two waves is 3 times the energy of the original 1064 nm light; as the energy of the combined beam is three times the original, the wavelength will be three times smaller, i.e. ~355 nm (Andrews, 1997).

Subsequently, the 355 nm light produced from Nd:YAG laser can be converted to the 118 nm light required for photoionization by 'frequency tripling' 355 nm light in xenon gas (Hilbig and Wallenstein, 1981). Although commonly referred to as 'frequency tripling', it can actually be more accurately described as 4-wave mixing (Abraham et al., 1985). This technique allows the conversion of three photons ($\omega_1 + \omega_2 + \omega_3$) to a single photon ($\omega_0$); the energy of the resultant photon emitted will be equal to the sum of the individual photons absorbed (E2.5):

$$\omega_1 + \omega_2 + \omega_3 = \omega_0 \qquad \text{(E2.5)}$$

For efficient 4-wave mixing to occur, phase-matching is often necessary (Abraham et al., 1985); note, collinearity of the interacting waves is an important component in phase-matching.

2.3.4 Dye Lasers - Sirah Precision Scan

Although mass spectrometry is often described as a universal technique sensitive to all species, there are certain species which cannot be easily ionized. One such example is the hydroxyl radical, OH, which is an important reactant in the atmosphere. However, the OH radical can be detected if it is excited prior to detection with 282.5 nm light. The PIMS set-up utilised a Sirah precision scan laser to produce light of wavelength 282.5 nm. The Sirah precision scan is an example of a dye laser and will therefore be described concurrently.

Dye lasers usually operate as *pseudo-four level* lasers, using solutions of organic dyes as the active medium. For efficient lasing the laser dye must absorb strongly at the excitation wavelength of the pump laser and have a broad fluorescence spectrum. The wavelength of light emitted is always greater (i.e. lower in energy) than the wavelength of light absorbed. Most laser dyes are polyatomic, conjugated molecules with high fluorescence quantum yields (Drexhage, 1976). The electrons within polyatomic, conjugated molecules are usually highly delocalised and have numerous vibrational modes. Before usage, the laser dye must be dissolved into solution (often in either alcohol or water). In solution, the multitude of available energy levels is broadened (due to enhanced intermolecular interactions within the solution), causing them to overlap and giving the laser dyes emission spectrum its characteristic broadness (Nemkovich et al., 1981). It is due to the broad emission spectrum that the laser can be tuned to output different wavelengths of light (Figure 2.7); however, in order for the laser output to be monochromatic a diffraction grating must be used. For simplicity the diffraction grating can be thought of as a mirror within the optical cavity of the dye laser (Figure 2.5). However, unlike a mirror, the grating will only resonate light of a certain wavelength; this light is directed back into the cavity where it can stimulate further emissions, and hence allow the amplification of light at this single wavelength (Loewen and Popov, 1997, Hermann and Ducuing, 1972).

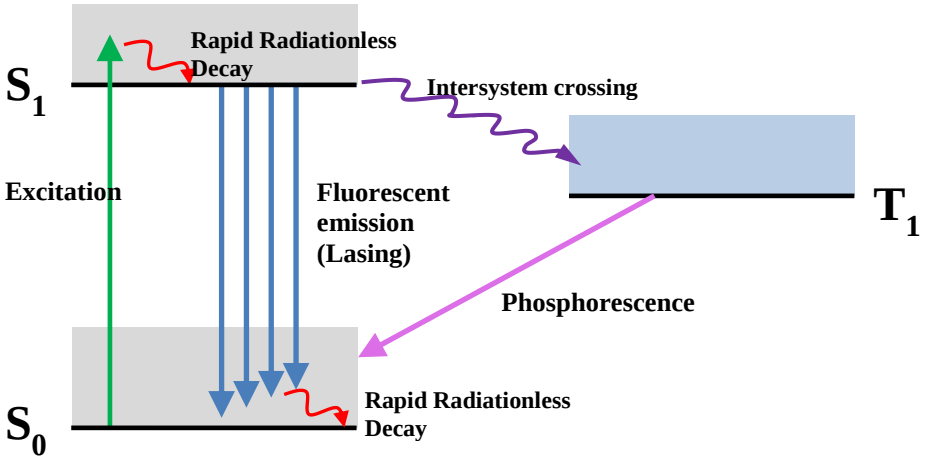

Figure 2.7: Simplified Jablonski diagram for a laser dye. S_0 is the ground singlet state, whilst S_1 is the first excited singlet state; T_1 ground triplet state.

Figure 2.7 shows a 4-level laser system, by which most dye lasers operate. This diagram also highlights the added complications caused by intersystem crossing from the singlet to triplet states (Andrews, 1997). Although intersystem crossing is slow (spin forbidden), it does still compete with fluorescent emissions, and hence detract from the laser output. Moreover, it also leads to phosphorescent emissions which interfere with the monochronicity of the laser output.

To generate 282.5 nm light, light from the Nd:YAG laser was pumped into the Sirah precision scan, with the dye Rhodamine 6G dissolved in methanol. Rhodamine 6G absorbs strongly at the 532 nm (the 2nd harmonic of the Nd:YAG output), the emitted light can be tuned to wavelengths of ~565 nm. Rhodamine-6G can be dissolved in a number of different solvents; however methanol was used as the wavelength of its peak intensity is closer to the desired wavelength for OH excitation (Zehentbauer et al., 2014). Furthermore, it yields the largest relative intensity of light at this peak wavelength (Table 2.2). The required 565 nm light generated was then passed through a doubling-crystal to generate light of ~282.5 nm in wavelength, a suitable wavelength of OH excitation.

Table 2.2: Solvent properties and emission characteristics of Rhodamine-6G in organic solvents (Zehentbauer et al., 2014). Note: peak intensities are all relative in methanol signal.

Solvent	Molar mass in g/mol	Density / g/ml at 20 °C	Refractive index at 20 °C	Peak wavelength in nm	Relative intensity at peak
Methanol	32.0	0.792	1.328	568	1
Ethanol	46.1	0.789	1.361	573	0.67
n-Propanol	60.1	0.803	1.387	570	0.64
i-Propanol	60.1	0.786	1.378	570	0.77
n-Butanol	74.1	0.81	1.399	572	0.72
n-Pentanol	88.2	0.814	1.409	574	0.73
Acetone	58.1	0.791	1.359	575	0.57
DMSO	78.1	1.104	1.479	579	0.41

2.4 Radical Detection Techniques

There are many different experimental techniques that have been utilised to monitor species in gas kinetics; within this section of my thesis selected detection techniques, commonly used to monitor short-lived radical species will be described. The selected techniques are: laser-induced fluorescence (LIF) and absorption detection; these techniques will then be compared to mass spectrometry. As the majority of the work described in this thesis was done using mass spectrometry this technique will be explained in the most detail. However, prior to this a brief summary of the other selected detection techniques will be given.

2.4.1.1 Laser Induced Fluorescence – OH Detection

Within the field of atmospheric chemistry there are few species more important than the hydroxyl radical, OH. Therefore, it is of the utmost importance that there are sensitive techniques available to detect this species (Creasey et al., 1997). Currently, the most common technique used for OH detection is laser induced fluorescence (LIF). During LIF, the target species (i.e. OH) is excited from its ground state using a probe laser; dye lasers are commonly used for excitation, which means the output from the laser can be tuned to match specific transitions. Following excitation, a corresponding fluorescence signal is emitted, this signal is then detected using a photomultiplier tube (PMT). Using LIF OH radicals can be probed using either on- or off-resonance detection (Figure 2.8). In OH off-resonance detection the wavelength of fluorescence (308 nm) is different from the excitation wavelength (~282.5 nm), due to relaxation of excited state from the $v' = 1$ to the $v' = 0$ energy level. On-resonance detection differs slightly as the wavelength of fluorescence emitted is equal to the excitation wavelength.

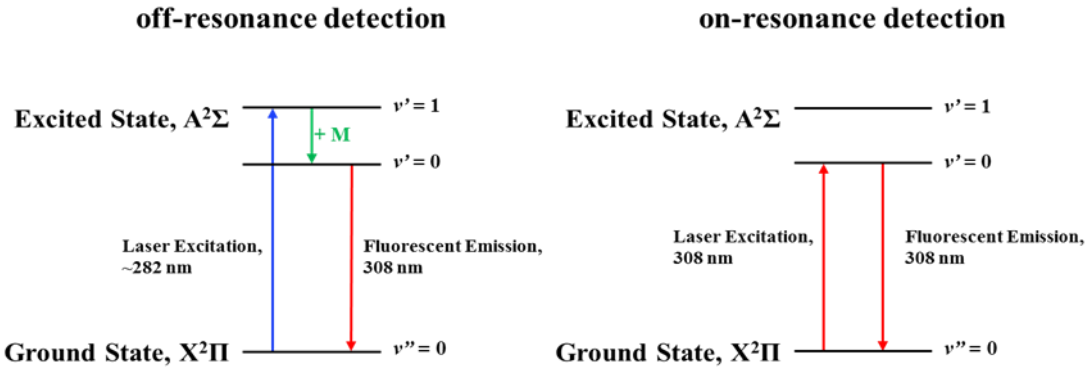

Figure 2.8: A schematic showing the OH transitions for both off- and on-resonance detection.

In order to optimise the technique, any interference from the probe laser must be minimised. It is for this reason that in most LIF configurations OH detection is perpendicular to the direction of probe laser propagation; this is of greater importance for on-resonance detection as optical filters cannot be utilized to reduce scattered light.

As previously mentioned LIF is a highly sensitive technique and is of particular use for OH detection during field campaigns as atmospheric concentrations of OH are low; [OH] ≈ 10^6 molecule cm^{-3}. However, there are certain disadvantages of this technique; for example, LIF only provides relative (and not an absolute) measurement of concentration and calibration is required before the concentration of species can be determined. Furthermore, most OH studies which utilise LIF are generally limited to relatively low pressures (p < 100 Torr), due to collisional quenching. However, recent developments in the sampling and detection

methods have meant high pressure measurements can be made (Stone et al., 2016). Finally, the technique is not universal, meaning that it can only be used to monitor certain species.

In Chapter IV of this thesis, results from a study investigating the chemically activated decomposition of acetyl radicals formed in CH_3CHO + OH reaction are discussed. This study primarily utilized PLP-PIMS to probe this reaction; however, complementary work was done using pulsed laser photolysis laser induced fluorescence (PLP-LIF). Using the PLP-LIF instrumentation the hydroxyl radical was monitored in the presence and absence of O_2 (Figure 2.9); notably in the presence of O_2, OH was recycled (details of these experiments can be found in Chapter IV, Section 4.4). The OH recycling study described was conducted by James Lockhart and Tamas Varga.

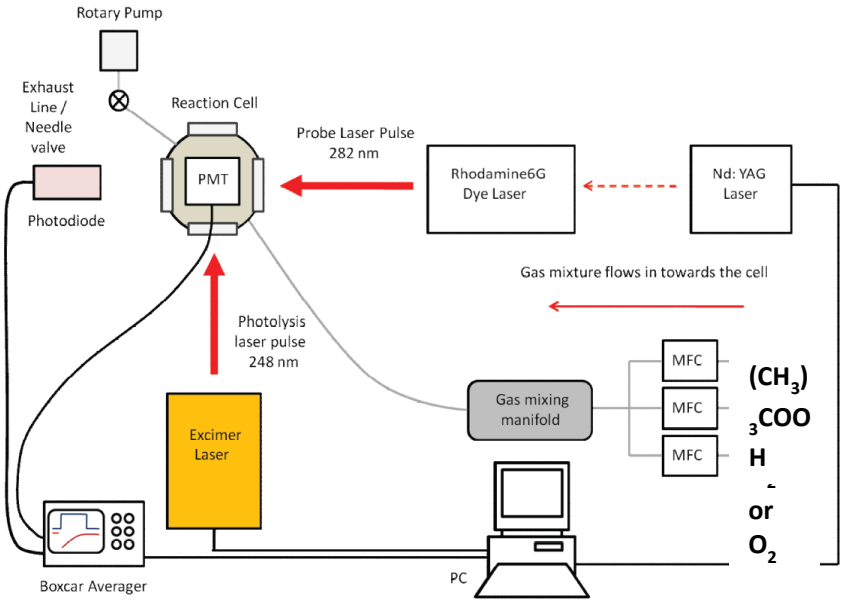

Figure 2.9: A schematic of the PLP-LIF system used to probe the CH_3CHO + OH reaction (Lockhart, 2014).

2.4.1.2 Absorption Spectroscopy

Absorption spectroscopy is also a commonly used detection technique; this method is of considerable use in the monitoring of fast reactions. Theoretically, absorption spectroscopy is a universal technique, as all molecules/atoms/radicals absorb light at certain wavelengths (specific to the species) in the UV/visible spectra. Typically, during absorption spectroscopy a 'white light' source, such as a xenon arc lamp, is shone through a sample of the reaction mixture. The target species will absorb some light at certain characteristic wavelengths; the fraction of light absorbed is proportional to the concentration of the target species in the sample, as described by the Beer-Lambert law (E2.4). One of the major advantages of absorption spectroscopy highlighted by the Beer-Lambert law, is that absolute concentrations of the target species can be determined (provided the cross section

of the target species and path length of the sample are known). An example of a typical absorption spectroscopy set-up can be seen in Figure 2.10. As with all kinetic techniques described, experiments are usually initiated using pulsed laser photolysis (Section 2.3.2); furthermore, complete decay traces are collected per laser pulse (high duty-cycle), making it an efficient detection technique.

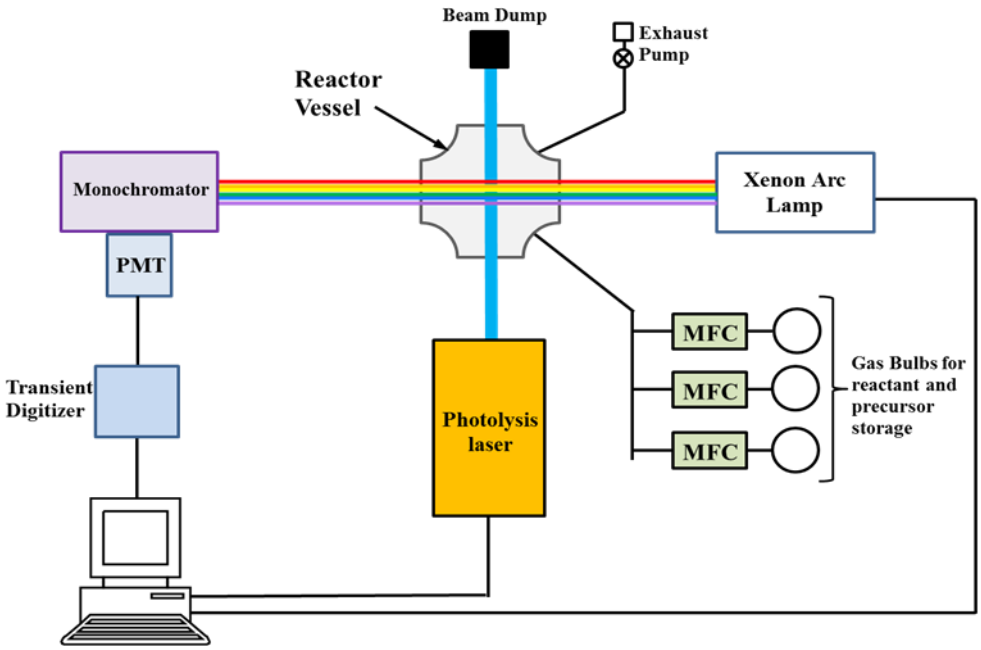

Figure 2.10: A schematic of basic absorption spectroscopy set-up, adapted from Pilling (1995).

Figure 2.10 is a schematic of a basic absorption spectroscopy set-up; however, there are several additional measures available to further enhance the technique. As can be seen from E2.4, the amount of light absorbed is directly related to the product of concentration of the target species and optical path length through the sample. This means that the sensitivity of the technique can be improved by the strategic placement of highly reflective mirrors, which allow the probe light to pass multiple times through the reactor prior to detection; this type of system is commonly known as a multipass cell. The main disadvantage of absorption spectroscopy is caused when a number of different species absorb at similar wavelengths, causing overlapping spectra. However, these problems can be minimised by resolving the time profiles at all wavelengths, so that individual species can be observed at single wavelengths, meaning background interferences can be minimised (Lewis et al., 2015).

2.4.2 Intercomparison of Detection Techniques

LIF, absorption and mass spectrometry are all highly sensitive detection techniques, which can yield invaluable information on the kinetics and mechanisms of specific gaseous reactions (Heard, 2008); yet, all of these techniques both have their strengths and their weaknesses.

Of the three techniques LIF is the most sensitive. Intuitively, it may be thought that absorption spectroscopy is the more sensitive technique as the number of photons being detected is much greater. However, at low species concentrations the difference between the intensity of light entering and exiting the system is small, making it difficult to measure. This is less of a problem for LIF detection as the background level of light is zero, this makes it much easier to detect small variations.

LIF can only be used to detect certain species, i.e. those which have large enough fluorescence quantum yields to be detected. Whereas, both mass spectrometry and absorption spectroscopy have the advantage of being 'universal' techniques and can measure many different chemical species. However, in absorption spectroscopy, if more than one species absorbs in the same region it can cause interference in the spectrum, as differentiating between the species can be complex. Moreover, in differential optical absorption spectroscopy (DOAS), measurements are often limited to tri- or diatomic molecules, as in larger molecules the absorption spectra get significantly less structured, due to overlapping of spectral lines (Heard, 2008); note that it is the lack of structure which causes the difficulties in differentiating the species. Conversely, it is relatively easy to distinguish between species using time of flight mass spectrometry, making this technique particularly useful for yielding mechanistic information about the reaction. However, it should be noted that the PLP-PIMS set-up used for the majority of the work presented could not be used to distinguish between isobaric species due to certain experimental limitation; however, other similar instruments have been able to successfully differentiate isobaric species, and even isomers, by measuring the photoionization efficiency spectra of the species detected (Osborn et al., 2008).

The principle advantage of absorption spectroscopy is that it is an absolute technique. Unlike both LIF and mass spectrometry, by using absorption spectroscopy absolute values of the species concentration are known; provided both the species cross section and path length are known.

2.5 Mass Spectrometry

The basic principle behind mass spectrometry is that different atoms and molecules can be separated due to their differing masses. This idea was first developed in the late 19th century / early 20th century, first by Wien and then by Thompson - who was the first person to separate ions using the mass-to-charge ratios, *m/z* (Thomson, 1910). Since its development, mass spectrometry has become an important detection technique used throughout scientific research: most notably, a mass spectrometer called a Calutron was developed and used in the Manhattan Project to separate uranium isotopes (Frederic P. Miller, 2010).

The aim of this section (Section 2.5) is to give specific details regarding the different types of mass spectrometers commonly used for gas kinetics (e.g. quadrupole and time-of-flight). Following this will be a focussed discussion of the history of mass spectrometry within gas-phase kinetics; in particular, the previous studies which inspired the design of the PIMS system at the University of Leeds are highlighted (Blitz et al., 2007). It must also be recognised that there are many other techniques within the field of reaction kinetics and dynamics which exploit mass spectrometry. One such example is velocity map imaging, a technique used primarily to probe reaction dynamics (Eppink and Parker, 1997); however, as the applications and methods of techniques such as this are not directly related to that of the Leeds PIMS set-up , they are not included within the history.

2.5.1 The Principles behind Mass Spectrometry

Mass spectrometry operates on the principle that a charged species (i.e. ions) in motion can be deflected by a magnetic field. The magnitude of the force induced by the charged species is directly proportional to the mass-to-charge of the individual charge species, this relationship can be derived from the Lorentz force law (E2.6):

$$F = z \times \big(E + (v \times B)\big) \qquad \text{(E2.6)}$$

In the Lorentz force law: *F* refers to the force experienced by the charged particle, *z* is the charge of the particle, *v* is the particle's velocity, *E* is the electric field strength and *B* is the strength of the magnetic field (Dirk Schulze-Makuch, 2008).

There are four key stages which are coupled together in mass spectrometry: ionization, acceleration, separation and detection. As referred to in E2.6 only charged particles can be deflected in a mass spectrometer, this means that before entering the spectrometer the target species must already be ionized. A caveat to this is that for the mass spectrometer to yield quantitative information all atoms/molecules must only be ionized by the same amount (i.e. to +1 ions); otherwise the mass-to-charge ratio will not be proportional to the mass of the original species. In this work a Nd:YAG laser was used to photoionize the gas sample before it enters the mass spectrometer, details of this can be found in Section 2.3.3. After ionization the newly formed ions must be accelerated toward the spectrometer; this is done by having a large potential difference between the gas sample inlet and the mass spectrometer (~3000 V), this process will be discussed in more detail in Section 2.5.1.2.

It is the mass analyser within the spectrometer that is used to separate the charged particles according to their individual mass-to-charge ratios. There are a number of different mass analysers that are utilised by mass spectrometry, the two most common being the quadrupole detector and the time-of-flight mass spectrometer (Harris, 2007).

2.5.1.1 The Quadrupole Mass Analyser

A quadrupole mass analyser is used, effectively, as a 'filter', selecting ions of a specific mass. The quadrupole itself is comprised of four parallel metal rods. In the quadrupole the transverse rods are coupled together yielding two sets of rods - opposing radio frequency voltages being applied on each pair. By applying these voltages to the rods only ions with a certain mass-to-charge ratio are able to pass through the quadrupole to the detector. Ions which do not have the required *m/z* ratio will not resonate properly within the quadrupole and will therefore not reach the detector (Figure 2.11). It should be noted that the mass-to-charge ratio range detected can be tuned varying the voltages across the rods.

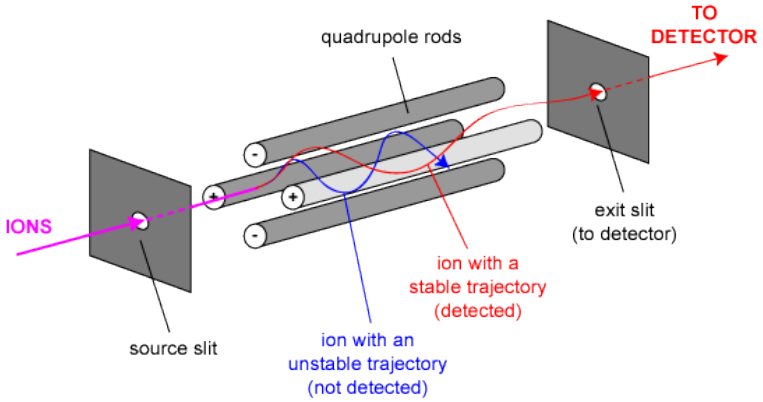

Figure 2.11: A schematic of a Quadrupole mass analyser (Gates, 2009).

The quadrupole mass analyser is a popular technique for separating ions and is a low cost method for detection; however, this method does have some limitations (see Section 2.5.2).

2.5.1.2 Time-of-Flight Mass Spectrometry

The second common type of mass analyser is time-of-flight mass spectrometry (ToF-MS), and it is this form of detection used in the Leeds PIMS set-up. With the ToF-MS all of the fundamental stages of mass spectrometry are done other than ionization; this is done *via* VUV-photoionization (Baeza-Romero et al., 2012). As can be seen from Figure 2.14, ions are initially accelerated from the ionization region into the mass spectrometer; high voltages of up to 3.5 kV have been used to accelerate the charged species towards the detector. By accelerating the ions through a constant electric field, the kinetic energy of all the ions is the same; however the speeds at which they accelerate are dependent on the individual masses of the ions (E2.7 - E2.9):

$$E_{\mathrm{P}} = z \times V \tag{E2.7}$$

$$E_{\mathrm{K}} = \frac{1}{2} \times m \times v^2 \tag{E2.8}$$

$$E_{\mathrm{K}} = E_{\mathrm{P}} \;\therefore\; z \times V = \tfrac{1}{2}\times m \times v^2 \qquad \text{(E2.9)}$$

In equations E2.7 – E2.9: E_{P} is the potential energy of the electric field, E_{K} is the kinetic energy of the ions, z is the charge on the ions, V is the voltage of the electric field, m is the mass of the ions and v is the velocity of the ions.

As can be seen in E2.9, because the energy of all the ions is constant, their speeds will vary depending on the mass of the ion. This means that the lightest ions will accelerate to the fastest speeds. Consequently, as speed is equal to distance over time, and the distance is approximately (but not quite) constant, the lightest ions will arrive first at the electron multiplier - the detector. This is the basic principle behind ToF-MS and the equations below confirm this mathematically and shows that the time of flight is proportional to the square root of the mass-to-charge ratio (E2.10 to E2.12) (Schlag, 1994).

$$z \times V = \tfrac{1}{2}\times m \times v^2 = \tfrac{1}{2}\times m \times \left(\frac{\mathrm{d}}{t}\right)^2 \qquad \text{(E2.10)}$$

$$t^2 = \frac{\mathrm{d}^2}{2\times V}\times\frac{m}{z} \qquad \text{(E2.11)}$$

$$t = \frac{\mathrm{d}}{\sqrt{2\times V}}\times\sqrt{\frac{m}{z}} \qquad \text{(E2.12)}$$

E2.10 – E2.12: Where t is the time of flight through the spectrometer, m/z is the mass-to-charge on the ions, V is the voltage of the electric field, and d is the distance travelled through the spectrometer. Note: v=d/t (i.e. speed = distance/time).

Data can only be collected from a ToF-MS if the extraction of ions into the spectrometer is pulsed (where length of the pulse is ~10 µs). If ions were allowed into the mass spectrometer at all times then ions of different masses would arrive at the detector simultaneously, depending on when they entered the spectrometer. For a meaningful mass spectrum to be collected a time zero is needed; this can be achieved by injecting the ions into mass spectrometer at specific time intervals. Typically, ions are extracted from the photoionization region into the spectrometer at ~50 µs intervals; as the time-of-flight even for the larger ions is significantly less than 50 µs.

The time-of-flight mass spectrometer used in experimentation developed by Kore technology in conjunction with the University of Leeds (Blitz et al., 2007). After the ions have been initially accelerated into the spectrometer, X and Y plates were used to direct the ions towards the reflectron: it should be noted that the lighter (and hence faster) ions will induce a larger force (see E2.6). Previously, it was stated that after acceleration all the ions possess equivalent kinetic energies – this is an oversimplification of the matter and fails to

take into account the initial energy of the ions before acceleration. This means that there is a small energy distribution within ions of the same mass-to-charge ratios. For time-of-flight mass spectrometry to be a valid method for mass separation, ions of the same mass must arrive at the detector at the same time. If there is an energy distribution within the ions this will not happen – making the technique ineffective. However, this problem may be rectified by using a reflectron, which accounts for the distribution of energies within the ions (Wiley and McLaren, 1955, Edmond de Hoffmann, 2007). Reflectrons use an electric field to reverse the direction of the ions in the mass spectrometer and direct towards the electron multiplier. Ions with low energy have less inertia and their direction can be quickly reversed in the reflectron. Although higher energy ions (with the same mass-to-charge ratio) reach the reflection faster their greater momentum means it take more energy and hence these ions will penetrate deeper into the electric field of the reflection, which increase their flight paths. The increased distance the high energy ions travel is proportional to the speed they were travelling at; this means that all the ions with the same mass-to-charge ratio will arrive simultaneously at the electron multiplier.

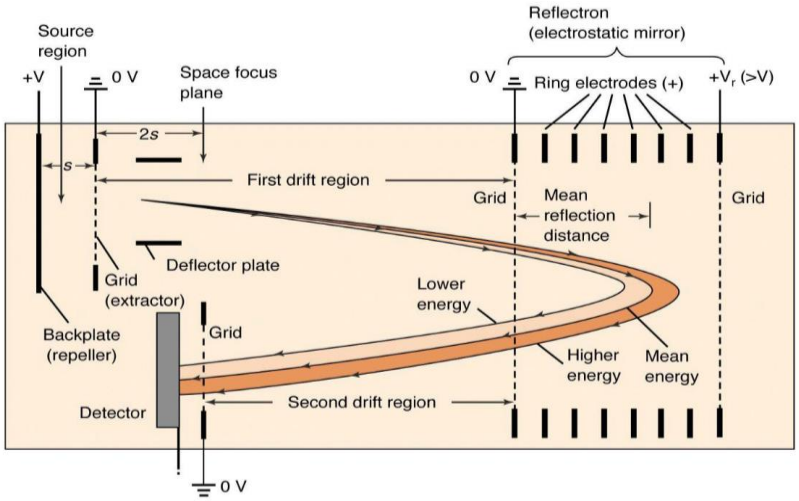

Figure 2.12: A schematic of a Time-of-Flight Mass Spectrometer, including reflectron; from Harris (2007).

Using a reflectron greatly improves the mass resolution of the time-of-flight mass spectrometer, hence making it a more sensitive technique for measuring kinetics and product yields.

In the PLP-PIMS set-up ions were detected using an electron multiplier. When a charged species hits the multiplier it initiates the secondary emission of (up to ~3) electrons, creating an exponential increase in the number of electrons and hence amplifies the signal. This ion signal was passed through a preamplifier to further increase the signal, before it was sent to the data acquisition hardware (Blitz et al., 2007).

2.5.2 Mass Spectrometry in Gas Kinetics: A brief history

Flash photolysis initiated mass spectrometry was first used to investigate gas-phase kinetics by Kistiakowsky et al. (1957). In these experiments the samples were ionized by single-pulse photolysis using a high energy flash lamp. The gas sample was ionized using a Bendix ion gun (continuous source) before reaching the spectrometer; the sample was then separated using time of flight mass spectrometry, as were most flash photolysis initiated mass spectrometry experiments at the time (Kistiakowsky and Mahan, 1957, Meyer, 1967). An electron multiplier coupled to an oscilloscope was used to present the data, however due to technological limitation it could not be used to store the data electronically; this had to be done instead using a Polaroid camera to photograph the screen of the oscilloscope. Fluctuations in the number of ions formed were common from pulse to pulse; this was accounted for by using neon (an inert substance) as a point of reference. However, even with the neon reference the observed fluctuations made it very difficult to collect quality data using this method of collection at this time (Carr, 2007).

It was not until 1970 that quadrupole mass analysers were used in flash photolysis time-resolved mass spectrometry (FP-TRMS); but following development, using quadrupole mass analysers for separation became the most popular method of FP-TRMS, until recent years (Strausz et al., 1970, Strausz et al., 1971, Slagle et al., 1981, Eskola and Timonen, 2003). At the forefront of this technique were Gutman and his colleagues who were amongst the first groups to utilise a pulsed laser for photolytic purposes (Slagle et al., 1981). In the Gutman set-up the photolysed samples of the reactant gases were continually injected into the path of a VUV ionizing resonance lamp through a sampling pinhole (~0.5 mm in diameter). The ionized sample was then separated using the quadrupole and then finally detected using a Daly scintillation detector (Figure 2.13). The ionization source in this set-up was continuous (as were all the ionization sources used in FP-TRMS previously).

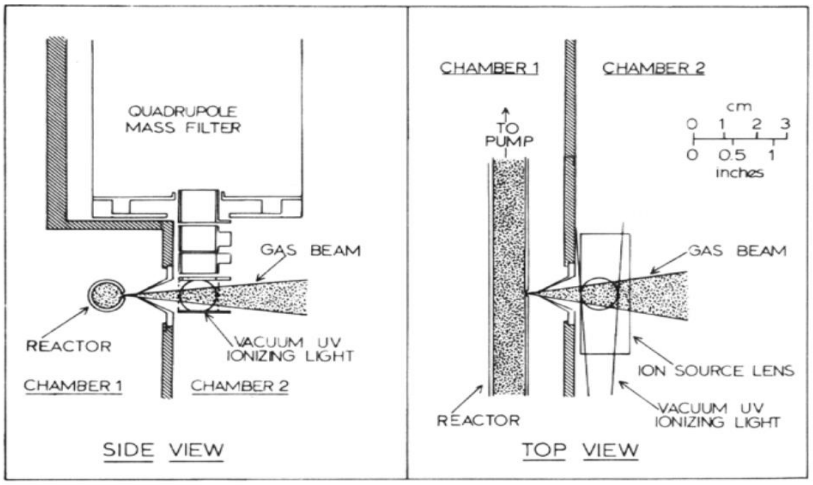

Figure 2.13: A schematic of Gutman's experimental set-up, presented in Slagle et al. (1981).

In comparison with the earlier work using time-of-flight mass spectrometry, using the quadrupole gave better reproducibility (Carr, 2007). However, there were other advantages for using quadrupole mass analyser: first of all in comparison to ToF-MS quadrupoles are relatively inexpensive and compact. Quadrupoles are also simpler to operate as complete time-resolved traces can be taken per laser pulse, unlike in ToF-MS where the delay time between the pump and probe pulses is scanned. Additionally, as both the quadrupole mass analyser and the resonance ionization lamp are in continuous operation, this system has high ion transmission efficiency (Carr, 2007). This means the all of the ions (of a certain mass) produced are detected, unlike the Kistiakowsky ToF-MS system described earlier which has a low duty cycle, hence better sensitivity could be accomplished using the Gutman system. Note that the duty cycle of a system can be defined as: the proportion of time a device is active (or on) within the period of a complete on/off cycle; devices with higher duty cycles are more efficient (Graf, 1999). Unlike, the early FP-TRMS systems Gutman's set-up could provide reliable kinetic data, although to gain accurate results the data were averaged 10^3-10^4 times (Carr, 2007, Slagle et al., 1981).

Although, initial studies using the PIMS had greater success using quadrupole mass analysers, ToF-MS has one major advantage – it can be used to detect many species at once. Therefore, theoretically, the decay of the reactants and the growth of the products can be measured simultaneously. Also because ToF-MS can detect multiple species at once it was possible to measure the different products formed in multichannel reactions and determine product yields. However, due to the low sensitivity of the early ToF-MS systems, this technique was overlooked until the late nineties.

As mentioned above the biggest problem with ToF-MS was sensitivity, the low sensitivity was partially due to inefficient ion transmission. This was solved by Fockenberg et al. (1999) who pioneered pulsed ionization time-of-flight mass spectrometry experiment. By

synchronising the ion pulse with ion extraction into the spectrometer the sensitivity of the ToF-MS was increased, allowing more reliable kinetics data to be recorded (Fockenberg et al., 1999). However, the improvement in the duty cycle in this system was still only 25% and to produce good data, long acquisition times were needed. In the PIMS set-up at the University of Leeds, the sensitivity was improved by over an order of magnitude by changing the ion source from a pulsed VUV resonance lamp to a pulsed laser. Using the pulsed laser gave significant improvements to the quality of data and reduced data acquisition times (Baeza-Romero et al., 2012).

In recent years, however, the most notable PIMS system is that used by the Sandia National Laboratories (Osborn et al., 2008). This specific set-up has been utilised in multiple high-impact studies, including: the first direct measurements of the C_1 Criegee intermediate (Taatjes et al., 2008, Welz et al., 2012); and the first direct observation of the hydroperoxyalkyl radical (QOOH), which is thought to be a key intermediary species in low temperature combustion (Savee et al., 2015). Notably, the work of Welz et al. (2012) is of particular relevance, as it was the inspiration for much of work in this thesis (Chapter VI). The generic construction of the gas flow and vacuum systems for this instrument are thought to be similar to the PIMS set-up at the University of Leeds (Figure 2.14); that said, there are key differences in both the ionization and detection steps.

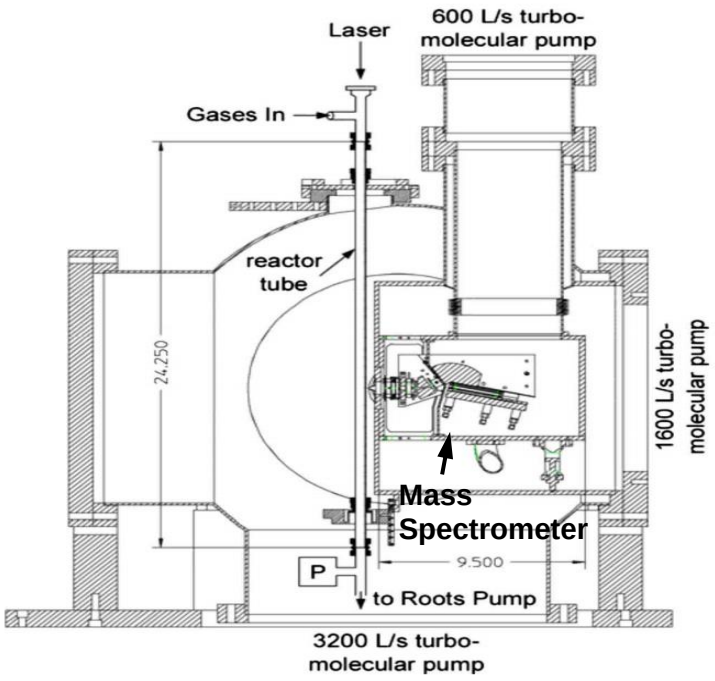

Figure 2.14: A schematic of the PIMS set-up utilized by the Sandia National Laboratories (Osborn et al., 2008).

Possibly the greatest advantage the Sandia National Laboratories PIMS system has over the majority of the other PIMS set-ups in use, is its ionization procedure. In the PIMS set-up

pioneered by Osborn et al. (2008) light from the Advanced Light Source (ALS) was used in photoionization; the advantage this has over other ionization techniques is that the light source is highly tuneable, capable of continuous ionization wavelengths between 50 – 175 nm. Therefore, by gradually varying the photoionization wavelengths the Sandia PIMS set-up can decipher between different isomers because of their varying photoionization efficiency, PIE, spectra (i.e. plots of the ion yield versus excitation energy) (Osborn et al., 2008). It should be noted that the Leeds PIMS set-up relies on dye lasers to tune the photoionization wavelength; using this methodology it is much more difficult to (smoothly) vary the photoionization energy (Baeza-Romero et al., 2012).

The method of detection for the Sandia National Laboratories instrument is also different, instead of a time-of-flight mass spectrometer; a multiplexed mass spectrometer (Mattauch–Herzog geometry) is used. Similarly to Gutman's set-up, the Sandia National Laboratories PIMS system has a 100% duty cycle, meaning that the instrument is highly sensitive. However a slight drawback of using the multiplexed mass spectrometer is that not all masses can be probed at once. Indeed, using this configuration allows for the detection of all mass signals between $m/z = 14 – 112$ (Osborn et al., 2008). This does limit the Sandia National Laboratories instrument somewhat; a simple illustration of this problem can be highlighted in the photolysis of methyl iodide:

$$CH_3I + h\nu \rightarrow CH_3 + I \qquad \text{(R2.5)}$$

Within this simple system there are three species; however, using the PIMS set-up pioneered by Osborn et al. (2008) only one of these species, the methyl radical, could be detected. Notably, even the methyl radical ($m/z = 15$) would be right on the limit of masses detected. However, in the Leeds PIMS system all three masses could be monitored. This is the major advantage of the Leeds PIMS set-up, which utilizes a ToF-MS and can therefore monitor all masses ($m/z < 300$), which ionize below ~10.5 eV.

2.6 Gas Handling System

The precursor and reactant gases were stored either in gas bulbs or gas cylinders. The flow of gases was controlled using various different sized mass flow controllers (Tylan: 25, 300 and 3000 sccm) and combined in a manifold before entering the reactor (Figure 2.15).

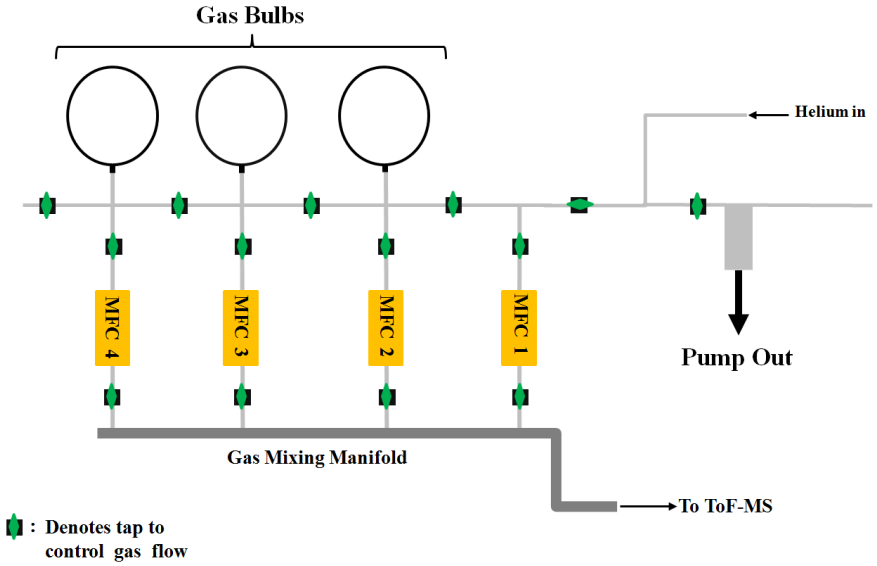

Figure 2.15: A schematic of the gas manifold.

The reactor was comprised of a steel flow-tube (internal diameter of 10.5 mm and ~70 cm in length); a 1 mm sampling orifice was located half-way along the flow-tube. Schematic representations of the flowtube and ToF-MS can be seen in Figures 2.1-2.2. The pressure in the reactor can be varied between 0.25 – 5 Torr, but experiments were typically run at ~2 Torr; note that the pressure was monitored at several places in the PIMS set-up using Edwards and MKS baratrons. The mass flow controllers were calibrated so that the total gas flow-rate could be determined. To guarantee that a fresh sample reached the reactive region per laser shot (10 Hz) the total velocity of the gases was kept above 400 cm s^{-1} for all the experiments; this ensured that the per laser shot gas mixture travelled a minimum of 40 cm (i.e. over half the length of the flowtube).

As previously discussed, a 1 mm sampling orifice was located half-way along the flow-tube; gas effuses through the sampling orifice into ToF-MS via the ionization region (see Section 2.3.3). The pressure inside the mass spectrometer must be kept extremely low ($p \approx 5 \times 10^{-6}$ Torr); so that the mean free path was significantly large enough that the ions do not collide on their way to the electron multiplier (as this will interfere with detection). To achieve this, an oil diffusion pump (Varian, VHS-6) was utilised to create a high vacuum environment in the ionization region (~10^{-5} Torr).

The mean free path is defined as the average distance that a moving particle (e.g. an atom, an ion, or a molecule) travels between successive collisions (Atkins, 1992); and can be calculated using kinetic theory (assuming the velocities of particles have a Maxwell distribution):

$$l = \frac{k_B \times T}{(\sqrt{2} \times \pi \times d^2 \times p)} \quad \text{(E2.13)}$$

In equation E2.13: l represent the mean free path (m); k_B is the Boltzmann constant (J K^{-1}); T is temperature (K); d is the estimated diameter of the particle (m); and p is the pressure (Pa).

The equation can be used to calculate the mean free path in the University of Leeds PIMS system. For the benefit of this calculation the following was assumed: $T = 293$ K; $d = 3.8 \times 10^{-10}$ m (note: this is equal to the van der Waal's diameter of acetaldehyde, a compound used frequently during the work discussed in Chapter IV) (El-Sayed and Bandosz, 2001); and $p = 5 \times 10^{-6}$ Torr (or 0.00067 Pa).

$$l = \frac{(1.3806 \times 10^{-23}) \times 293}{(\sqrt{2} \times \pi \times (3.8 \times 10^{-10})^2 \times (0.00067))} \quad \text{(E2.14)}$$

$$l \approx 9.5 \text{ m} \quad \text{(E2.15)}$$

Given that the distance the ions travel from the point of photoionization to the point of detection was approximately 50 cm, it suggests that the vast majority of the ions will not collide inside the PLP-PIMS system.

Lastly, it should be noted that to maintain the potential difference between the ionization region and the mass spectrometer, a 1 inch-squared earthing plate was attached to the flow-tube directly above the sampling orifice (Figure 2.16).

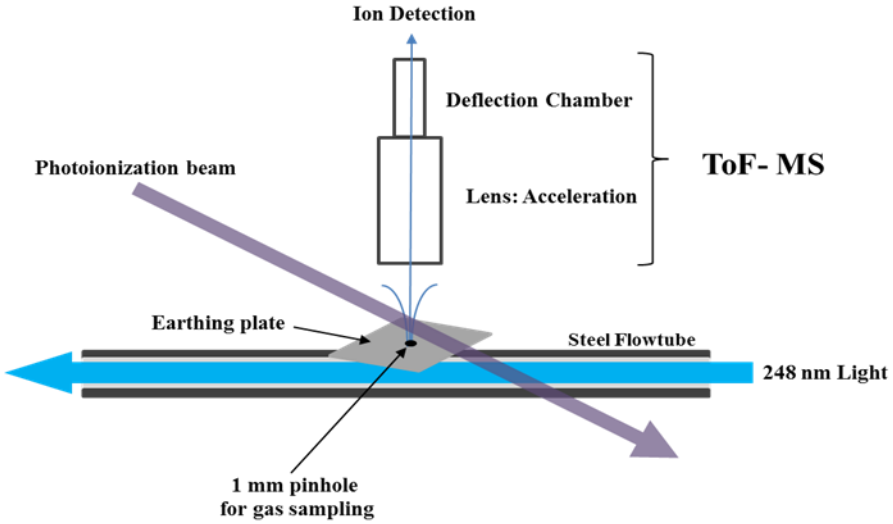

Figure 2.16: A schematic of the vacuum chamber, adapted from Blitz et al. (2007).

2.7 Data Acquisition

An electron multiplier was used to convert the ion signal of the reactive species into an electronic signal which was then sent to an oscilloscope (LeCroy Waverunner-2, LT354) *via* a signal amplifier (Figure 2.17). In the oscilloscope the electronic signal was then integrated (using Boxcar averaging) to give the (ion) signal intensity of the individual masses being tracked (Baeza-Romero et al., 2012). Note that the time delay observed between ionization and detection was proportional to the square-root of mass-to-charge ratio of the signal (Section 2.5.1). Crucially, by using ToF-MS several different masses can be observed simultaneously using the different channels available on the oscilloscope.

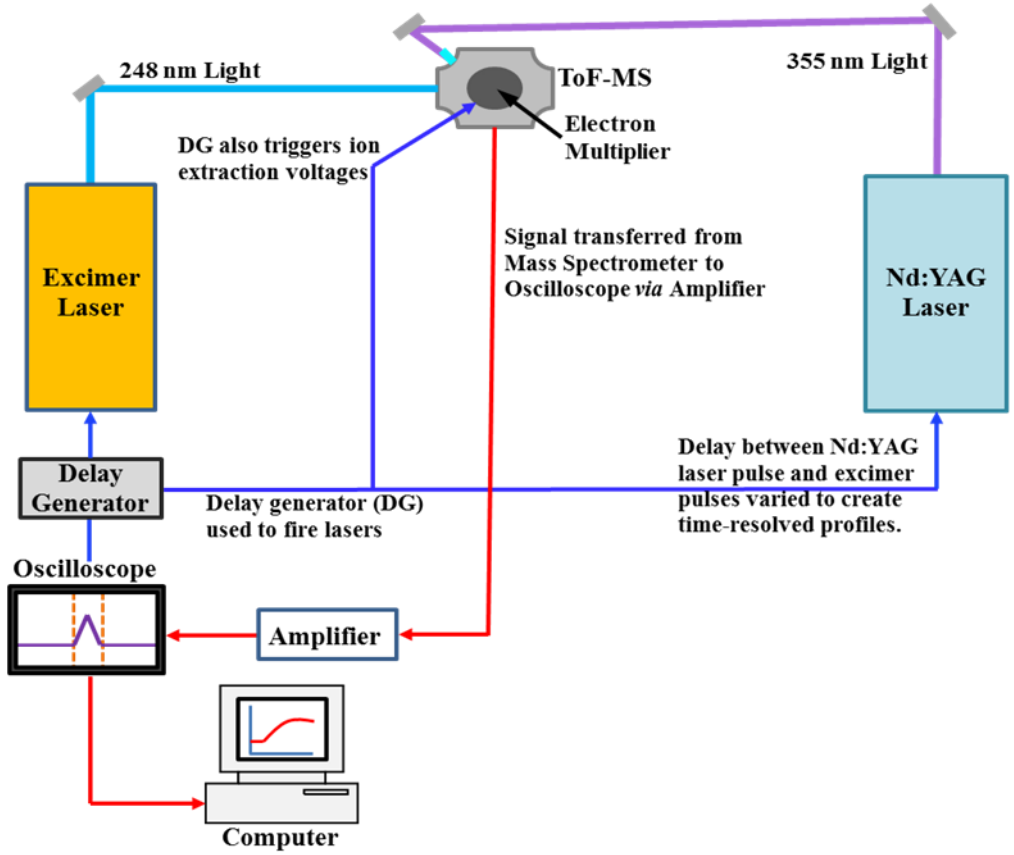

Figure 2.17: Schematic of Data Acquisition and Collection System.

To initiate data collection a pulse from a delay generator (SRS DG535) was used to fire the excimer laser. The same delay generator was then used to fire the Nd:YAG laser to photoionize the sampled gas. The temporal evolution of the reaction was monitored by increasing the delay time between the photolysis and probe lasers. By varying the delay time of the Nd:YAG pulse relative to the excimer pump, it was possible to map the kinetics of a reaction system (Blitz et al., 2007). Additionally, the Nd:YAG laser pulse was synchronised with the ion extraction pulse of the mass spectrometer to maximise the efficiency of the system. Experiments were run using a LabVIEW™ program, designed

specifically for data collection and storage for this setup. Note: the LabVIEW™ script was written by A. Goddard. Each experiment was run over a specific time range, where the delay time (between pump and probe pulses) was altered with each probe laser pulse by a preset amount each time. In general, 200 to 500 data points (+ 20 to 50 background points) were collected over a timescale of 1-10 ms, the individual scans were repeated 10-20 times to improve the quality of the data (Figure 2.18). For detection of a species to be considered as valid using the PLP-PIMS set-up, the data must have minimum signal-to-noise ratio (*SNR*) of approximately three. Note: from the data collected the signal-to-noise ratio were calculated using the following equation:

$$SNR = \frac{S_{height}}{\sigma_{BG}} \tag{E2.16}$$

where S_{height} is the maximum height of the signal; and σ_{BG} is the standard deviation of the background points.

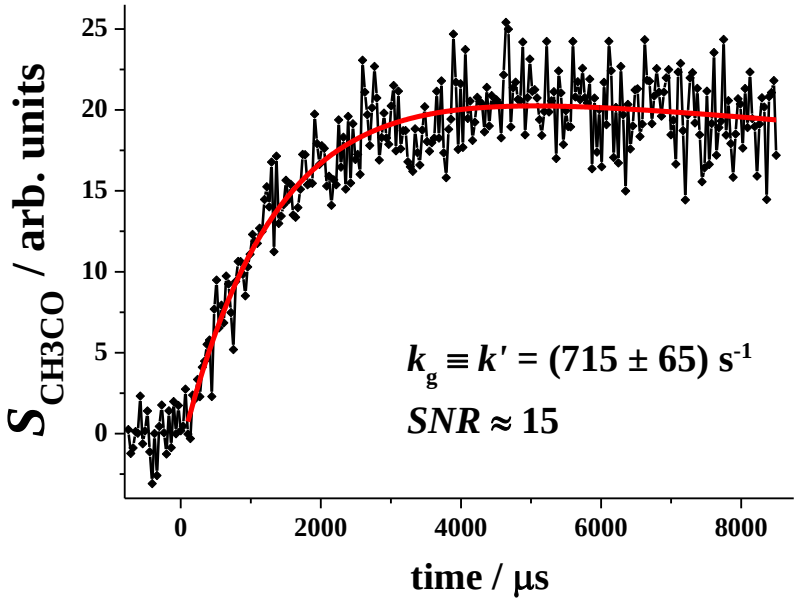

Figure 2.18: An example of the data collected using the PIMS set-up, where S_{CH3CO} is the time-resolved acetyl signal (see Chapter IV). Note that S_{CH3CO} is given in arbitrary units (denoted as arb. units).

2.8 Data Analysis

The majority of the experiments conducted using the PLP-PIMS set-up utilised the isolation method (Chapter I, Section 1.5.2). However, thus far the analysis of the raw data is yet to be discussed.

2.8.1 Analysis of Raw Data, Non-linear Fittings

All of the raw data acquired from the individual traces were initially analysed using OriginPro graphical software. A generic form of the equation used to fit the data can be found below (E2.17); an example of a non-linear fitting using E2.17 can be seen in Figure 2.19 (red line).

$$S_{X,\ t} = \frac{S_{\text{height}}\, k_{\text{g}} k_{\text{samp}}}{k_{\text{l}} - k_{\text{g}}}\left[\frac{e^{-k_{\text{g}}t} - e^{-k_{\text{samp}}t}}{k_{\text{eff}} - k_{\text{g}}} - \frac{e^{-k_{\text{l}}t} - e^{-k_{\text{samp}}t}}{k_{\text{eff}} - k_{\text{l}}}\right] + \frac{S_{\text{instant}}\, k_{\text{samp}}}{k_{\text{samp}} - k_{\text{l}}}\left[\frac{e^{-k_{\text{l}}t} - e^{-k_{\text{samp}}t}}{k_{\text{samp}} - k_{\text{l}}}\right] + S_0 \qquad \text{(E2.17)}$$

In equation E2.17: $S_{X,t}$ is equivalent to the time-resolved signal of the monitored species X; t is time; S_{height} represents the maximum height of the signal; k_g is the coefficient rate of formation of the signal; k_l is rate coefficient for the loss rate; k_{samp} is the rate of transportation for the sampled gas into the mass spectrometer (this was constrained to $k_{\text{samp}} \approx 30000\ \text{s}^{-1}$ in the analysis); S_{instant} refers to any instantaneous signal observed (photolytic); and S_0 is the signal at $t = 0$ s (Baeza-Romero et al., 2007).

For all of the data collected some variation of equation E2.17 was used to determine the pseudo first-order rate coefficient, *k'*, from the individual experiments conducted. It should be noted that the term in E2.17 equivalent to *k'* varied depending on whether the monitored species was a reactant or a product; if the species targeted was a reactant then the *k'* is equivalent to the term k_{l}. However, if the monitored species was a product, then it is k_{g} which is equals *k'*. This is a slight oversimplification of the system, which is described more accurately below (E2.18).

In the case where species X (i.e. CH_2OO) is a reactant:

$$k_{\text{l}} \equiv k' + k'_{\text{other}} \qquad \text{(E2.18)}$$

k'_{other} is a combined rate constant, which in E2.18 represents all of the other loss reaction from the system, such as secondary chemistry of the target species reaction, any impurities in the system, and diffusion to the walls. To obtain accurate values of *k'* it is preferable that $k' >> k'_{\text{other}}$ and measures were taken to minimise k'_{other}. Figure 2.19 shows some of the analysed data collected from an investigation into the reactivity of Criegee intermediates (see Chapters VI and VII). In this reaction the pseudo first-order rate coefficient can be determined from the loss rate coefficient, k_{l}.

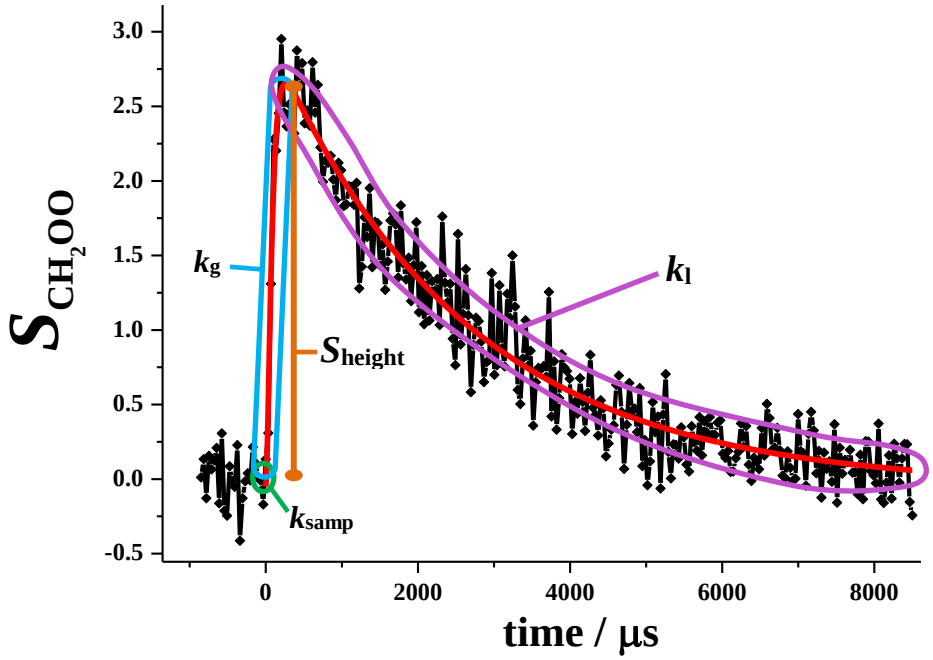

Figure 2.19: Depicts some of the data collected and subsequently analysed using the equation E2.17, in addition the time periods over which parameters are key is highlighted.

Figure 2.19 highlights the time scales over which some of the parameters operate. In Figure 2.19 the (rapid) formation and subsequent loss of the C_1 Criegee intermediate (CH_2OO) can be observed. Moreover, the data can be fitted using equation E2.17 (red line). In this system the transport times of the sampled gas were fast, meaning k_{samp} was large; if k_{samp} then the gradient of the plot close to time zero will be large (highlighted in green). During this experiment the concentration of oxygen present in the system was kept high ($[O_2] = 1 \times 10^{16}$ molecule cm^{-3}). As the bimolecular rate coefficient for CH_2OO formation is $k_{CH2I+O2} = 1.8 \times 10^{-12}$ molecule cm^{-3}, the observed rate of Criegee formation should be fast. Moreover this was observed experimentally and the growth rate coefficient, k_g, was evaluated at $k_g \approx 18{,}000$ s^{-1} (highlighted in blue). The final rate coefficient which can be extracted from the in the Criegee loss rate coefficient (k_l, highlighted in purple). As highlighted above, in the Criegee studies k_l is of particular importance as it can be used to the rate coefficient for the reaction of the Criegee intermediate with a trace species. It is therefore essential that equation E2.17 can be used to give accurate values of k_l from this analysis. The results shown in Table 2.3 indicate how the evaluations of the loss rate, k_l, vary with different constraints applied. Notably, all of the values of k_l determined using equation E2.17 are in ~95% agreement with each other. Furthermore, when the errors, σ_l, are taken into account there is no significant difference in any of the evaluations of k_l. Typically when analysing the experimental data the parameters k_{samp} and S_{bg} were fixed and

all other parameters were allowed to vary, although k_g parameter constraints of 17,500 < k_g (s^{-1}) < 22,500. It should that a simplified version of E2.17 was used to fit the data, this equation assumes $S_{instant} = 0$.

Table 2.3: Highlights the sensitivity of equation E2.17 towards k_l.

Constraints	S_{height}	k_g	k_{samp}	S_{bg}	k_l	σ_l
None	2.96	18447.95	31082.64	-0.05	391.79	21.40
k_{samp}, S_{bg}	2.94	18233.68	30000	0	414.595	10.65
k_{samp}, k_g, S_{bg}	2.94	18000	30000	0	414.95	10.06

Clearly, equation E2.17 is a non-linear function, when analysing non-linear expressions an iterative approach is used to minimise chi-squared, χ^2. It should be highlighted that the parameter χ^2 can be thought to represent the 'goodness' of the fitting to the data (Bevington, 1969); and the process minimising χ^2, minimises the deviations of the non-linear fitting from the experimental points. Notably, the OriginPro software used for the analysis utilises the Levenberg-Marquardt algorithm to minimise χ^2 (OriginPro). For the non-linear least squares analysis, the OriginPro software calculates a standard error between the modelled fit and the experimental data. As the kinetic traces contain between 150-400 points, it was thought that the sample size was large enough, so that the standard error calculated was a good estimation of the variation of the data.

2.8.2 Linear Fittings, Bimolecular Plots

Once the raw data was analysed the individual pseudo first-order rate coefficients were then used to construct a bimolecular plot (Chapter I, Section 1.5). The pseudo first-order rate coefficients determined were plotted with the associated standard error calculated from the non-linear least squares fitting. The bimolecular plot itself was then analysed using a linear least square fit, which was weighted using 'instrumental' weighting; this weights the data so that more emphasis is put upon the point with a smaller associated errors. The weighting factor used in the instrumental fittings is $1/\sigma^2$. The linear fittings utilised in OriginPro also calculate standard errors associated with the different parameters, these were calculated using the following expression (E2.19):

$$SE_{\bar{x}} = \frac{s}{\sqrt{n}} \qquad \text{(E2.19)}$$

In equation E2.19: $SE_{\bar{x}}$ is the standard error of the mean, s is the sample standard deviation, and n is the number of measurements in the sample.

It should be noted that when the sample size is small ($n < 25$), the sample standard deviation is not always a good representation of the standard deviation of the population, σ. Due to the added level of uncertainty this causes, the errors quoted for small sample sizes should be magnified to accommodate for possible differences in σ and *s*. To take into account the smaller sample sizes, the bimolecular plots were fitted with confidence limits (68%, or 1σ level); the confidence interval half-width (i.e. a value equal to half the magnitude of the difference between the upper and lower limits) was also calculated, which is a good alternative estimation of the uncertainty. Unlike the standard error, the confidence intervals determined in OriginPro do take the sample size into consideration as they are calculated using Student's *t* statistics. Student's *t* is a commonly used test for small sample sizes, which adjusts the total error quoted for the added uncertainty of the limited sample by multiplying the standard error by a *t* value. The magnitudes of the *t* values are dependent on the level of confidence required from the measurement and the sample size; when the sample size (and hence the degrees of freedom) is small the *t* value will be large and *vice versa*. Additionally, the *t* values also increase as the level of confidence required increases; at the 68% confidence level, the *t* values range from $\sim 2 > t > 1$ as the degrees of freedom (df) vary from $1 < df < \infty$. For the majority of the bimolecular plots in this thesis (if there were sufficient degrees of freedom) there were not significant differences between the values of the standard error and the 68% confidence interval half-width (calculated using the Student's *t*). However, on the occasions where there was a significant difference the largest value of the error (i.e. confidence interval half-width) was chosen, as it was thought to be a better representation of the random errors of the data.

Table 2.4: Show the variation of the data collected from the reaction between the C_1 Criegee intermediate and SO_2 (see Chapter VI for details).

$CH_2OO + SO_2$	k_{C1SO2} (10^{-11} cm^3 $molecule^{-1}$ s^{-1})	Uncertainty
i	3.6	0.3
ii	3.7	0.2
iii	4.0	0.4
iv	3.8	0.1
v	3.7	0.2
Average	**3.8**	**0.1**
Standard deviation	**0.2**	

From Table 2.4 can be clearly be seen that the spread of the data observed experimentally (i.e. the standard deviation) is greater than the uncertainty propagated from the random errors. The reason for this is that there were other errors associated with the experiments, such as systematic errors, which were not taken into account statistically.

There were a number of factors which contribute to the systematic errors of the PLP-PIMS technique: firstly the Baratron pressure gauges used to measure the pressure may have given systematically low or high readings, leading to errors in concentration. However, two pressure gauges were used (one before and one after the flow-tube) which typically within 5% to 10%, when the valve to the exhaust pump was closed. Note: the Baratron located at the end of the flow-tube was located right next to the exhaust pump, when the valve to this pump was opened the pressure reading from the adjacent Baratron was reduced. The mass flow controllers (MFCs) could also lead to systematic errors in the reactant concentration. However, the MFCs were calibrated regularly and there was often little change their calibration plots. Moreover, when updating the spreadsheets with the new calibration values it was common for variation to reactant concentrations to be less than 5%. A final area where systematic error may be introduced is the reactant concentrations in the gas bulbs. The gas bulbs concentration were thought to be accurate as the amount of the reactant gas in comparison to the bulk gas (usually helium) was monitored carefully during the bulb preparation procedure, using the Baratron directly attached to the gas line. However, this concentration may become inaccurate if there are impurities or decomposition of the sample chemicals. Again, a systematic error of ±5% is assumed in the gas bulb concentration.
All of the systematic errors discussed above were propagated together using E2.20, the results of which can be seen in Table 2.5.

$$\sigma_{\text{total}}{}^2 = \sqrt{\sigma_{\text{PG}}{}^2 + \sigma_{\text{MFC}}{}^2 + \sigma_{[\text{GB}]}{}^2} \qquad \text{(E2.20)}$$

In equation E2.20: σ_{total} is the uncertainty of the propagated errors; σ_{PG} is the uncertainty associated with the pressure gauge readings; σ_{MFC} is the uncertainty associated with the MFC calibration; and $\sigma_{[\text{GB}]}$ is the uncertainty associated with the gas bulb concentrations.

Table 2.5: Highlights possible sources of systematic errors within the PLP-PIMS system.

Source of Error	Associated Uncertainty (%)
Pressure Gauge Reading	7.5
MFC calibration	3
Gas Bulb Concentration	5
Total Propagated Uncertainty	9.5

Following this analysis it was decided that an additional systematic experimental error of 10% would be applied to all of the data. This additional random error was propagated with the random errors (from OriginPro) to give a total error for the experiments. Unless otherwise stated, it is this total error that will be used throughout this thesis to describe the uncertainty in the data.

2.9 References

ABRAHAM, N. B., ARECCHI, F. T., MOORADIAN, A. & SONA, A. 1985. Physics of New Laser Sources. New York: Springer Science.
ANDERSON, J. G. 1987. Free radicals in the earth's atmosphere: their measurement and interpretation. *Annual Review of Physical Chemistry,* 38**,** 489-520.
ANDREWS, D. 1997. *Lasers in Chemistry,* Berlin, Springer-Verlag.
ATKINS, P. W. 1992. *The Elements of Physical Chemistry,* Oxford, Oxford University Press.
ATKINSON, R. 2000. Atmospheric chemistry of VOCs and NO_x. *Atmospheric Environment,* 34**,** 2063-2101.
BAEZA-ROMERO, M. T., BLITZ, M. A., GODDARD, A. & SEAKINS, P. W. 2012. Time-of-flight mass spectrometry for time-resolved measurements: Some developments and applications. *International Journal of Chemical Kinetics,* 44**,** 532-545.
BAEZA-ROMERO, M. T., GLOWACKI, D. R., BLITZ, M. A., HEARD, D. E., PILLING, M. J., RICKARD, A. R. & SEAKINS, P. W. 2007. A combined experimental and theoretical study of the reaction between methylglyoxal and OH/OD radical: OH regeneration. *Physical Chemistry Chemical Physics,* 9**,** 4114-4128.
BEVINGTON, P. R. 1969. *Data Reduction and Error Analysis for the Physical Sciences,* New York, McGraw-Hill.
BLITZ, M. A., GODDARD, A., INGHAM, T. & PILLING, M. J. 2007. Time-of-flight mass spectrometry for time-resolved measurements. *Review of Scientific Instruments,* 78.
CARR, R. W. 2007. Flash Photolysis with Time-Resolved Mass Spectrometry. *Advances in Photochemistry.* John Wiley & Sons, Inc.
CATHONNET, M. 1994. Chemical kinetic modeling of combustion from 1969 to 2019. *Combustion Science and Technology,* 98**,** 265-279.
CREASEY, D., HALFORD-MAW, P., HEARD, D., PILLING, M. & WHITAKER, B. 1997. Implementation and initial deployment of a field instrument for measurement of OH and HO_2 in the troposphere by laser-induced fluorescence. *Journal of the Chemical Society, Faraday Transactions,* 93**,** 2907-2913.
DIRK SCHULZE-MAKUCH, L. N. I. 2008. Life in the Universe: Expectations and Constraints. Berlin: Springer-Verlag.
DREXHAGE, K. H. 1976. Fluorescence efficiency of laser-dyes. *Journal of Research of the National Bureau of Standards Section a-Physics and Chemistry,* 80**,** 421-428.
EDMOND DE HOFFMANN, V. S. 2007. Mass Spectrometry: Principles and Applications. Chichester: John Wiley & Sons Ltd.
EL-SAYED, Y. & BANDOSZ, T. J. 2001. A study of acetaldehyde adsorption on activated carbons. *Journal of colloid and interface science,* 242**,** 44-51.
EPPINK, A. T. J. B. & PARKER, D. H. 1997. Velocity map imaging of ions and electrons using electrostatic lenses: Application in photoelectron and photofragment ion imaging of molecular oxygen. *Review of Scientific Instruments,* 68**,** 3477-3484.
ESKOLA, A. J. & TIMONEN, R. S. 2003. Kinetics of the reactions of vinyl radicals with molecular oxygen and chlorine at temperatures 200–362 K. *Physical Chemistry Chemical Physics,* 5**,** 2557-2561.
FOCKENBERG, C., HALL, G. E., PRESES, J. M., SEARS, T. J. & MUCKERMAN, J. T. 1999. Kinetics and product study of the reaction of CH_3 radicals with $O(P^3)$ atoms using time resolved time-of-flight spectrometry. *Journal of Physical Chemistry A,* 103**,** 5722-5731.
FREDERIC P. MILLER, A. F. V., MCBREWSTER JOHN 2010. Calutron. Saarbrücken VDM Publishing.
FRISCH, M. J., TRUCKS, G. W., SCHLEGEL, H. B., SCUSERIA, G. E., ROBB, M. A., CHEESEMAN, J. R., SCALMANI, G., BARONE, V., MENNUCCI, B., PETERSSON, G. A., NAKATSUJI, H., CARICATO, M., LI, X., HRATCHIAN, H. P., IZMAYLOV, A. F., BLOINO, J., ZHENG, G., SONNENBERG, J. L., HADA, M., EHARA, M., TOYOTA, K., FUKUDA, R., HASEGAWA, J., ISHIDA, M., NAKAJIMA, T., HONDA, Y., KITAO, O., NAKAI, H., VREVEN, T., MONTGOMERY, J. A., JR.; PERALTA, J. E., OGLIARO, F., BEARPARK, M., HEYD, J. J., BROTHERS, E., KUDIN, K. N., STAROVEROV, V. N., KOBAYASHI, R., NORMAND, J., RAGHAVACHARI, K., RENDELL, A., BURANT, J. C.,

IYENGAR, S. S., TOMASI, J., COSSI, M., REGA, N., MILLAM, J. M., KLENE, M., KNOX, J. E., CROSS, J. B., BAKKEN, V., ADAMO, C., JARAMILLO, J., GOMPERTS, R., STRATMANN, R. E., YAZYEV, O., AUSTIN, A. J., CAMMI, R., POMELLI, C., OCHTERSKI, J. W., MARTIN, R. L., MOROKUMA, K., ZAKRZEWSKI, V. G., VOTH, G. A., SALVADOR, P., DANNENBERG, J. J., DAPPRICH, S., DANIELS, A. D., FARKAS, Ö., FORESMAN, J. B., ORTIZ, J. V., CIOSLOWSKI, J. & FOX, D. J. 2009. Gaussian 09, Revision. Wallingford CT: Gaussian, Inc.

FUENTES, J. D., LERDAU, M., ATKINSON, R., BALDOCCHI, D., BOTTENHEIM, J. W., CICCIOLI, P., LAMB, B., GERON, C., GU, L., GUENTHER, A., SHARKEY, T. D. & STOCKWELL, W. 2000. Biogenic hydrocarbons in the atmospheric boundary layer: A review. *Bulletin of the American Meteorological Society,* 81**,** 1537-1575.

GATES, P. 2009. *Quadruple & Triple Quadrupole (QQQ) Mass Analysis* [Online]. Bristol: University of Bristol. Available: http://www.chm.bris.ac.uk/ms/theory/quad-massspec.html 28/03/2013].

GRAF, R. F. 1999. Modern Dictionary of Electronics. Woburn, MA: Butterworth-Heinemann.

HARRIS, D. 2007. *Quantitative Chemical Analysis,* New York, Freeman.

HEARD, D. 2008. *Analytical Techniques for Atmospheric Measurement,* Wiley.

HERMANN, J. P. & DUCUING, J. 1972. Dispersion of the two-photon cross section in rhodamine dyes. *Optics Communications,* 6**,** 101-105.

HILBIG, R. & WALLENSTEIN, R. 1981. Enhanced production of tunable VUV radiation by phase-matched frequency tripling in Krypton and Xenon. *The Journal of Quantum Electronics,* 17**,** 1566-1573.

JENKIN, M. E., SAUNDERS, S. M., DERWENT, R. G. & PILLING, M. J. 1997. Construction and application of a master chemical mechanism (MCM) for modelling tropospheric chemistry. *Abstracts of Papers of the American Chemical Society,* 214**,** 116-COLL.

KISTIAKOWSKY, G. B. & MAHAN, B. H. 1957. The Photolysis of Methyl Ketene. *Journal of the American Chemical Society,* 79**,** 2412-2419.

KOECHNER, W. & BASS, M. 2003. Solid-State Lasers: A Graduate Text. New York: Springer-Verlag.

LACKNER, M. 2008. *Lasers in Chemistry: Probing Matter,* Weinheim, Wiley-VCH Verlag GmbH & co.

LEWIS, T. R., BLITZ, M. A., HEARD, D. E. & SEAKINS, P. W. 2015. Direct evidence for a substantive reaction between the Criegee intermediate, CH_2OO, and the water vapour dimer. *Physical Chemistry Chemical Physics,* 17**,** 4859-4863.

LOCKHART, J. 2014. *The Role of Chemical Activation in the Formation and Loss of Atmospheric Carbonyl Species.* PhD, University of Leeds.

LOEWEN, E. G. & POPOV, E. 1997. Diffraction Gratings and Applications. New York: Marcel Dekker.

MEYER, R. T. 1967. Apparatus for flash photolysis and time resolved mass spectrometry. *Journal of Scientific Instruments,* 44**,** 422.

NELSON, L. S. & RAMSAY, D. A. 1956. Flash photolysis experiments with a sapphire flash lamp. *Journal of Chemical Physics,* 25**,** 372-372.

NEMKOVICH, N. A., RUBINOV, A. N. & TOMIN, V. I. 1981. Kinetics of luminescence spectra of rigid dye solutions due to directed electronic energy transfer. *Journal of Luminescence,* 23**,** 349-361.

ORIGINPRO OriginLab. Northampton, MA.

OSBORN, D. L., ZOU, P., JOHNSEN, H., HAYDEN, C. C., TAATJES, C. A., KNYAZEV, V. D., NORTH, S. W., PETERKA, D. S., AHMED, M. & LEONE, S. R. 2008. The multiplexed chemical kinetic photoionization mass spectrometer: A new approach to isomer-resolved chemical kinetics. *Review of Scientific Instruments,* 79**,** 104103.

PILLING, M. J. & SEAKINS, P. W. 1995. *Reaction Kinetics,* Oxford, Oxford University Press.

PLANCK, M. 1901. Law of energy distribution in normal spectra. *Annalen Der Physik,* 4**,** 553-563.

PORTER, G. 1950. Flash photolysis and spectroscopy a new method for the study of free radical reactions. *Proceedings of the Royal Society of London Series a-Mathematical and Physical Sciences,* 200**,** 284-&.

SAVEE, J. D., PAPAJAK, E., ROTAVERA, B., HUANG, H., ESKOLA, A. J., WELZ, O., SHEPS, L., TAATJES, C. A., ZÁDOR, J. & OSBORN, D. L. 2015. Direct observation and kinetics of a hydroperoxyalkyl radical (QOOH). *Science,* 347**,** 643-646.
SCHLAG, E. W. 1994. Time-of-Flight Mass Spectrometry and its Applications. Amsterdam: Elsevier.
SEAKINS, P. W. & BLITZ, M. A. 2011. Developments in Laboratory Studies of Gas-Phase Reactions for Atmospheric Chemistry with Applications to Isoprene Oxidation and Carbonyl Chemistry. *In:* LEONE, S. R., CREMER, P. S., GROVES, J. T. & JOHNSON, M. A. (eds.) *Annual Review of Physical Chemistry, Vol 62.* Palo Alto: Annual Reviews.
SLAGLE, I. R., YAMADA, F. & GUTMAN, D. 1981. Kinetics of free-radicals produced by infrared multiphoton-induced decompositions 1. Reactions of allyl radicals with nitrogen-dioxide and bromine. *Journal of the American Chemical Society,* 103**,** 149-153.
STONE, D., BLITZ, M., INGHAM, T., ONEL, L., MEDEIROS, D. J. & SEAKINS, P. W. 2016. An instrument to measure fast gas phase radical kinetics at high temperatures and pressures. *Review of Scientific Instruments,* 87**,** 054102.
STRAUSZ, O., BARTON, S., DUHOLKE, W., GUNNING, H. & KEBARLE, P. 1971. Flash Photolysis with Kinetic Mass Spectrometry. *Canadian Journal of Chemistry,* 49**,** 2048-2052.
STRAUSZ, O. P., DUHOLKE, W. K. & GUNNING, H. E. 1970. Flash photoionization studies with kinetic mass spectrometry. *Journal of the American Chemical Society,* 92**,** 4128-4129.
TAATJES, C. A., MELONI, G., SELBY, T. M., TREVITT, A. J., OSBORN, D. L., PERCIVAL, C. J. & SHALLCROSS, D. E. 2008. Direct observation of the gas-phase Criegee intermediate (CH_2OO). *Journal of the American Chemical Society,* 130**,** 11883-11885.
THOMSON, J. J. 1910. LXXXIII. Rays of positive electricity. *Philosophical Magazine Series 6,* 20**,** 752-767.
WELZ, O., SAVEE, J. D., OSBORN, D. L., VASU, S. S., PERCIVAL, C. J., SHALLCROSS, D. E. & TAATJES, C. A. 2012. Direct Kinetic Measurements of Criegee Intermediate (CH_2OO) Formed by Reaction of CH_2I with O_2. *Science,* 335**,** 204-207.
WILEY, W. & MCLAREN, I. H. 1955. Time-of-flight mass spectrometer with improved resolution. *Review of Scientific Instruments,* 26**,** 1150-1157.
ZÁDOR, J., TAATJES, C. A. & FERNANDES, R. X. 2011. Kinetics of elementary reactions in low-temperature autoignition chemistry. *Progress in Energy and Combustion Science,* 37**,** 371-421.
ZEHENTBAUER, F. M., MORETTO, C., STEPHEN, R., THEVAR, T., GILCHRIST, J. R., POKRAJAC, D., RICHARD, K. L. & KIEFER, J. 2014. Fluorescence spectroscopy of Rhodamine 6G: Concentration and solvent effects. *Spectrochimica Acta Part A: Molecular and Biomolecular Spectroscopy,* 121**,** 147-151.

Chapter III:

Development of Alternative Configurations for the PIMS Set-up

3. Development of Alternative Configurations for the PIMS Set-up

A number of adjustments have been made to the PLP-PIMS system used for the experimental work described in this thesis. These changes to the PIMS configuration were primarily used to either expand the range of conditions used for experimentation, or to allow for the detection of specific species. Within this thesis chapter will be an in depth account of the development of two different configurations of the PIMS set-up: the first being the addition of OH detection (Beames et al., 2011); and the second being a high pressure configuration ($p \approx 350$ Torr). It should be noted that for both of the configurations described in this chapter, more testing and further development is needed before either technique could be used reliably over extended periods of time.

The first of the configuration changes led to the detection of hydroxyl radicals using a multiphoton ionization scheme, however, currently, the simultaneous generation of the 355 nm and 282.5 nm light required has not yet been optimized. As a result, the intensity of the 282.5 nm light from the Sirah dye laser reduces rapidly and constant realignment was needed.

Even greater problems encountered with the high pressure system and significant work is still required to achieve time-resolved detection of species. In addition to this, the sensitivity of the technique (particularly when using the 6-way cross configuration) was orders of magnitude lower than in the basic PIMS set-up, described in Chapter II.

3.1 OH Detection Technique

Mass spectrometry is often referred as a universal technique (Heard, 2008); this is theoretically a correct description of the method, although is somewhat misleading in the context of the PLP-PIMS system reported in Chapter II. In reality, only species which have an ionization potential below the threshold of the ionization source can be detected. The PLP-PIMS system used utilises 118 nm light (~10.5 eV) to ionize the sample prior to detection (Baeza-Romero et al., 2012); this method could be described as ‘soft’ ionization, meaning that any photo-fragmentation of the gases sampled will be low. However, a flaw with this ionization technique is that not all species will be ionized using 118 nm of light, the hydroxyl radical being one. From Chapter I it is clear that OH is an important atmospheric oxidant. Additionally, in a number of the reaction systems investigated within this body of work, OH was either a reactant or a potential product. Therefore, it would be advantageous if OH could be monitored using the PLP-PIMS set-up; unfortunately, the hydroxyl radical has an ionization potential of ~13 eV and cannot be monitored using the

basic PIMS technique. However, in a recent publication by Beames et al. (2011) a 1 + 1′ multiphoton ionization (MPI) scheme was used; this technique utilizes the same $A^2\Sigma \leftarrow X^2\Pi$ transition, often exploited in off-resonance LIF detection of OH (~282.5 nm). The combined energy of the 282.5 nm (4.39 eV) light and the original photoionization laser (118 nm, 10.49 eV) has a total energy of 14.88 eV; notably, this is precisely equivalent to the energy of a transition to the *n*d Rydberg series converging on the $A^3\Pi$ state (Beames et al., 2014). From the $A^3\Pi$ state, auger decay to an autoionized OH^+ $X^3\Sigma$ energy level is possible (Figure 3.1) (Beames et al., 2014).

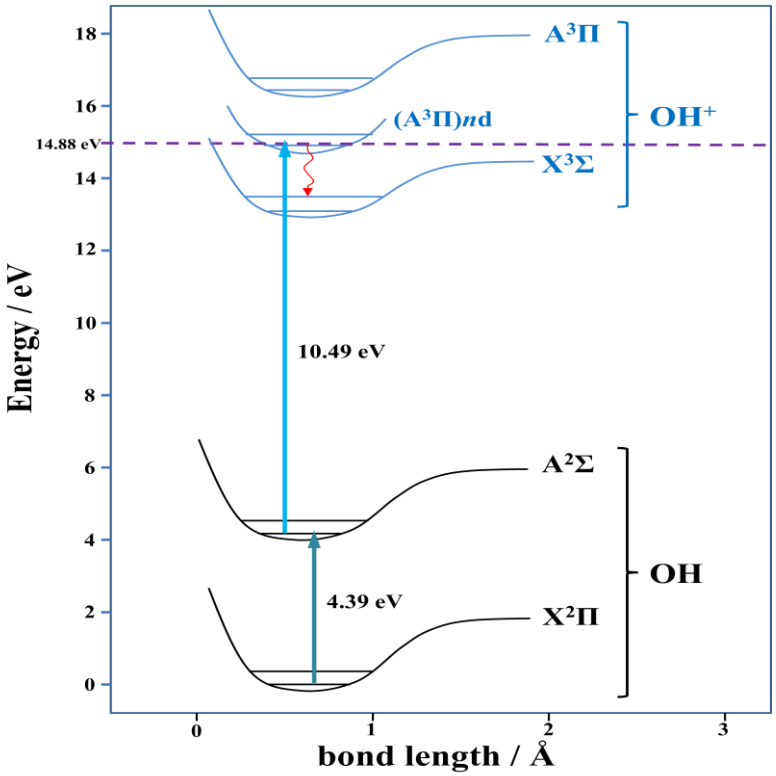

Figure 3.1: Depicts a model potential energy curves for the neutral, ionic, and Rydberg states relevant to the 1 + 1′ OH MPI detection scheme (Varandas and Voronin, 1995). The dashed horizontal lines represent the combined total energy (UV + VUV) after initial excitation to $A^2\Sigma$, *v* = 0, 1, and 2. The OH^+ $X^3\Pi$ state is usually inaccessible from the $A^2\Sigma$ state.

For hydroxyl radical detection, changes to the basic PLP-PIMS set-up were necessary. In order to generate the ~282.5 nm light, the Sirah Precision Scan dye laser was used (see Chapter II, Section 2.3.4). Green light from the Nd:YAG laser (532 nm, ~150 mJ $pulse^{-1}$) was directed into the Sirah precision scan, here it was converted to approximately 565 nm using the laser dye Rhodamine 6G (in methanol). The 565 nm radiation was then frequency doubled to approximately 282.5 nm (~2.5 mJ $pulse^{-1}$), and then was focussed into the vacuum chamber; the 118 nm and 282.5 nm light were overlapped directly above the sampling orifice (1 mm pinhole). In order to ensure the two laser beams were synchronized at the point of photoionization, the 355 nm light (~30 mJ $pulse^{-1}$) was relayed the length of

the laser bench, to accommodate for the extra distance taken by the light travelling through dye laser. The path length of the 355 nm radiation was increased by 2.5 m, equating to a delay time of approximately 8 ns. A schematic of the adaptations to the PIMS set-up can be seen in Figure 3.2.

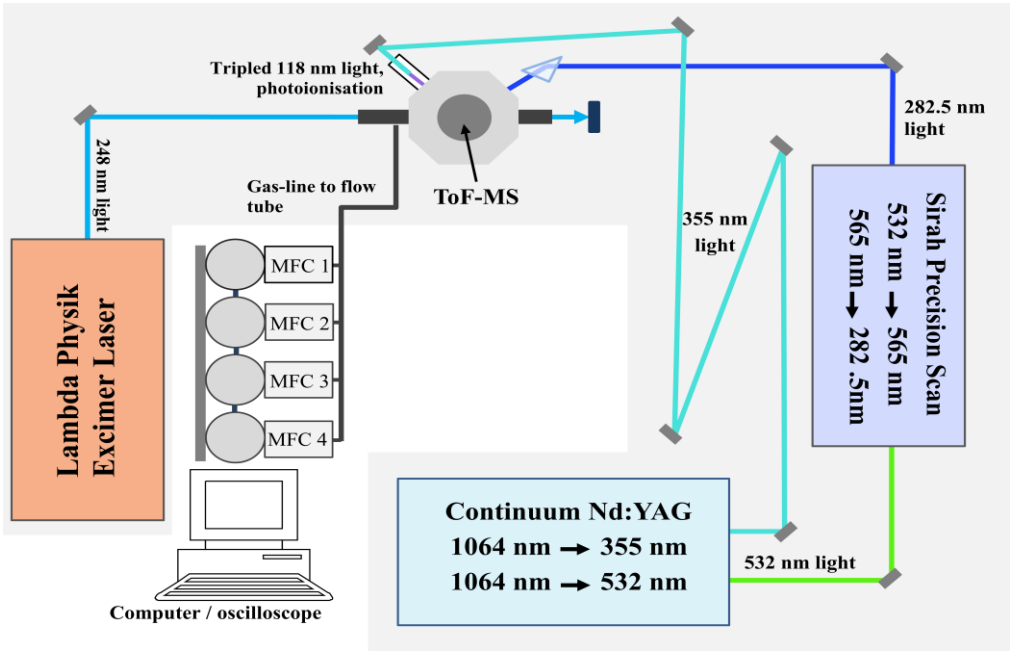

Figure 3.2: A schematic of the PLP-PIMS system with OH detection.

After the reconfiguration of the system was completed, OH detection was tested by utilising the O_3 / H_2 system to produce large quantities of hydroxyl radicals (R3.1-3.3).

$$O_3 + h\nu\ (\lambda{=}248\ \text{nm}) \rightarrow O(^1D) + O_2 \qquad \text{(R3.1)}$$

$$O(^1D) + H_2 \rightarrow OH + H \qquad \text{(R3.2)}$$

$$O_3 + H \rightarrow OH + O_2 \qquad \text{(R3.3)}$$

Then using the Sirah control 2.6 software (LabView™, 2008), the wavelength of light output from the dye laser was varied until the maximum OH signal was achieved. During the experiments described the optimal wavelength from the dye laser was $\lambda_{(\text{vacuum})}$ = 566.04 nm, which was doubled to give an initial OH excitation wavelength of 283.02 nm; this corresponds to the OH A-X (v = 1), $P_1(3.5)$ transition (Luque and Crosley, 1999). An example of the data collected from these tests can be seen in Figure 3.3.

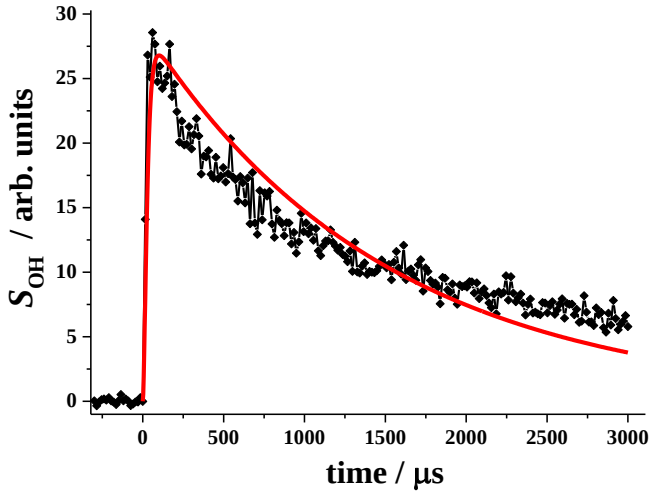

Figure 3.3: A sample of the OH signal, S_{OH}, collected reconfigured PLP-PIMS set-up. p = 0.5 Torr; [H_2] = 1×10^{16} molecule cm^{-3}; [O_3] = 5×10^{15} molecule cm^{-3}. The concentration of hydroxyl radicals is estimated at [OH] ≈ 5 ×10^{13} molecule cm^{-3}. The red line shows the fit to the data using a first order exponential decay.

From Figure 3.3, a signal-to-noise ratio of $SNR \approx 150$ was determined for the OH detection technique; the minimum signal-to-noise ratio of a species which can be reliably detected in the PIMS system is $SNR \approx 3$. Moreover, from this plot an estimation of the minimum [OH], which can be detected from this technique can be determined. The loss of OH observed in Figure 3.3 cannot be fit by a first order exponential decay (red line, Figure 3.3); therefore it was suggested that the loss was second order, implying that the dominant sink for the OH radicals was through self-reaction:

$$OH + OH \rightarrow H_2O_2 \qquad (R3.3)$$

As the rate coefficient of the OH self-reaction, $k_{OHSR,}$ is well known, $k_{OHSR} = 2.6 \times 10^{-11}$ cm^3 molecule^{-1} s^{-1} (Atkinson et al., 2004). The initial hydroxyl radical concentration, $[OH]_0$, can be extracted from the second order analysis, $[OH]^{-1}$ vs. time (see Chapter I, Table 1.2). In Figure 3.4 the OH signal, which was given in arbitrary units, was scaled to give the initial [OH] / molecules cm^{-3}. The scaling factor was thought to be correct when the gradient of the $[OH]^{-1}$ vs. time plot was equal to literature evaluation, 2.6 × 10^{-11} molecule^{-1} cm^3 s^{-1} (Atkinson et al., 2004).

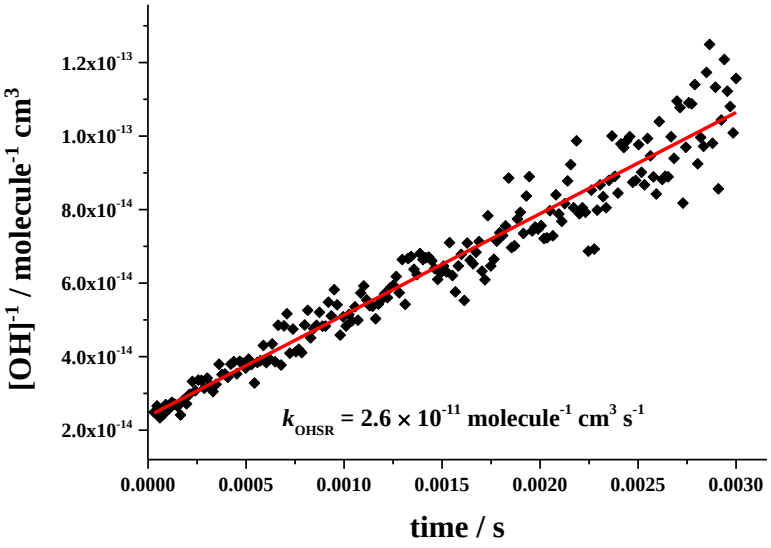

Figure 3.4: A second order plot of 1/[OH] vs. time, where values of 1/[OH] were scaled until the gradient of the plots yields the correct rate coefficient, k_{OHSR}.

Using Figure 3.4 an OH concentration of [OH] ≈ 3.5×10^{13} molecule cm^{-3} was calculated at 100 μs. From Figure 3.3 it was estimated that after 100 μs has passed the quality of OH signal was 50 times larger than the minimum *SNR* required for detection. Therefore it was estimated that the OH detection technique described above will be able to measure [OH] ≈ 7×10^{11} molecule cm^{-3}. It should be noted that although this may seem high for a limit of detection, it is a conservative estimate. In fact, although not quantitative, the most sensitive method for detecting species using the PLP-PIMS set-up bypasses the LabVIEW™ data collection system, and instead averages the data from the mass spectrometer on the oscilloscope (Figure 3.5). Using the oscilloscope the whole mass spectrum can be averaged (up to 1000 times) at a specific point in time (where high [OH] are expected, 200 μs) in under two minutes. In comparison, when collecting data using the LabVIEW™ program, where each individual trace is typically comprised of 250 points (+25 background points), only 4 traces will be collected in two minutes. Therefore, for a specific point in time (i.e. 200μs) the LabVIEW™ program has averaged 4 data points (at t = 200 μs) whilst the oscilloscope has averaged 1000 data points; meaning that for a given length of time, the signal-to-noise ratios from the oscilloscope are much greater, hence smaller mass signals can be reliably detected. As an estimate, when using the oscilloscope method, the signal-to-noise ratios observed were at least an order of magnitude higher than using the LabVIEW™ for data collection.

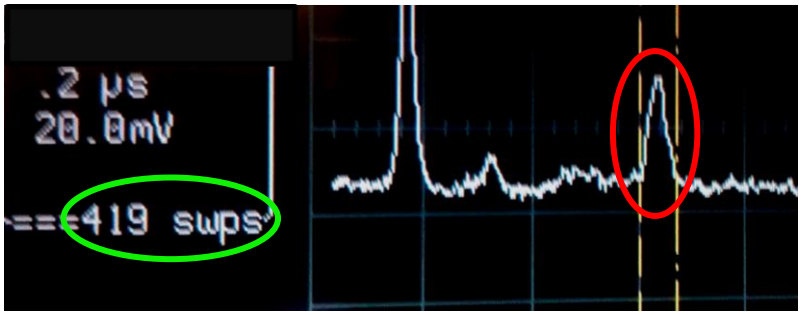

Figure 3.5: A photograph showing the display of the oscilloscope. An example of the OH signal can be shown, circled in red, at *t* =200 µs; whilst circled in green is the number of times the spectrum has been averaged.

It should be noted that, when using the LabVIEW™ for data collection, the sensitivity of OH detection technique was still sufficient to be of use in PLP-PIMS system, where the initial radical concentration of the reactants was typically ~10^{12} molecule cm^{-3} (Figure 3.6).

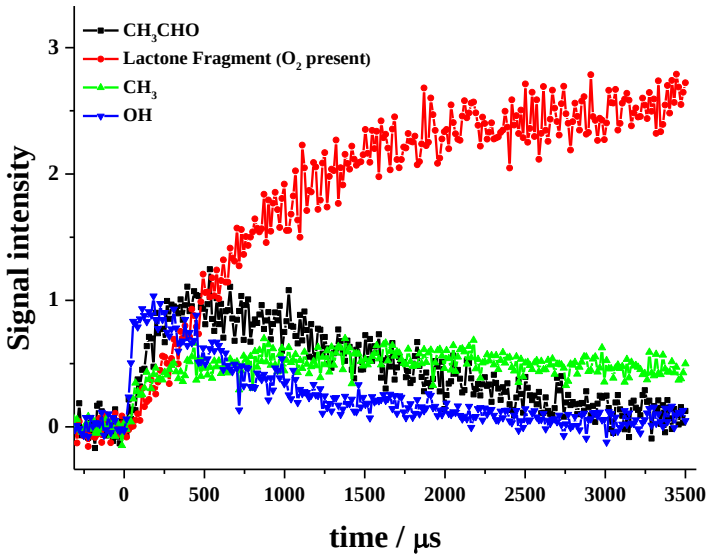

Figure 3.6: A example of the OH data collected from a study investigating the reaction between CH_3CHO + OH. [CH_3CHO] = 1×10^{14} molecule cm^{-3}; [H_2O] = 1×10^{15} molecule cm^{-3}; [O_3] = 1×10^{15} molecule cm^{-3}; [O_2] = 1×10^{15} molecule cm^{-3}

3.1.1 Conclusions

The section above details the changes to the PIMS configuration to incorporate OH detection, and progress made with the technique thus far. It was currently estimated that the technique should be able to measure [OH] < 7×10^{11} molecule cm^{-3}; however using the oscilloscope method it is possible that concentrations as low as [OH] ≈ 10^{11} molecule cm^{-3} could be measured. It was thought the sensitivity of the technique could be further improved if the simultaneous output of the 355 nm and 532 nm light was optimised properly. In order for the Nd:YAG to generate the 532 nm and the 355 nm at the required laser powers, the 532 nm radiation was tuned on edge of the doubling crystal to reduce its power. A

consequence of using this method to detune the 532 nm light was the laser output decreased relatively rapidly, as any slight change to the alignment would have a large effect on the radiation transmitted through the doubling crystal, and meant constant retuning was necessary. It may be possible to overcome this problem with a careful retuning of the laser, or possibly using a filter to reduce the light intensity, rather than detuning the laser. Alternatively, the problem would be eliminated if two different Nd:YAG lasers were used simultaneously.

3.2 High Pressure PIMS System

3.2.1 High Pressure System: Injector Set-up

Thus far all of the previous experiments conducted using the PLP-PIMS at the University of Leeds were done so at low pressures (p < 5 Torr). Clearly, the results from experiments conducted at low pressures were not always relevant to either atmospheric or combustion reactions, which predominantly occur at much higher pressure than can be reached using the PLP-PIMS system (Brasseur et al., 1999, Griffiths, 1995). To increase the application of the PIMS set-up, the ability to conduct experiments at higher pressures would be advantageous.

3.2.1.1 Experimental

To accommodate high pressures in the reactor tube several changes were made. Firstly, the method of gas sampling was changed significantly; previously, the gas was sampled halfway along the flowtube *via* a 1 mm orifice. Using the basic set-up the sampled gas was allowed to effuse through the pinhole, which was directed towards the mass spectrometer. However, in order to obtain higher pressures inside the reactor tube, but maintain the same low pressure within the flight tube, a more efficient exhaust system was needed inside the vacuum chamber. To keep the pressure inside the vacuum chamber low ($p \approx 2 \times 10^{-5}$ Torr) a second Turbo pump (Leybold, 600 l s^{-1}) was utilized. However, the only position (i.e. flange) which the new turbo pump could be attached was directly opposite the flowtube. Therefore, unlike most conventional flowtube set-ups, where the gas enters the instrument at one side and exits from the opposite side, in the high pressure system the gas enters, was sampled, and was then pumped all *via* the same flange, i.e. an injector-type system (see Figure 3.7). The new design of the flow reactor was comprised of an inner and an outer tube; the inner tube was a quartz tube approximately 0.75 m long with a 12.5 mm diameter. The outer tube was a stainless steel tube ~0.6 m long with a diameter of 25 mm; notably, the outer tube (or injector tube) was moveable, meaning that the distance between the pinhole and the point of photoionization (d_H) could be varied.

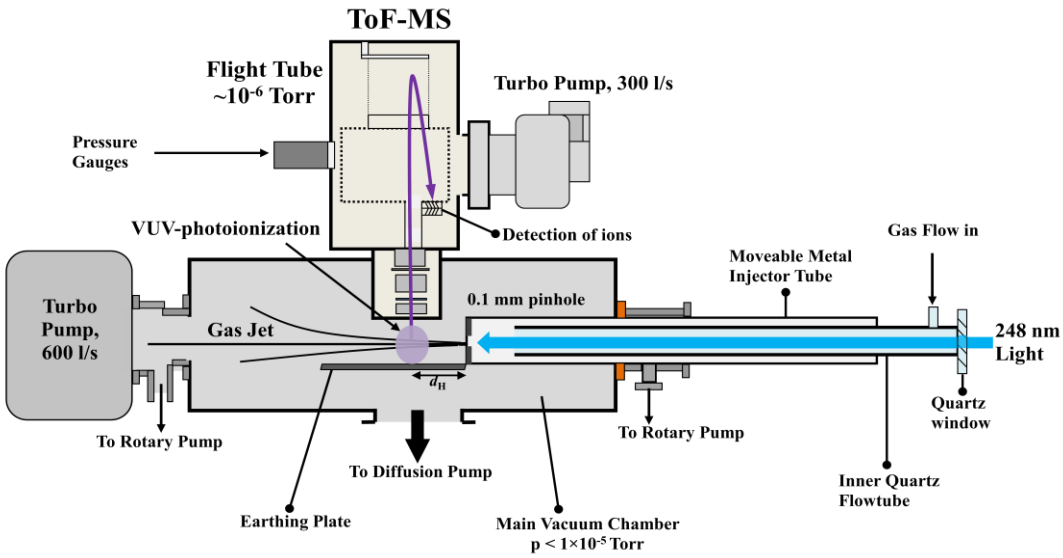

Figure 3.7: Cross section of the high pressure PIMS configuration, Injector system.

Additionally, in the high pressure set-up the gas was sampled coaxially to the direction of gas flow. A disadvantage of using this method of gas sampling was that after photoionization, the ions formed were not directed toward the mass spectrometer, but instead were moving perpendicularly to it; this was thought to be a less efficient method of ion extraction into the mass spectrometer.

There were other changes made to the configuration to allow higher pressures within the reactor tube. First of all, the size of the pinhole was reduced; by reducing the pinhole size the flow of gas out of the reactor was reduced, meaning the pressure could build-up within the reactor tube. Various sizes of pinholes were used during the development of the configuration; however, most commonly a silica pinhole of 0.1 mm was used. Using the 0.1 mm pinhole pressures of $p > 350$ Torr were attainable.

3.2.1.2 Preliminary Test of the High Pressure System

It should be noted that, due to the large pressure drop either side of the (small) pinhole, the sampled gas on the low pressure side forms a gaseous jet of molecules (Morse, 1996). The distance over which the gas jets (commonly referred to as the Mach disk location within the field of molecular dynamics) can be determined simply for a free jet expansion using the following equation (Pauly, 2000):

$$x_M = 0.67 \times d \times \sqrt{\frac{p_b}{p_a}} \qquad \text{(E3.1)}$$

In equation E3.1: x_M refers to the Mach disk location; d is the diameter of the pinhole/orifice; p_b is the pressure before the pinhole (i.e. the high pressure side); and p_a is the pressure after the pinhole (low pressure side).

$$x_M = 0.67 \times (1 \times 10^{-4}) \times \sqrt{\frac{250}{2.5 \times 10^{-5}}} \quad \text{(E3.2)}$$

$$x_M = 0.21 \text{ m} \quad \text{(E3.3)}$$

When using equation E3.1 to determine the Mach disk location (x_M) for the conditions inside high pressure set-up (p_b = 250 Torr, p_a = 2.5×10^{-5} Torr, d =1×10^{-4} m) a value of x_M = 0.21 m was calculated. The nature of gas jet was then probed experimentally through a simple study where the signal height of acetone was measured as a function of d_H, the horizontal distance between the pinhole and the point of photoionization.

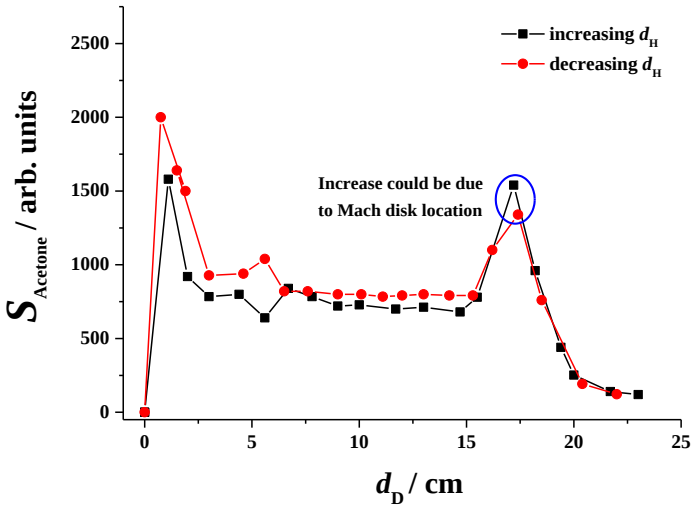

Figure 3.8: A plot showing the relationship between the acetone signal and the distance between the injector and the detector, d_H.

From Figure 3.8 there are a number of interesting conclusions to be made: Firstly, it can be seen that when d_H = 0 there was no acetone signal seen. It was thought that the lack of signal was due to the induced voltage from the inlet of the mass spectrometer to the injector (and subsequently the earthing plate). Consequently, the potential difference between the earthing plate and mass spectrometer was lowered, so the ions are not extracted from the vacuum chamber correctly, and hence will not be detected.

As d_H was increased, the acetone signal increases sharply to a maximum at ~1 cm. After reaching this apex the signal height starts to decrease rapidly between 1 < d_H < 3; notably, if no jetting was occurring, the acetone signal would be expected to decrease proportionally to d_H^2. However, the signal plateaus at ~3 cm and stays relatively constant (±20%) until approximately 15 cm; as the intensity of the signal does not follow the inverse square law, it suggests that jetting was occurring.

At distances d_H > 15 cm there was a second spike in the acetone signal, peaking between 17-18 cm. It is thought that this spike indicates the Mach disc location (x_M) as the higher pressures associated with x_M would lead to an increase in number density of acetone, and hence a larger acetone signal.

From Figure 3.8 it can also be seen that acetone signal measurements were taken as the injector was pulled out (increasing d_H) and then pushed back in (decreasing d_H). Notably, consistently larger measurements were taken with decreasing d_H, there were two possible reasons for this: firstly it was significantly easier / smoother pushing the reactor tube back in, which could mean the alignment remained more constant during this part of the experiment. Secondly, the pressure within the reactor tube increased gradually (~5%) during the course of the whole experiment. As the injector was first pulled out, then pushed back in, the acetone concentration would have been higher for the during the decreasing d_H experiments; this would in turn lead to the larger acetone signal measured.

However, the key finding from this experiment was that the observed acetone signal remained constant at distance between 5 cm < d_H < 15 cm; the implication of this being that the gas was jetting over this distance. It addition to this, it was observed that the magnitude of the acetone signal measured was highly sensitive to the directionality of the injector tube. The injector tube was sealed to the vacuum chamber using an O-ring, which allowed for the orientation of the injector tube to be varied. As the magnitude of the acetone signal was sensitive towards the position of the injector tube it, again, suggests that the sampled gas was jetting inside the vacuum chamber.

To successfully obtain time-resolved data it was essential that the sampled gas was jetting, particularly when the horizontal distance between the pinhole and the detector, d_H, was significant (d_H > 5 cm). In an effusive gas beam the velocity of the molecules can be described by a Maxwell-Boltzmann distribution (Campargue, 2001); within this distribution there is a large range of molecular velocities. During the expansion of the gas through the pinhole all of the molecular flow velocities are orientated to the same direction (note prior to the pinhole the molecules move at random); this leads to an increase in total flow velocity of the gas and a larger root mean square velocity (Smalley et al., 1977). The ordering of the direction of flow velocity also leads to a rapid decrease in temperature, which in turn leads to a narrowing of the velocity distribution (Figure 3.9).

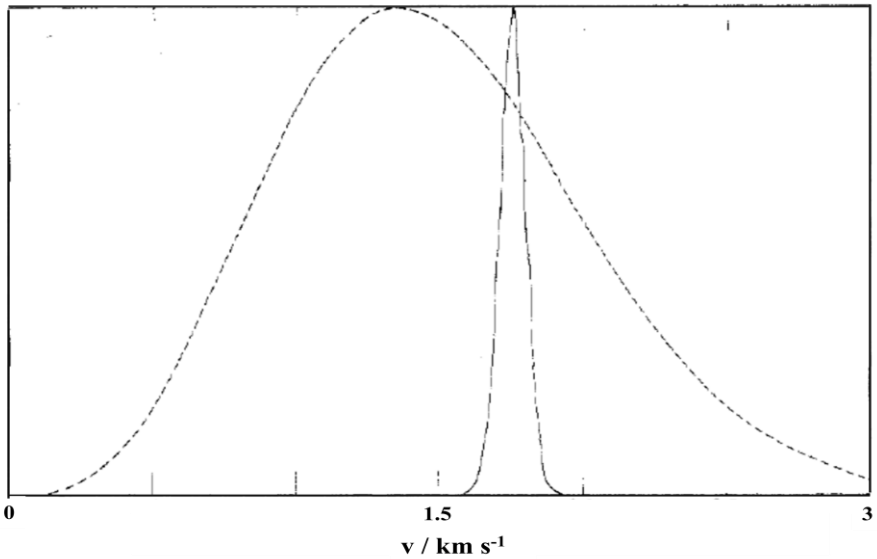

Figure 3.9: Velocity distributions of in an effusive molecular beam (dashed curve) and in a free jet / supersonic molecular beam (solid curve). Schematic sourced from Smalley et al. (1977).

Therefore, if the distance between the pinhole and the detector is large and a supersonic molecular beam has not been formed, the time resolution of the gas sample can be called into question as there would be a huge range in molecular velocities, with the molecules with larger velocities will take less time to travel the distance d_H (Stone et al., 2016). However, in the case of the free jet all of the molecules move at similar velocities, meaning that even when d_H is large the time resolution of the sampled gas should remain.

From the high pressure experiments it was evident that the sensitivity of the mass spectrometer was much worse under these conditions. However, this was expected as the pressure within the flight tube must remain constant ($\sim 5 \times 10^{-6}$ Torr); to maintain this pressure within the flight tube at higher pressures the fraction of the gas sampled from the reactor tube will be proportionally lowered. For example, the probability of a given gas molecule being detected by the mass spectrometer at p = 100 Torr is one hundred times less than the same molecule being detected at p = 1 Torr. Therefore, to attain the same signal height at high pressures, larger acetone number densities must be present in the system; as more molecules of acetone are required to yield the same signal it implies the system must be less sensitive at higher pressures.

3.2.1.3 Testing Time-resolution of the High Pressure System

Following this investigation, the time-resolved nature of the system was probed; in particular, the photolysis of methyl iodide (MeI) was studied (R3.3).

$$CH_3I + h\nu\ (\lambda = 248\ nm) \rightarrow CH_3 + I \qquad (R3.3)$$

When studying this reaction, the iodine atom signal was followed (m/z =127); from the preliminary experiments, a time-resolved photolytic signal was evident, however, the I atom

signal ($S_{I\ atom}$) had a sharp spike in signal intensity, which then decayed away very rapidly (Figure 3.10).

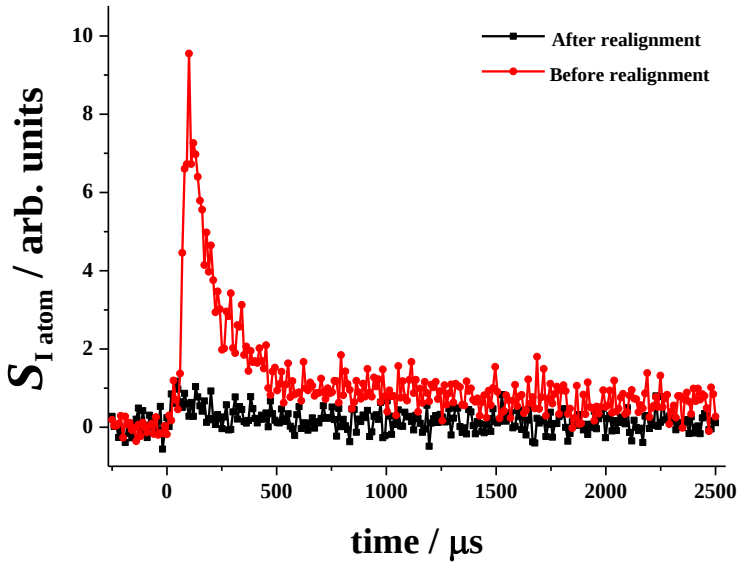

Figure 3.10: A plot of the time-resolved data collected using the high pressure PIMS set-up (Injector system).

This type of decay had been previously observed during other photolytic experiments and was found to be a consequence of poor alignment of the photolysis laser. Indeed, it was understood that at the 248 nm excimer light used in photolysis exceeds work function of the metal tubing (and pinholes) used within the PLP-PIMS set-up; consequently, electrons were produced *via* the photoelectric effect (Einstein, 1905). It was thought that the plume of electrons formed during photolysis interferes with the mass spectrometers extraction voltages leading to the sharp spike observed in the data. Therefore, it was decided realignment of the excimer laser was necessary. It should be noted that the realignment was known to be accurate as the excimer light (irised down to a minimum diameter) could be seen to be hitting the pinhole *via* the viewing port in the vacuum chamber.

Upon the realignment of the system the observed photolytic signal was reduced by an order of magnitude. This was the expected result as the observed 'spike' in I atom signal was thought to be caused by electron formation at the pinhole during the photolysis laser pulse, and not a real acetone signal. However, although the 'spike' in the acetone signal was much less apparent after the laser realignment, it was still there, which suggests that some electrons are still being formed at the pinhole. To rectify this problem, a gated-voltage was applied to the earthing plate very close after t = 0 s; by briefly applying a voltage across the earthing plate it was hoped that any charged particles formed at the pinhole would be removed from the system prior to photoionization (see Figure 3.11).

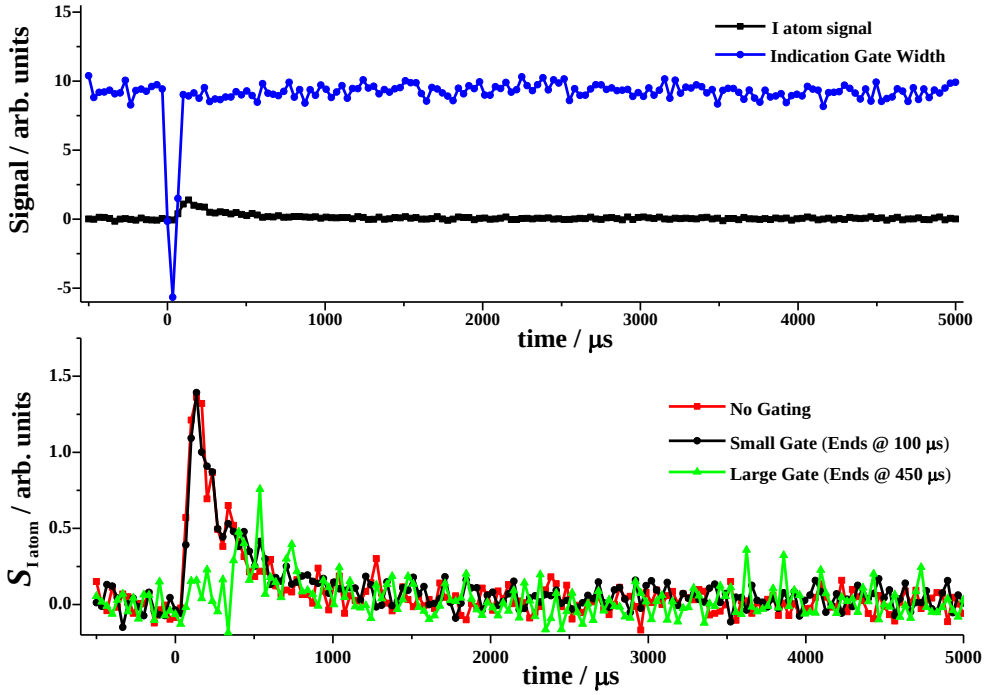

Figure 3.11: (Upper) A plot demonstrating the synchronization of the gating-voltage and the I atom signal. (Lower) A plot showing the variation of the I atom signal with varying lengths of gating-voltage.

As can be seen from Figure 3.11, the applied voltage gate was overlapped in time with photolysis laser pulse (i.e. t = 0 s); moreover the voltage applied to the earthing plate was switched off marginally after the excimer pulse, so as to ensure any charged particles formed were removed from the system. However, what was also apparent from Figure 3.11 was that gating the earthing plate does not change the I atom signal measured experimentally, unless the gate was too wide (i.e. the voltage was applied for too long), which resulted in a further decrease in the I atom signal. Assuming that the voltage-gate functioned as described, this result suggests that the observed decay in Figure 3.10 was not a consequence of the formation of charged particles at the pinhole.

However, no matter how the photolysis laser was aligned, no sensible photolytic data of the I atoms could be measured (i.e. a step change, with minimal decay losses). In addition, the photolytic signal observed was minimal, even though the concentration of methyl iodide was high ([MeI] > 1×10^{15} molecule cm^{-3}) and it was decided that an alternative method of photolysis may be necessary. It should be noted that the transmission of light through the length of the flowtube was calculated to be > 90%, so this was not the cause of the poor photolytic signal.

3.2.2 The 6-way Cross Set-up

As no sensible time-resolved data could be collected using a coaxial approach to gas flow, gas sampling and photolysis pulse, it was clear that the configuration of the high pressure

system needed to be changed and the method of photolysis rethought. Therefore, it was decided that the orientation of the photolysis beam should be at right-angles to the direction of gas flow (Figure 3.12 & Figure 3.13). Initially, the 6-way cross set-up was constructed with a 0.1 mm pinhole; however, shortly after construction the pinhole was damaged and replaced with a 0.7 mm pinhole, which limited the maximum pressure of the system (p_{max} > 10 Torr). Additionally, in the 6-way cross set-up the distance between the pinhole and the detector, d_H, was fixed at 15 cm. However, according to equation (E3.1), and under the experimental conditions used, this should still be within the Mach disk of the gas jet.

$$x_M = 0.67 \times d \times \sqrt{\frac{p_b}{p_a}} \tag{E3.1}$$

$$x_M = 0.67 \times (7 \times 10^{-4}) \times \sqrt{\frac{3.5}{2.5 \times 10^{-5}}} \tag{E3.4}$$

$$x_M = 0.18\ \text{m} \tag{E3.5}$$

For the Mach disk location calculation shown (E3.5) the following conditions were assumed; p_b = 3.5 Torr; p_a = 2.5 × 10^{-5} Torr; d = 0.7 mm.

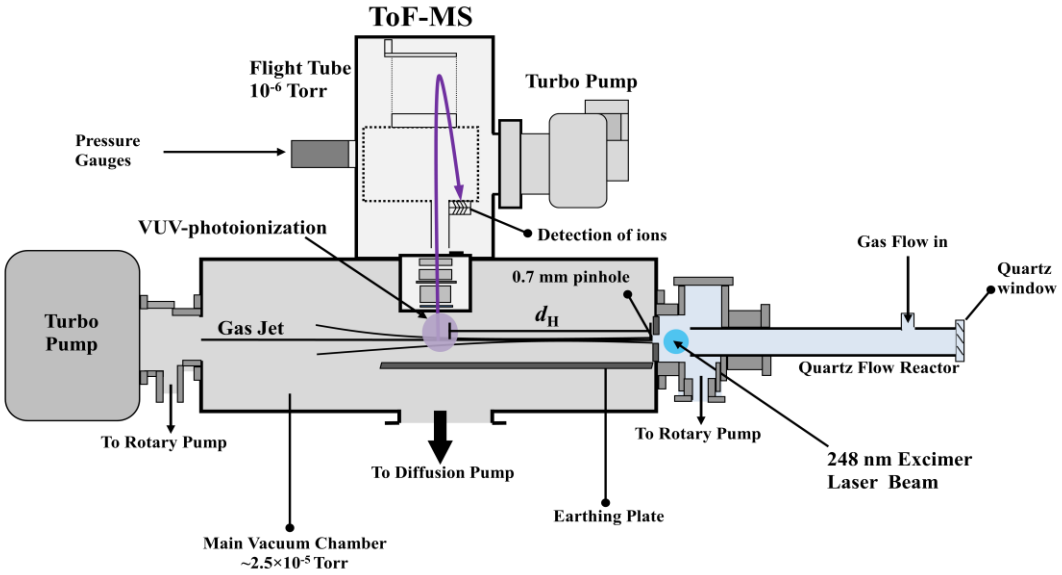

Figure 3.12: Cross section of the high pressure PIMS set-up, 6-way cross configuration.

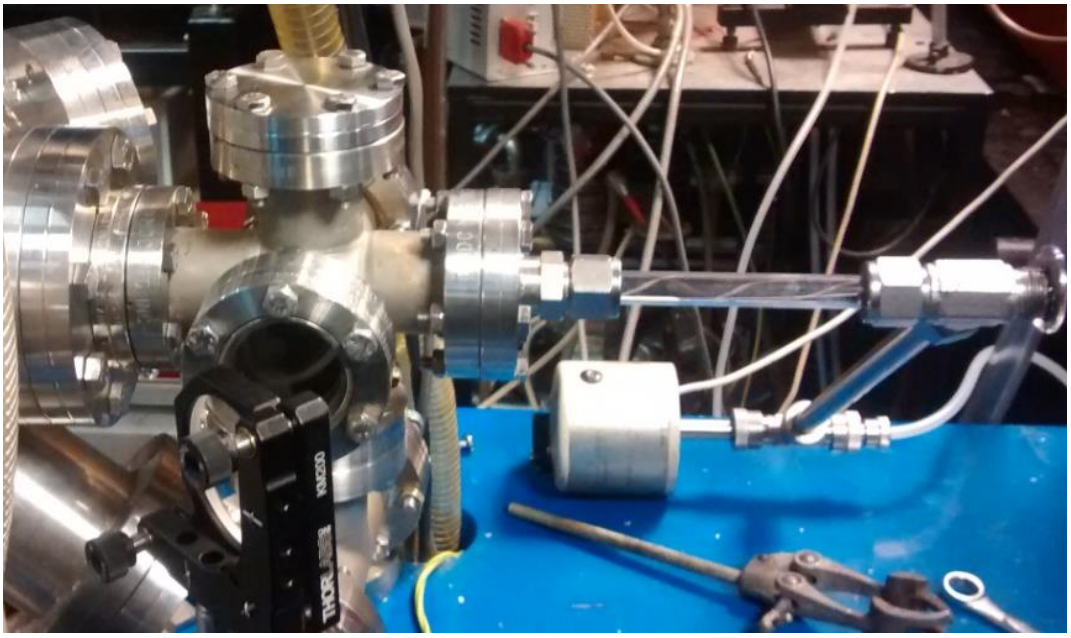

Figure 3.13: A photograph of the 6-way cross configuration.

Using the 6-way cross set-up methyl iodide photolysis experiments were conducted; however, whilst using this methodology no photolytic signal was observed. Indeed, as can be seen from Figure 3.14 no instantaneous was evident; moreover, the peak I atom signal was not observed until ~8 ms.

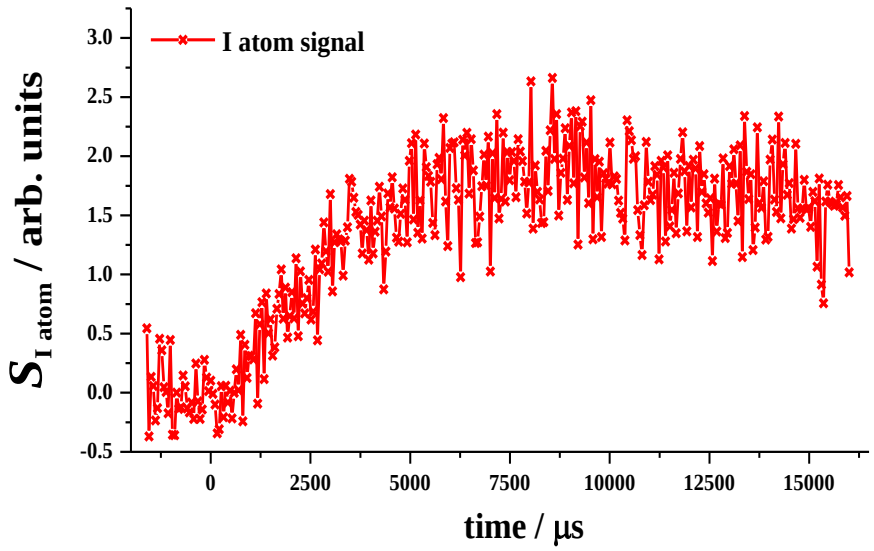

Figure 3.14: A plot of the data collected from the methyl iodide photolysis.

There are two possible reasons for the observed signal: firstly, the delay in the signal may be due to the time it takes for the photolysed gas sample to diffuse to the pinhole on the high pressure side. However, it should be noted that the photolysis laser was irised down to approximately 1 cm in diameter and photolysis beam was aligned so that the gas was

photolysed approximately ~1 mm in front of the pinhole, minimising the distance the gas must travel prior to the pinhole. The second, and more likely, possibility was that the gas on the low pressure side was not jetting across the entire distance between the pinhole and detection region (i.e. x_M < 0.15 m). It should be noted that if a free jet has formed the molecular velocity will be large, v_{RMS} > 1000 m s^{-1}, at this velocity the time for the gas to travel d_H should be ~150 μs.

To establish whether the gas in the low pressure region was jetting, a metal barrier was placed between the pinhole and the ionization region (Figure 3.15). The barrier approximately 5 cm in height and was the same width as the earthing plate (~4 cm). If the gas forms a jet (with x_M > 15 cm) then sensitivity of the instrument should be severely compromised by the placement of the barrier between the pinhole and the detector; however, if the gas was not jetting, then the impact on the instrument sensitivity will not be significant.

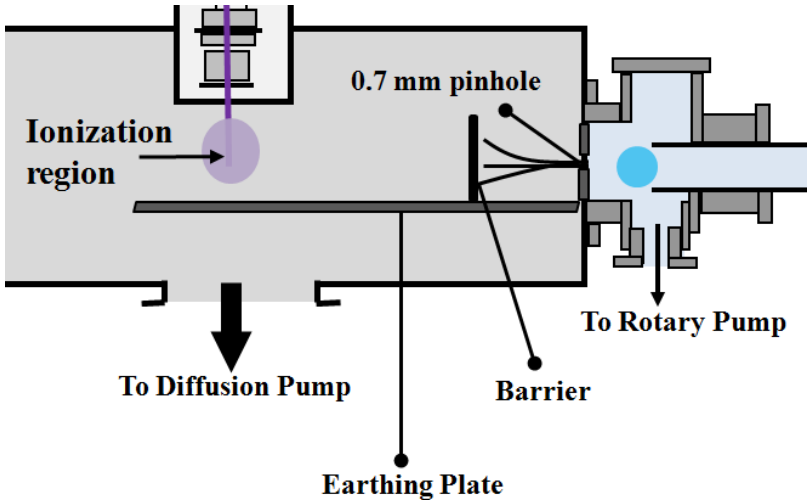

Figure 3.15: A schematic focused on the barrier used to block the 'gas jet'.

Data collected from the experiment with the barrier was then compared to data from experiments performed directly before the barrier was positioned, and directly after it was removed; the results from which can be seen in Figure 3.16.

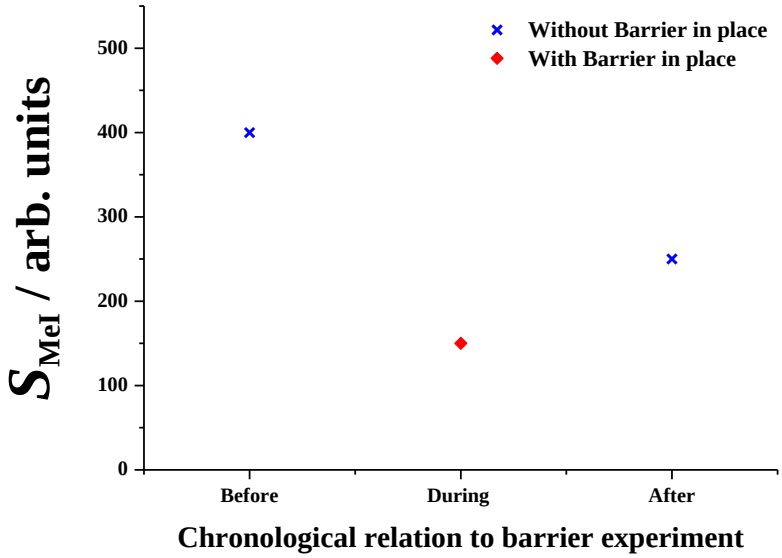

Figure 3.16: A plot comparing the maximum MeI signal (S_{MeI}) observed (at [MeI] ≈ 1.5 × 10^{14} molecule cm^{-3}) with and without the barrier blocking the gas jet.

From Figure 3.16 it can be seen that the maximum signal height measured was lower when the barrier was used to block the sampled gas; that said, the proportional decrease in signal height was relatively small. If the sampled gas had formed a free jet (x_M > 0.15 m), it would be expected that the observed signal height with the barrier in place would be orders of magnitude lower as the concentration of MeI within the gas jet should remain undiluted, therefore any disruption to the jet (i.e. the barrier) should lead to a large decrease in the MeI signal detected. Conversely, if the sampled gas has not formed a supersonic beam (or x_M < 0.15 m) the dilution will be significantly greater by the time the sampled gas has travelled the length d_H. Consequently, this means that the difference between the observed MeI signal, with and without the barrier in place, will be much less. The results shown in Figure 3.16 seem to the mimic the second scenario described, thus suggesting the sampled gas was not jetting properly. The most likely explanation for this was that the pressure inside the vacuum chamber was not as low as was measured (p_a = 2.5 × 10^{-5} Torr). Indeed, if p_a = 5 × 10^{-5} Torr, then the x_M = 0.12 m; critically under these conditions x_M < d_H, meaning that the gas jet will not reach the ionization region. It should be noted that no time-resolved data was recorded during the barrier experiment. However, if the sampled gas was jetting properly, this would explain why no instantaneous signal was observed whilst the 6-way cross set-up was used.

3.2.3 Conclusions

From the experimental testing done using the 6-way cross configuration an important observation was made, which as of yet has not been fully discussed; the sensitivity of the 6-

way cross set-up was significantly worse than was seen using the basic PIMS set-up (described in Chapter II). To quantify this, the original PIMS set-up was reconstructed, it was immediately apparent that the sensitivity of the system was at least two orders of magnitude lower than the original set-up. It is known that mass spectrometer sensitivity is dependent upon the mean free path inside the flight tube, and hence the sensitivity is expected to be lower at higher pressures (see Chapter II, Section 2.6). However, most of the experiments using the 6-way cross were performed at relatively low pressure (p_b < 5 Torr); meaning that even when the difference in pressure is taken into account, the sensitivity of the 6-way cross configuration was approximately 50 times worse than the original set-up. It is certain that the reduction in sensitivity was due to the problems with the gas jet under this configuration; however, it does highlight a significant problem with both of the high pressure configurations.

For many of the low pressure (p = 1 Torr) experiments conducted, the sensitivity of the radicals measured on the oscilloscope were close to the limit of detection. Therefore, if the same experiments were conducted at 100 Torr, to attain the same signal heights for these radical species, the number density of the initial reaction would need to be approximately 100 times greater. Crucially, the experiments performed using the PIMS set-up are typically conducted on the millisecond timescale; however, if number densities of the reactants used were 100 times larger, the reactions will take place on a nano/microsecond timescale; notably, this is not within the scope of the PIMS set-up. A further problem associated with this method is that the transport times from the pinhole to the photoionization region are hugely dependent upon the nature of the gas jet. If the gas jet is not properly formed the molecular velocities within the 'jet' will be lower and more variable; this means that the time resolution of the sampled species will be compromised (Stone et al., 2016).

From the results from this chapter it is clear that the development of the high pressure PIMS set-up is not facile, explaining why there has been very limited work done using high pressure mass spectrometry, previously documented in the literature (Biordi, 1977). It is also evident that major reconstruction is still needed before it could be used as a legitimate technique to monitor gas-phase kinetics.

3.3 References

ATKINSON, R., BAULCH, D. L., COX, R. A., CROWLEY, J. N., HAMPSON, R. F., HYNES, R. G., JENKIN, M. E., ROSSI, M. J. & TROE, J. 2004. Evaluated kinetic and photochemical data for atmospheric chemistry: Volume I - gas phase reactions of O_x, HO_x, NO_x and SO_x species. *Atmos. Chem. Phys.,* 4**,** 1461-1738.

BAEZA-ROMERO, M. T., BLITZ, M. A., GODDARD, A. & SEAKINS, P. W. 2012. Time-of-flight mass spectrometry for time-resolved measurements: Some developments and applications. *International Journal of Chemical Kinetics,* 44**,** 532-545.

BEAMES, J. M., LIU, F. & LESTER, M. I. 2014. 1+ 1′ resonant multiphoton ionisation of OH radicals via the A2Σ+ state: insights from direct comparison with AX laser-induced fluorescence detection. *Molecular Physics,* 112**,** 897-903.

BEAMES, J. M., LIU, F., LESTER, M. I. & MURRAY, C. 2011. Communication: A new spectroscopic window on hydroxyl radicals using UV + VUV resonant ionization. *The Journal of Chemical Physics,* 134**,** 241102.

BIORDI, J. C. 1977. Molecular beam mass spectrometry for studying the fundamental chemistry of flames. *Progress in Energy and Combustion Science,* 3**,** 151-173.

BRASSEUR, G. P., ORLANDO, J. J. & TYNDALL, G. S. 1999. *Atmospheric Chemistry and Global Change,* Oxford, Oxford University Press.

CAMPARGUE, R. 2001. Atomic and Molecular Beams: The State of the Art 2000. Germany: Springer-Verlag Berlin Heidelberg.

EINSTEIN, A. 1905. On a heuristic point of view about the creation and conversion of light. *On a Heuristic Point of View about the Creation and Conversion of Light 1 On the Electrodynamics of Moving Bodies 10 The Development of Our Views on the Composition and Essence of Radiation 11 The Field Equations of Gravitation 19 The Foundation of the Generalised Theory of Relativity 22***,** 1.

GRIFFITHS, J. F. 1995. *Flame and Combustion,* Glasgow, Blackie Academic & Professional.

HEARD, D. 2008. *Analytical Techniques for Atmospheric Measurement,* Wiley.

LABVIEW^{TM} 2008. Sirah Control 2.6. Grevenbroich: Sirah Lasertechnik GmbH.

LUQUE, J. & CROSLEY, D. R. 1999. *LIFbase: Database and Spectral Simulation*.

MORSE, M. D. 1996. Atomic, Molecular, and Optical Physics: Atoms and Molecules. *In:* DUNNING, F. B. & HULET, R. G. (eds.) *Supersonic Beams.* London: Academic Press.

PAULY, H. 2000. *Atom, Molecule, and Cluster Beams I: Basic Theory, Production and Detection of Thermal Energy Beams,* New York, Springer-Verlag Berlin Heidelberg.

SMALLEY, R. E., WHARTON, L. & LEVY, D. H. 1977. Molecular optical spectroscopy with supersonic beams and jets. *Accounts of chemical research,* 10**,** 139-145.

STONE, D., BLITZ, M., INGHAM, T., ONEL, L., MEDEIROS, D. J. & SEAKINS, P. W. 2016. An instrument to measure fast gas phase radical kinetics at high temperatures and pressures. *Review of Scientific Instruments,* 87**,** 054102.

VARANDAS, A. J. C. & VORONIN, A. I. 1995. Calculation of the asymptotic interaction and modelling of the potential energy curves of OH and OH^+. *Chemical Physics,* 194**,** 91-100.

Results - Part i

Mechanistic Study of the OH + Acetaldehyde Reaction

Chapter IV:

An alternative channel in the reaction of Acetaldehyde with the OH radical

4. An alternative channel in the reaction of Acetaldehyde with the OH radical

This chapter aims to provide a detailed kinetic and mechanistic study of the reaction between acetaldehyde (ethanal, CH_3CHO) and OH. Using the PLP-PIMS set-up described in Chapter II, a rate coefficient of $k_{OH} = (1.6 \pm 0.2) \times 10^{-11}$ cm^3 molecule^{-1} s^{-1} was measured for the reaction. Furthermore, in addition to the expected reaction products (see R4.7), methyl radicals (CH_3) were also detected as primary products from the OH + acetaldehyde reaction, and a yield of ~15% was determined at 1-2 Torr of helium bath gas. Subsequently, complementary measurements have been done using laser induced fluorescence to measure the OH recycling from a $OH/CH_3CHO/O_2$ system. Notably, the results from the LIF study are consistent with the PIMS experiments and suggest the reaction must have an alternative mechanism, leading to methyl radical formation. Indeed, it is proposed that the source of the methyl radicals is from the dissociation of nascent, chemically activated acetyl radicals (D'Anna et al., 2003). Significantly, this result is consistent with previous studies which have shown that the OH + acetaldehyde reaction proceeds *via* an abstraction mechanism, rather than addition/elimination reaction.

4.1 Introduction

Acetaldehyde (ethanal, CH_3CHO), a potential carcinogen (EPA, 1987), is an important primary and secondary atmospheric pollutant. The predominant source of acetaldehyde in the atmosphere is through hydrocarbon oxidation (Calvert and Madronich, 1987) producing 128 Tg of acetaldehyde each year (Millet et al., 2010); it is also a significant by-product from ethanol combustion. Concentrations of acetaldehyde are typically thought to be < 1 ppbv in remote areas (Read et al., 2012) but can be > 10 ppbv in major cities (Fortner et al., 2009).

Unsurprisingly, due to large consumption of bioethanol in Brazil, some of the highest atmospheric acetaldehyde measurements have been recorded in downtown Rio De Janeiro where the maximum concentration of CH_3CHO exceeded 30 ppbv (Corrêa et al., 2010). In light of this, the Department for Environment, Food and Rural Affairs (DEFRA) has become increasingly interested in the possible effects of increased acetaldehyde levels in the atmosphere (Air Quality Expert Group, 2011). It is therefore of great importance to have a clear understanding of the lifetime, reactivity and reaction mechanisms of acetaldehyde; this was the motivation for this body of work.

4.1.1 Atmospheric Sources of Acetaldehyde

As mentioned above the chief source of acetaldehyde in the atmosphere is from the oxidation of hydrocarbons, a prime example being the oxidation of ethane:

$$C_2H_6 + OH \rightarrow CH_3CH_2 + H_2O \quad \text{(R4.1)}$$

$$CH_3CH_2 + O_2 \rightarrow CH_3CH_2O_2 \quad \text{(R4.2)}$$

As with many oxidation processes in the lower atmosphere the initial step is an abstraction by an oxidising species, most commonly an OH radical (R4.1); following this the newly formed alkyl radical reacts with an O_2 molecule forming a peroxy radical (e.g. $CH_3CH_2O_2$) (Calvert, 2011). In urban environments these ethyl peroxy radicals are rapidly reduced by NO, producing an ethoxy radical and NO_2 (R4.3). It should be noted that the conversion of NO to NO_2 is the key step driving tropospheric ozone formation (Atkinson, 2000). The final step leading to acetaldehyde formation is an abstraction reaction involving O_2 (R4.4).

$$CH_3CH_2O_2 + NO \rightarrow CH_3CH_2O + NO_2 \quad \text{(R4.3)}$$

$$CH_3CH_2O + O_2 \rightarrow CH_3CHO + HO_2 \quad \text{(R4.4)}$$

Another minor, but important, source of acetaldehyde is from ethanol combustion. Over recent years the UK has looked more towards using ethanol-containing fuel blends in an attempt to reduce fossil fuel emissions. Crucially, a likely consequence of increased bioethanol burning is a significant increase in acetaldehyde emissions (Niven, 2005). Indeed, experiments have demonstrated CH_3CHO emissions are three orders of magnitude greater from E85 (a high strength 85:15 ethanol:fuel blend) than from conventional fuels in current use (Karavalakis et al., 2012). As well as being a principal primary emission from ethanol combustion, acetaldehyde is also a secondary emission (Poulopoulos et al., 2001). The reason being is that ethanol, itself, is also a major emission from bioethanol combustion and promptly (τ = 4 days) converts to acetaldehyde in the troposphere (Norton and Dryer, 1992, Calvert, 2011):

$$CH_3CH_2OH + OH \rightarrow CH_3CHOH + H_2O \quad \text{(R4.5)}$$

$$CH_3CHOH + O_2 \rightarrow CH_3CHO + HO_2 \quad \text{(R4.6)}$$

4.1.2 Acetaldehyde in the Atmosphere

As with many atmospheric species the main destruction pathways of CH_3CHO vary diurnally. At night the main loss channel of acetaldehyde is caused by reaction with NO_3. This reaction has a rate coefficient of $k = 3 \times 10^{-15}$ cm^3 molecule^{-1} s^{-1} and occurs very

slowly during the day, particularly in high [NO] environments where any nitrate radicals formed are rapidly converted to NO_2 (Wayne et al., 1991).

During the day there are several competing processes removing acetaldehyde from the atmosphere; photolysis or reaction by chlorine radicals (Cl) being examples. However, the most dominant sink for atmospheric acetaldehyde is the OH radical (the focal reaction of this study), see Figure 4.1:

$\Delta_r H$ = -123 kJ mol^{-1} $\quad CH_3CHO + OH \rightarrow CH_3CO + H_2O$ (R4.7a)

It is understood that the H atom is abstracted from the acyl group (H-C=O) as there is no significant change observed in reactivity as the length of the alkyl chain is increased (Semmes et al., 1985). This suggests that the alkyl substituent has only a minimal effect on the reaction rate and therefore implies abstraction occurs on the acyl carbon.

As the major source of acetyl radicals, the reaction between OH and acetaldehyde is of significant importance as it is key to the production of peroxyacetyl nitrate (PAN) in the lower atmosphere (Jenkin and Clemitshaw, 2000):

$$CH_3CO + O_2 + M \rightarrow CH_3C(O)O_2 + M \quad \text{(R4.8)}$$

$$CH_3C(O)O_2 + NO_2 + M \rightleftharpoons CH_3C(O)O_2NO_2 + M \quad \text{(R4.9)}$$

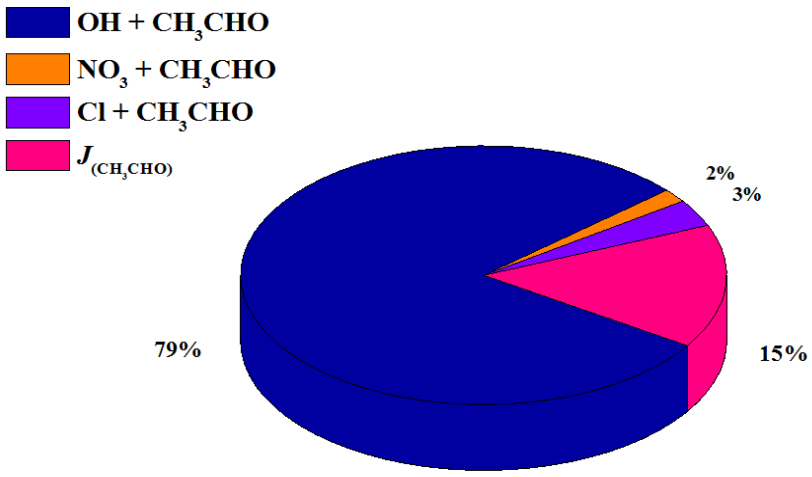

Figure 4.1: **A schematic showing the relative magnitudes of the removal pathways for acetaldehyde in the atmosphere (midday). The rate coefficients, atmospheric concentrations and lifetimes used for this calculation were obtained from Calvert (2011) and Winer et al. (1984). Note: there are other minor reaction channels; however, their contributions to CH_3CHO loss are thought to be negligible.**

PAN is a central component of photochemical smog. PAN also functions as a long range transporter for nitrogen oxides (NO_x) into rural regions, *via* R4.9, and causes ozone formation in the global troposphere. Due to this direct link between acetaldehyde oxidation

and peroxyacetylnitrate formation, the kinetics of reaction R4.7 have been comprehensively studied for over 40 years and therefore considered to be well understood (Morris et al., 1971, Tyndall et al., 1995). The rate coefficients measured for this reaction range from k_{OH} = (12.2 – 16.9) ×10^{-12} cm^3 $molecule^{-1}$ s^{-1} at 298 K and the reaction has a recommended value of (1.5 ± 0.2) × 10^{-11} cm^3 $molecule^{-1}$ s^{-1} (Calvert, 2011). The reaction between acetaldehyde + OH has been characterised between 200 – 400 K and exhibits a negative temperature dependence described by the following Arrhenius expression (Atkinson et al., 2006):

$$k_{OH} = 4.4 \times 10^{-12} e^{(365/T)}\ cm^3\ molecule^{-1}\ s^{-1} \quad \text{(E4.1)}$$

4.1.3 Acetaldehyde + OH Reaction Mechanism

There was renewed interest in this reaction when Wollenhaupt et al. (2000) discovered the non-Arrhenius behaviour of the OH + acetone reaction below ~200 K. This observation was rationalised as a temperature dependent change in the reaction mechanism (Wollenhaupt et al., 2000, Vasvari et al., 2001). Earlier work by Taylor et al. (1996) had also observed a similar non-Arrhenius temperature dependence for the acetaldehyde + OH reaction (T = 295 - 900 K); leading to the proposal that OH + carbonyl reactions may have more complex mechanisms than previously thought. Wollenhaupt et al. (2000) went on to suggest that the non-Arrhenius behaviour was due to an alternative addition-elimination pathway competing with H atom abstraction at low temperatures. The possible reaction channels for the addition/elimination mechanisms are seen in R4.7b-R4.7c (Sander, 2011).

$\Delta_r H$ = -103 kJ mol^{-1} $CH_3CHO + OH \rightarrow CH_3 + HCOOH$ (R4.7b)

$\Delta_r H$ = -86 kJ mol^{-1} $CH_3CHO + OH \rightarrow CH_3C(O)OH + H$ (R4.7c)

Yet, following the hypothesis of these alternative channels multiple different product studies were completed all of which heavily implied that the dominant reaction channel for OH with acetaldehyde was R4.7a. One such study quantitatively measured water formation from the acetaldehyde + OH reaction reporting a yield of 0.89 ± 0.06 (Vandenberk and Peeters, 2003). Furthermore, other supporting work reported an acyl H atom abstraction yield of ~95% for the reaction (Butkovskaya et al., 2004). Cameron et al. (2002) took a different approach and attempted to observe the expected products from the addition/elimination reaction channels (R4.7b and R4.7c). This study UV transient absorption spectroscopy was used to monitor both the formation of acetyl (R4.7a) and methyl radicals (R4.7b) simultaneously. The results concluded that the primary reaction channel was R4.7a and an acetyl yield of 0.93 ± 0.18 was determined and, significantly, a small yield of methyl radicals was also observed. However, the formation of the methyl

radicals was on a considerably longer timescale than acetyl production, so Cameron et al. (2002) postulated a radical-radical type mechanism for CH_3 production as a feasible source of methyl radicals.

However, UV transient absorption spectroscopy may not be the best method for observing a small CH_3 yield as there is significant overlap of acetyl and methyl signals. Therefore it is possible that the broad, featureless acetyl spectrum may mask the signal of more distinct CH_3 spectrum (a weaker signal due to the lower concentration of CH_3 radicals), thus making it difficult to separate the spectrums and obtain quantitative values of the methyl yields (Howes et al., 2016). In Cameron et al. (2002) upper limits of 3% and 2% on reactions R4.7b and R4.7c respectively; these results were corroborated by a complementary study that placed similar upper limit of 5% for both reaction channels (Wang et al., 2003).

All of this work suggests that H atom abstraction from the acyl carbon is indeed the exclusive mechanism for the acetaldehyde + OH reaction. In addition to this, work done at the University of Leeds proposed that the increased rate coefficients observed at low temperatures for carbonyl + OH reactions were due to quantum mechanical tunnelling (Shannon et al., 2013, Shannon et al., 2010). This body of work makes a very compelling argument about the origin of the non-Arrhenius behaviour observed in many carbonyl + OH reactions and hence dismisses the possibility of addition/elimination pathways.

The study by Shannon et al. (2010) suggests that the only possible minor product would be the vinoxyl radical, CH_2CHO:

$\Delta_r H$ = -103 kJ mol^{-1} $\quad CH_3CHO + OH \rightarrow CH_2CHO + H_2O$ (R4.7d)

This raises questions about some of the previous literature, such as origin of the methyl radicals observed in the work of Cameron et al. (2002) and Wang et al. (2003). However, another alternative reaction channel has been hypothesised; this channel accounts for the formation of methyl radicals, but is also is consistent with a 100% yield of water (D'Anna et al., 2003):

$\Delta_r H$ = -77 kJ mol^{-1} $\quad CH_3CHO + OH \rightarrow CH_3CO^* \rightarrow CH_3 + CO + H_2O$ (R4.7e)

Note: the '*' signifies that the acetyl radical is chemically activated.

As part of the study by D'Anna et al. (2003), long-path FTIR was used to monitor the products of the CH_3CHO + OH reaction (in a high NO_x environment). In addition to PAN, small yields of HCHO, the stable product of methyl oxidation in high NO_x conditions, and CO were observed. From the study it was concluded that the acetaldehyde + OH reaction occurred *via* two pathways (R4.7a and R4.7e) with a branching ratio of approximately 9:1.

The interpretation of this observation is that the activation energy required for acetyl decomposition (R4.7e) is only ~71 kJ mol^{-1} (Baeza-Romero et al., 2007): there is therefore sufficient exothermicity from R4.7a (-123 kJ mol^{-1}) to permit some acetyl fragmentation to occur in a chemically activated process (Figure 4.2). However, this would require a non-dynamical distribution of energy amongst the products and therefore a greater proportion of the excess energy in the acetyl fragment (Polanyi, 1987). The *ab initio* calculations reported by D'Anna et al. (2003) indicate that a post-reaction complex would allow for a more statistical distribution of the reaction exothermicity between the final products: henceforth making acetyl decomposition possible.

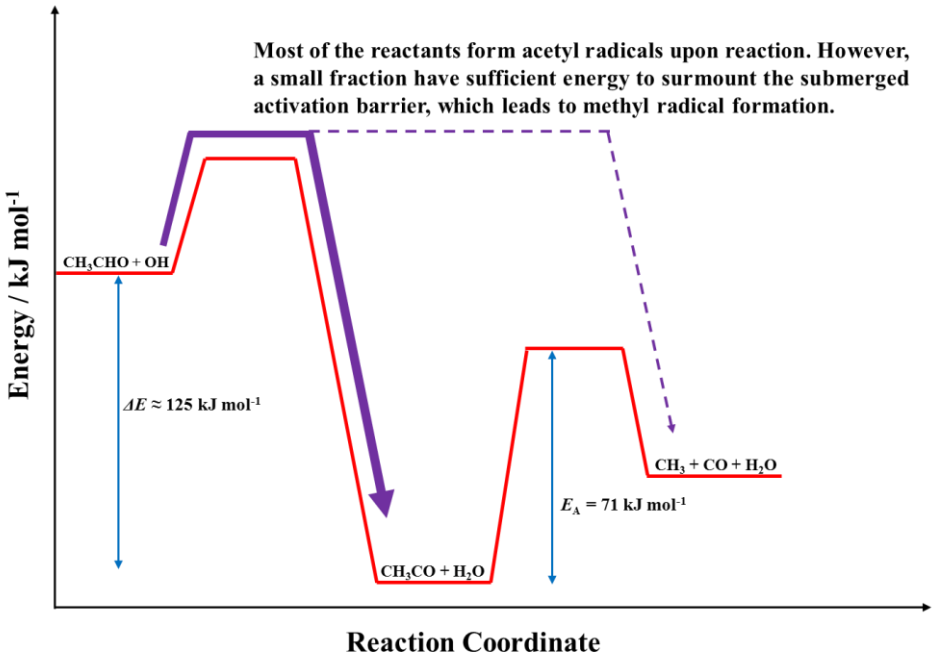

Figure 4.2: A simplified version of the potential energy surface described in D'Anna et al. (2003).

Previous work done at the University of Leeds has also observed this type of non-dynamical energy partition in the reactions of methylglyoxal and glyoxal with OH radicals (Baeza-Romero et al., 2007, Lockhart et al., 2013). In the experiments by Lockhart et al. (2013) OH recycling was measured for the glyoxal + OH reaction in the presence of O_2. This implied that the following reaction sequence was taking place:

$$HC(O)C(O)H + OH \rightarrow HC(O)CO^* + H_2O \quad \text{(R4.8)}$$

$$HC(O)CO + O_2 \rightarrow OH + CO_2 + CO \quad \text{(R4.9)}$$

From the subsequent Stern-Volmer analysis ($1/\Phi_{OH}$ vs. [M] plot) an intercept of >1 was calculated: where $1/\Phi_{OH}$ is the reciprocal of the yield of hydroxyl radicals recycled and [M] is the number density of the bulk gas present, typically nitrogen (Lockhart et al., 2013). The intercept of the Stern-Volmer plot ($1/\Phi_{OH}$ at [M] = 0) should be equal to unity if all the OH

is fully recycled (i.e. 100% of the HC(O)CO reacts with O_2 to form OH once more). However, this clearly is not what was observed, which suggests alternate removal channel for the HC(O)CO* radical species:

$$HC(O)CO^* \rightarrow HCO + CO \qquad (R4.10)$$

Lockhart et al. (2013) proposed the reaction above (R4.10) as one such feasible removal channel. This reaction pathway is an example of the decomposition of a chemically activated species, in this case HC(O)CO, and is very similar to channel proposed by D'Anna et al. (2003) (see R4.7e).

In this study the acetaldehyde + OH reaction has been investigated using two complementary methodologies: PLP-PIMS and a laser induced fluorescence (LIF)/OH recycling technique described in Baeaza-Romero et al. (2007), the PIMS technique was employed to simultaneously identify CH_3CO and CH_3 as primary products from the reaction (R4.7). The OH recycling technique was then used to confirm the results by demonstrating that there is less than 100% acetyl production. Finally, the Master Equation Solver for Multi-Energy Well Reactions (MESMER) package was used to determine if chemically activated acetyl fragmentation is even possible (Glowacki et al., 2012a). It should be noted that the OH recycling experiments were conducted primarily by Dr. James Lockhart and the MESMER calculations by Dr. Robin Shannon; therefore this chapter will concentrate predominantly on the results obtained using the PLP-PIMS set-up.

4.2 Experimental

4.2.1 PLP-PIMS Experiments

The OH and CH_3CHO reaction was investigated using time-resolved mass spectrometry to directly monitor acetyl radical (m/z = 43) and methyl radicals (m/z = 15) simultaneously, see Chapter II for details on PIMS technique. In these experiments 2 – 5% samples of CH_3CHO (Sigma-Aldrich: 99.5%) were prepared in He and stored in a glass bulbs. Other reactants used throughout this study such as: Acetone (99.9% VWR), Oxalyl Chloride (98% Alfa Aesar), Acetyl Chloride (98% Sigma-Aldrich), were prepared and stored in a similar fashion.

For the initial data sets ozone was used as a precursor for the OH radical (R4.11 – R4.12). Gas bulbs of O_3 were made using an ozone generator coupled to a silica trap to concentrate the ozone. This technique commonly yielded ~ 25 Torr of ozone, producing a 2 – 3% bulb when the sample was diluted in helium. During these experiments gas flows were set using calibrated mass flow controllers of varying size (2 – 500 sccm). The $CH_3CHO/He/O_3/H_2O$ gaseous mixture was combined in a manifold and then flowed into the reactor: note, these

experiments were all performed at low pressures (1.0 - 2.5 Torr). The concentrations of acetaldehyde (0.2-1.5) × 10^{14} molecule cm^{-3} were also kept high (in comparison with [OH] = 5 × 10^{12} molecule cm^{-3}) to ensure pseudo-first-order conditions. The concentration of water was also high ([H_2O] = 2 × 10^{15} molecule cm^{-3}) to ensure all the $O(^1D)$ radical were captured to form OH and to help quench vibrationally excited OH. Chemistry was initiated using an excimer laser pulse (248 nm, ~75 mJ cm^{-2}); the gas mixture was sampled, ionized and delivered to the mass spectrometer to detect the products.

$$O_3 + h\nu\ (\lambda = 248\ nm) \rightarrow O(^1D) + O_2 \qquad (R4.11)$$

$$O(^1D) + H_2O \rightarrow 2\ OH \qquad (R4.12)$$

Later, experiments were run using 193 nm excimer light as some problems were encountered when working at 248 nm. It was observed that there was a small photolytic signal interfering with the methyl ion signal at high excimer energies. At 193 nm the cross section of acetaldehyde is smaller and it was thought that the photolytic methyl signal would be negligible. Furthermore, ozone decomposes to O_2 (τ = 3-5 days), which caused secondary reactions to interfere with the methyl ion signal. At 193 nm nitrous oxide (N_2O) was used as an OH precursor instead of O_3, creating an oxygen-free system, hence avoiding any O_2 based interference. Again, pseudo-first order conditions were maintained by keeping acetaldehyde concentrations high in relation to [OH].

$$N_2O + h\nu\ (\lambda = 193\ nm) \rightarrow O(^1D) + N_2 \qquad (R4.13)$$

$$O(^1D) + H_2O \rightarrow 2\ OH \qquad (R4.12)$$

Only minor methyl radical interference was observed when using 193 nm photolysis. It should be noticed that the energy of the excimer was lower at 193 nm, typically ~ 50 mJ cm^{-2}. The experiments were controlled using LabVIEW™ software; note, specific details of the data acquisition and collection can be found in Chapter II, Section 2.7.

The kinetic traces were then analysed using OriginPro graphical software to describe the rate of formation of the acetyl signal (S_{Ac}), the signal from the mass spectrometry was fitted using the following equation (E4.2); an example of the quality of data fitted using E4.2 can be seen in Figure 4.3. The corresponding equation used to fit the methyl signal (S_{Me}) can be seen in E4.3; note that this equation has an additional term, which takes into account any instantaneous methyl signal formed during photolysis ($S_{instant}$).

$$S_{Ac} = \frac{S_{Acheight}\, k_g k_{samp}}{k_l - k_g}\left[\frac{e^{-k_g t} - e^{-k_{samp} t}}{k_{samp} - k_g} - \frac{e^{-k_l t} - e^{-k_{samp} t}}{k_{samp} - k_l}\right] + S_0 \qquad (E4.2)$$

$$S_{\mathrm{Me}} = \frac{S_{\mathrm{Meheight}}\, k_{\mathrm{g}} k_{\mathrm{samp}}}{k_{\mathrm{l}} - k_{\mathrm{g}}}\left[\frac{e^{-k_{\mathrm{g}}t} - e^{-k_{\mathrm{samp}}t}}{k_{\mathrm{eff}} - k_{\mathrm{g}}} - \frac{e^{-k_{\mathrm{l}}t} - e^{-k_{\mathrm{samp}}t}}{k_{\mathrm{eff}} - k_{\mathrm{l}}}\right] + \frac{S_{\mathrm{instant}}\, k_{\mathrm{samp}}}{k_{\mathrm{samp}} - k_{\mathrm{l}}}\left[\frac{e^{-k_{\mathrm{l}}t} - e^{-k_{\mathrm{samp}}t}}{k_{\mathrm{samp}} - k_{\mathrm{l}}}\right] + S_0 \qquad \text{(E4.3)}$$

In equations E4.2 & E4.3: S_{Ac} and S_{Me} are equivalent to the time-resolved signal observed for acetyl and methyl radicals respectively; S_{Acheight} is proportional to the maximum height of the acetyl signal; similarly, S_{Meheight} is proportional to the maximum height of the methyl signal; k_{g} is the coefficient rate of growth of the signal (note: $k_{\mathrm{g}} \equiv k'_{\mathrm{OH}}$ *or* k'_{Cl} depending on the reactants used); k_l is rate coefficient for the loss rate; k_{samp} is the rate the gas is sampled into the mass spectrometer (this was constrained to $k_{\mathrm{samp}} \approx 30000\ \mathrm{s}^{-1}$); S_{instant} refers to any instantaneous signal observed (photolytic); S_0 is the signal at time zero, and t is time. Adapted from Baeza-Romero et al. (2007).

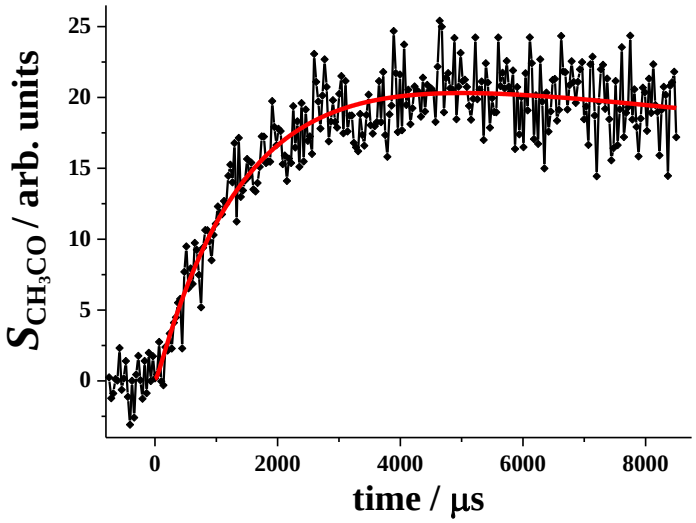

Figure 4.3: An example of the data collected from the experiment, where S_{CH3CO} is the time-resolved acetyl signal. In addition, the red line is the fit to the data given by E4.2.

4.2.2 Laser induced fluorescence / OH recycling Experiments

This part of the study was performed by J. Lockhart and T. Varga; a more detailed account of these experiments can be found in the thesis of J. Lockhart (2014).

This work was completed using a pulsed laser photolysis, laser induced fluorescence (PLP-LIF) system that have been used in several previous publications (Carr et al., 2007, Glowacki et al., 2012b, Lockhart et al., 2013). Similarly to the PIMS apparatus, the gas flow was regulated using mass flow controllers, mixed and flowed into the reactor (in this case a stainless steel 6-way cross). Temperature variations were made possible through customisation of the experiment. Low temperature measurements at 212 K were performed using a bath of dry ice/chloroform and positioning this around the reactor. High

temperatures were achieved by using a slightly different reaction cell, with a ceramic heater attached (Lockhart, 2014). For all PLP-LIF experiments the reactions were also carried out at relatively low pressure ($p < 60$ Torr), the reaction pressure was measured using a capacitance manometer.

OH radicals were generated from the laser photolysis of *t*-butyl hydroperoxide at 248 nm (Baasandorj et al., 2010); photolysis energies were typically 25 - 75 mJ cm^{-1}.

$$t\text{-}C_4H_9OOH + h\nu \rightarrow OH + \text{co-products} \qquad \text{(R4.14)}$$

Off-resonance laser induced fluorescence (excitation at ~282 nm, detection at ~308 nm) was used to detect the OH radicals. The OH fluorescence signal was obtained using a photomultiplier tube perpendicular to the probe beam. The photomultiplier signal was integrated using a boxcar average (SRS) and digitized before being sent to a personal computer for data analysis. The time delay between the photolysis and probe lasers was controlled by Labview software and was varied to build up a record of the OH signal following photolysis. Kinetic traces were typically 200 – 400 data points each averaged 2 - 10 times until the data were of sufficient quality.

4.3 Results from the PIMS Experiment

4.3.1 Kinetics of the CH_3CHO + OH Reaction

The first objective of this study was to investigate the kinetics of the OH and acetaldehyde reaction using the PIMS technique. Numerous studies have investigated this reaction and the kinetics are thought to be well understood (Calvert, 2011, Atkinson et al., 2006). The reaction has an IUPAC recommended rate coefficient of $k_{OH} = (1.5 \pm 0.2) \times 10^{-11}$ cm^3 $molecule^{-1}$ s^{-1}; it therefore seemed prudent see if these results could be replicated using the PIMS set-up.

Initially, there were concerns with the data collected as the observed *y*-intercept was very high (> 5000 s^{-1}). This limited the range of the data that could be accurately collected; this was because the equation used to fit the data was problematic when fitting coefficients greater than 10000 s^{-1}. It was thought that the large intercepts observed were due to a high OH wall-loss rate. The flow-tube was recoated with halocarbon wax, which seemed to help lower the intercept and meant a greater range of data could be reliably measured.

Pseudo first-order data sets were collected by varying the concentration of acetaldehyde. It was observed that the *y*-intercept differed slightly from day-to-day, presumably due to slight changes in flow-tube conditions. Consequently, it was decided that each data set should be collected in one session and not averaged over the course of several days / weeks. It should also be noted that the concentration of hydroxyl radicals was calculated as approximately

[OH] = 5×10^{12} molecule cm^{-3}, this meant that some of the experiments conducted at low acetaldehyde concentrations ([CH_3CHO] < 5×10^{13} molecule cm^{-3}) were not strictly under pseudo first-order conditions. However, in all of the experiments performed the inclusion of the pseudo first-order rate coefficients, *k'*, determined from the low [CH_3CHO] did not significantly change the bimolecular rate constant for the reaction, k_{OH}. Furthermore, the pseudo-first order rate coefficients from the low [CH_3CHO] traces usually corresponded well to the high [CH_3CHO] data and so were generally included in the bimolecular plots (*k'* vs. [CH_3CHO], Figure 4.4). Notably, from the bimolecular plots the rate coefficient for the acetaldehyde + OH reaction could be determined (see Chapter I, Section 1.5)

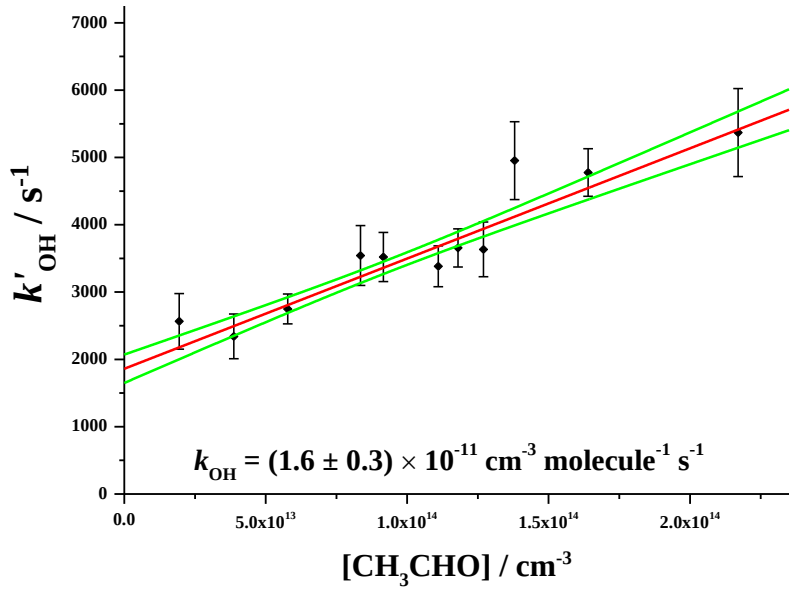

Figure 4.4: An example of an OH + CH_3CHO bimolecular plot collected using the PIMS technique. Error quoted are propagated from random errors of bimolecular plot and a 10% systematic experimental error. Confidence limits at 1σ level.

The kinetic data collected were in good agreement with the literature, with a rate coefficient of k_{OH} = (1.6±0.2) × 10^{-11} cm^3 $molecule^{-1}$ s^{-1} recorded (Atkinson et al., 2006). The precision of these measurements is somewhat lower than those found in literature (see Table 4.1). However, this is to be expected as reaction products were being monitored, not the reactants and accurately fitting an exponential growths correctly using E4.2 is more difficult than fitting a decay. These measurements, however, are in good agreement with the literature, verifying that the set-up can be used to accurately determine kinetic data.

As part of this study the reaction of acetaldehyde with Cl radicals (using oxalyl chloride as a precursor) was also probed. Like the OH reaction this process is thought to be well understood. The reaction has a recommended rate coefficient of k_{Cl} = (7.8 ± 1.3) 10^{-11} cm^3

molecule^{-1} s^{-1} (Tyndall et al., 1999); the kinetic data collected from the PIMS system were, again, in reasonable agreement with the literature (Table 4.1).

Table 4.1: Kinetic data of the OH and Cl reactions with Acetaldehyde (Howes et al., 2016).

CH_3CHO + OH			**CH_3CHO + Cl**		
Set-up	***Date***	**10^{11} k_{OH} / cm^3 s^{-1}**	***Set-up***	***Date***	**10^{11} k_{Cl} / cm^3 s^{-1}**
248 nm[a],OD[b]	22/10/2012	2.0 ± 0.3[d]	248 nm, OD	Oct. 2012	6.7 ± 2.2
248 nm, OD	23/10/2012	1.6 ± 0.3	248 nm, OD	Nov. 2012	8.8 ± 1.3
248 nm, OD	12/11/2012	1.5 ± 0.7	193 nm, ND	Nov. 2013	8.2 ± 2.2
248 nm, OD	13/11/2012	1.6 ± 0.3	193 nm, ND	May 2014	7.7 ± 1.0
193 nm[a,c], OD	Oct. 2013[c]	1.2 ± 0.2			
193 nm, ND[b]	Nov. 2013	1.4 ± 0.3			
Average		**1.6 ± 0.2**	**Average**		**7.9 ± 0.9**

a – 248 nm, O_3 photolysis in the presence of water. 193 nm, N_2O photolysis in the presence of water.
b – OD, old detector, ND – new detector. Although both detectors are of the same type, their differing sensitivities mean that different ion extraction potentials will have been used, and a possibility of different fragmentation patterns.
c – When no specific date is given, the bimolecular rate coefficients have been collected over a period of several days where the main focus has been yield determinations.
d – The error for the individual evaluations of k_{OH} and k_{Cl} are propagated using the random errors associated with the bimolecular plot (±1σ) and a systematic experimental error of 10%.

From Table 4.1 it can be seen that the precision of the initial acetaldehyde + Cl experiments is low (Oct. 2012 and Nov. 2012), this was because many of the pseudo first-order rate coefficients, $k_g \equiv k'_{Cl}$, determined were very large (k'_{Cl} > 10000 s^{-1}). This was problematic when it came to fitting the data (E4.2). The reason for this being that, even though each trace is made up of ~200 time-resolved data points, if the growth rate coefficient is too large, only the first ~10 points contain the important kinetic information. Secondly, due to the nature of E4.2, it becomes increasingly difficult distinguish between k_{samp} and k_g, when k_g is large (k_g > 10,000 s^{-1}). To minimise corrections needed to be made for these transport effects, the experiments were repeated at lower concentrations of CH_3CHO; these changes yielded better, more precise, results (Figure 4.5).

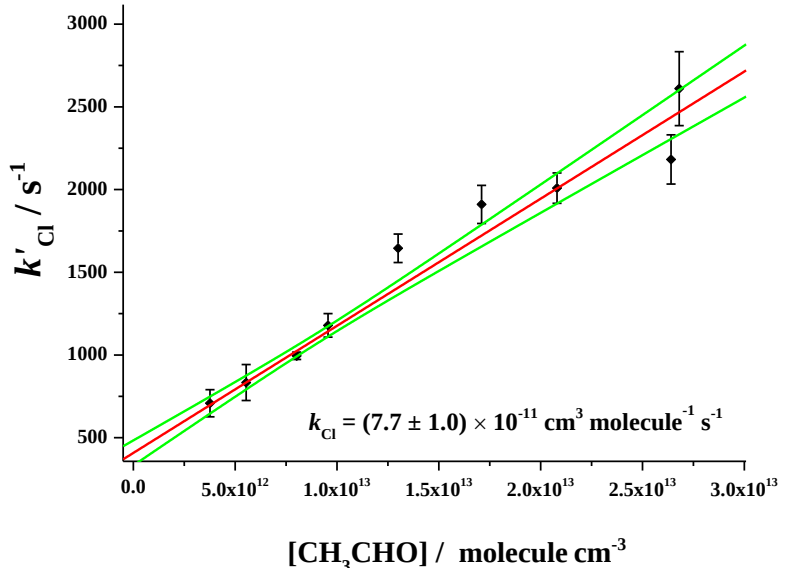

Figure 4.5: An example of an OH + CH_3CHO bimolecular plot collected using the PIMS technique. Confidence limits given to 1σ.

It should be noted that, as both rate coefficients correspond well to those previously reported in literature, it suggests that the target reactions have been isolated and are well characterised (Calvert, 2011).

4.3.2 Preliminary Evidence for Acetyl Fragmentation and the Subsequent Methyl Yields

Unlike most previous studies which have investigated acetaldehyde + OH product formation (R4.7), the PIMS technique can give high quality time-resolved data for multiple species concurrently; note that the technique can also provide accurate kinetic information (Section 4.3.1.1). Using the PLP-PIMS set-up it was possible to monitor both the acetyl (*m/z* = 43) and methyl (*m/z* = 15) signals simultaneously, allowing temporal correlation between these two species to be observed. When these signals are overlaid it is obvious that there is a direct link between these two species (Figure 4.6).

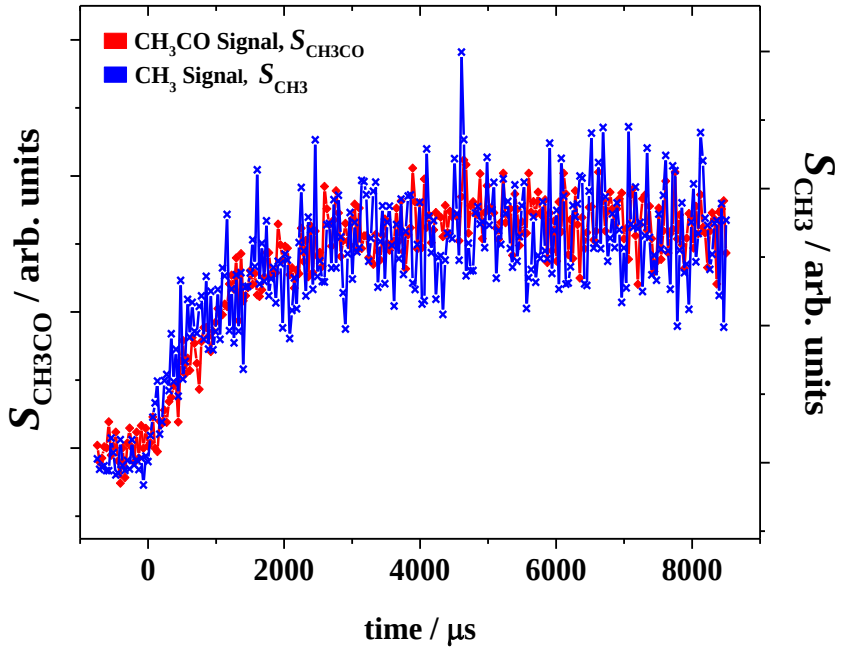

Figure 4.6: Superimposed plots of acetyl and methyl signal from the same experiment (1.5 Torr He, N_2O/H_2O as the OH source, [CH_3CHO] = 4 × 10^{13} molecule cm^{-3}) showing that they are produced on the same timescale.

The similarity of the time-resolved profiles for CH_3CO and CH_3 strongly implies that these species must have originated from the same source. This behaviour is most easily explained by R4.7e.

However, before assigning R4.7e as the production channel for the methyl radicals, we must first rule out the other possible sources of the observed CH_3 signal. For example it was suggested that the methyl radical may be produced during photoionization. To investigate whether or not this was true, the reaction of acetaldehyde and Cl was explored:

$\Delta_r H$= -57.8 kJ mol^{-1} $\quad CH_3CHO + Cl \rightarrow CH_3CO + HCl$ (R4.15)

This reaction was chosen for comparison because its exothermicity is significantly smaller than that of the OH reaction (Sander, 2011). Therefore, unlike in the OH reaction, none of the nascent acetyl radicals formed will have sufficient energy to surmount the activation barrier leading to methyl production ($\Delta_r H$ = -57.8 kJ mol^{-1} and E_a = 71 kJ mol^{-1}) (Atkinson et al., 2006, D'Anna et al., 2003). This means that any CH_3 radical signal observed in the Cl reaction is due photo-fragmentation by the ionization laser pulse and not from acetyl decomposition. The relative signal ratios of CH_3:CH_3CO radicals for the OH and Cl reactions are shown below (Figure 4.7).

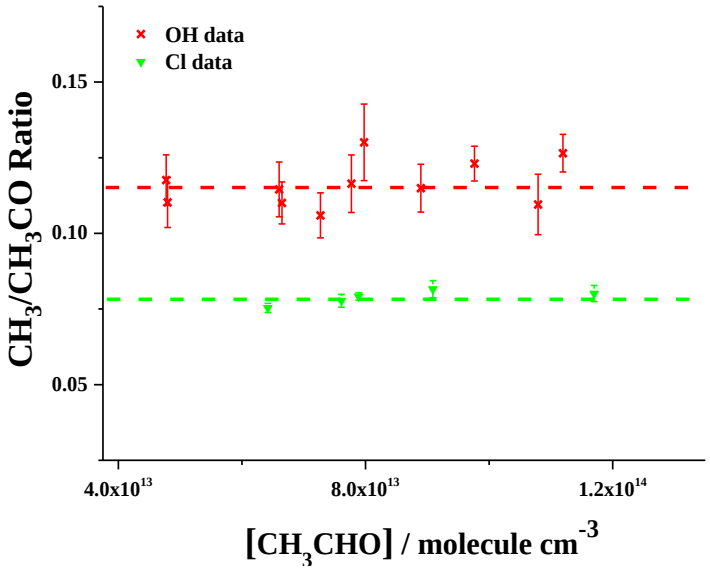

Figure 4.7: An example of some of CH_3:CH_3CO signal ratios obtained from the reaction of OH with acetaldehyde and Cl with acetaldehyde. The dashed lines are the average values in these experiments.

The results from Figure 4.7 show that the CH_3:CH_3CO signal ratio was larger for OH reaction than the Cl reaction. This result fits well with our hypothesis: the OH reaction gives a larger CH_3:CH_3CO signal ratio as a small fraction of the acetyl radical formed have sufficient energy (> 71 kJ mol^{-1}) to fragment further producing methyl radicals and CO. The acetaldehyde + Cl reaction does yield a very small CH_3 signal and it was assumed that this was due to photo-fragmentation of acetyl radicals by the probe laser.

In addition to the acetaldehyde + OH / chlorine inter-comparison study, other experiments were run that, again, suggest the methyl signal it not from fragmentation by photoionization. These experiments were initially considered redundant as there was a leak on the line, causing small amount of O_2 (~25 mTorr) to be added to the gas mixture. However, the results from this experiment provide conclusive proof that the methyl formation was not caused during photoionization (Figure 4.8).

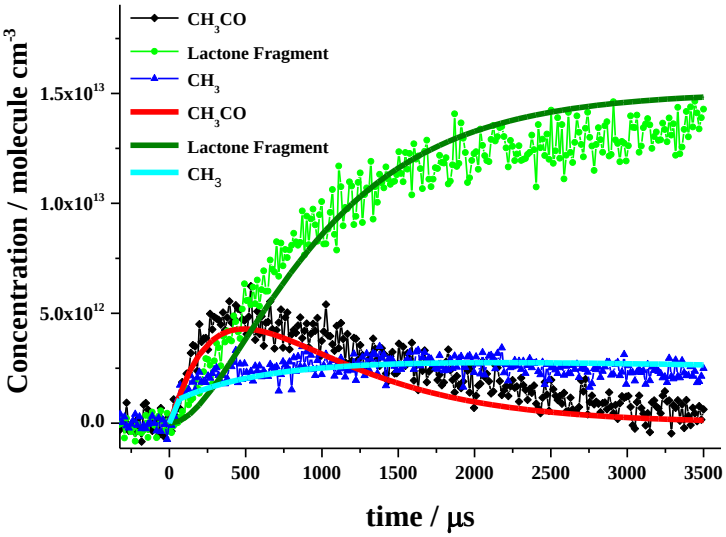

Figure 4.8: Time-resolved signals of acetyl, methyl and lactone species in an OH/CH_3CHO/O_2 system. The solid points are the experimental data and the lines are a numerical simulation based on a kinetic model. Note: the experimental data were scaled to match the numerical simulation.

The experiments carried out in the presence of O_2 are essentially examples of an OH-recycling experiment (note: this methodology is discussed in detail in Section 4.4). As can be seen in R4.16a, the presence of O_2 in the reaction system leads to the recycling of OH; in addition, R4.16 is also responsible for the observed loss of CH_3CO from the system, a process that does not rapidly occur in the absence of O_2 (see Figure 4.8).

$$CH_3CO + O_2 \rightarrow CH_3C(O)O_2^* \rightarrow OH + \textit{cyclo}\text{-}CH_2C(O)O \qquad \text{(R4.16a)}$$

$$\rightarrow CH_3C(O)O_2^* + M \rightarrow CH_3C(O)O_2 \qquad \text{(R4.16b)}$$

From Figure 4.8 it can be seen that the loss methyl signal from these experiments does not mirror the observed acetyl loss. If the methyl signal was formed during photoionization of the acetyl signal, it would be expected that the methyl signal would have the same time evolution as the acetyl species (as photoionization occurs after all chemistry). However, as methyl radicals have a different time evolution to the acetyl radicals (in the presence of O_2), it indicates that the methyl radicals must be formed through chemical reaction and not photoionization. Of all the possible reactions that could be responsible for CH_3 formation, the only mechanism which also accounts for ~100% yield of water is R4.7e (D'Anna et al., 2003).

4.3.3 Quantitative Evaluation of Methyl Radical Yields

Figures 4.6-4.8 give strong qualitative evidence for the chemically activated decomposition of acetyl radicals. However, the acetaldehyde + OH data alone cannot reveal any

quantitative information about the methyl radical yields. This is because the ionization efficiencies of the CH_3^+ and CH_3CO^+ radicals are not the same, meaning the relative heights of the methyl and acetyl signals measured from the acetaldehyde + OH reaction are not directly proportional to the fraction of CH_3CO decomposition. To quantify the signals the CH_3:CH_3CO signal ratio determined from the ethanal + OH reaction experimentally must be scaled to the concentration i.e. [CH_3]:[CH_3CO], this can be done using calibration factors. By calibrating the system it was possible to quantify the methyl radical yield for the chemically activated decomposition of acetyl radicals from the acetaldehyde + OH reaction. As the CH_3:CH_3CO signal ratio is independent of the ionization efficiencies, it was used instead of the signal heights to accurately quantify the methyl radical yield, Y_{CH3}.

The minimum value of the CH_3:CH_3CO signal ratio was calculated from the acetaldehyde + Cl reaction. This reaction was ideal as methyl radicals will only be formed from acetyl fragmentation during photoionization (i.e. no chemistry should lead to the production of methyl radicals). However, calculating a maximum value for the CH_3:CH_3CO signal ratio (i.e. the observed ratio if there are equal numbers of CH_3 and CH_3CHO radicals present in the detector) was more difficult. It should be noted that different calibration methods were necessary for the experiments done using 248 nm and 193 nm excimer light.

4.3.3.1 CH_3 and CH_3CO Calibration at 248 nm

The aim of the calibration process is to determine a quantitative value for the yield of CH_3, Y_{CH3}, from the reaction between CH_3CHO and OH:

$$Y_{CH3} = \frac{[CH_3]_{OH}}{[CH_3CO]_{OH} + [CH_3]_{OH}} = 1 + \frac{[CH_3]_{OH}}{[CH_3CO]_{OH}} \quad \text{(E4.4)}$$

However, to determine this [CH_3]:[CH_3CO] ratio from the experiments is difficult; firstly the heights of the CH_3 signal, $(S_{CH3})_{OH}$, and CH_3CO signal, $(S_{CH3CO})_{OH}$, are not directly proportional to [CH_3] and [CH_3CO] respectively (due to differing ionization efficiencies). Secondly, it is also known that a small proportion of CH_3CO fragment during photoionization to produce CH_3.

$$(S_{CH3})_{OH} = \alpha[CH_3]_{OH} + \beta[CH_3CO]_{OH} \quad \text{(E4.5)}$$

$$(S_{CH3CO})_{OH} = \gamma[CH_3CO]_{OH} \quad \text{(E4.6)}$$

where $(S_x)_{OH}$ is the long-time signal of CH_3 or CH_3CO and α, β, γ are coefficients that link the signal to the concentration. Note: that the term $\alpha[CH_3]_{OH}$ refers to the signal of methyl radicals produced from R4.7e; the term $\beta[CH_3CO]_{OH}$ refers to the CH_3 signal caused by CH_3CO photoionization; finally $\gamma[CH_3CO]_{OH}$ refers to the acetyl signal measured during the experiments.

The Y_{CH3} can be quantified from the CH_3:CH_3CO signal ratio determined experimentally using the following equations:

$$\frac{(S_{CH3})_{OH}}{(S_{CH3CO})_{OH}} = \frac{\alpha[CH_3]_{OH} + \beta[CH_3CO]_{OH}}{\gamma[CH_3CO]_{OH}} \quad \text{(E4.7)}$$

$$\frac{(S_{CH3})_{OH}}{(S_{CH3CO})_{OH}} = \frac{\alpha}{\gamma}\frac{[CH_3]_{OH}}{[CH_3CO]_{OH}} + \frac{\beta}{\gamma} \quad \text{(E4.8)}$$

However, before a quantitative value for Y_{CH3} can be calculated, evaluations of both α/γ and β/γ must be found; this can be done by using other reactions to calibrate the system and determine α/γ and β/γ.

The calibration to find needed to find β/γ is straightforward and was done using by investigating the reaction between acetaldehyde and chlorine (R4.15). As previously stated the exothermicity of chlorine reaction (ΔH_{Cl} = -57.8 kJ mol^{-1}) is significantly lower than the OH reaction (ΔH_{OH} = -123 kJ mol^{-1}); this means that, unlike in the OH reactions, there will no methyl radicals formed from R4.15 (i.e. no CH_3 formed from $\alpha[CH_3]_{OH}$). This simplifies equation (E4.5) to:

$$(S_{CH3})_{Cl} = \beta[CH_3CO]_{Cl} \quad \text{(E4.9)}$$

Therefore:

$$\frac{(S_{CH3})_{Cl}}{(S_{CH3CO})_{Cl}} = \frac{\beta[CH_3CO]_{Cl}}{\gamma[CH_3CO]_{Cl}} = \frac{\beta}{\gamma} \quad \text{(E4.10)}$$

To reiterate, the methyl radical signal, $(S_{CH3})_{Cl}$, observed in the acetaldehyde + Cl reaction is solely formed from acetyl fragmentation during photoionization (and not R4.15). To determine α/γ was more convoluted, although it was made possible by using acetyl chloride (CH_3COCl) as a precursor to investigate the reaction CH_3CHO + Cl (R4.17). Note: in previous acetaldehyde + Cl experiments oxalyl chloride was used as a Cl precursor.

$$CH_3C(O)Cl + h\nu\ (\lambda\text{=248 nm}) \rightarrow CH_3CO + Cl \qquad (\varphi_{P1} \approx 0.45) \qquad \text{(R4.17a)}$$

$$\rightarrow CH_3 + CO + Cl \qquad (\varphi_{P2} \approx 0.55) \qquad \text{(R4.17b)}$$

$$CH_3CHO + Cl \rightarrow CH_3CO + HCl \qquad \text{(R4.14)}$$

The reason for using acetyl chloride (AcCl) as a precursor is that it is known to fragment in a characteristic manner, producing both CH_3 and CH_3CO during photolysis (M.T. Baeza-Romero, 2016). The chlorine radicals produced subsequently react with acetaldehyde producing solely acetyl (R4.15), meaning that any long-time methyl signal observed arises from fragmentation in the ionization process. In Figure 4.9 both the prompt acetyl signal,

$(S_{CH3CO})_{instant}$, corresponding to the photolysis channel R4.17a, and the longer time signal, $(S_{CH3CO})_{growth}$, corresponding to acetyl production from the acetaldehyde + Cl reaction, are seen. It should be noted that the chlorine radicals are formed from both the photolysis channels $\varphi_{P1} + \varphi_{P2}$ (hence: $[Cl]_{total} = [Cl]_{\varphi P1} + [Cl]_{\varphi P2}$).

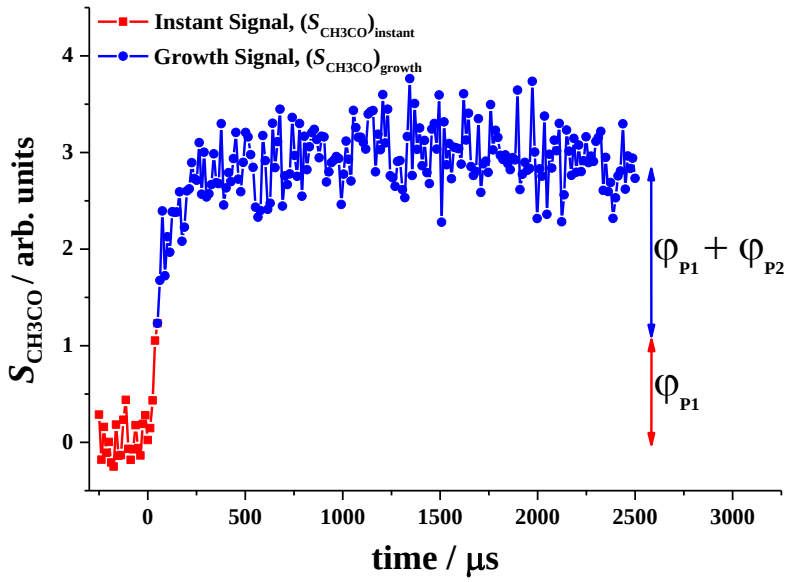

Figure 4.9: An example of the CH_3CO signal, in particular the contributions of the from the photolysis channel R4.17.

Furthermore, from Figure 4.9 it is possible to determine a precise ratio of CH_3/CH_3CO from the photolysis of acetyl chloride (i.e. $\varphi_{P2}/\varphi_{P1}$). If it is assumed that $\varphi_{P1} = 1$ and $(\varphi_{P1} + \varphi_{P2}) = \varphi_{total}$, equations E4.11-4.12 hold true.

$$\varphi_{total} = (1 + \varphi_{P2}) \quad \text{(E4.11)}$$

$$\frac{\varphi_{P2}}{\varphi_{P1}} = \varphi_{total} - 1 \quad \text{(E4.12)}$$

From the analysis of these experiments an average value of $\varphi_{P2}/\varphi_{P1} \approx 1.25$ was determined. This evaluation of $\varphi_{P2}/\varphi_{P1}$ can then be used in combination with the CH_3:CH_3CO signal ratios measured to determine the α/γ (E4.13-4.17):

$$[CH_3] = \left(\frac{\varphi_{P2}}{\varphi_{P1}}\right) \times [CH_3CO] = 1.25 \times [CH_3CO] \quad \text{(E4.13)}$$

$$(S_{CH3})_{AcCl} = \alpha[CH_3]_{AcCl} + \beta[CH_3CO]_{AcCl} \quad \text{(E4.14)}$$

$$(S_{CH3})_{AcCl} = 1.25 \times (\alpha[CH_3CO]_{AcCl}) + \beta[CH_3CO]_{AcCl} \quad \text{(E4.15)}$$

Therefore:

$$\frac{(S_{CH3})_{AcCl}}{(S_{CH3CO})_{AcCl}} = \frac{1.25 \times (\alpha[CH_3CO]_{AcCl}) + \beta[CH_3CO]_{AcCl}}{\gamma[CH_3CO]_{AcCl}} \quad \text{(E4.16)}$$

$$\frac{(S_{CH3})_{AcCl}}{(S_{CH3CO})_{AcCl}} = \frac{1.25 \times \alpha}{\gamma} + \frac{\beta}{\gamma} \quad \text{(E4.17)}$$

As β/γ has been previously calculated (from the CH_3CHO + Cl reaction data) using E4.10, hence α/γ can be calculated; it should be noted that $(S_{CH3})_{AcCl}/(S_{CH3CO})_{AcCl}$ is equivalent to a CH_3:CH_3CO signal ratio where there are equal numbers of CH_3 and CH_3CHO radicals present in the system.

Utilising the values of α/γ and β/γ calculated above a quantitative evaluation of Y_{CH3} for the acetaldehyde + OH experiments could be made using equations E4.4 and E4.8; this analysis led to an evaluation of Y_{CH3} = (15.5 ± 6.0) %.

4.3.3.2 An Alternative Methodology to Determine Y_{CH3} at 193 nm

For the experiments done using 193 nm light to initiate the reaction a different methodology was used to calculate Y_{CH3} from acetyl decomposition. Here, the photolytic behaviour of acetone at 193 nm, which is thought to be well understood (Lightfoot et al., 1988), was used to help determine the yield of methyl radicals. As with the experiments done at 248 nm, the acetaldehyde + OH and acetaldehyde + Cl reactions were both investigated. However, at 193 nm these experiments were done back-to-back with some acetone photolysis experiments. Analogous to the OH production channel used which yields two hydroxyl radicals (R4.12), the predominant photolytic channel for acetone (R4.18) is known to produce two methyl radicals:

$$CH_3C(O)CH_3 + h\nu\ (\lambda=193\ nm) \rightarrow 2\ CH_3 + CO \qquad (\varphi \geq 0.95) \qquad \text{(R4.18)}$$

The raw methyl radical data collected from the acetone photolysis experiments were calibrated so that it was equivalent to the N_2O environment used in the acetaldehyde + OH reactions. The photolytic acetone signal was tuned to $[N_2O]$ so that the CH_3 signal observed could be equated to the CH_3 signal measured the acetaldehyde + OH experiments:

$$M_{A1} = M_{A0} \times \frac{[N_2O] \times \sigma_{N2O} \times n_C}{[CH_3COCH_3] \times \sigma_{acetone}} \quad \text{(E4.18)}$$

where M_{A1} is the adjusted methyl signal from photolytic acetone, M_{A0} is the raw methyl radical signal from acetone experiments and σ represent the relevant cross-sections of the two species (N_2O and acetone respectively). Finally n_c is a factor used to balance the equation based on the conversion of $O(^1D)$ to OH (R4.12-4.13); this was estimated from the NO signal monitored during the experiments, a product from a competing reaction.

$$O(^1D) + N_2O \rightarrow 2\,NO \qquad (R4.19)$$

The adjusted methyl signal from acetone photolysis was then compared with methyl signal obtained from the acetaldehyde + OH experiments. This parameter, $f_{M_{OH}/M_{A1}}$, can be thought of the fraction of CH_3 formed from the reaction with OH in comparison to the maximum CH_3 signal. This component was then multiplied by the parameter analogous to the proportional difference in CH_3:CH_3CO signal ratios obtained from OH and Cl experiments, $f_{\frac{SR_{OH}-SR_{Cl}}{SR_{OH}}}$. This calculation gives evaluation of the yield of methyl radicals:

$$Y_{CH3}\,(\%) = f_{\frac{M_{OH}}{M_{A1}}} \times f_{\frac{SR_{OH}-SR_{Cl}}{SR_{OH}}} \times 100\% \qquad (E4.19)$$

From the experiments that were conducted using 193 nm light, an average yield of methyl radicals of $Y_{CH3} = (15.7 \pm 4.1)\%$ was determined. The calculated yield is in excellent agreement with the methyl radical yield determined at 248 nm; this suggests that both methodologies are viable. A full list of all the experiments done using the PIMS system can be seen in Table 4.2.

Table 4.2: Yield of Methyl Radicals from the OH + CH_3CHO Reaction. Experiments were conducted between 1-2 Torr He; OD = Old Detector, ND = New Detector.

Experiment	Year	Y_{CH3} (%)
193 nm N_2O/H_2O OH generation (OD)	2007	19.9 ± 4.6[a]
248 nm O_3/H_2O OH generation (OD)	2012	15.5 ± 6.0
193 nm N_2O/H_2O OH generation (OD)	2013	17.1 ± 2.4
193 nm N_2O/H_2O OH generation (ND)	2013	14.2 ± 2.3
Average, λ = 193 nm (±2σ) =		15.7 ± 4.1
Total Average (±2σ) =		**16.7 ± 4.9**

a – This experiment was performed by Dr. Mark Blitz using the same instrumentation.

The experiments at 193 nm produced a consistent yield, even when the electron multiplier used to detect the radicals was changed; this consistency suggests that the methodology used was reliable. However, initially there was some concern with these experiments, particularly with the monitored NO signal.

When water was bubbled into the system the monitored NO signal did not completely disappear, this means that not all of the $O(^1D)$ reacted with water to OH. The best explanation for this is that the concentration of water was lower than was expected. Using the NO signal data, the water concentration was extrapolated and evaluated at approximately 8×10^{14} molecule cm^{-3}. This is significantly lower than the concentration

previously estimated, which suggested $[H_2O] \approx 2 \times 10^{15}$ molecule cm^{-3}. This result suggests a sizable portion of the water was lost to the walls.

In addition to removing $O(^1D)$ from the reaction system, water is also plays an important role in quenching vibrationally excited hydroxyl radicals, OH(v).

$$O(^1D) + H_2O \rightarrow 2\ OH(v) \qquad \text{(R4.20)}$$

$$OH(v=1) + H_2O \rightarrow OH(v=0) + H_2O \qquad \text{(R4.21)}$$

If there is a significant proportion of the OH(v) radicals formed are left unquenched it could interfere with the observed methyl radical yield. For example, it may be that the reaction between OH(v=1) and CH_3CHO has a $Y_{CH3} = 1$ (worst-case scenario):

$$CH_3CHO + OH(v=1) \rightarrow CH_3 + CO + H_2O \qquad Y_{CH3} = 1 \qquad \text{(R4.22)}$$

If this were true, it would lead an amplification in the methyl radical yield making the results in Table 4.2 invalid. To test the validity of these experiments a Kintecus model was run (Ianni, 2002); the initial conditions (in Table 4.3) and the reaction scheme (Table 4.4) are listed below. In this reaction system under these experimental conditions much depends on the rate coefficient for OH(v=1) quenching by H_2O, k_q. However, there appears to be a considerable discrepancy between the literature values. Most early work seems to suggest a quenching rate coefficient between 2.5 -7.5 $\times 10^{-10}$ cm^3 $molecule^{-1}$ s^{-1} (Lee, 1980), but more recent work indicates a lower rate of $k_q \approx 1 \times 10^{-11}$ cm^3 $molecule^{-1}$ s^{-1} (McCabe et al., 2006). Clearly, if the quenching rate coefficient is smaller then there will be more OH(v=1) present in the system and therefore R4.15 will have greater importance. In the model a lower limit of k_q was used to explore the influence of this channel.

Table 4.3: Shows the initial conditions assumed. T= 298 K for all modelling.

Reactants	Concentrations / molecule cm^{-3}
O	5×10^{12}
N_2O	1×10^{15}
H_2O	8×10^{14}
CH_3CHO	$2 - 10\times10^{13}$

Table 4.4: Kintecus model of reaction scheme + rate coefficients, *k*.

Modelled Reaction Scheme	k / cm^3 molecule^{-1} s^{-1}	Reference†
$O + N_2O \rightarrow NO + NO$	1.5×10^{-10}	(Dillon et al., 2008)
$O + H_2O \rightarrow OH_{(v)} + OH_{(v)}$	2.0×10^{-10}	(Dunlea and Ravishankara, 2004)
$OH(v) + H_2O \rightarrow OH + H_2O$	1.25×10^{-11}	(McCabe et al., 2006)
$OH + CH_3CHO \rightarrow CH_3CO + H_2O$*	1.3×10^{-11}	(Atkinson et al., 2001)
$OH + CH_3CHO \rightarrow CH_3 + CO + H_2O$*	2×10^{-12}	
$OH_{(v)} + CH_3CHO \rightarrow CH_{3(v)} + CO + H_2O$	1.5×10^{-11}	(Atkinson et al., 2001)

†It should be noted that the value of rate coefficients are not exactly quoted from the references given, however, these were the sources used to give the approximate values of *k* used in the model.
***Note the sum of the rate coefficient highlighted is equal to the total rate coefficient for the reaction between CH_3CHO and OH, i.e. 1.5×10^{-11} (Atkinson et al., 2001).**

Figure 4.10 shows two sets of graphs with varying initial concentrations of acetaldehyde used: for graphs a) $[CH_3CHO] = 3 \times 10^{13}$ molecule cm^{-3} and in graphs b) $[CH_3CHO] = 1 \times 10^{14}$ molecule cm^{-3}. In graphs ai) and bi) the concentrations of CH_3 radical formed from acetaldehyde + OH(v=1)(red) and acetaldehyde + OH (blue) are shown, named CH_3(v) and CH_3 respectively. Both plots show a significant CH_3 radical component from the OH(v=1) channel, unsurprisingly this effect is greater at larger acetaldehyde concentrations. If indeed modelled behaviour is real, it indicates that a large fraction of the Y_{CH3} measured is actually due to the reaction between acetaldehyde + OH(v=1) and not because of the chemically activated fragmentation of acetyl radicals. In graphs aii) and bii) the relationship between the total concentrations of CH_3 radicals (i.e. CH_3(v) + CH_3, orange) and CH_3CO radicals (green) is shown for different acetaldehyde concentrations. From these graphs it is shown that the model predicts larger methyl radical yields at higher acetaldehyde concentration. Crucially, this was not observed experimentally (see Figure 4.11).

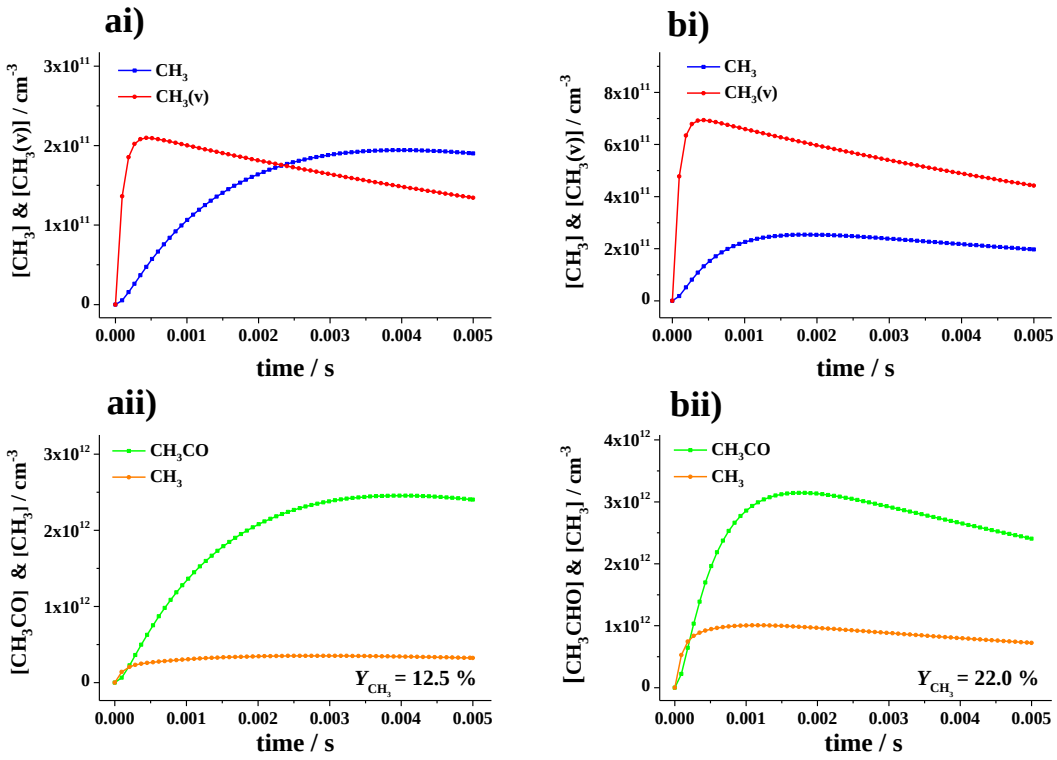

Figure 4.10: graphs ai) and bi) the concentrations of CH_3 radical formed from acetaldehyde + OH(v=1)(red) and acetaldehyde + OH (blue) are shown. In graph aii) and bii) the relationship between the concentrations of CH_3 radicals (orange) and CH_3CO radicals (green) for differing acetaldehyde concentrations. In plots ai) + aii) [CH_3CHO] = 3 × 10^{13} molecule cm^{-3}; and in plots bi) + bii) [CH_3CHO] = 1 × 10^{14} molecule cm^{-3}.

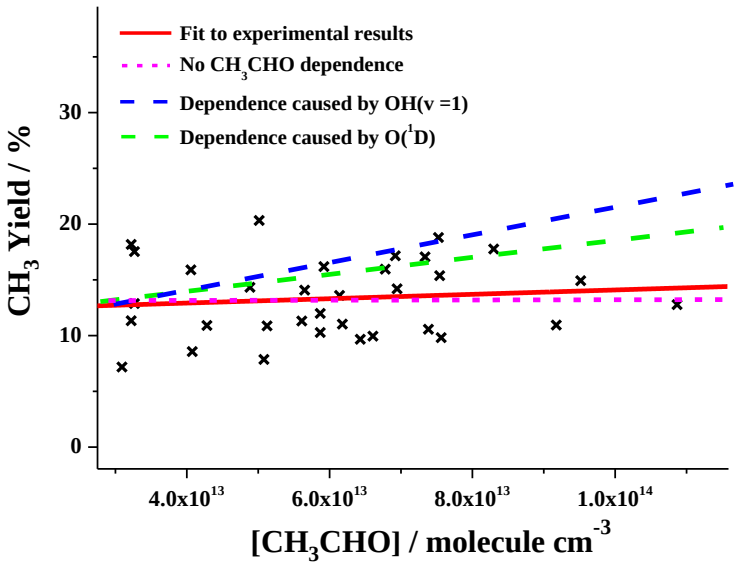

Figure 4.11: a plot to show the measured and modeled CH_3 yield dependency on acetaldehyde concentration.

In Figure 4.11 the CH_3 yields measured experimentally are plotted against the concentration of acetaldehyde (red line). Theoretically, the yield of methyl radicals formed should not

vary with concentration if the source of the methyl radicals is from chemically activated decomposition of acetyl radicals (Figure 4.11, pink dashed line). However, in Figure 4.11 indicates there is a small dependency on acetaldehyde concentration (red line), with slightly larger CH_3 yield predicted at higher acetaldehyde concentrations (Y_{CH3} = 12.8% at [CH_3CHO] = 3×10^{13} molecule cm^{-3} and Y_{CH3} = 14.2% at [CH_3CHO] = 1×10^{14} molecule cm^{-3}). However, if a significant fraction of the methyl radical yield was caused by the reaction between acetaldehyde + OH(v=1) reaction then the increase in Y_{CH3} at high acetaldehyde concentrations would be much greater than was observed experimentally (Figure 4.11, blue dashed line) (Y_{CH3} = 12.8% at [CH_3CHO] = 2.5×10^{13} cm^{-3} and Y_{CH3} = 22.0% at [CH_3CHO] = 1×10^{14} cm^{-3}). It should be noted that interference from the reaction between $O(^1D)$ + CH_3CHO was also modelled (green dashed line, Figure 4.11), like the OH(v) channel this reaction suggests a dependency on acetaldehyde concentration. As there was only a slight dependency on [CH_3CHO] observed this too suggests that the dominant process for methyl radical formation is R4.7e.

There are two possible reasons for the discrepancy between the experimental and modelled data. It may be because the NO data measured did not give an accurate evaluation of the concentration of water. However, multiple experiments were conducted over several days and were fairly consistent (± 10%). A second and possibly more likely explanation is the rate of OH(v=1) quenching by H_2O is larger than was used for modelling. If a quenching rate coefficient of k_q = 2×10^{-10} cm^3 $molecule^{-1}$ s^{-1} is used in the model then the Y_{CH3} is nearly independent of acetaldehyde concentration. In Figure 4.12 it can be seen in plots ai) and bi) that there is still a small contribution to the Y_{CH3} from the acetaldehyde + OH(v=1) channel (5% < R4.21 < 15%).

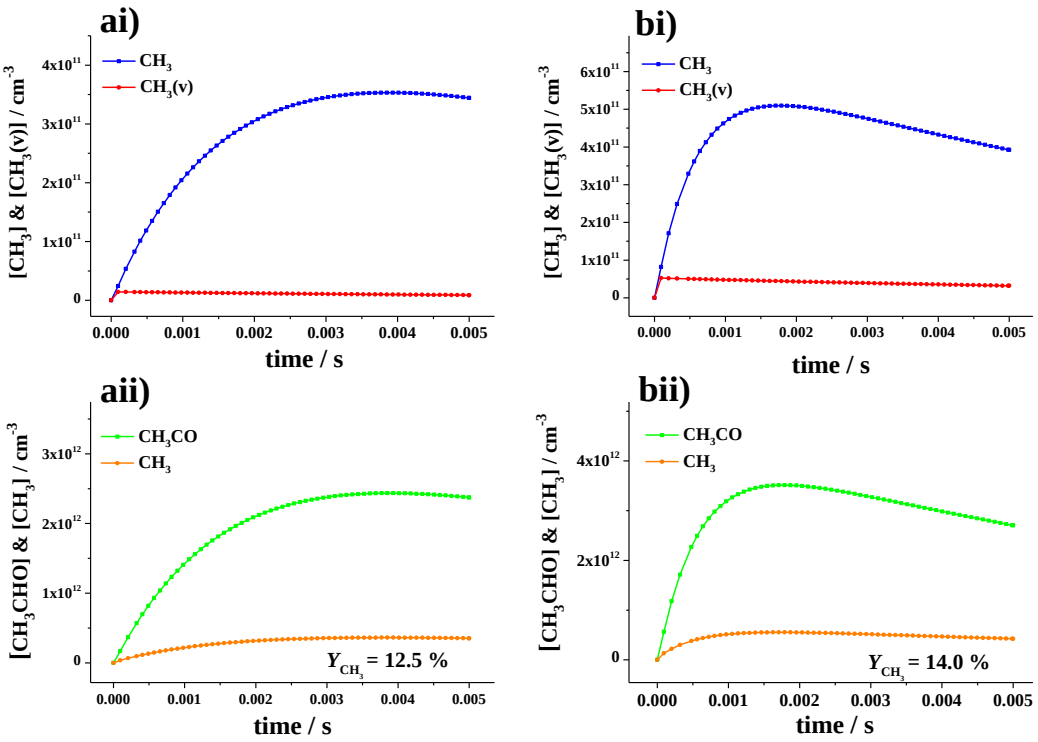

Figure 4.12: Simulations done using k_q = 2 × 10^{-10} cm^3 $molecule^{-1}$ s^{-1}. In graphs ai) and bi) the concentrations of CH_3 radical formed from acetaldehyde + OH(v=1)(red) and acetaldehyde + OH (blue) are shown. In graph aii) and bii) the relationship between the total concentrations of CH_3 radicals (orange) and CH_3CO radicals (green) for differing acetaldehyde concentrations. In plot ai) + bi) [CH_3CHO] = 3 × 10^{13} molecule cm^{-3}; and in plot aii) + bii) [CH_3CHO] = 1 × 10^{14} molecule cm^{-3}

However, this does mean that the CH_3 radical yields predicted from these experiments may slightly over predict the chemically activated acetyl fragmentation channel. The analysis was redone to take the minor OH(v=1) and O(^{1}D) contributions into account. A concentration dependent parameter was use to adjust the methyl yields. This analysis lowered the methyl radical yield for the chemically activated acetyl fragmentation, giving a new $Y_{CH3} \approx 14\%$ (see Table 4.5).

Table 4.5: Updated yields of Methyl Radicals from the OH + CH_3CHO Reaction. Experiments were conducted between 1-2 Torr He; OD = Old Detector, ND = New Detector. *The errors associated with the average values are quoted at the 95% Student's t Confidence interval half-width.

Experiment	Year	Corrected Y_{CH3} (%)
193 nm N_2O/H_2O OH generation (OD)	2007	17.3 ± 3.1
248 nm O_3/H_2O OH generation (OD)	2012	14.2 ± 5.8
193 nm N_2O/H_2O OH generation (OD)	2013	14.5 ± 2.0
193 nm N_2O/H_2O OH generation (ND)	2013	11.8 ± 1.6
Unweighted Average* =		14.5 ± 3.7
Weighted Average* =		**13.5 ± 3.6**

The actual contributions from the acetaldehyde + OH(v=1)/O(^{1}D) channels to the methyl radical yield may not be this large. However, by including these possible channels in our evaluation we can confidently predict a methyl radical yield in the range of 11.8% > Y_{CH3} > 17.3%, with a preferred (and conservative) evaluation of Y_{CH3} = (13.5 ± 3.6) %. Note that both an unweighted and a weighted average were calculated for the data; however, the weighted average is preferred as it yields a slightly more conservative evaluation of Y_{CH3}. The corrected methyl radical yields listed in Table 4.5 are solely caused by CH_3 production from the chemically activated decomposition of acetyl radicals.

4.4 Complementary Work

4.4.1 OH recycling of the CH_3CHO+ OH reaction with and without O_2

A kinetics study of the CH_3CHO + OH reaction (with and without additional oxygen) was carried out under pseudo first-order conditions such that the concentration of acetaldehyde (and oxygen if used) was always in excess over the OH. Under these conditions, hydroxyl radicals are removed by reaction with acetaldehyde and loss to the walls. However, when molecular oxygen is present acetyl radicals will react with O_2, regenerating a fraction of OH, though this channel is pressure dependent:

$$CH_3CO + O_2 \rightarrow CH_3C(O)O_2^* \rightarrow OH + \text{products} \qquad \text{(R4.16a)}$$

$$CH_3C(O)O_2^* + M \rightarrow CH_3C(O)O_2 + M \qquad \text{(R4.16b)}$$

As mentioned in Section 4.2.2 this technique uses off-resonance laser induced fluorescence to detect OH radicals at ~ 308 nm. The rate coefficients for these experiments were determined from the time resolved change in OH signal (inset graph in Figure 4.13). Due to OH recycling from R4.16 the bimolecular rate coefficient for OH loss in the presence of oxygen, k_{O2}, will be reduced compared to nitrogen, k_{N2}, (see lower traces in Figure 4.13); with the yield of OH, Φ_{OH}, is given by:

$$\Phi_{OH} = 1 - \frac{k_{O2}}{k_{N2}} \qquad \text{(E4.20)}$$

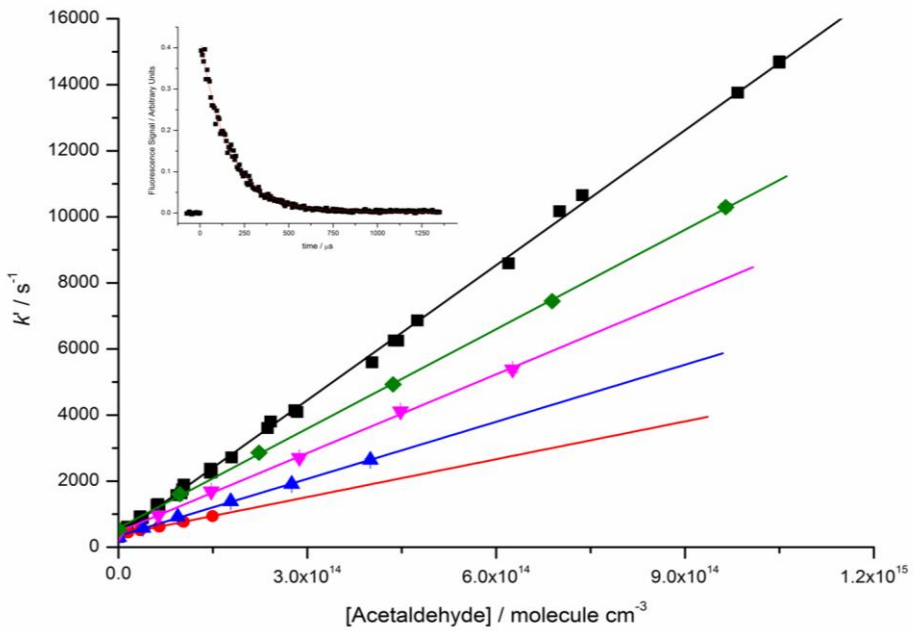

Figure 4.13: Bimolecular plots at 298 K. (■) no oxygen, (♦) O_2 present, p = 10 Torr; (▼) O_2 present, p = 5 Torr; (▲) O_2 present, p = 2 Torr; (●) O_2 present, p = 1 Torr.

The OH yield from the $CH_3CHO/OH/O_2$ system was determined as a function of pressure at 212, 298 and 385 K. At low pressure the greatest reduction in the rate coefficient, k_{O2}, is observed. This is because channel R4.16b is less prominent, meaning collisional quenching is slower, and OH recycling is more favourable.

Figure 4.14 shows the Stern Volmer plots for the three different temperatures studied and the results are tabulated in Table 4.6. If all of the OH was fully recycled the intercept of these Stern-Volmer plots can be extrapolated to give a Φ_{OH} of 1 at zero pressure (no collisional stabilisation occurring and $k_{O2}/k_{N2} = 0$). However, this result was not seen and an intercept significantly greater than 1 was measured from all the experiments. This suggests that a fraction of the acetaldehyde + OH is generating a product which does not regenerate OH in the presence of O_2 at low total pressures. One explanation for this would be chemically activated decomposition of acetyl (R4.7e).

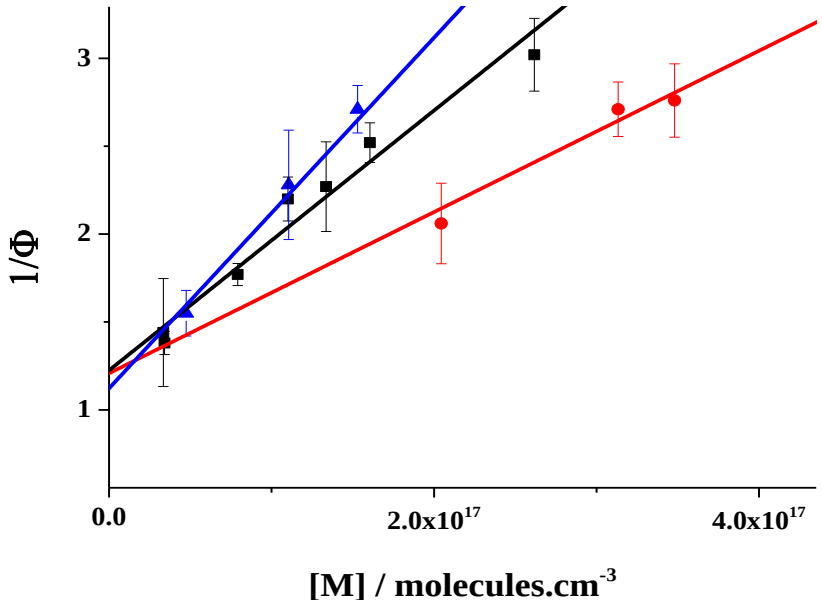

Figure 4.14: Stern Volmer plots of the reciprocal of the OH yield vs total pressure of nitrogen. (▲) = 212 K, (■) = 298 K, (●) = 385 K.

Table 4.6: Results from the kinetic studies of OH recycling from R4.7

Temperature / K	$10^{11}k_1$/ cm^3 s^{-1} [a]	Intercept of Stern Volmer plot	Intercept Range	SV Gradient/ 10^{-18} cm^3
212	2.07 ± 0.31[b]	1.20	1.33 1.06	9.09 ± 0.67[c]
298	1.35 ± 0.13	1.18	1.23 1.13	7.57 ± 0.16
385	1.27 ± 0.24	1.20	1.36 1.04	4.53 ± 0.26

a – Bimolecular rate coefficient for reaction in N_2 in the absence of oxygen.
b – Error is 95% confidence interval.
c – Error at 68% confidence interval.

All the results from this study are shown in Table 4.6, the bimolecular rate coefficients measured for R4.7 are in good agreement with the previous work in literature (Sander et al., 2011). As previously stated, the *y*-intercept of the Stern-Volmer plots are equal to the reciprocal of the OH yield ($1/\Phi_{OH}$). Therefore, the results from these experiments suggest that ~84% of the OH is recycled, implying a methyl radical yield of $Y_{CH3} \approx (16 \pm 3)$ %, this is within error of the value determined from the PIMS technique.

4.4.2 Master Equation Calculations

To complement the experimental results, Master equation calculations were performed (by R. Shannon), these also give a significant methyl radical yield. Initially these calculations were done using a purely statistical distribution of energy (i.e. the energy distributed according to the number of energy states in of both the products respectively). When the

master equation calculations were performed in this manner the dissociation of the activated CH_3CO radical was over predicted because most of the exothermicity is distributed into the acetyl species (12 modes vs. 3 modes). These calculations lead to a methyl radical yield of 83%. To model the experimental data, it was found that the amount of energy deposited in the CH_3CO needed to be reduced. A prior distribution of the vibrational energy was used alter allocation of exothermicity until a dissociation yield of ~18% was obtained (Y_{CH3} comparable to experimental value). The prior energy distributions used for the calculation at low pressures (p = 1.5 Torr) can be seen in Figure 4.15.

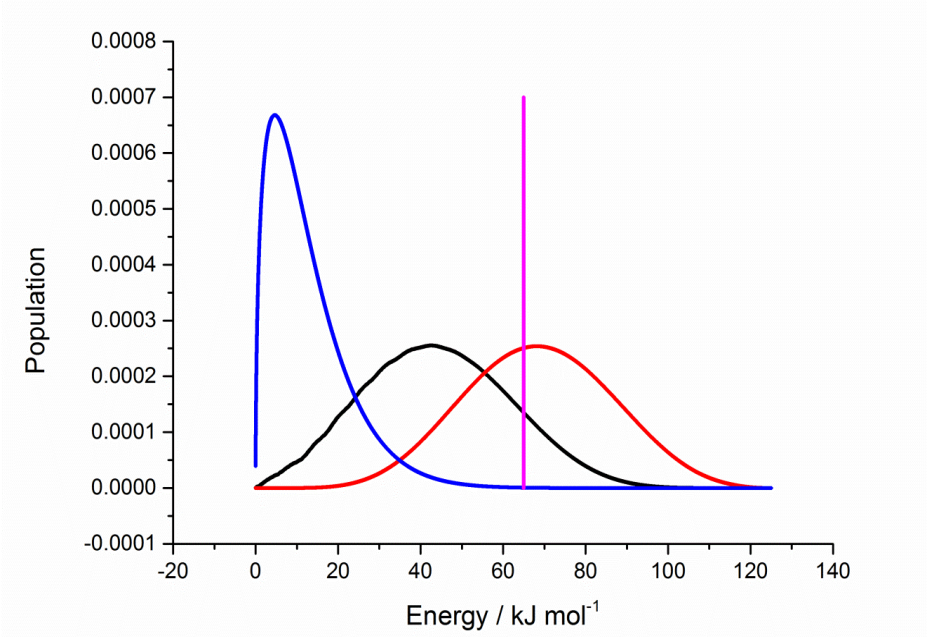

Figure 4.15: Energy distributions in acetyl (black line), H_2O (red line) and in translational motion of the fragments (blue line) calculated using a prior distribution calculation modified to give ~18% acetyl fragmentation at 1.5 Torr He and 298 K. The pink line indicates 52% of the total reaction exothermicity (124.9 kJ mol^{-1}) which is the proportion of the energy measured to be apportioned into the H_2O (Butkovskaya and Setser, 2000). Figure from Howes et al. (2016), work of R. Shannon.

The pressure dependence of acetyl decomposition was also probed using MESMER (R. Shannon). Notably, the calculated pressure dependence of the reaction was not large and a $Y_{CH3} \approx$ 14% at 760 Torr was estimated, assuming a Y_{CH3} = 18% ($p \approx$ 0 Torr), Figure 4.16. Admittedly, this may be a slight overestimation of the methyl yield at low pressures; however, it is thought that Y_{CH3} at 760 Torr would still be > 10%, if a zero pressure methyl yield of 15% was used.

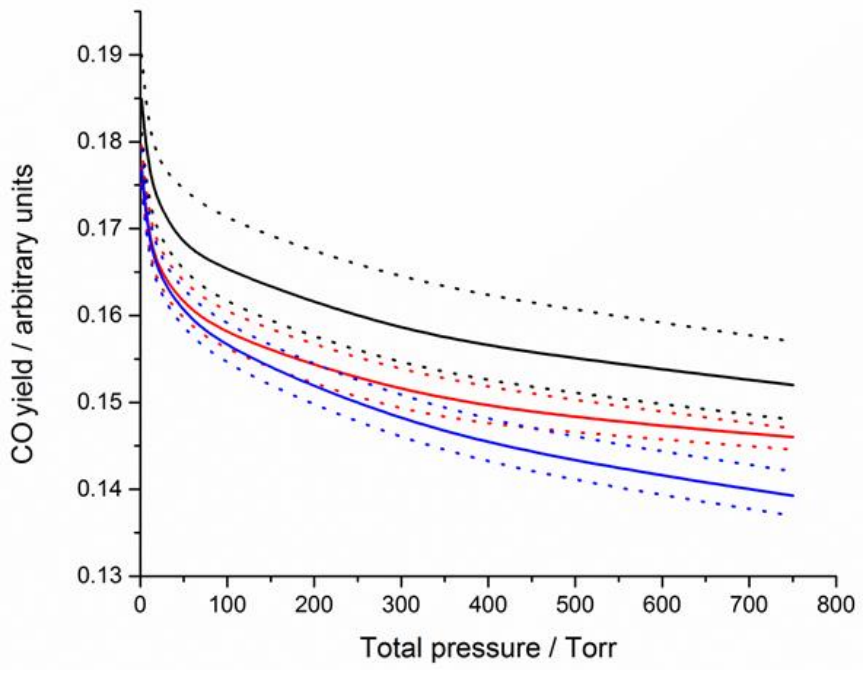

Figure 4.16: Calculated CO yields using MESMER as a function of pressure with three bath gases, He (black), N_2 (red) and air (blue). The dotted lines indicate the uncertainty of these calculations. Figure from Howes et al., (2016), work of R. Shannon.

4.5 Concluding Remarks

Both the PIMS study and the OH recycling technique generate consistent results giving zero pressure yields of 10% < Y_{CH3} < 20%. In addition to this pressure dependent Master equation calculations have been performed which predict significant methyl radical yields at 760 Torr. These results are in agreement with a majority of previous product studies and suggest that an abstraction reaction is the dominant mechanism. However, these results also conflict with the classical model of an abstraction process by predicting the formation of methyl radicals from a chemically activated channel. In addition to this the methyl yield determined do not agree with the majority of those previously in literature, which put an upper limit of Y_{CH3} = 5% (Wang et al., 2003, Cameron et al., 2002). Owing to these discrepancies in methyl radical yields we have tried to ensure that our PIMS results are not subject to systematic errors by using a variety of OH precursors and repeating the experiments under a range of different conditions (e.g. coated or uncoated walls, different detectors, wide range of acetaldehyde concentrations and OH precursors). Literature values for OH and Cl rate coefficients with acetaldehyde were reproducible using the PIMS apparatus. In addition a complementary LIF study has also been completed; the results from this study also suggest similar methyl radical yields. The thorough nature of the work presented provides strong evidence for the chemically activated channel hypothesised.

The qualitative data on the PIMS methyl yields clearly shows an enhanced CH_3:CH_3CO signal ratio for the acetaldehyde + OH reaction. This does not prove the methyl radicals are

exclusively generated from acetyl fragmentation. However, the time-resolved correlation between the kinetics of the methyl and acetyl radicals does suggest that these radicals are being generated from the same source, this is predicted by R4.7e.

There are other possible origins of methyl radicals, for example if insufficient water was added, then acetaldehyde can compete with water for the $O(^1D)$ produced from photolysis:

$$O(^1D) + CH_3CHO \rightarrow CH_3 + \text{co-products} \qquad \text{(R4.23)}$$

However, the fast timescale of $O(^1D)$ chemistry means that methyl radicals produced in this way will appear as an 'instant' growth rather than on the same time scale as acetyl radicals. In addition to this, the yield of methyl radicals determined would be dependent on acetaldehyde concentration and this was not observed experimentally.

Interference from vibrationally 'hot' OH was also investigated; the reaction also suggests an [acetaldehyde] dependency which was not observed experimentally. The results from the modelling of these reaction channels implies that the dominant source of methyl radicals is the chemically activated decomposition of acetyl radicals.

To complement this work an indirect kinetic study to measure OH recycling was also performed. For these experiments the intercept measured on the Stern Volmer plot was greater than 1. This suggests that the reaction does not fully recycle OH radicals. There are two reaction channels that lead to only partial OH recycling R4.7d and R4.7e. However, the work done by Butkovskaya et al. (2004) puts an upper limit of 7.5% on the yield of CH_2CHO radical formation; as the fraction of OH not recycled is ~16% the reaction channel R4.7d cannot fully account for the increased intercept on the Stern-Volmer plots (Butkovskaya et al., 2004). This suggests that R4.7e must contribute to non-recycling of OH radicals observed in the PLP-LIF experiments. It should be noted that R4.7d may actually lead to OH recycling, R4.24, meaning R4.7d may contribute to the fraction of OH recycled.

$$CH_2CHO + O_2 \rightarrow OH + HCHO + CO \qquad \text{(R4.24)}$$

This channel (R4.24) could account for the results of D'Anna et al. who observed a 10% yield of HCHO and CO in a chamber study at 760 Torr. However, the observed yield of HCHO and CO is greater than the initial vinoxy yield measured (~5%) from study by Butkovskaya et al. (2004), again, suggesting the presence of an additional reaction channel.

Two studies probing the CH_3CHO + OH reaction previously looked for methyl radicals. Wang et al. used IR absorption to monitor the production of ground vibrational state methyl radicals from reaction and observed a prompt methyl signal was observed attributed to reaction to the reaction of $O(^1D)$ + acetaldehyde (Wang et al., 2003). The work done by Cameron et al. used UV transient absorption spectroscopy to monitor both the formation of

acetyl (R4.7a) and methyl radicals (R4.7b) simultaneously. The study concluded that the primary reaction channel was R4.7a and acetyl yield of 0.93 ± 0.18 was determined (Cameron et al., 2002). A small yield of methyl radicals was also observed. However, the formation of the methyl radicals was on a considerably longer timescale than acetyl production, so Cameron et al. (2002) postulated a radical-radical type mechanism for CH_3 production as a feasible source of methyl radicals. Both these studies put an upper limit of 5% on the yield of methyl radicals. However, UV transient absorption spectroscopy is not an ideal method for observing small yields of methyl as there is significant overlap of acetyl and methyl signals. The PIMS technique allows for a more accurate time-resolved yield of methyl radical to be calculated.

In recent years there has been a lot of work done to try and identify the reaction mechanism of R4.7a. The general consensus is that H atom abstraction from the acyl carbon is the exclusive mechanism for the acetaldehyde + OH reaction. The work presented in this chapter does not disagree with these studies and gives an alternative pathway for methyl radical formation which complements this mechanism. However, although mechanistically R4.7e rationalizes the experimental observations well, the dynamics of the reaction suggest that acetyl decomposition should not be energetically favourable. Indeed, the transition state species of R4.7 is depicted in Figure 4.17.

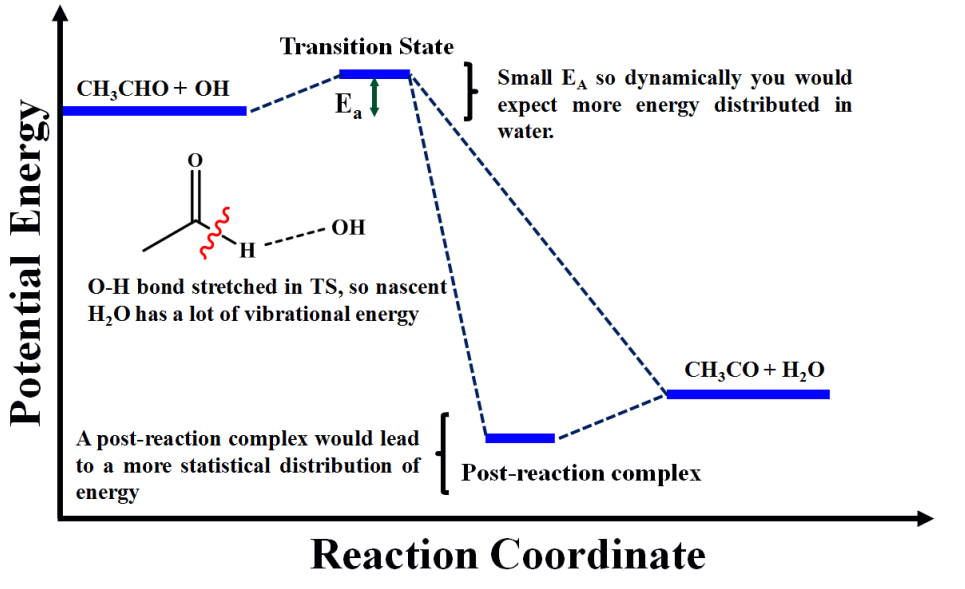

Figure 4.17: A schematic of the potential energy surface of the CH_3CHO + OH reaction, including a hypothesized post-reaction complex.

From Figure 4.17 it can be seen that newly formed OH bond is hypothesised to be stretched at the transition state; which suggests that, dynamically, more of the energy should be stored in the nascent H_2O molecule. If this were the case, it is unlikely that any of the nascent acetyl radicals formed would have sufficient energy to decompose to CH_3 and CO

radicals (R4.7e). However, D'Anna et al. (2003) resolve this issue by postulating the formation of a post-reaction complex, which would allow for a more statistical redistribution of the energy; this in turn would means that (some of) the nascent acetyl radicals formed would have sufficient energy to undergo the activated decomposition, yielding CH_3.

The observation of methyl radicals from the acetaldehyde + OH reaction does indicate some unusual features in the mechanism of this reaction, although, as R4.7e is only a minor channel its atmospheric implications will likely be minimal. However, MESMER calculations do suggest that the yield of methyl radicals at 760 Torr may still be significant, Y_{CH3} = 14%, if a zero pressure methyl yield of 18% is used (Figure 4.16). However, if reaction R4.7e does occur within the troposphere it could affect the composition of the atmosphere in several ways. Firstly, higher concentrations of methyl radicals would lead to an increase in formaldehyde in polluted environments (R4.25-4.27). Secondly, the concentration of peroxyacetyl radicals will be smaller, and hence a lower concentration of PAN would be expected; this will impact upon the transportation of NO_x into remote environments.

$$CH_3 + O_2 \rightarrow CH_3O_2 \quad \text{(R4.25)}$$

$$CH_3O_2 + NO \rightarrow CH_3O + NO_2 \quad \text{(R4.26)}$$

$$CH_3O + O_2 \rightarrow HCHO + HO_2 \quad \text{(R4.27)}$$

The implications of this study could be important in low temperature combustion, as aldehydes are known to be important intermediates in oxyfuel combustion regimes (Marinov, 1999). Moreover, acetyl radical oxidation is hypothesised to be significant channel in low temperature combustion (T < 600 K) of oxyfuels (Lee et al., 2002). However, the work from this study suggests that acetyl decomposition (R4.7e) may be amplified under low temperature combustion conditions and will therefore reduce the yield of $CH_3C(O)O_2$ radicals formed. It should be noted that acetyl peroxy radicals are thought to be key intermediates which lead to chain branching and chain branching steps drive all low temperature combustion processes (R4.8,R2.28-4.29).

$$CH_3CO + O_2 \rightarrow CH_3C(O)O_2 \quad \text{(R4.8)}$$

$$CH_3C(O)O_2 + CH_3CHO \rightarrow CH_3C(O)O_2H + CH_3CO \quad \text{(R4.28)}$$

$$CH_3C(O)O_2H \rightarrow CH_3 + CO_2 + OH \quad \text{(R4.29)}$$

4.6 References

AIR QUALITY EXPERT GROUP, A. 2011. Road Transport Biofuels: Impact on UK Air Quality - Department for Environment, Food and Rural Affairs. United Kingdom: Crown.
ATKINSON, R. 2000. Atmospheric chemistry of VOCs and NO_x. *Atmospheric Environment,* 34**,** 2063-2101.
ATKINSON, R., BAULCH, D., COX, R., CROWLEY, J., HAMPSON JR, R., KERR, J., ROSSI, M. & TROE, J. 2001. Summary of evaluated kinetic and photochemical data for atmospheric chemistry. *IUPAC***,** 1-56.
ATKINSON, R., BAULCH, D. L., COX, R. A., CROWLEY, J. N., HAMPSON, R. F., HYNES, R. G., JENKIN, M. E., ROSSI, M. J. & TROE, J. 2006. Evaluated kinetic and photochemical data for atmospheric chemistry: Volume II - gas phase reactions of organic species. *Atmospheric Chemistry and Physics,* 6**,** 3625-4055.
BAASANDORJ, M., PAPANASTASIOU, D. K., TALUKDAR, R. K., HASSON, A. S. & BURKHOLDER, J. B. 2010. $(CH_3)_3COOH$ (tert-butyl hydroperoxide): OH reaction rate coefficients between 206 and 375 K and the OH photolysis quantum yield at 248 nm. *Physical Chemistry Chemical Physics,* 12**,** 12101-12111.
BAEZA-ROMERO, M. T., GLOWACKI, D. R., BLITZ, M. A., HEARD, D. E., PILLING, M. J., RICKARD, A. R. & SEAKINS, P. W. 2007. A combined experimental and theoretical study of the reaction between methylglyoxal and OH/OD radical: OH regeneration. *Physical Chemistry Chemical Physics,* 9**,** 4114-4128.
BUTKOVSKAYA, N. I., KUKUI, A. & LE BRAS, G. 2004. Branching fractions for H_2O forming channels of the reaction of OH radicals with acetaldehyde. *Journal of Physical Chemistry A,* 108**,** 1160-1168.
BUTKOVSKAYA, N. I. & SETSER, D. W. 2000. Infrared chemiluminescence study of the reaction of hydroxyl radical with acetaldehyde and the secondary reactions of acetyl radical with NO_2, OH, and H. *Journal of Physical Chemistry A,* 104**,** 9428-9435.
CALVERT, J. G. & MADRONICH, S. 1987. Theoretical-study of the initial products of the atmospheric oxidation of hydrocarbons *Journal of Geophysical Research-Atmospheres,* 92**,** 2211-2220.
CALVERT, J. G. M., A; ORLANDO, J. J; PILLING, M. J AND WALLINGTON, T. J 2011. The Mechanisms of Atmospheric Oxidation of the Oxygenates. New York: Oxford University Press.
CAMERON, M., SIVAKUMARAN, V., DILLON, T. J. & CROWLEY, J. N. 2002. Reaction between OH and CH_3CHO - Part 1. Primary product yields of CH_3 (296 K), CH_3CO (296 K), and H (237-296 K). *Physical Chemistry Chemical Physics,* 4**,** 3628-3638.
CARR, S. A., BAEZA-ROMERO, M. T., BLITZ, M. A., PILLING, M. J., HEARD, D. E. & SEAKINS, P. W. 2007. OH yields from the CH_3CO+O_2 reaction using an internal standard. *Chemical Physics Letters,* 445**,** 108-112.
CORRÊA, S. M., ARBILLA, G., MARTINS, E. M., QUITÉRIO, S. L., DE SOUZA GUIMARÃES, C. & GATTI, L. V. 2010. Five years of formaldehyde and acetaldehyde monitoring in the Rio de Janeiro downtown area – Brazil. *Atmospheric Environment,* 44**,** 2302-2308.
D'ANNA, B., BAKKEN, V., BEUKES, J. A., NIELSEN, C. J., BRUDNIK, K. & JODKOWSKI, J. T. 2003. Experimental and theoretical studies of gas phase NO_3 and OH radical reactions with formaldehyde, acetaldehyde and their isotopomers. *Physical Chemistry Chemical Physics,* 5**,** 1790-1805.
DILLON, T., HOROWITZ, A. & CROWLEY, J. 2008. The atmospheric chemistry of sulphuryl fluoride, SO_2F_2. *Atmospheric Chemistry and Physics,* 8**,** 1547-1557.
DUNLEA, E. J. & RAVISHANKARA, A. R. 2004. Measurement of the rate coefficient for the reaction of $O(^1D)$ with H_2O and re-evaluation of the atmospheric OH production rate. *Physical Chemistry Chemical Physics,* 6**,** 3333-3340.
EPA, U. S. 1987. "Health Assessment Docuement for Acetaldehyde". *In:* DEVELOPMENT, O. O. H. A. E. A. O. O. R. A. (ed.). Washington D.C.: United States Environmental Protection Agency.
FORTNER, E. C., ZHENG, J., ZHANG, R., BERK KNIGHTON, W., VOLKAMER, R. M., SHEEHY, P., MOLINA, L. & ANDRÉ, M. 2009. Measurements of Volatile Organic

Compounds Using Proton Transfer Reaction – Mass Spectrometry during the MILAGRO 2006 Campaign. *Atmos. Chem. Phys.,* 9**,** 467-481.
GLOWACKI, D. R., LIANG, C.-H., MORLEY, C., PILLING, M. J. & ROBERTSON, S. H. 2012a. MESMER: an open-source master equation solver for multi-energy well reactions. *The Journal of Physical Chemistry A,* 116**,** 9545-9560.
GLOWACKI, D. R., LOCKHART, J., BLITZ, M. A., KLIPPENSTEIN, S. J., PILLING, M. J., ROBERTSON, S. H. & SEAKINS, P. W. 2012b. Interception of Excited Vibrational Quantum States by O_2 in Atmospheric Association Reactions. *Science,* 337**,** 1066-1069.
HOWES, N., LOCKHART, J., BLITZ, M., SHANNON, R., CARR, S., VARGA, T., HEARD, D. & SEAKINS, P. 2016. Observation of a new channel in the abstraction reaction of OH with Acetaldehyde. University of Leeds.
IANNI, J. C. 2002. Kintecus , Windows Version 2.80, 2002, www.kintecus.com.
JENKIN, M. E. & CLEMITSHAW, K. C. 2000. Ozone and other secondary photochemical pollutants: chemical processes governing their formation in the planetary boundary layer. *Atmospheric Environment,* 34**,** 2499-2527.
KARAVALAKIS, G., DURBIN, T. D., SHRIVASTAVA, M., ZHENG, Z., VILLELA, M. & JUNG, H. 2012. Impacts of ethanol fuel level on emissions of regulated and unregulated pollutants from a fleet of gasoline light-duty vehicles. *Fuel,* 93**,** 549-558.
LEE, J., CHEN, C.-J. & BOZZELLI, J. W. 2002. Thermochemical and Kinetic Analysis of the Acetyl Radical ($CH_3C•O$) + O_2 Reaction System. *The Journal of Physical Chemistry A,* 106**,** 7155-7170.
LEE, L. C. 1980. OH(A $^2\Sigma^+ \rightarrow X\ ^2\Pi i$) yield from H_2O photodissociation in 1050–1370 Å. *The Journal of Chemical Physics,* 72**,** 4334-4340.
LIGHTFOOT, P. D., KIRWAN, S. P. & PILLING, M. J. 1988. Photolysis of acetone at 193.3 nm. *The Journal of Physical Chemistry,* 92**,** 4938-4946.
LOCKHART, J. 2014. *The Role of Chemical Activation in the Formation and Loss of Atmospheric Carbonyl Species.* PhD, University of Leeds.
LOCKHART, J., BLITZ, M., HEARD, D., SEAKINS, P. & SHANNON, R. 2013. Kinetic Study of the OH + Glyoxal Reaction: Experimental Evidence and Quantification of Direct OH Recycling. *The Journal of Physical Chemistry A,* 117**,** 11027-11037.
M.T. BAEZA-ROMERO, M. A. B., S. CARR, N. HOWES, M.J. PILLING, P.W. SEAKINS 2016. Acetyl and methyl yields in the 248 nm photolysis of several acetyl compounds. Leeds: University of Leeds.
MARINOV, N. M. 1999. A detailed chemical kinetic model for high temperature ethanol oxidation. *International Journal of Chemical Kinetics,* 31**,** 183-220.
MCCABE, D. C., SMITH, I. W. M., RAJAKUMAR, B. & RAVISHANKARA, A. R. 2006. Rate coefficients for the relaxation of OH by O_2 at temperatures from 204–371 K and by N_2O from 243–372K. *Chemical Physics Letters,* 421**,** 111-117.
MILLET, D. B., GUENTHER, A., SIEGEL, D. A., NELSON, N. B., SINGH, H. B., DE GOUW, J. A., WARNEKE, C., WILLIAMS, J., EERDEKENS, G., SINHA, V., KARL, T., FLOCKE, F., APEL, E., RIEMER, D. D., PALMER, P. I. & BARKLEY, M. 2010. Global atmospheric budget of acetaldehyde: 3-D model analysis and constraints from in-situ and satellite observations. *Atmospheric Chemistry and Physics,* 10**,** 3405-3425.
MORRIS, E. D., STEDMAN, D. H. & NIKI, H. 1971. Mass spectrometric study of reactions of hydroxyl radical with ethylene, propylene, and acetaldehyde in a discharge-flow system. *Journal of the American Chemical Society,* 93**,** 3570-3580.
NIVEN, R. K. 2005. Ethanol in gasoline: environmental impacts and sustainability review article. *Renewable and Sustainable Energy Reviews,* 9**,** 535-555.
NORTON, T. S. & DRYER, F. L. 1992. An experimental and modeling study of ethanol oxidation-kinetics in an atmospheric-pressure flow reactor. *International Journal of Chemical Kinetics,* 24**,** 319-344.
POLANYI, J. C. 1987. Some concepts in reaction dynamics. *Science,* 236**,** 680-690.
POULOPOULOS, S. G., SAMARAS, D. P. & PHILIPPOPOULOS, C. 2001. Regulated and unregulated emissions from an internal combustion engine operating on ethanol-containing fuels. *Atmospheric Environment,* 35**,** 4399-4406.
READ, K. A., CARPENTER, L. J., ARNOLD, S. R., BEALE, R., NIGHTINGALE, P. D., HOPKINS, J. R., LEWIS, A. C., LEE, J. D., MENDES, L. & PICKERING, S. J. 2012.

Multiannual Observations of Acetone, Methanol, and Acetaldehyde in Remote Tropical Atlantic Air: Implications for Atmospheric OVOC Budgets and Oxidative Capacity. *Environmental Science & Technology,* 46**,** 11028-11039.
SANDER, S. P., FRIEDL, R. R., ABBATT, J. P. D., BARKER, J., GOLDEN, D. M., KOLB, C. E., KURYLO, M. J., MOORTGAT, G. K., WINE, P. H., HUIE, R. E. & ORKIN, V. L. 2011. Chemical kinetics and photochemical data for use in atmospheric studies - Evaluation 17. Pasadena CA: Jet Propulsion Laboratory.
SANDER, S. P. F., R. R.; ABBATT, J. P. D.; BARKER, J.; GOLDEN, D. M.; KOLB, C. E.; KURYLO, M. J.; MOORTGAT, G. K.; WINE, P. H.; HUIE, R. E.ET AL. . 2011. "Chemical Kinetics and Photochemical Data for Use in Atmospheric Studies - Evaluation 17,"
SEMMES, D. H., RAVISHANKARA, A. R., GUMP-PERKINS, C. A. & WINE, P. H. 1985. Kinetics of the reactions of hydroxyl radical with aliphatic aldehydes. *International Journal of Chemical Kinetics,* 17**,** 303-313.
SHANNON, R. J., BLITZ, M. A., GODDARD, A. & HEARD, D. E. 2013. Accelerated chemistry in the reaction between the hydroxyl radical and methanol at interstellar temperatures facilitated by tunnelling. *Nat Chem,* 5**,** 745-749.
SHANNON, R. J., TAYLOR, S., GODDARD, A., BLITZ, M. A. & HEARD, D. E. 2010. Observation of a large negative temperature dependence for rate coefficients of reactions of OH with oxygenated volatile organic compounds studied at 86-112 K. *Physical Chemistry Chemical Physics,* 12**,** 13511-13514.
TYNDALL, G. S., ORLANDO, J. J., KEGLEY-OWEN, C. S., WALLINGTON, T. J. & HURLEY, M. D. 1999. Rate coefficients for the reactions of chlorine atoms with methanol and acetaldehyde. *International Journal of Chemical Kinetics,* 31**,** 776-784.
TYNDALL, G. S., STAFFELBACH, T. A., ORLANDO, J. J. & CALVERT, J. G. 1995. Rate coefficients for the reactions of OH radicals with methylgloxal and acetaldehyde *International Journal of Chemical Kinetics,* 27**,** 1009-1020.
VANDENBERK, S. & PEETERS, J. 2003. The reaction of acetaldehyde and propionaldehyde with hydroxyl radicals: experimental determination of the primary H_2O yield at room temperature. *Journal of Photochemistry and Photobiology A: Chemistry,* 157**,** 269-274.
VASVARI, G., SZILAGYI, I., BENCSURA, A., DOBE, S., BERCES, T., HENON, E., CANNEAUX, S. & BOHR, F. 2001. Reaction and complex formation between OH radical and acetone. *Physical Chemistry Chemical Physics,* 3**,** 551-555.
WANG, J. J., CHEN, H. B., GLASS, G. P. & CURL, R. F. 2003. Kinetic study of the reaction of acetaldehyde with OH. *Journal of Physical Chemistry A,* 107**,** 10834-10844.
WAYNE, R. P., BARNES, I., BIGGS, P., BURROWS, J. P., CANOSA-MAS, C. E., HJORTH, J., LE BRAS, G., MOORTGAT, G. K., PERNER, D., POULET, G., RESTELLI, G. & SIDEBOTTOM, H. 1991. The nitrate radical: physics, chemistry, and the atmosphere. *Atmospheric Environment. Part A. General Topics,* 25**,** 1-203.
WINER, A., ATKINSON, R. & PITTS, J. N. 1984. Gaseous Nitrate Radical: Possible Nighttime Atmospheric Sink for Biogenic Organic Compounds. *Science,* 224**,** 156-159.
WOLLENHAUPT, M., CARL, S. A., HOROWITZ, A. & CROWLEY, J. N. 2000. Rate coefficients for reaction of OH with acetone between 202 and 395 K. *Journal of Physical Chemistry A,* 104**,** 2695-2705.

Results - Part ii

Criegee Intermediate Reactivity

Chapter V:

An Introduction to Criegee Intermediates

5. An Introduction to Criegee Intermediates

Since the first direct observation of C_1 Criegee intermediate (CI) reactivity with the trace gas species SO_2 and NO_2 was reported by Welz et al. (2012), there has been an increased interest in understanding both the characteristics of these elusive species, and their reactivity within the atmosphere. The subsequent chapters of this thesis (Chapters VI and VII) are concerned about the reactivity of both the C_1 and C_2 Criegee intermediates with various atmospheric trace gases, however prior to discussing these results, some background information about these species is necessary. Therefore, the aim of this chapter is to give a detailed overview of CI production (*via* alkene ozonolysis) and to discuss what is currently understood about the nature of the C_1 and C_2 Criegee intermediates.

5.1 Alkene Ozonolysis and Criegee Intermediates

5.1.1 Formation and Properties of Criegee Intermediates

Criegee intermediates (CIs) are carbonyl oxide biradicals and have the generic formula $\cdot CR_2OO\cdot$. CIs were first hypothesised as long ago as 1949 by their namesake Rudolph Criegee, however, the first direct observation of a CI (confirming their existence) was only made as recently as 2008 (Taatjes et al., 2008).

Criegee biradicals are primarily produced in the atmosphere *via* alkene ozonolysis, with the proposed mechanism being a [3+2] cycloaddition across the double bond of the alkene forming a cyclic 1,2,3-trioxolane intermediate, known as a primary ozonide (Criegee and Wenner, 1975). This bond-forming reaction is highly exothermic (~250 kJ mol^{-1}) leaving the ozonide with a large excess of internal energy, causing it to rapidly decompose by one of two different channels; both reaction pathways involve the homolytic cleavage of an O – O bond and the remaining C – C bond, leading to the formation of two pairs of products; a carbonyl molecule and a Criegee intermediate (Figure 5.1). Criegee intermediates are all biradicals, meaning they contain two unpaired electrons and it has been hypothesised that this may give them zwitterionic characteristics (Su et al., 2013).

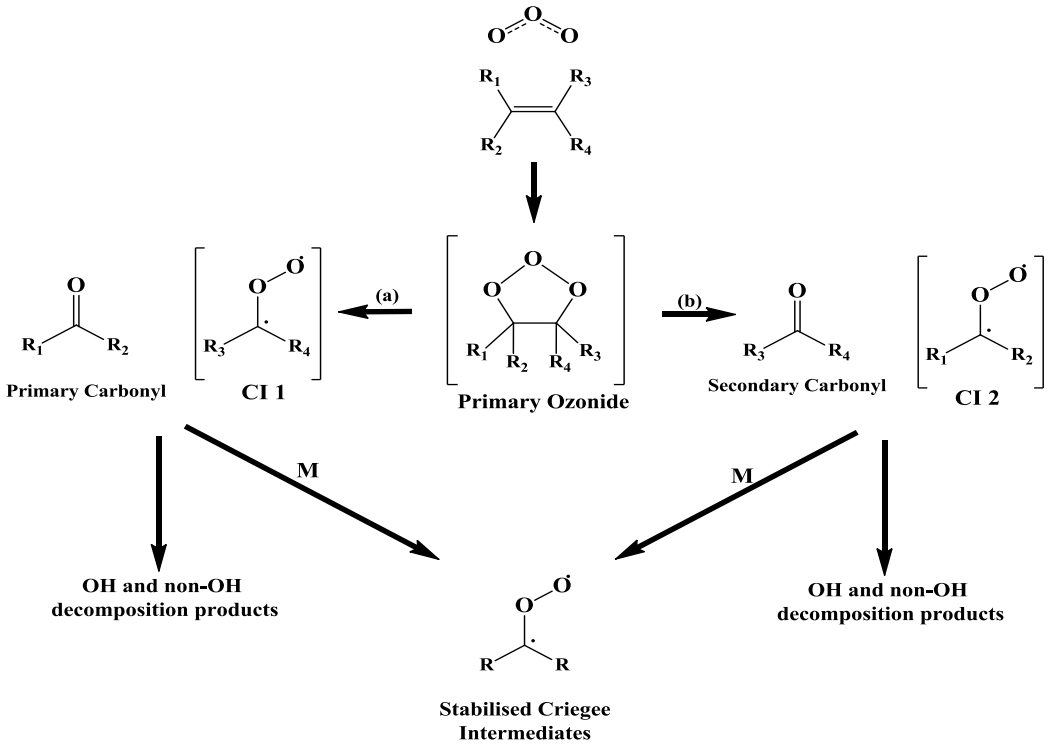

Figure 5.1: Alkene ozonolysis: formation of a primary ozonide *via* addition of ozone to the alkene double bond, decomposition to form a CI and Primary Carbonyl species and subsequent decomposition / stabilization of the excited CI. Adapted from Malkin (2010).

All CIs can either be described as unsubstituted or substituted. The former describes only the simplest CI possible, $\cdot CH_2OO\cdot$, also commonly known as the C_1 Criegee intermediate. The C_1 Criegee is produced during the ozonolysis of ethene and terminal alkenes (i.e. 1-alkenes). Larger (substituted) Criegee intermediates, which contain more than one carbon atom can be described as being either monosubstituted ($R\cdot CHOO\cdot$) or disubstituted ($RR'\cdot COO\cdot$). In monosubstituted CIs, like CH_3CHOO (known as the C_2 Criegee intermediate), there are two different Criegee conformations formed; *syn*- and *anti*-conformers (Figure 5.2). Interestingly, the zwitterionic nature of the Criegee intermediates hinders rotation around the central carbon atom causing the conformers exhibit distinct chemical properties. In fact, calculations predict that the barrier to interconversion between the conformers is ~160 kJ mol^{-1} (Kuwata et al., 2010). The final class of CIs are known as disubstituted Criegee intermediates, they differ from monosubstituted CIs as both end group are carbon-based chains (Johnson and Marston, 2008). However, as the results described in the subsequent chapters concern only the C_1 and C_2 Cis, so the focus of this chapter will be on the unsubstituted and monosubstituted CIs.

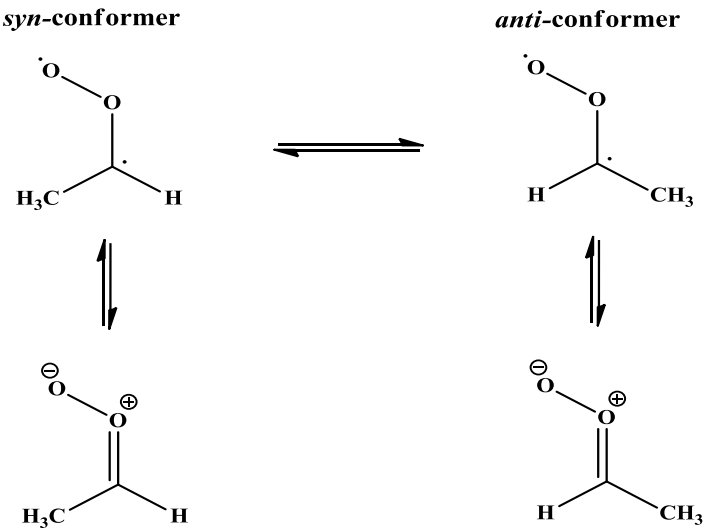

Figure 5.2: A schematic to highlight the difference between *syn*- and *anti*- Criegee conformers.

Once formed, Criegee intermediates can undergo two different types of reactions in the atmosphere: the first is decomposition and comes as a result of the excited nature of the nascent Criegee intermediate, which has sufficient energy to break up the CI (though not enough to fragment stable carbonyl species). Their alternative atmospheric fate is stabilisation *via* collisional quenching, forming stabilised Criegee intermediates (SCIs); the SCIs formed are thought to react readily with a number of trace gases in the atmosphere (Taatjes et al., 2012).

For a long time the Criegee intermediate eluded detection, it is now thought that this was because CIs are formed slowly but react quickly, meaning low steady state concentrations are yielded from alkene ozonolysis experiments. The first direct measurement of the Criegee intermediate was made in 2008 at the Advanced Light Source (ALS) in Berkley, California. In this study, the C_1 Criegee was generated from the chlorine-initiated, gas-phase oxidation of dimethyl sulphoxide (DMSO, R5.1-5.2) and was monitored using synchrotron photoionization mass spectrometry.

$$(CH_3)_2SO + Cl \rightarrow CH_3SOCH_2 + HCl \quad \text{(R5.1)}$$

$$CH_3SOCH_2 + O_2 \rightarrow CH_3SO + CH_2OO \quad \text{(R5.2)}$$

However, one problem with this method of Criegee production is that there is interference in the detection of the C_1 Criegee from CH_2S, as both have a mass of $m/z = 46$. To differentiate between these two species and to irrefutably prove the existence of CIs, the photoionization wavelength (supplied by the ALS synchrotron) was varied as these two species were known to have different ionization potentials. Figure 5.3 shows difference between the $m/z = 46$ photoionization efficiency spectrum from DMSO oxidation and the reference CH_2S spectrum (Ruscic and Berkowitz, 1993). It is clear to see that at photon

energies above ~10 eV there is an extra species being ionized and contributing to the signal at *m/z* = 46 in DMSO oxidation, this signal is attributed to the ionization of CH_2OO (Taatjes et al., 2008). This was (and still is) considered a major breakthrough within the field of atmospheric chemistry.

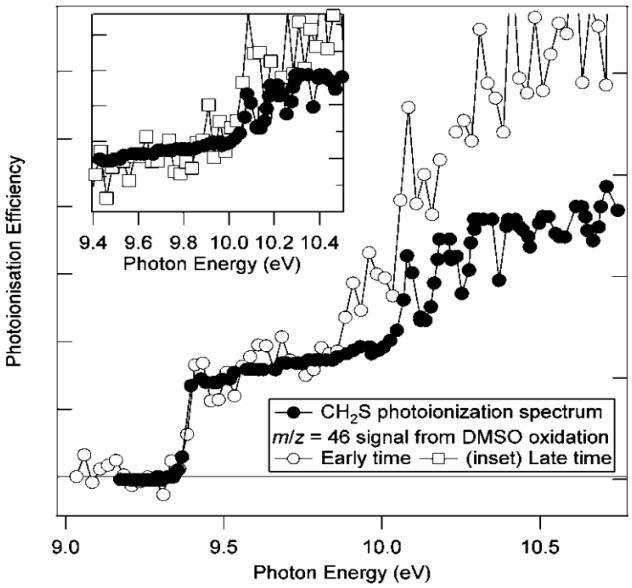

Figure 5.3: Photoionization efficiency (PIE) spectrum of the *m/z* = 46 signal observed in the Cl-initiated oxidation of DMSO, compared to the PIE spectrum of CH_2S. The difference between the two spectra is thought to be ionization of the C_1Criegee intermediate (Taatjes et al., 2008).

Although this study allowed for the detection of the Criegee intermediates, it still did not yield large enough concentrations of the CH_2OO, and hence a high enough signal-to-noise ratio, for the kinetic measurements to be made (Taatjes et al., 2008). In fact, it was not until a different CH_2OO precursor was discovered that any further (direct) measurements were made. However, an alternative route to CH_2OO formation has since been developed using diiodomethane photolysis in the presence of oxygen:

$$CH_2I_2 + h\nu\ (\lambda = 248\ \text{nm}) \rightarrow CH_2I + I \qquad \text{(R5.3)}$$

$$CH_2I + O_2 + M \rightarrow ICH_2OO + M \qquad \text{(R5.4a)}$$

$$CH_2I + O_2 \rightarrow CH_2O + IO \qquad \text{(R5.4b)}$$

$$CH_2I + O_2 \rightarrow CH_2OO + I \qquad \text{(R5.4c)}$$

Similar reaction schemes using diiodomethane photolysis had previously been used in studies exploring the importance of halogen chemistry at the marine boundary layer (Enami et al., 2004, Eskola et al., 2006, Gravestock et al., 2010); however, at this time the products of this reaction scheme were not fully understood and its potential as a precursor for CH_2OO was not appreciated.

This method was first exploited for CI production by Welz et al. (2012) using the same PIMS detection pioneered by Taatjes et al. (2008), critically this method of Criegee intermediate generation forms significant concentrations of CH_2OO, and hence allowed for kinetics of CIs with various atmospherically relevant species to be probed (Welz et al., 2012). This was a vital discovery as it gave an insight as to the atmospheric fates of these elusive biradical species. Note: the atmospheric reactions of CIs are discussed in more detail in the subsequent section of this chapter (Section 5.2).

Following this discovery there have been a number different studies which have utilised this method of CI production to develop a variety of techniques to directly monitor CH_2OO (Beames et al., 2012, Sheps, 2013, Lee, 2015, Su et al., 2013). The work by Beames et al. (2012) probed the B ← X transition of CH_2OO species with UV absorption coupled to a jet-cooled photoionization mass spectrometry (λ = 118 nm). Using this technique an absorption spectrum was determined by measuring the UV-induced depletion at m/z = 46 (CH_2OO was the only possible isomer present at photoionization wavelength, 10.5 eV, for m/z = 46). From these experiments a broad absorption between 280-420 nm was observed, with a maximum measured at 335 nm. Furthermore, work by Lehman et al. (2013) observed that the dissociation energy for the $CH_2OO \rightarrow HCHO$ reaction was greater than typically required for O-O single bonds (e.g. CH_3OOH); however this can be explained by the conjugated (zwitterionic) nature of the Criegee intermediate. Sheps (2013) used time-resolved cavity-enhanced absorption spectroscopy to produce a UV spectrum of the C_1 Criegee intermediate; in addition, the time-resolved capabilities of this set-up used made it possible for the kinetics of reaction between $CH_2OO + SO_2$ to be measured (Sheps, 2013). Both these studies yielded similar UV spectra for CH_2OO, however, under the thermal conditions of Sheps work the maxima is shifted longer wavelengths (Figure 5.4).

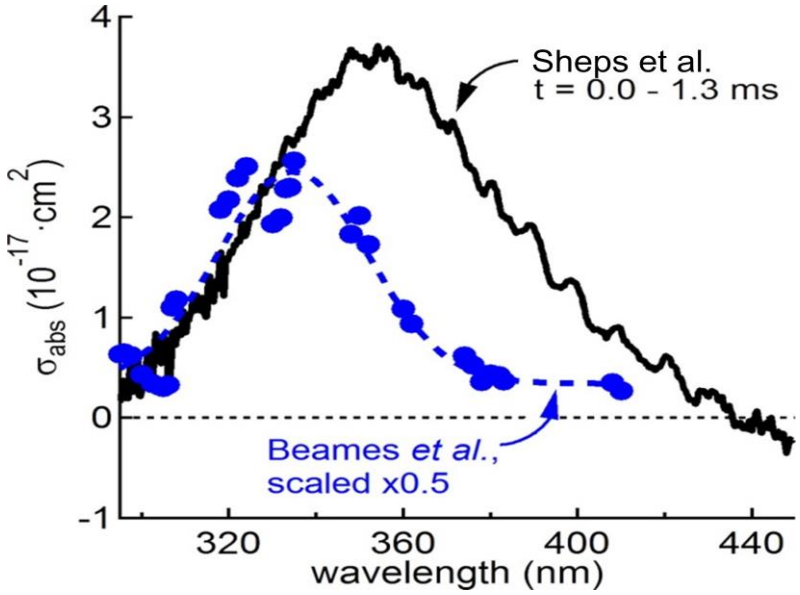

Figure 5.4: UV absorption spectrum of CH_2OO. Blue symbols and the dotted line are the action spectrum of Beames et al., scaled by 0.5 to match the absorption spectrum on the high-energy side (Sheps, 2013).

In other work, *via* the same production scheme, Su et al. (2013) used FTIR to map the infra-red spectrum of CH_2OO. Using this technique some interesting observations about the C_1 Criegee intermediate were made; it was noted that O-O stretching mode of CH_2OO was ~200 cm^{-1} weaker than the corresponding mode in CH_3OO. Conversely, the C-O stretching mode is significantly larger than its counter-part in CH_3OO. The weakening of the O-O bond and the strengthened C-O are a distinct indicator of zwitterionic nature of Criegee intermediates.

5.2 Criegee Intermediates in the Atmosphere

Having a full appreciation of alkene ozonolysis and the subsequent Criegee intermediates formed is thought to be crucial to our understanding of, not only, tropospheric ozone budgets, but also tropospheric levels of volatile organic compounds, organic acids and even secondary organic aerosols (Marston, 2012). Therefore, even though Criegee intermediates have only a low atmospheric concentration ([CI] ≈ 10^3 – 10^5 molecule cm^{-3} (Percival et al., 2013, Newland et al., 2015)), it is still imperative that we have a thorough understanding of the reactions of CIs.

It is understood that nascent activated CIs can undergo several different reactions upon formation; these reactions can be separated into two categories: unimolecular reactions and collisional stabilisation. It should be noted that both these reaction channels can yield OH, but do so on different timescales (Liu et al., 2014).

5.2.1 Unimolecular Reactions

All nascent Criegee intermediates are hypothesised to undergo similar unimolecular reactions, where it is postulated that dissociation of the CI will yield radical fragments that include OH (Figure 5.5) (Vereecken et al., 2012, Donahue et al., 2011). This makes understanding the chemistry of the Criegee intermediate of fundamental importance as the OH radical is known to largely control the oxidising capacity of the lower atmosphere (see Chapter I, Section 1.3).

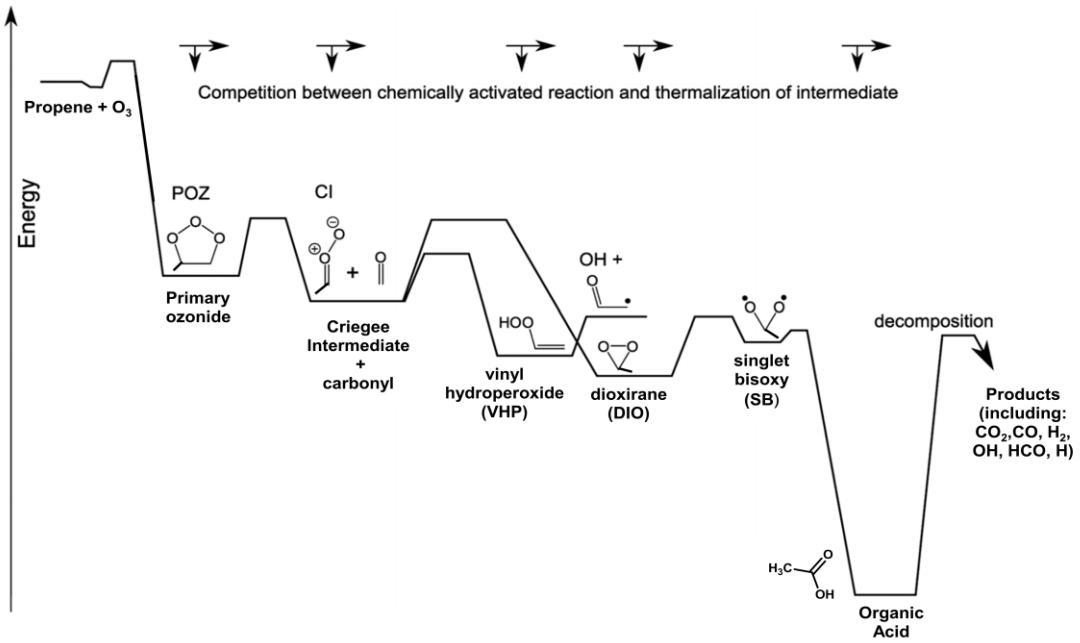

Figure 5.5: A simplified reaction mechanism showing formation of Criegee intermediates and their subsequent reactions. Adapted from Vereecken et al., 2012.

In fact, alkene ozonolysis is thought to be an important source of night-time OH, expected to be responsible for approximately 65% of OH formed at night (Geyer et al., 2003). Furthermore, modelled data from the PUMA campaign has indicated that in an urban setting (Birmingham, UK) alkene ozonolysis will contribute significantly to the formation of HO_x radicals. This is particularly apparent in winter as solar photolysis rates are low and it was calculated that the majority of OH (~95 %) is produced *via* the ozonolysis of alkenes (Harrison et al., 2006, Heard et al., 2004).

Figure 5.5 shows the two primary channels for unimolecular reactions of the Criegee. The first of these reactions channel is caused by tautomerisation of the Criegee intermediate to an excited vinyl hydroperoxide (VHP) species which decomposes readily form a vinyloxyl radical and OH. This channel was first postulated by Niki et al. (1987) and is proposed to be the major reaction channel for *syn*-substituted CIs as it has a lower energy barrier than the dioxirane channel. However, it is only a minor channel for the C_1 Criegee as the isomerisation to the VHP species occurs favourably *via* a five-membered transition state,

but not a four-membered one (Figure 5.6). It should be noted that the C_1 Criegee intermediate does not actually form the vinyl hydroperoxide species shown in Figure 5.6b, but instead form a single carbon dioxirane species (Kroll et al., 2002).

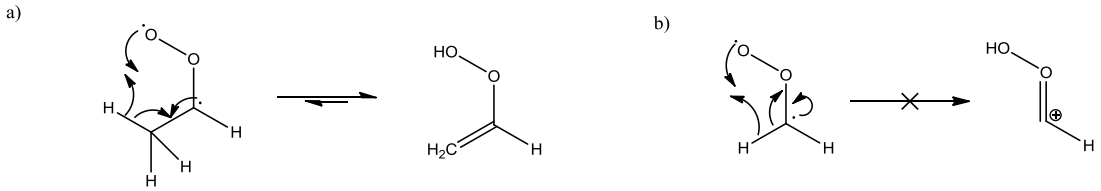

Figure 5.6: a) highlights CI and the subsequent VHP readily tautomerise via a 5-membered cyclic transition state; b) indicates the same mechanism cannot occur for the C1 Criegee.

Alternatively, Criegee decomposition can go via a dioxirane channel which eventually reacts to form an energetically stable ester, RC(O)OR' or a carboxylic acid. Indirect evidence has been documented which suggests that this decomposition channel is significant for the C_1 Criegee species. Work done by Horie and Moortgat (1998) identified a number of the products from this reaction pathway using Fourier transform infrared spectroscopy (FTIR) including CO_2, CO and formic acid, the simplest of the organic acids. More interestingly, the intermediate dioxirane species has also been observed for ethene ozonolysis using microwave spectroscopy at low temperatures (Lovas and Suenram, 1977). This work included an isotopic labelling study (^{13}C and ^{2}H) to distinguish the dioxirane species from other possible products (such as performic acid).

A number of studies have independently identified OH as a product of C_1 Criegee dissociation using both direct (Kroll et al., 2001) and indirect (Atkinson et al., 1992) monitoring techniques. The direct measurements were done using an off-resonance laser induced fluorescence (LIF) technique to detect the hydroxyl radicals at approximately 308 nm (Wennberg et al., 1994). It should be noted that the production of OH was an unexpected result as the C_1 Criegee cannot tautomerise to a vinyl hydroperoxide and so was expected to have an OH yield (Y_{OH}) of zero. To establish the mechanism of OH production a series of experiments were done using monosubstituted *anti*-Criegee intermediates, which were also assumed to have small OH yields (Kroll et al., 2002). For this study the CIs were selectively deuterated in the *anti*-position to investigate how this affected the Y_{OH}, and give insight to the reaction mechanism (Figure 5.7).

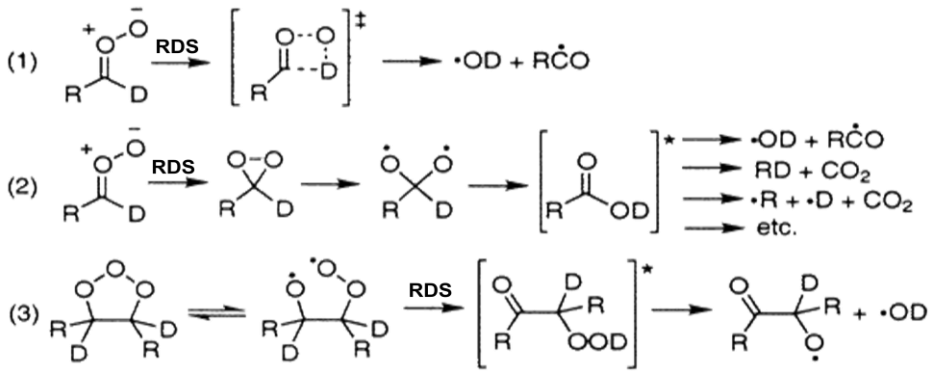

Figure 5.7: A schematic to show the possible mechanisms of OD formation. From Kroll et al., (2002).

The results of these experiments showed that the total $Y_{OH/OD}$ was unchanged upon deuteration of the Criegee. This result suggests that the second reaction pathway is the most likely as the rate determining processes in reactions (1) and (3) involve a hydrogen/deuterium transfer, and therefore should be altered by the deuteration of the CI. However, for reaction (2) the rate determining step involves a ring-closure and should independent of any kinetic isotope effects (Kroll et al., 2002).

One final interesting trend of the unimolecular reactions of the Criegee intermediates is the observed dependence of OH yields upon alkene size. As can be seen in Table 5.1, for the smaller CIs the IUPAC (2005) recommended OH yields are relatively small (for CH_2OO, $Y_{OH} = 0.16$); however, for the larger Criegee intermediates the Y_{OH} is close to unity (Johnson and Marston, 2008, Liu et al., 2014). Notably, this is that it is in accordance with the postulated mechanism for Criegee dissociation. For the C_1 Criegee, OH is only expected to be a minor product due to the high stability of formic acid; hence a low Y_{OH} would be predicted. Conversely, for the larger CIs, OH is expected to be a major product because the isomerism to the excited vinyl hydroperoxide is favoured, a species which will readily decompose generating an OH radical. It should be noted that this is only a general trend and there are anomalies and certain aspects have been overlooked, for example, the varying Y_{OH} of *Z*- and *E*- conformers of 2-butene.

Table 5.1: IUPAC-recommended OH yields for the alkene ozonolysis reactions (2005).

Alkene	*OH yields*
Ethene	0.16 ± 0.03
Propene	0.34 ± 0.02
Isoprene	0.26 ± 0.03*****
Z-2-butene	0.33 ± 0.04
E-2-butene	0.64 ± 0.09
2-Methylpropene	0.62 ± 0.07
2-Methyl-2-butene	0.88 ± 0.07
2,3-Dimethyl-2-butene	0.90 ± 0.13

***Result made since the publication of the IUPAC-recommended OH yields (Malkin et al., 2010a).**

5.2.2 Stabilised Criegee Intermediates

The alternative atmospheric fate of a Criegee intermediate formed from alkene ozonolysis is collisional quenching to form a stabilised Criegee intermediate (SCI). Experimental observations suggest that approximately 15 – 60 % of CIs formed are stabilised (Rickard et al., 1999, Hasson et al., 2001a, Drozd and Donahue, 2011, Berndt et al., 2012); the work done by Donahue and co-workers confirmed, unsurprisingly, that the yield of stabilised Criegee intermediates (Y_{SCI}) is pressure dependent. In addition to this, two of the studies noted a correlation between the Y_{SCI} and the size / complexity of the respective CI: typically, the simpler CIs appear to be more readily stabilised (Rickard et al., 1999, Hasson et al., 2001a). This result is somewhat counterintuitive as it might be expected that smaller CIs which have fewer bonds to distribute the nascent energy between would decompose more readily and hence have a lower Y_{SCI}. However, this result can be justified if the stabilised Criegee intermediate yields are compared to the OH yields from unimolecular CI reaction (Hasson et al., 2001a); upon comparison there is a clear anti-correlation between Y_{SCI} and Y_{OH}. Unsurprisingly, the same logic used to account for Criegee intermediate OH yields can be extended to rationalise Y_{SCI}.

Figure 5.5 highlights that Criegee intermediates can tautomerise to form a vinyl hydroperoxide (VHP) *via* the mechanism shown in Figure 5.5. From the ozonolysis of propene a pair of *syn*- and *anti*- monosubstituted Criegee intermediates are formed. As shown in Figure 5.6a tautomerisation of the *syn*-C_2 Criegee occurs passing through a five-membered cyclic transition state, form a VHP, giving the C_2 Criegee a moderate Y_{OH} of 0.34 ± 0.02. However, the formation of this vinyl hydroperoxide directly reduces the yield of stabilised Criegee intermediates ($Y_{SCI} \approx 0.2$) (Alam, 2011). This is further highlighted in Figure 5.6b, for the C_1 Criegee tautomerisation is far less favourable as four-membered cyclic transition state is more strained and the VHP is unstable. Therefore, giving the C_1 Criegee only a small yield of hydroxyl radicals ($Y_{OH} = 0.16 \pm 0.03$), but a significant yield of stabilised CIs ($Y_{SCI} = 0.39 \pm 0.08$) (Hasson et al., 2001b).

5.2.2.1 SCI Reactivity

Measurements of stabilised CI reactions have been made over a number of years (Johnson et al., 2001, Fenske et al., 2000). However, until recently (Welz et al., 2012) these measurements were all indirect as the Criegee biradical itself was not being monitored. From the work of Johnson et al. (2001) it was assumed that the reactions of SCI with trace species were generally very slow and therefore, due to its high atmospheric concentration, H_2O would be the sole sink for the SCIs in the troposphere. However, recent work has demonstrated an enhanced reactivity for both the C_1 and C_2 Criegee intermediates towards

certain atmospheric trace gases (Welz et al., 2012, Taatjes, 2013, Welz et al., 2014). It is clear that more work is needed to understand the significance of these more minor atmospheric channels and in the following chapters selected SCI reactions have been investigated. In Chapter VI the reactivity of C_1 and C_2 SCIs with SO_2 and NO_2 is probed and in Chapter VII the reactivity of CH_2OO with formic and acetic acid is examined. In both of these subsequent chapters the experiments were performed using the PLP-PIMS technique described in Chapter II.

Lastly, the subsequent chapters of this thesis when discussing the reactivity of the 'stabilised Criegee intermediates', they are often referred to as simply 'Criegee intermediates'. It should be noted that this is just an abbreviation and all of the kinetics and mechanistics discussed actually describe the reactivity of C_1 and C_2 stabilised Criegee intermediates.

5.3 References

2005. IUPAC Subcommittee for Gas Kinetic Data Evaluation, Data sheet Ox_VOC3_O3.
ALAM, M. S. 2011. *Total radical production and degradation products from Alkene Ozonolysis.* University of Birmingham.
ATKINSON, R., ASCHMANN, S. M., AREY, J. & SHOREES, B. 1992. Formation of OH radicals in the gas phase reactions of O_3 with a series of terpenes. *Journal of Geophysical Research: Atmospheres,* 97**,** 6065-6073.
BEAMES, J. M., LIU, F., LU, L. & LESTER, M. I. 2012. Ultraviolet Spectrum and Photochemistry of the Simplest Criegee Intermediate CH_2OO. *Journal of the American Chemical Society,* 134**,** 20045-20048.
BERNDT, T., JOKINEN, T., MAULDIN, R. L., PETÄJÄ, T., HERRMANN, H., JUNNINEN, H., PAASONEN, P., WORSNOP, D. R. & SIPILÄ, M. 2012. Gas-Phase Ozonolysis of Selected Olefins: The Yield of Stabilized Criegee Intermediate and the Reactivity toward SO_2. *The Journal of Physical Chemistry Letters,* 3**,** 2892-2896.
CRIEGEE, R. & WENNER, G. 1975. Ann. 1949, 564, 9.(b) Criegee, R. Ann. 1953, 583, 1.(c) Criegee, R. *Angew. Chem., Int. Ed,* 11**,** 745.
DONAHUE, N. M., DROZD, G. T., EPSTEIN, S. A., PRESTO, A. A. & KROLL, J. H. 2011. Adventures in ozoneland: down the rabbit-hole. *Physical Chemistry Chemical Physics,* 13**,** 10848-10857.
DROZD, G. T. & DONAHUE, N. M. 2011. Pressure Dependence of Stabilized Criegee Intermediate Formation from a Sequence of Alkenes. *The Journal of Physical Chemistry A,* 115**,** 4381-4387.
ENAMI, S., UEDA, J., GOTO, M., NAKANO, Y., ALOISIO, S., HASHIMOTO, S. & KAWASAKI, M. 2004. Formation of Iodine Monoxide Radical from the Reaction of CH2I with O2. *The Journal of Physical Chemistry A,* 108**,** 6347-6350.
ESKOLA, A. J., WOJCIK-PASTUSZKA, D., RATAJCZAK, E. & TIMONEN, R. S. 2006. Kinetics of the reactions of CH2Br and CH2I radicals with molecular oxygen at atmospheric temperatures. *Physical Chemistry Chemical Physics,* 8**,** 1416-1424.
FENSKE, J. D., HASSON, A. S., HO, A. W. & PAULSON, S. E. 2000. Measurement of Absolute Unimolecular and Bimolecular Rate Constants for CH_3CHOO Generated by the trans-2-Butene Reaction with Ozone in the Gas Phase. *The Journal of Physical Chemistry A,* 104**,** 9921-9932.
GEYER, A., BÄCHMANN, K., HOFZUMAHAUS, A., HOLLAND, F., KONRAD, S., KLÜPFEL, T., PÄTZ, H.-W., PERNER, D., MIHELCIC, D., SCHÄFER, H.-J., VOLZ-THOMAS, A. & PLATT, U. 2003. Nighttime formation of peroxy and hydroxyl radicals during the BERLIOZ campaign: Observations and modeling studies. *Journal of Geophysical Research: Atmospheres,* 108**,** n/a-n/a.
GRAVESTOCK, T. J., BLITZ, M. A., BLOSS, W. J. & HEARD, D. E. 2010. A Multidimensional Study of the Reaction $CH_2I + O_2$: Products and Atmospheric Implications. *ChemPhysChem,* 11**,** 3928-3941.
HARRISON, R., YIN, J., TILLING, R., CAI, X., SEAKINS, P., HOPKINS, J., LANSLEY, D., LEWIS, A., HUNTER, M. & HEARD, D. 2006. Measurement and modelling of air pollution and atmospheric chemistry in the UK West Midlands conurbation: Overview of the PUMA Consortium project. *Science of the Total Environment,* 360**,** 5-25.
HASSON, A. S., HO, A. W., KUWATA, K. T. & PAULSON, S. E. 2001a. Production of stabilized Criegee intermediates and peroxides in the gas phase ozonolysis of alkenes: 2. Asymmetric and biogenic alkenes. *Journal of Geophysical Research: Atmospheres,* 106**,** 34143-34153.
HASSON, A. S., ORZECHOWSKA, G. & PAULSON, S. E. 2001b. Production of stabilized Criegee intermediates and peroxides in the gas phase ozonolysis of alkenes: 1. Ethene, trans-2-butene, and 2,3-dimethyl-2-butene. *Journal of Geophysical Research: Atmospheres,* 106**,** 34131-34142.

HEARD, D. E., CARPENTER, L. J., CREASEY, D. J., HOPKINS, J. R., LEE, J. D., LEWIS, A. C., PILLING, M. J., SEAKINS, P. W., CARSLAW, N. & EMMERSON, K. M. 2004. High levels of the hydroxyl radical in the winter urban troposphere. *Geophysical Research Letters,* 31**,** n/a-n/a.

HORIE, O. & MOORTGAT, G. K. 1998. Gas-phase ozonolysis of alkenes. Recent advances in mechanistic investigations. *Accounts of chemical research,* 31**,** 387-396.

JOHNSON, D., LEWIN, A. G. & MARSTON, G. 2001. The Effect of Criegee-Intermediate Scavengers on the OH Yield from the Reaction of Ozone with 2-methylbut-2-ene. *The Journal of Physical Chemistry A,* 105**,** 2933-2935.

JOHNSON, D. & MARSTON, G. 2008. The gas-phase ozonolysis of unsaturated volatile organic compounds in the troposphere. *Chemical Society Reviews,* 37**,** 699-716.

KROLL, J. H., DONAHUE, N. M., CEE, V. J., DEMERJIAN, K. L. & ANDERSON, J. G. 2002. Gas-Phase Ozonolysis of Alkenes: Formation of OH from Anti Carbonyl Oxides. *Journal of the American Chemical Society,* 124**,** 8518-8519.

KROLL, J. H., HANISCO, T. F., DONAHUE, N. M., DEMERJIAN, K. L. & ANDERSON, J. G. 2001. Accurate, direct measurements of oh yields from gas-phase ozone-alkene reactions using an in situ LIF Instrument. *Geophysical Research Letters,* 28**,** 3863-3866.

KUWATA, K. T., HERMES, M. R., CARLSON, M. J. & ZOGG, C. K. 2010. Computational Studies of the Isomerization and Hydration Reactions of Acetaldehyde Oxide and Methyl Vinyl Carbonyl Oxide. *The Journal of Physical Chemistry A,* 114**,** 9192-9204.

LEE, Y.-P. 2015. Perspective: Spectroscopy and kinetics of small gaseous Criegee intermediates. *The Journal of Chemical Physics,* 143**,** 020901.

LEHMAN, J. H., LI, H., BEAMES, J. M. & LESTER, M. I. 2013. Communication: Ultraviolet photodissociation dynamics of the simplest Criegee intermediate CH_2OO. *The Journal of Chemical Physics,* 139**,** 141103.

LIU, Y., BAYES, K. D. & SANDER, S. P. 2014. Measuring Rate Constants for Reactions of the Simplest Criegee Intermediate (CH_2OO) by Monitoring the OH Radical. *The Journal of Physical Chemistry A.*

LOVAS, F. J. & SUENRAM, R. D. 1977. Identification of dioxirane (H_2COO) in ozone-olefin reactions via microwave spectroscopy. *Chemical Physics Letters,* 51**,** 453-456.

MALKIN, T. L. 2010. *Detection of free-radicals and other species to investigate atmospheric chemistry in the HIRAC chamber.* Thesis (Ph D), University of Leeds

MALKIN, T. L., GODDARD, A., HEARD, D. E. & SEAKINS, P. W. 2010. Measurements of OH and HO_2 yields from the gas phase ozonolysis of isoprene. *Atmos. Chem. Phys.,* 10**,** 1441-1459.

MARSTON, G. 2012. An Elusive Intermediate Gets Caught. *Science,* 335**,** 178-179.

NEWLAND, M. J., RICKARD, A. R., ALAM, M. S., VEREECKEN, L., MUÑOZ, A., RÓDENAS, M. & BLOSS, W. J. 2015. Kinetics of stabilised Criegee intermediates derived from alkene ozonolysis: reactions with SO_2, H_2O and decomposition under boundary layer conditions. *Physical Chemistry Chemical Physics,* 17**,** 4076-4088.

NIKI, H., MAKER, P. D., SAVAGE, C. M., BREITENBACH, L. P. & HURLEY, M. D. 1987. FTIR spectroscopic study of the mechanism for the gas-phase reaction between ozone and tetramethylethylene. *The Journal of Physical Chemistry,* 91**,** 941-946.

PERCIVAL, C. J., WELZ, O., ESKOLA, A. J., SAVEE, J. D., OSBORN, D. L., TOPPING, D. O., LOWE, D., UTEMBE, S. R., BACAK, A., M C FIGGANS, G., COOKE, M. C., XIAO, P., ARCHIBALD, A. T., JENKIN, M. E., DERWENT, R. G., RIIPINEN, I., MOK, D. W. K., LEE, E. P. F., DYKE, J. M., TAATJES, C. A. & SHALLCROSS, D. E. 2013. Regional and global impacts of Criegee intermediates on atmospheric sulphuric acid concentrations and first steps of aerosol formation. *Faraday Discussions,* 165**,** 45-73.

RICKARD, A. R., JOHNSON, D., MCGILL, C. D. & MARSTON, G. 1999. OH Yields in the Gas-Phase Reactions of Ozone with Alkenes. *The Journal of Physical Chemistry A,* 103**,** 7656-7664.

RUSCIC, B. & BERKOWITZ, J. 1993. Photoionization mass spectrometry of CH_2S and HCS. *The Journal of Chemical Physics,* 98**,** 2568-2579.

SHEPS, L. 2013. Absolute Ultraviolet Absorption Spectrum of a Criegee Intermediate CH_2OO. *The Journal of Physical Chemistry Letters,* 4**,** 4201-4205.
SU, Y.-T., HUANG, Y.-H., WITEK, H. A. & LEE, Y.-P. 2013. Infrared absorption spectrum of the simplest Criegee intermediate CH_2OO. *Science,* 340**,** 174-176.
TAATJES, C. A., MELONI, G., SELBY, T. M., TREVITT, A. J., OSBORN, D. L., PERCIVAL, C. J. & SHALLCROSS, D. E. 2008. Direct observation of the gas-phase Criegee intermediate (CH_2OO). *Journal of the American Chemical Society,* 130**,** 11883-11885.
TAATJES, C. A., WELZ, O., ESKOLA, A. J., SAVEE, J. D., OSBORN, D. L., LEE, E. P. F., DYKE, J. M., MOK, D. W. K., SHALLCROSS, D. E. & PERCIVAL, C. J. 2012. Direct measurement of Criegee intermediate (CH_2OO) reactions with acetone, acetaldehyde, and hexafluoroacetone. *Physical Chemistry Chemical Physics,* 14**,** 10391-10400.
TAATJES, C. W., O; ESKOLA, A; SAVEE, J; SCHEER, A; SHALLCROSS, D; ROTAVERA, B; LEE, E;DYKE, J; MOK, D; OSBORN, D AND PERCIVAL C 2013. Direct Measurements of Conformer-Dependent Reactivity of the Criegee Intermediate CH_3CHOO. *Science,* 340.
VEREECKEN, L., HARDER, H. & NOVELLI, A. 2012. The reaction of Criegee intermediates with NO, RO_2, and SO_2, and their fate in the atmosphere. *Physical Chemistry Chemical Physics,* 14**,** 14682-14695.
WELZ, O., ESKOLA, A. J., SHEPS, L., ROTAVERA, B., SAVEE, J. D., SCHEER, A. M., OSBORN, D. L., LOWE, D., MURRAY BOOTH, A., XIAO, P., ANWAR H. KHAN, M., PERCIVAL, C. J., SHALLCROSS, D. E. & TAATJES, C. A. 2014. Rate Coefficients of C_1 and C_2 Criegee Intermediate Reactions with Formic and Acetic Acid Near the Collision Limit: Direct Kinetics Measurements and Atmospheric Implications. *Angewandte Chemie International Edition,* 53**,** 4547-4550.
WELZ, O., SAVEE, J. D., OSBORN, D. L., VASU, S. S., PERCIVAL, C. J., SHALLCROSS, D. E. & TAATJES, C. A. 2012. Direct Kinetic Measurements of Criegee Intermediate (CH_2OO) Formed by Reaction of CH_2I with O_2. *Science,* 335**,** 204-207.
WENNBERG, P. O., COHEN, R. C., HAZEN, N. L., LAPSON, L. B., ALLEN, N. T., HANISCO, T. F., OLIVER, J. F., LANHAM, N. W., DEMUSZ, J. N. & ANDERSON, J. G. 1994. Aircraft-borne, laser-induced fluorescence instrument for the in situ detection of hydroxyl and hydroperoxyl radicals. *Review of Scientific Instruments,* 65**,** 1858-1876.

Chapter VI:

Kinetic Studies of Criegee Intermediates with SO_2 and NO_2

6. Kinetic Studies of Criegee Intermediates with SO_2 and NO_2

Recent, direct studies have shown that the reactivity of Criegee intermediates (CIs) with the trace gas species SO_2 and NO_2 are several orders of magnitude greater than earlier evaluations (Welz et al., 2012, Johnson et al., 2001). Within this thesis chapter is a detailed investigation of the reactivity of both the C_1 and C_2 Criegee intermediates with both SO_2 and NO_2. The results of this study also indicate an enhanced Criegee reactivity with CI + SO_2 rate coefficients of k_{C1SO2} = (3.8 ± 0.2) × 10^{-11} cm^3 $molecule^{-1}$ s^{-1} and k_{C2SO2} = (1.8 ± 0.3) × 10^{-11} cm^3 $molecule^{-1}$ s^{-1} obtained for the C_1 and *syn*-C_2 Criegee intermediates respectively; these measurements are in good agreement with other recent measurements (Welz et al., 2012, Taatjes, 2013). Furthermore, some information about the products of the C_2 CI reaction are also reported, as by using the PIMS technique it was possible to observe a species at *m/z* = 44 forming on the same time-scale as the CI decay. The products observed are suspected to be acetaldehyde; notably, the co-products of this reaction is SO_3 and suggests that the reaction could lead to the oxidation of sulphur from the $S_{(IV)}$ state to the $S_{(VI)}$ state in the atmosphere.

Additionally, enhanced rate coefficients of k_{C1NO2} = (1.2 ± 0.3) × 10^{-12} cm^3 $molecule^{-1}$ s^{-1} and k_{C2NO2} = (7.0 ± 1.5) × 10^{-13} cm^3 $molecule^{-1}$ s^{-1} for the C_1 and *syn*-C_2 Criegee intermediates were determined. Significantly, these evaluations are approximately half an order of magnitude lower than the rate coefficients measured in Welz et al. (2012) and Taatjes et al. (2013); however, the value of k_{C1NO2} does compare well to the work of Stone et al. (2014) measured using an indirect laser induced fluorescence technique.

6.1 CH_2OO Reactivity

6.1.1 Atmosphere reactions of the C_1 Criegee intermediate

Despite their low tropospheric concentration ([CI] ≈ 10^3-10^5 molecule cm^{-3}) (Percival et al., 2013, Newland et al., 2015), stabilized Criegee intermediates have been proposed as potential atmospheric oxidants (Mauldin et al., 2012). Prior to the work of Welz et al. (2012), it was understood that the C_1 Criegee exhibited limited reactivity towards other trace gases in the atmosphere. Therefore, it was assumed that the dominant sink of CH_2OO in the troposphere would be its removal by H_2O (due to the abundance of H_2O in the atmosphere). However, recent work has measured enhanced reactivity for both the C_1 + C_2 Criegee intermediates towards certain atmospheric trace gases. In the work of Welz et al. (2012), the kinetics of the C_1 Criegee intermediate was directly probed using photoionization mass spectroscopy (PIMS) at low pressure (*p* = 4 Torr). During these

experiments, the Criegee intermediates were generated by the photolysis of CH_2I_2 in the presence of O_2 (R6.1-6.2).

$$CH_2I_2 + h\nu \rightarrow CH_2I + I \quad \text{(R6.1)}$$

$$CH_2I + O_2 \rightarrow CH_2OO + I \quad \text{(R6.2)}$$

In addition to verifying the existence of the C_1 Criegee intermediate, this study also demonstrated that CH_2OO reacts much more readily with certain trace gases (NO_2 and SO_2) than previously thought (Welz et al., 2012). In fact, the rate coefficient of CH_2OO with SO_2, k_{C1SO2}, was found to be approximately four orders of magnitude larger than those previously documented in the literature (see Table 6.1). This result not only highlighted the potential importance of SCI reactions in the atmosphere, but also that there is much still unknown about the chemistry of these biradicals.

Table 6.1: A selection of bimolecular rate coefficients for the reaction of CH_2OO + SO_2 as a function of pressure. Errors are ±1σ for Welz et al. (2012), Liu et al. (2014) and Stone et al. (2014) and 25% for work by Johnson et al. (2001).

Pressure / Torr	k_{C1SO2} / 10^{-14} cm^3 molecule^{-1} s^{-1}	Reference
760	0.4 ± 0.1	(Johnson et al., 2001)
4	3900 ± 700	(Welz et al., 2012)
1.5[a]	3600 ± 500	(Stone et al., 2014)
50	3620 ± 100	(Liu et al., 2014)
250	3680 ± 200	(Stone et al., 2014)

[a] Measurements taken using PIMS in Leeds; the impetus for this body of work.

The enhanced reactivity of the C_1 Criegee intermediate has since been verified by a number of different studies, including work done at the University of Leeds (Stone et al., 2014). In this study, the kinetics of the C_1 CI were measured using two different methods: laser-induced fluorescence (LIF) spectroscopy of HCHO; and pulsed laser photolysis – photoionization mass spectrometry (as described in Chapter II), where the Criegee intermediate was directly monitored. In Stone et al. (2014), it was demonstrated that the Criegee reactivity was independent of pressure for the reactions of NO_2 and SO_2. There was also no significant change in the yield of HCHO as a function of pressure; this is in keeping with the observed independence of the kinetics as a function of pressure. This result indicates that there is no collisional stabilisation of the secondary ozonide intermediates (SOZ) for the SO_2 and NO_2 reaction with the C_1 Criegee intermediate (Figure 6.1). As a 100% yield of HCHO was measured for these reactions, 100% yields of SO_3 and NO_3 are also implied (Stone et al., 2014). Furthermore, the result from the C_1 CI + SO_2 study agrees with the theoretical calculations of Vereecken et al. (2012) and indicate that this reaction could therefore play a small, but significant, role in the oxidation of SO_2 to SO_3 and may lead to H_2SO_4 production in forested areas (Figure 6.1) (Mauldin et al., 2012).

NO_3 has previously been identified as a product from the $CH_2OO + NO_2$ reaction (Ouyang et al., 2013); this reaction is also of particular interest given the importance of the NO_2 in the troposphere (see Chapter I, Section 1.3.2) and the importance of nitrate radical as a night time oxidant (Brown and Stutz, 2012).

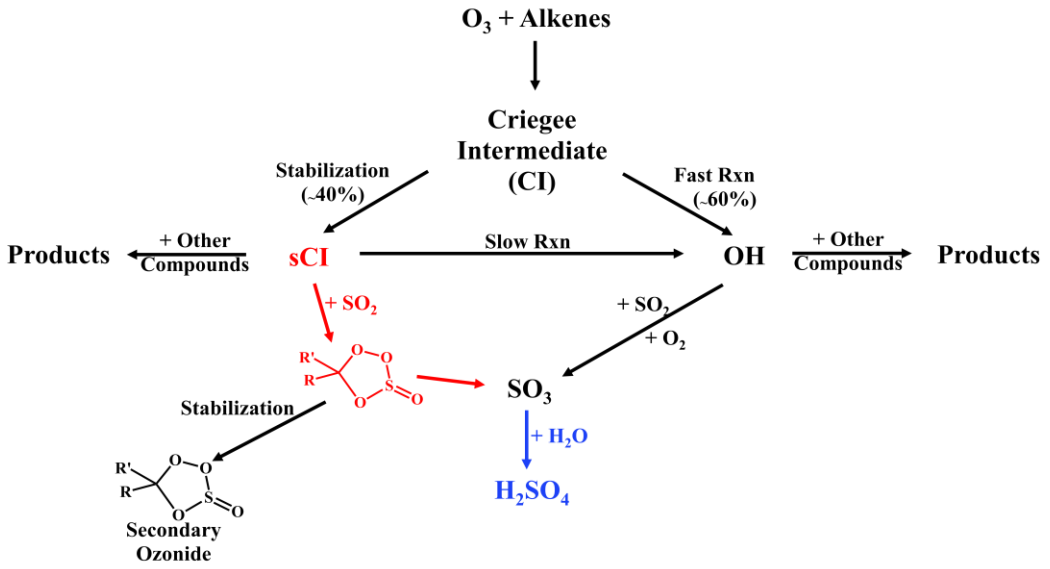

Figure 6.1: Proposed atmospheric oxidation mechanism for Criegee intermediates, adapted from Mauldin et al. (2012). The reaction highlighted in red is the reaction investigated in this chapter, the blue reaction is highlights the pathway leading to H_2SO_4 formation.

To fully comprehend the atmospheric importance of the trace gases on Criegee chemistry, the reactivity of the C_1 Criegee intermediate towards water and its dimer must be understood. Previously it was assumed that any thermalised Criegee intermediates would react with water, or its dimer, $(H_2O)_2$. However, the enhanced reactivity of SCIs with trace gas species could potentially be important as minor sinks for SCIs in the atmosphere. From previous studies it was understood that the CI + H_2O reaction was extremely slow, $k_{C1H2O} \leq 1 \times 10^{-16}$ cm^3 molecule^{-1} s^{-1} (Johnson et al., 2001). However, in light of the work done by Welz et al. (2012) this reaction has, again, been the focus of many studies in recent years; amongst these is a series of experiments completed using the EUPHORE reaction chamber (Newland et al., 2015). In this study alkene ozonolysis was used to investigate Criegee reactivity and a relative rate approach was employed to probe the CI + H_2O reaction by comparing O_3 loss rates at different relative humidities (at a constant $[SO_2]$). This study estimates a $CH_2OO + H_2O$ rate coefficient of $(1.3 \pm 0.4) \times 10^{-15}$ cm^3 molecule^{-1} s^{-1}, and $(5.5 \pm 7.0) \times 10^{-13}$ cm^3 molecule^{-1} s^{-1} for the reaction between CH_2OO and the water dimer, $(H_2O)_2$ (Newland et al., 2015). These rate coefficients are significant larger than those previously measured and suggest that the removal by water is the main sink for CIs in the atmosphere. Work by Lewis et al. (2015) directly monitored the C_1 Criegee biradicals using a time-resolved UV absorption (TRUVA) at $T = 295$ K. In this study a quadratic

dependence on [H_2O] was observed, which suggests that the sole sink for C_1 CIs is the reaction with the water dimer (Lewis et al., 2015); a rate coefficient of $k_{C1+(H2O)2} = (4.0 \pm 1.2) \times 10^{-12}$ cm^3 molecule^{-1} s^{-1} was measured for this reaction (Figure 6.2). In addition to this, a strong negative temperature dependence has been observed for the $CH_2OO + (H_2O)_2$ reaction, which implies that the rate coefficient will be even larger in many regions of the atmosphere, where temperatures are typically colder than 295 K (Smith et al., 2015). It should be noted that Smith et al. (2015) also report a large rate coefficient for the C_1 CI and water dimer reaction of $k_{C1+(H2O)2} = (7.4 \pm 0.6) \times 10^{-12}$ cm^3 molecule^{-1} s^{-1} at 295 K. These results are all indicative that the reaction with the water dimer is the major atmospheric sink for CH_2OO (Lewis et al., 2015).

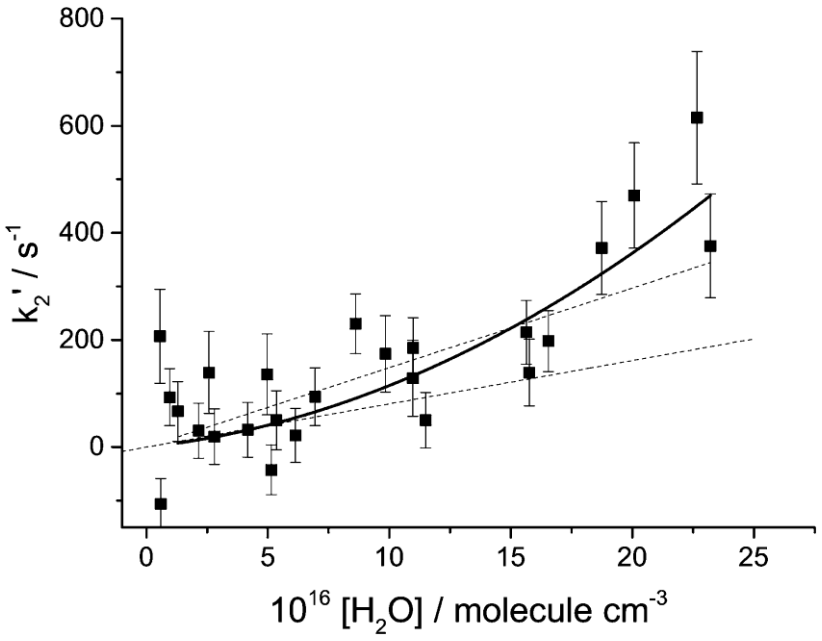

Figure 6.2: A bimolecular plot shows the quadratic dependence on [H_2O], implying that the C_1 CI reacts with the water dimer, $(H_2O)_2$.

Not all of the literature is in complete agreement; a study by Stone et al. (2014) using LIF spectroscopy measured a much smaller rate coefficient for the reaction CH_2OO and water, $k_{C1H2O} < 9 \times 10^{-17}$ cm^3 molecule^{-1} s^{-1} (Stone et al., 2014). Although it is possible that there were other reactions removing HCHO from the system, hence interfering with the $CH_2OO + H_2O$ reaction. However, if this evaluation of the rate coefficient is correct, trace gases such as SO_2 and NO_2 could be small sinks for Criegee intermediates in arid environments. Moreover, in the certain environments CIs may also prove to be significant sinks for SO_2 and NO_2.

Clearly, more work is still necessary to understand the significance of some of the more minor atmospheric channels; in the following sections of this thesis the reactivity for the reactions of the C_1 (and C_2) Criegee intermediates with SO_2 and NO_2 will be reported and

the atmospheric implications of these finding will be discussed. However, before proceeding with the specific results from this study, the experimental conditions used for the individual experiments will be considered.

6.1.2 Experimental

The kinetics of the C_1 Criegee intermediate with SO_2 and NO_2 was studied by directly monitoring the C_1 CI (*m/z* = 46) using laser flash photolysis coupled to time-resolved mass spectrometry; in depth details of the PIMS technique can be found in Chapter II.

For the C_1 studies a CH_2I_2/O_2/He/trace gas mixture was flowed through the reactor *via* calibrated mass flow controllers (MFCs); note that the trace gas added was kept in excess of [CH_2OO] to ensure pseudo-first-order conditions ([trace gas] = 10^{13}-10^{14} molecule cm^{-3}). Moreover, all the experiments were done using the PIMS technique and were conducted at low pressures (1.0-2.5 Torr). Initially, there were problems introducing the diiodomethane (Sigma-Aldrich, 99%) into the reactor through the MFC. To ensure a reproducible amount of CH_2I_2 was added a bubbler, placed after the MFC, was used (Figure 6.3). The flow of helium (BOC 99.999%) from the MFC and the flow of gases (He and CH_2I_2) out of the bubbler were balanced using a needle valve to ensure that only small amounts of the diiodomethane ([CH_2I_2] < 1-10 × 10^{13} molecule cm^{-3}) were added during the experiments. This ensured that the majority of the gas exiting the bubbler was helium, with only the diluted vapours of the diiodo-species being introduced into the reactor. However, initially it was difficult to consistently control concentrations with this technique and it is thought that during some preliminary experiments the [CH_2I_2] was significantly higher than 1×10^{14} molecule cm^{-3}. Neat O_2 (BOC 99.999%) was also added to generate the CH_2OO biradicals (R6.1-6.3). There are other possible reactions which the CH_2I radicals can undergo, however, these are pressure dependent and it is predicted that at the low pressures used in this study, R6.2 is the dominant channel (Gravestock et al., 2010, Stone et al., 2013). Moreover, As the experiments were conducted at low pressure the concentration of ICH_2OO in the system was predicted to be negligible (Stone et al., 2013).

$$CH_2I_2 + h\nu \rightarrow CH_2I + I \qquad \text{(R6.1)}$$

$$CH_2I + O_2 \rightleftharpoons ICH_2O_2^* \rightarrow CH_2OO + I \qquad \text{(R6.2)}$$

$$CH_2I + O_2 \rightleftharpoons ICH_2O_2^* + M \rightarrow ICH_2O_2 + M \qquad \text{(R6.3)}$$

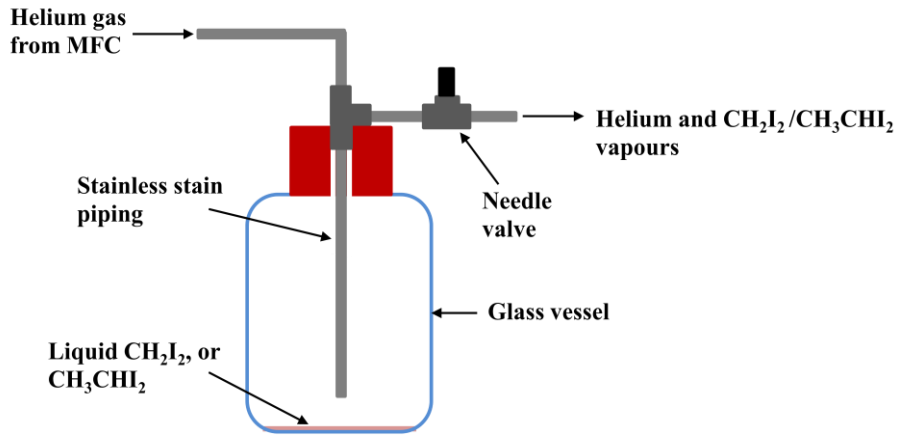

Figure 6.3: A schematic representation of the bubbling apparatus used to introduce diiodo-compounds into the reactor.

In the experiments the C_1 Criegee intermediates formed were then reacted with either SO_2 or NO_2. Typically 2 - 4% samples of SO_2 and NO_2 (Sigma-Aldrich: 99.9%, 99.5% respectively) were prepared in He and stored in covered glass bulbs. The reactions were initiated by pulsed laser photolysis using an excimer laser (λ = 248 nm, ~ 50 mJ cm^{-2}) and the gas sampled was photoionised using λ = 118 nm light (for details see Chapter II). At this photoionization energy the only CH_2OO isomer ionized is the C_1 Criegee intermediate (Welz et al., 2012).

As described in Chapter II all of the experiments were controlled using a LabVIEW™ program, designed specifically for data collection and storage from the PIMS apparatus (Baeza-Romero et al., 2012). The data collected from individual traces were then analysed using OriginPro graphical software to describe the time-resolved ion signal and were fitted using the equations outlined below (E6.1-6.3). A pseudo-first order bimolecular plot of the data-set was produced by plotting these data points (see Figure 6.4).

$$M_1 = \frac{(S_{\mathrm{C1height}} \times k'_{\mathrm{CH2I+O2}} \times k_{\mathrm{samp}})}{(k'_{\mathrm{C1total}} - k'_{\mathrm{CH2I+O2}})} \qquad \text{(E6.1)}$$

$$M_2 = \frac{e^{-k'_{\mathrm{CH2I+O2}} \times t} - e^{-k_{\mathrm{samp}} \times t}}{(k_{\mathrm{samp}} - k'_{\mathrm{CH2I+O2}})} - \frac{e^{-k'_{\mathrm{C1total}} \times t} - e^{-k_{\mathrm{samp}} \times t}}{(k_{\mathrm{samp}} - k'_{\mathrm{C1total}})} \qquad \text{(E6.2)}$$

$$S_{\mathrm{CH2OO}} = M_1 \times M_2 + S_{\mathrm{bg}} \qquad \text{(E6.3)}$$

where S_{CH2OO} is the time-resolved Criegee signal; S_{C1height} is the maximum height of S_{CH2OO}; $k'_{\mathrm{CH2I+O2}}$ is the rate of CH_2OO formation; k'_{C1total} is the total loss rate of CH_2OO; k_{samp} is the rate of transportation of the gas to the mass spectrometer (this was held constant during data analysis, k_{samp} = 30000 s^{-1}); t is time; and S_{bg} represents the background signal measured for the individual data traces.

6.1.3 $CH_2OO + SO_2$

The following section will detail the subsequent reaction between the stabilised C_1 Criegee intermediate, CH_2OO, and SO_2 (R6.4). This reaction is expected form an intermediary secondary ozonide, which readily dissociates into HCHO and SO_3 at low pressures (R6.4a) (Vereecken et al., 2012).

$$CH_2OO + SO_2 \rightarrow \text{Products} \quad \text{(R6.4)}$$

$$CH_2OO + SO_2 \rightarrow SOZ^* \rightarrow HCHO + SO_3 \quad \text{(R6.4a)}$$

Using the PIMS technique it is possible to monitor the formation and subsequent decay of the C_1 stabilised Criegee intermediate, which can be measured at m/z = 46 in the mass spectrometer. At first, several problems were encountered whilst trying to observe the C_1 Criegee biradical; for example there were issues introducing diiodomethane into the PIMS set-up (see section 6.1.2). Initially, the total pseudo first-order loss rate of CH_2OO ($k'_{C1total}$) was extremely high, even in the absence of any SO_2, typical1y $k'_{C1total} > 3000$ s^{-1} at $[SO_2] = 0$ molecules cm^{-3}. To prevent confusion, the y-intercept of the bimolecular plot of the $CH_2OO + SO_2$ reaction will henceforth be referred to as k'_{other}. k'_{other} not only describes the loss from the Criegee self-reaction but also any other losses of CH_2OO from the system, for example the loss of CI to the walls of the reactor. Note that: $k'_{other} \equiv k'_{C1total}$ in the absence of SO_2.

$$2\ CH_2OO \rightarrow 2\ HCHO + O_2 \quad \text{(R6.5)}$$

$$CH_2OO \rightarrow \text{walls} \quad \text{(R6.6)}$$

At the time of these preliminary experiments, the wall losses (R6.6) were known to be large ($1000\ s^{-1} > k_{wall} > 2000\ s^{-1}$) due to contamination in the system from amino-compounds used in other work, and this partially explains the high k'_{other} observed. However, despite taking the high wall loss rate into account, the observed k'_{other} indicates that the initial Criegee intermediate concentration, $[CH_2OO]_0$, was very high ($[CH_2OO] \approx 2 \times 10^{13}$ molecule cm^{-3}), suggesting that self-reaction was contributing to the overall CI loss. Concentrations of CH_2OO this high bring into question the pseudo first-order nature and hence the validity of some of the earlier experiments completed during this study (Figure 6.4). Note: $[CH_2OO]$ was estimated assuming $k_{C1SR} \approx 7.1 \times 10^{-11}$ cm^3 $molecule^{-1}$ s^{-1}, an averaged value of recently reported rate coefficients of the CH_2OO self-reaction, k_{C1SR} (Buras et al., 2015, Ting et al., 2014, Chhantyal-Pun et al., 2015).

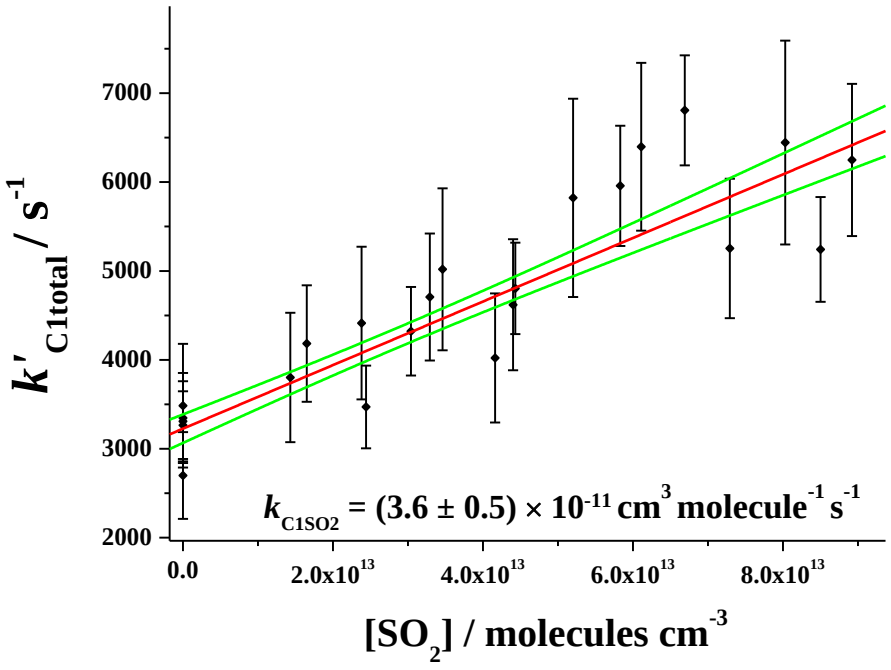

Figure 6.4: An early pseudo first-order bimolecular plot obtained in this study: note the large *y*-intercept. The error quoted is propagated using the random errors quoted from the experiments (1σ) and a 10% systematic error. Confidence limits quoted at 1σ.

Even though a sensible evaluation of k_{C1SO2} could be determined from the data shown in Figure 6.4, the quality of the data was generally poor. The linear regression fit shown in Figure 6.4 was weighted using the individual error of the $k'_{C1total}$ calculated from the non-linear equations E6.1-6.3; the same fitting procedure was used throughout this chapter. As can be seen from Figure 6.5 there are several different ways in which CH_2OO is lost in the system, and it was recognised that in order to improve the quality of the data collected, both the wall losses and initial concentrations of the C_1 Criegee intermediate must be reduced to minimise k'_{other}. Much time was therefore dedicated to optimizing the CH_2OO detection in the mass spectrometer, and minimising the initial concentration of CH_2I_2. In addition the walls of the flowtube were cleaned and a recoated using halocarbon wax.

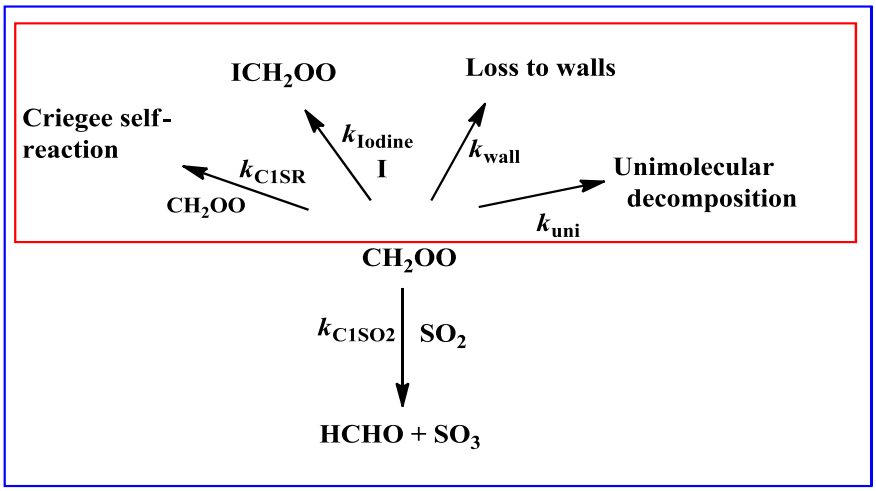

$$k'_{other}\ (s^{-1}) = k_{C1SR}[CH_2OO] + k_{wall} + k_{Iodine}[I] + k_{uni}$$

$$k'_{C1total}\ (s^{-1}) = k_{C1SO2}[SO_2] + k'_{other}$$

Figure 6.5: Diagram of the CH_2OO + SO_2 reaction scheme.

The quality of the Criegee signal (S_{CH2OO}) was further improved by increasing the [O_2], thus making CI formation very fast ($k_{CH2I+O2} \approx 20{,}000\ s^{-1}$), this both enhanced the amplitude of S_{CH2OO} and also made the data analysis more facile. An example of the CH_2OO signal observed (m/z = 46) can be seen in Figure 6.6. The data from this plot yield signal-to-noise-ratios (SNR) of approximately 30; this was not atypical for the data set as a whole, once the reaction system was better understood, and was well above the minimum signal-to-noise ratio required for detection ($3 < SNR_{min}$).

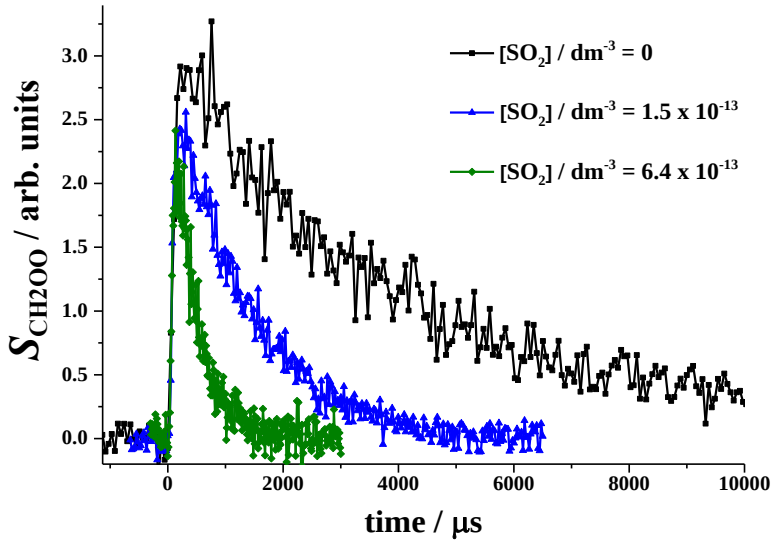

Figure 6.6: An example of time-resolved C_1 CI signal, S_{CH2OO}, in the presence and absence of SO_2.

As the technique was refined, the total Criegee loss rates (in the absence of SO_2) were slowly reduced and eventually values of $k'_{other} < 250\ s^{-1}$ were typically met. Interestingly, closer analysis suggests that, even for this relatively low value of k'_{other}, the CH_2OO decays looked to be mixed 1st and 2nd order, in the absence of SO_2 (Figure 6.7). Moreover, the first order analysis still gave a better fit to the data, implying that the loss contribution from k_{wall} was still greater than k_{C1SR} in these experiments.

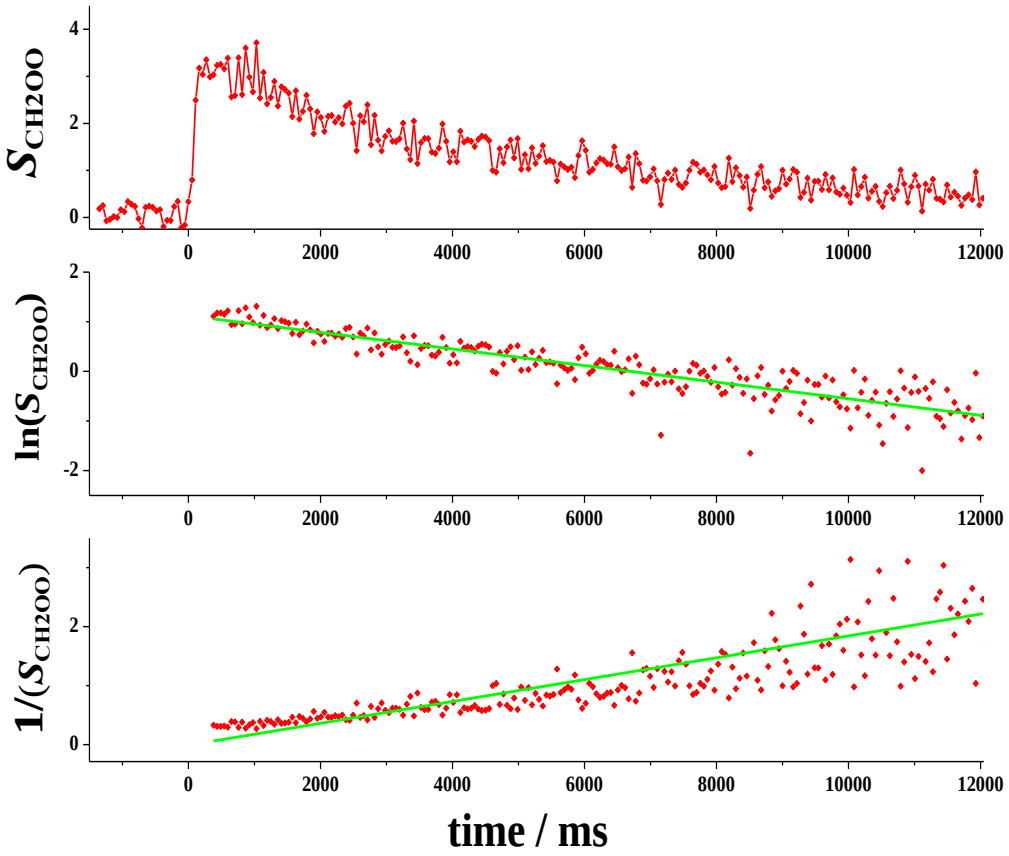

Figure 6.7: The upper graph is a raw data set for CH_2OO decay in the absence of any SO_2 (given in arb. units). The middle graph is a first order plot of $\ln(S_{CH2OO})$ vs. time, here, the linear fit to the data is good, suggesting the decay trace still is more first order in nature than second order. The lower graph is a second order plot of $1/(S_{CH2OO})$ vs. time and the linear fit to data is not very good, implying the second order characteristics are small. Note: S_{CH2OO} is equivalent to the observed experimental signal from CH_2OO.

To try and gain a better understanding of both the experimental conditions, and the mixed order nature of the data, a Kintecus model was created (Table 6.2 + 6.3) to describe a simplified version CH_2OO system (i.e. $[SO_2] = 0$ molecule cm^{-3}) (Ianni, 2002). In this system the only loss processes considered are the CH_2OO self-reaction ($k_{C1SR}[CH_2OO]$) and k'_{FOL}, where k'_{FOL} is the combined rate of all the first-order loss processes in the system (clearly, this excludes the rate coefficient for self- reaction, k_{C1SR}, and the CI + SO_2 rate coefficient, k_{C1SO2}). The sum of these components must equal the total loss rate CH_2OO observed (k'_{other}). Initially, the model assumed that the CI loss rate was entirely second-order and k'_{FOL} was equal to zero; this led to an estimated initial CH_2OO concentration of

$[CH_2OO]_0 \approx 2.8 \times 10^{12}$ molecule cm^{-3}. Subsequently, the first-order component (k'_{FOL}) was incrementally increased until $k'_{FOL} = 150\ s^{-1}$ ($[CH_2OO] \approx 0.8 \times 10^{12}$ molecule cm^{-3}). The output from these models were then scaled and plotted alongside some of the raw data collected (see Figure 6.8).

Table 6.2: Shows the simple reaction scheme used for the Kintecus simulations.

Reaction	Rate coefficient
$CH_2I + O_2 \rightarrow CH_2OO + I$	$k_{CH2I+O2} = 1.8 \times 10^{-12}\ cm^3\ molecule^{-1}\ s^{-1}$
$CH_2OO + CH_2OO \rightarrow 2\ HCHO + O_2$	$k_{C1SR} = 7.1 \times 10^{-11}\ cm^3\ molecule^{-1}\ s^{-1}$
$CH_2OO \rightarrow$ loss	$0 < k'_{FOL}\ (s^{-1}) < 150$

Table 6.3: Highlights the initial concentrations of the different species involved.

Species	Initial concentration / molecule cm^{-3}
CH_2I	$(0.8\text{-}2.8) \times 10^{12}$
O_2	1.0×10^{16}
CH_2OO	0
SO_2	0

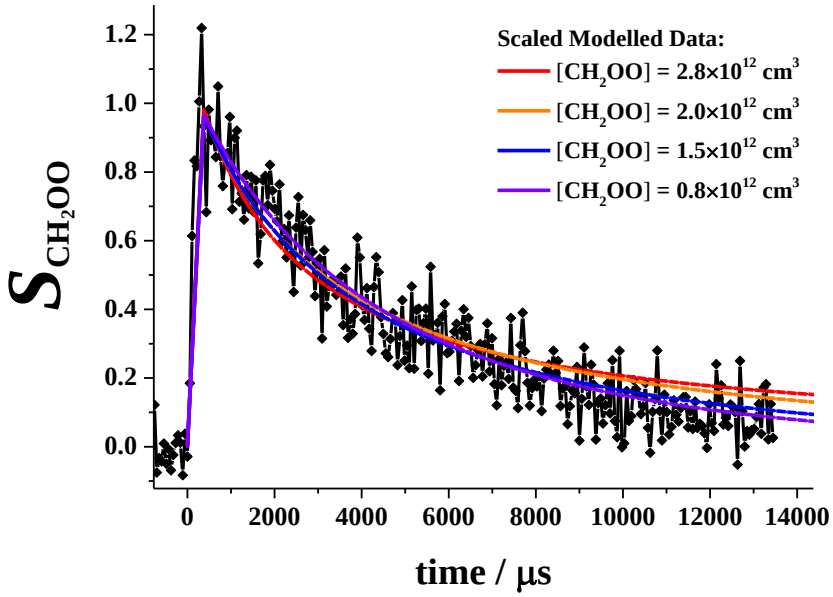

Figure 6.8: A plot of some raw CH_2OO data (where $[SO_2] = 0$ molecule cm^{-3}), additionally the scaled models simulated using the Kintecus software are also shown.

All of the Kintecus simulations do a reasonable job at fitting the raw data, however, it is clear the best fittings to the data correspond to those more first-order in their nature. The Kintecus models indicate that the initial Criegee intermediate concentrations, $[CH_2OO]_0$, could conceivably be below 1.0×10^{12} molecule cm^{-3}. However, a more conservative estimate of $[CH_2OO]_0 \approx (1.5 \pm 0.5) \times 10^{12}$ molecule cm^{-3} is recommended. Crucially, this means that the system can be considered to be under pseudo first-order conditions for $[SO_2]$ as low as $\sim 1.5 \times 10^{13}$ molecule cm^{-3}.

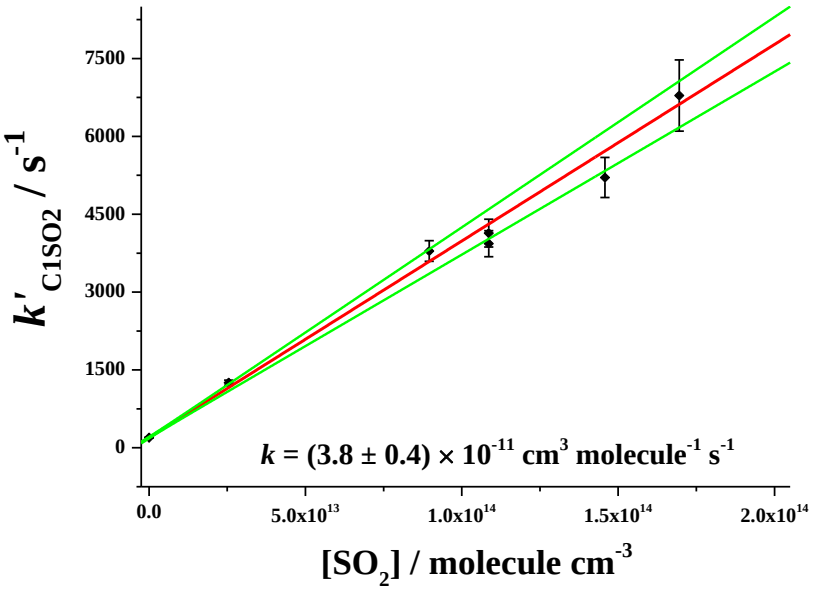

Figure 6.9: A bimolecular plot of the CH_2OO + SO_2 reaction. The red line is a weighted linear fit to the data; the confidence limits shown are quoted to 1σ level; the error quoted is propagated using the random errors quoted from the experiments and a 10% systematic error.

Figure 6.9 shows a bimolecular plot for the CH_2OO + SO_2 reaction with visible improvements in the data quality; firstly the *y*-intercept is far smaller (lower [CH_2OO], less Criegee self-reaction and a lower k_{wall}). Secondly, the scatter of the individual data points is less. It should be noted that for the analysis it was assumed that the initial concentration of CI was the same for all of the experiments performed in a given data set. This is thought to be a valid postulation as experiments where [SO_2] = 0 molecule cm^{-3} were made randomly during the course of each data set, were self-consistent. With this assumption, k'_{other} is constant and the gradient of the bimolecular plot is equivalent to k_{C1SO2}. A summary of all of the experiments conducted in this study is presented in Table 6.4, all of the measured rate coefficients are in excellent agreement with each other, despite being collected over the course of several years.

Table 6.4: k_{C1SO2} values obtained from this study. The data set named 11/2015b was taken at low SO_2 concentrations, [SO_2] < 8 × 10^{13} molecule cm^{-3}. *This rate coefficient was excluded from the average, see text.

Date of Experiments	k_{C1SO2} (10^{-11} cm^3 $molecule^{-1}$ s^{-1})	Level of Uncertainty
05/2013	3.6 ± 0.5*	1σ
01/2014	3.7 ± 0.4	1σ
07/2015	4.0 ± 0.6	1σ
11/2015a	3.8 ± 0.4	1σ
11/2015b	3.7 ± 0.4	1σ
Average	**3.8 ± 0.2**	1σ

The average value of k_{C1SO2} quoted in Table 6.4 excludes the data from May 2013 as it is thought that pseudo first-order conditions were not met for all of these experiments. From this work an average bimolecular rate coefficient of k_{C1SO2} = (3.8 ± 0.2) × 10^{-11} cm^3 $molecule^{-1}$ s^{-1} was measured. This value is in good agreement with many of the recently measured values of k_{C1SO2} (Table 6.5). It should be noted that all of the errors quoted were determined by propagating the random errors obtained from the bimolecular plots (1σ) with a systematic experimental error of 10%.

Table 6.5: A selection of rate coefficients, *k*, for the CH_2OO + SO_2 reaction measured using a variety of different techniques. Where: GC–FID = gas chromatography with flame ionization detection; UVA = ultra-violet absorption; CRDS = cavity ring down spectrometry. *Total CH_2OO removal rate measured in the presence of low SO_2, [SO_2] < 7 × 10^{12} molecule cm^{-3}.

Technique	k/ 10^{-11} cm^3 $molecule^{-1}$ s^{-1}	Reference
GC-FID	0.0004 ± 0.0001	(Johnson et al., 2001)
PIMS	3.9 ± 0.7	(Welz et al., 2012)
LIF and PIMS	3.42 ± 0.50	(Stone et al., 2014)
LIF	3.53 ± 0.29	(Liu et al., 2014)
Time resolved UVA	4.1 ± 0.3	(Sheps, 2013)
CRDS	3.80 ± 0.04	(Chhantyal-Pun et al., 2015)
CRDS	7.46 ± 0.29*	(Chhantyal-Pun et al., 2015)
PIMS	**3.8 ± 0.2**	**This Study**

The data presented in Table 6.5 show some anomalous results. The value reported by Johnson et al., (2001), k_{C1SO2} = (0.4 ± 0.1) × 10^{-14} cm^3 $molecule^{-1}$ s^{-1}, is the oldest of the measurements and was listed to highlight that, until very recently, the reactivity of CIs towards most trace gas species was thought to be low, and hence CI chemistry was thought to have little impact within the atmosphere. However, the enhanced reactivity of CH_2OO towards SO_2 indicates that Criegee chemistry may have a direct impact on atmospheric concentrations of H_2SO_4 from increased SO_2 oxidation.

The second anomalous value was measured by Chhantyal-Pun et al. (2015) at low [SO_2], where 1 × 10^{12} molecule cm^{-3} < [SO_2] < 7 × 10^{12} molecule cm^{-3}. The authors explain this enhanced CH_2OO removal rate using a complex mechanism (Figure 6.10). A simplified version of this mechanism is shown below (R6.4, R6.7-R6.9):

$$CH_2OO + SO_2 \rightarrow HCHO + SO_3 \quad \text{(R6.4)}$$

$$CH_2OO \rightarrow \text{Loss} \quad \text{(R6.7)}$$

$$CH_2OO + SO_2 \rightleftharpoons \text{intermediate} + SO_2 \quad \text{(R6.8)}$$

$$\text{intermediate} \rightarrow \text{Products} \quad \text{(R6.9)}$$

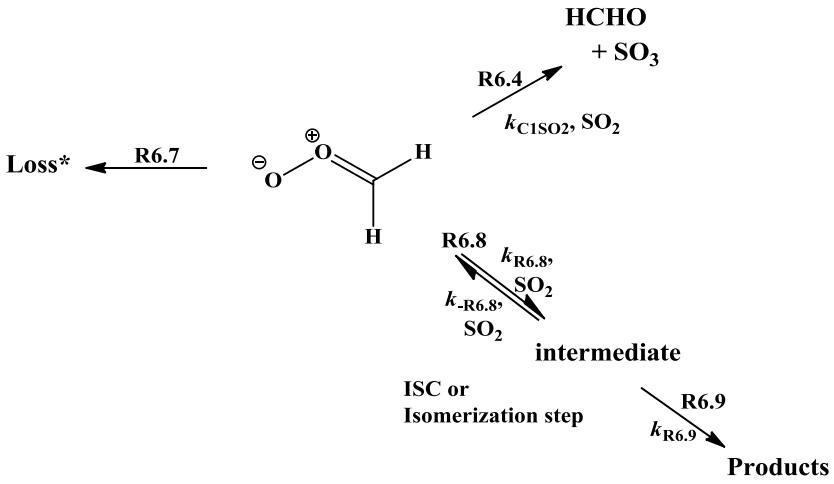

Figure 6.10: Simplified Mechanism of CH_2OO losses in the presence of SO_2. Adapted from Chhantyal-Pun et al. (2015). *Loss is equal sum of all other loss mechanisms (i.e. wall losses, diffusional losses, self-reaction, etc.)

In this mechanism an SO_2-catalysed reversible isomerisation/intersystem crossing (ISC) reaction is proposed to be in competition with the $CH_2OO + SO_2$ reaction. The impact this has on the overall reaction scheme is determined by invoking a steady state approximation upon the concentration of the intermediate product of this reaction. At high concentrations of SO_2: $k_{-R6.8}[SO_2] >> k_{R6.9}$, therefore the dominant loss mechanism of CH_2OO under these conditions is thought to be R6.4.

However, at low concentration of SO_2 things are slightly more complex. Under these conditions $k_{-R6.8}[SO_2] << k_{R6.9}$, meaning that any of the intermediate formed will be quickly lost *via* reaction channel R6.9 (see Figure 6.10), and thus the reaction forming the intermediate is the rate-determining step, hence the rate of reaction under low $[SO_2]$ will be dependent upon $k_{R6.8}$. Specifically, the rate of CH_2OO loss is dependent upon $(k_{C1SO2} + k_{R6.8})[SO_2]$ at low $[SO_2]$; a parameter which is dependent upon both k_{C1SO2} and $k_{R6.8}$. Therefore, if it is assumed that k_{C1SO2} that remains constant, the loss of CH_2OO must be greater at lower concentrations of SO_2, explaining the augmentation in the CH_2OO decay observed by Chhantyal-Pun et al. (2015). Figure 6.10 is a simplification of the original Chhantyal-Pun et al. (2015) mechanism and it should be noted that the loss channel R6.7 is an amalgamation of several different channels which are independent of $[SO_2]$.

This hypothesis is a very elegant solution to explain the observed behaviour; however, some of the methodology used in the low $[SO_2]$ experiments and subsequent analysis were both novel and unconventional. For example, all of the other studies probing the CH_2OO and SO_2 reaction were performed under pseudo first-order conditions, where the concentration of SO_2 was kept in excess over the Criegee concentration ($[SO_2] > 10 \times [CH_2OO]$). By doing this, a graph of the pseudo first-order rate coefficient, k'_{C1SO2}, versus $[SO_2]$ can be

plotted, and the rate coefficient k_{C1SO2} determined (see Chapter I, Section 1.5 for details of pseudo first-order reactions). However, in the work of Chhantyal-Pun et al. (2015) the experiments were not all conducted using pseudo first-order condition at low [SO_2], in fact, for some of the measurements the concentration of CH_2OO was larger than the concentration of SO_2. This meant that for these experiments the contribution to the loss of CH_2OO was greater from the CI self-reaction (R6.5) than from the Criegee + SO_2 reaction (R6.4). Furthermore, the loss of CH_2OO has mixed 1st and 2nd order components, with significant second-order character, thus making the analysis more complicated than if the experiments were done under pseudo first-order conditions. Due to this methodology, a simultaneous first and second order fit was used during the data analysis to extract k_{C1SO2}. This was a different approach to solving this problem and therefore it is important compare this newer method of data analysis with other more established techniques to test its validity for interpreting CI chemistry. It was therefore decided that the CH_2OO + SO_2 experiments should be repeated at low [SO_2] to try and replicate the results of Chhantyal-Pun et al. (2015), but using more conventional pseudo first-order reaction conditions. It should be noted at this point that the quality of data collected by Chhantyal-Pun et al. (2015) is very good; it is the reaction conditions used and the interpretation of the data that are novel. Note: the method of data analysis used attempts to fit loss rate constants for both the CI self-reaction, k_{C1SR}, and CI + SO_2 reaction, k_{C1SO2}, simultaneously.

As previously stated it is estimated that the initial concentration of CH_2OO radicals in these experiments was $[CH_2OO]_0 \approx (1.5 \pm 0.5) \times 10^{12}$ molecule cm^{-3}; before starting experiments it was necessary to probe the minimum [SO_2] where the Criegee loss rate could be described as first-order dominated (although actually mixed order in nature), and where the conditions close to pseudo first-order ($[SO_2]_{end} \approx 0.9 \times [SO_2]_0$). As a starting-point, it was assumed that to maintain pseudo first-order conditions [SO_2] must be greater than $3 \times [CH_2OO]_0$. A Kintecus model was run for the reaction under these starting conditions and from this it became apparent that the concentration of SO_2 remained almost constant during the course of this reaction (i.e. at t = 10 ms, $[SO_2]_t = 0.85 \times [SO_2]_0$), and this can be seen more clearly in Figure 6.11 (Ianni, 2002). As the k'_{FOL} component is significant ($k'_{FOL} \approx 100$ s^{-1}), reaction with SO_2 is not the only loss channel for CH_2OO. Hence, the concentration of SO_2 remains nearly constant throughout the course of the reaction and therefore the conditions can be considered as near pseudo first-order. Furthermore, the Kintecus model (see Figure 6.11) suggests that even at this low concentration of SO_2 the nature of the CH_2OO loss is dominated by the first-order processes (k'_{FOL} and $k_{C1SO2}[SO_2]$). Therefore a minimum [SO_2] of $3 \times [CH_2OO]_0$ was chosen for experiments.

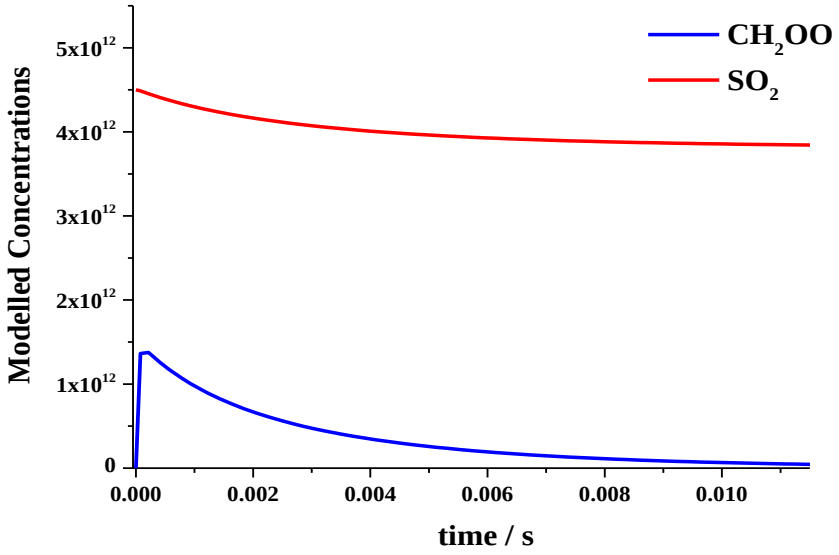

Figure 6.11: A model of the CH_2OO + SO_2 reaction; $[CH_2OO] = 1.5 \times 10^{12}$ molecule cm^{-3}, $[SO_2] = 4.5 \times 10^{12}$ molecule cm^{-3}. An estimate of k_{C1SR} = 7.1×10^{-11} cm^3 $molecule^{-1}$ s^{-1} and k_{wall} = 100 s^{-1} was used for modelling.

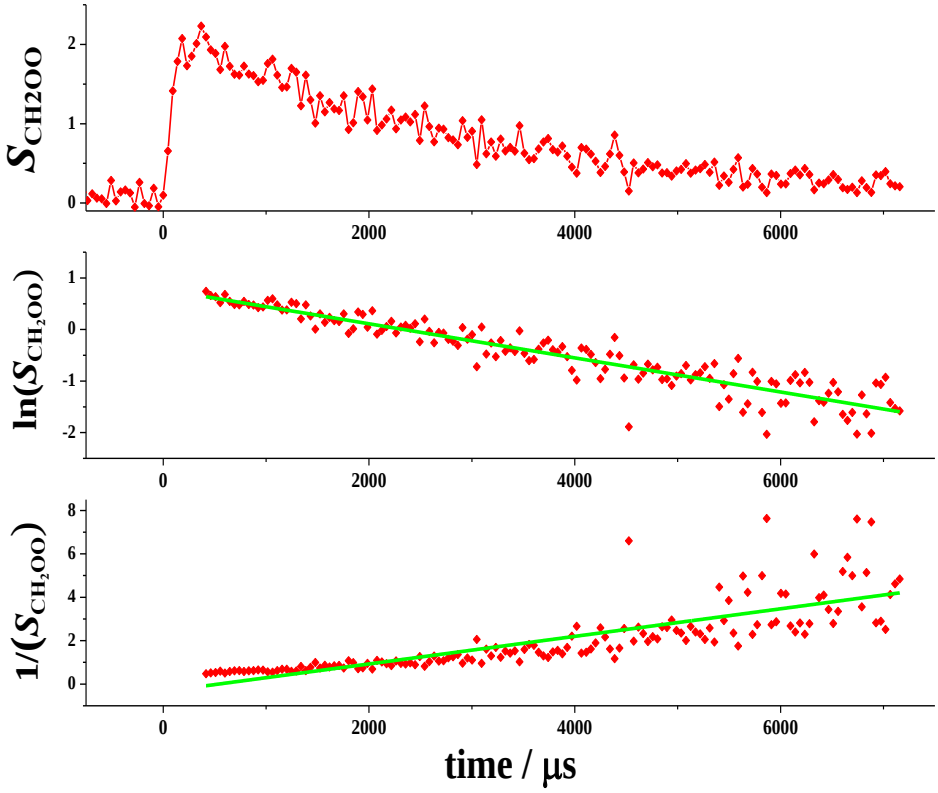

Figure 6.12: The upper graph is an example of a raw data set for CH_2OO decay (S_{CH2OO}, arb. units) with $[SO_2] \approx 4.5 \times 10^{12}$ molecule cm^{-3}. The middle graph is a first order plot of ln(S_{CH2OO}) vs. time, here, the linear fit to the data is very good suggesting the system is more first order in nature than second. The lower graph is a second order plot of 1/(S_{CH2OO}) vs. time and the linear fit to data is poor implying that the system is not second order. Note: S_{CH2OO} is equivalent to the experimental signal from CH_2OO observed.

In Figure 6.12 the data collected from the low [SO_2] experiment previously described (where [SO_2] = 3 × [CH_2OO]$_0$) is shown. Notably, closer analysis of this data indicates that although the CH_2OO decay must be mixed order, the decay can be better described using first-order analysis (plot of ln(S_{CH2OO}) vs. time) than second-order (plot of 1/(S_{CH2OO}) vs. time). This result suggests that the CH_2OO + SO_2 experiments is indeed under near pseudo first-order conditions at [SO_2] ≈ 4.5×10^{12} molecule cm^{-3}. Once this lower limit of [SO_2] was established, a full set of data was collected for 4×10^{12} < [SO_2] (molecule cm^{-3}) < 8×10^{13}. Using these data a bimolecular plot was constructed, the results from the low [SO_2] study can be seen below in Figure 6.13. It should be noted that although the conditions are near pseudo first-order for the low [SO_2] experiments, for the reactions where [SO_2] < 1×10^{13} molecule cm^{-3} concentration of SO_2 upon the completion of the reaction is below 90% of its initial concentration, and therefore cannot (conventionally) be considered as pseudo first-order (see Chapter I, Section 1.5). To account for this, these data points are plotted (on the *x*-axis) at their average concentration of SO_2 throughout the reaction, [SO_2]$_{av}$, rather than their initial SO_2 concentration, [SO_2]$_0$, as their initial concentration cannot be considered as constant; note [SO_2]$_{av}$ < [SO_2]$_0$. It should also be highlighted that the difference that these adjustments made to the overall rate coefficient, k_{C1SO2}, was negligible.

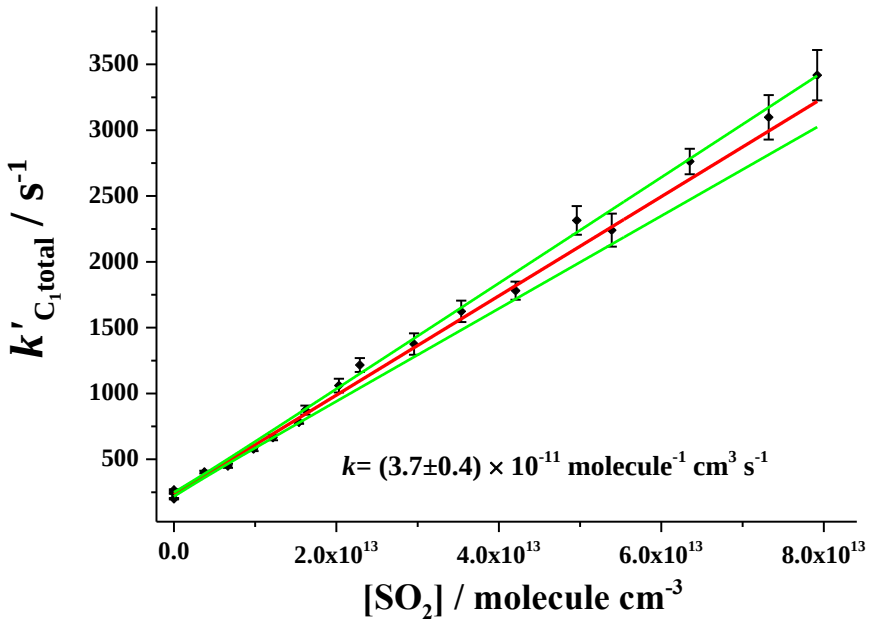

Figure 6.13: The bimolecular plot obtained for the CH_2OO + SO_2 reaction at low [SO_2] concentrations. The error quoted is propagated using the random errors quoted from the experiments (1σ) and a 10% systematic error. Confidence limits quoted at 1σ.

From this plot (Figure 6.13) it is apparent that there is no change in k_{C1SO2} at low concentrations of SO_2. However, to further verify this result a 'global fitting' procedure was used which allows multiple data sets to be fitted simultaneously. Global fitting uses parameters which are 'shared' across many individual data sets and yield a single best-fit value, which is then applied to the data set as a whole (OriginPro). For this analysis the rate coefficient, k_{C1SO2}, could be determined from a single fitting, as opposed to the $k'_{C1total}$ determined from the individual traces. An example of the global fitting can be seen in Figure 6.14; all of the fittings (red lines) were determined simultaneously to give the best universal fit to the whole data set.

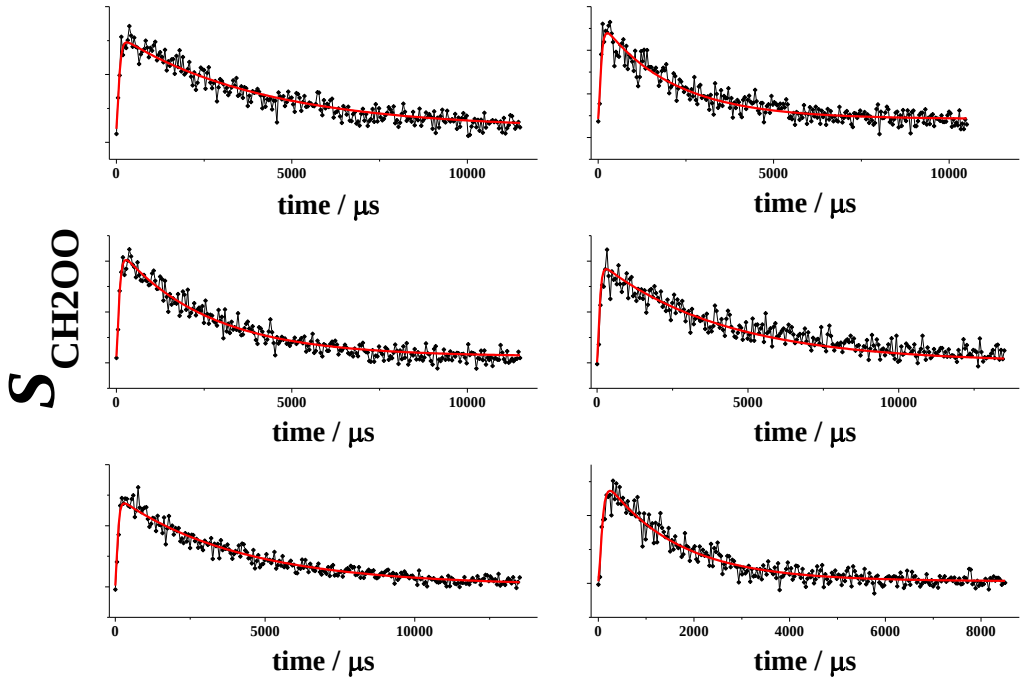

Figure 6.14: An example of the global fitting which is plotted across several individual traces simultaneously; the fitting uses all of data to give the 'global' fit.

$$k'_{\mathrm{C1total}} = (k_{\mathrm{C1SO2}} \times [\mathrm{SO_2}]) + k'_{\mathrm{other}} \quad \text{(E6.4)}$$

$$M_1 = \frac{(S_{\mathrm{C1height}} \times k'_{\mathrm{CH2I+O2}} \times k_{\mathrm{samp}})}{(k'_{\mathrm{C1total}} - k'_{\mathrm{CH2I+O2}})} \quad \text{(E6.1)}$$

$$M_2 = \frac{e^{-k'_{\mathrm{CH2I+O2}} \times t} - e^{-k_{\mathrm{samp}} \times t}}{(k_{\mathrm{samp}} - k'_{\mathrm{CH2I+O2}})} - \frac{e^{-k'_{\mathrm{C1total}} \times t} - e^{-k_{\mathrm{samp}} \times t}}{(k_{\mathrm{samp}} - k'_{\mathrm{C1total}})} \quad \text{(E6.2)}$$

$$S_{\mathrm{CH2OO}} = M_1 \times M_2 + \mathrm{S_{bg}} \quad \text{(E6.3)}$$

$S_{C1height}$ is the signal height of CH_2OO; $k'_{CH2I+O2}$ is the rate of CH_2OO formation; $k'_{C1total}$ is the total loss rate of CH_2OO; k_{samp} is the rate of transportation of the gas to the mass

spectrometer (this was held constant during data analysis, k_{samp} = 30000 s^{-1}); t is time; and S_{bg} represents the background signal measured for the individual data traces.

The equations used to fit the data globally are shown above (E6.1-6.4); notably the equations (E6.1-6.3) were also used to fit the individual traces. However, there are two subtle additions to the fitting procedure: firstly, the [SO_2] associated with each individual trace was input as a z parameter (i.e. a parameter local to each individual trace). This combined with the introduction of E6.4 directly links $k'_{C1total}$ and k_{C1SO2} (by multiplying with the [SO_2]) and allows for a direct evaluation of k_{C1SO2} for the whole dataset. As many of the parameters as possible were shared in the analysis: k_{C1SO2}, k'_{other}, $k_{CH2I+O2}$, k_{samp} and some of the parameters were kept constant: S_{bg} and k_{samp}. A number of the parameters were allowed to float during the iterations of the fitting until χ^2 was minimised; critically k_{C1SO2} was floated to give the best-fit to the data, the results from this analysis are in Table 6.6.

Table 6.6: Results of the global fitting technique, errors quoted were propagated from the associated error from the global fitting and a 12.5% systematic error.

[SO_2] Range / molecule cm^{-3}	[SO_2]	k_{C1SO2} / cm^3 $molecule^{-1}$ s^{-1}
$0 – 1.5 \times 10^{13}$	Low	$(3.46 \pm 0.40) \times 10^{-11}$
$0 – 2.5 \times 10^{13}$	medium	$(3.65 \pm 0.39) \times 10^{-11}$
$0 – 7.5 \times 10^{13}$	high	$(3.67 \pm 0.38) \times 10^{-11}$

Much information was gained from the global analysis: firstly, none of the calculated rate coefficients, k_{C1SO2}, were significantly different from the k_{C1SO2} obtained from the bimolecular plot (Figure 6.13, $k_{C1SO2} = (3.7 \pm 0.4) \times 10^{-11}$ cm^3 $molecule^{-1}$ s^{-1}), suggesting that the global analysis is a valid method for determining k_{C1SO2}. In addition, even the largest and smallest evaluations of k_{C1SO2} are in good agreement with each other, $k_{C1SO2} = (3.67 \pm 0.38) \times 10^{-11}$ cm^3 $molecule^{-1}$ s^{-1} and $(3.46 \pm 0.40) \times 10^{-11}$ cm^3 $molecule^{-1}$ s^{-1} respectively. Finally, and more interestingly, it is clear that for the data collected in this study, there is no evidence of an increased k_{C1SO2} at low concentrations of SO_2, unlike in the work of Chhantyal-Pun et al. (2015). In fact, the analysis suggests that k_{C1SO2} is lower at low [SO_2], however, the difference is very marginal and is not thought to be significant. In order to understand the discrepancies between the studies, a model of the CH_2OO + SO_2 system was created, Table 6.7, (using Kintecus software) and run for the reaction conditions reported in Chhantyal-Pun et al. (2015). Note: similar models had been used to model the data from this study and had accurately simulated the experimental data.

Initially, the model was run in the absence of any SO_2 to see if it was possible to reproduce the data collected in Chhantyal-Pun et al. (2015). This model was simple and excluded any ICH_2OO chemistry: ICH_2OO was assumed to be present in low concentrations due to the low pressures (~7 Torr) used by Chhantyal-Pun et al. (2015). Moreover, ICH_2OO is thought

to react rapidly with CH_2OO ($k_{ICH2OO} \approx 2 \times 10^{-10}$ cm^3 molecule^{-1} s^{-1}), therefore, if significant concentrations of ICH_2OO were present, the reaction between ICH_2OO and CH_2OO would have been the dominant loss process for CH_2OO. However, Chhantyal-Pun et al. (2015) suggest that 2nd order loss from the Criegee self-reaction is the dominant sink for CH_2OO. This means that any ICH_2OO formed is only present in small amounts. The reactions and the rate coefficients used to model the data are shown below (Table 6.7), and the initial conditions used in the model are listed in Table 6.8.

Table 6.7: The simplified version of the model used to reproduce the data collected by Chhantyal-Pun et al. (2015). All the rate coefficients listed were retrieved from Chhantyal-Pun et al. (2015), except $k_{CH2I+O2}$, which was measured by Sheps (2013).

Reaction	Rate coefficient
$CH_2I + O_2 \rightarrow CH_2OO + I$	$k_{CH2I+O2} = 1.8 \times 10^{-12}$ cm^3 molecule^{-1} s^{-1}
$CH_2OO + CH_2OO \rightarrow 2\ HCHO + O_2$	$k_{C1SR} = 7.35\times 10^{-11}$ cm^3 molecule^{-1} s^{-1}
$CH_2OO + I \rightarrow$ products	$k_{C1+I} = 1 \times 10^{-11}$ cm^3 molecule^{-1} s^{-1}
$CH_2OO + SO_2 \rightarrow$ products	$k_{C1SO2} = 7.46 \times 10^{-11}$ cm^3 molecule^{-1} s^{-1}
	or
	$k_{C1SO2} = 3.80 \times 10^{-11}$ cm^3 molecule^{-1} s^{-1}
$CH_2OO \rightarrow$ products	$k_{uni} = 11.6$ s^{-1}

Table 6.8: Initial concentrations of reactants used in the Kintecus model. The concentrations used were estimated from Chhantyal-Pun et al. (2015). Note that in Chhantyal-Pun et al. (2015) the $[CH_2OO] \approx 5.1 \times 10^{12}$ molecule cm^{-3}.

Species	Initial concentration / molecule cm^{-3}
CH_2I	5.1×10^{12}
O_2	3.0×10^{16}
I	5.1×10^{12}
CH_2OO	0
SO_2	0

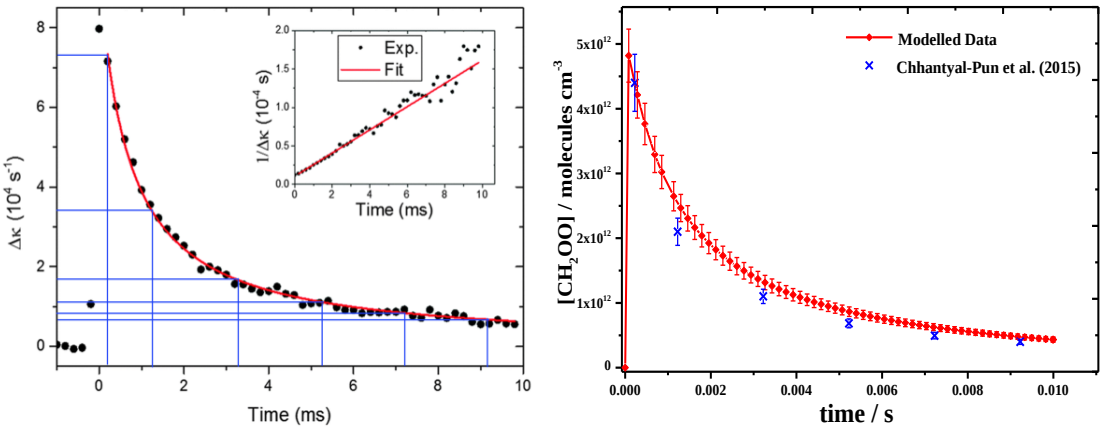

Figure 6.15: (Left) the graph shows a sample of the data collected from Chhantyal-Pun et al., (2015), where $[CH_2OO]_0 \approx 5.1 \times 10^{12}$ molecule cm^{-3}. The blue lines are used to scale the data from Chhantyal-Pun et al. (2015) to the modelled data to allow for comparison. (Right) the graph shows simulated data from a model run using Kintecus in red, input parameters are the conditions used in the study by Chhantyal-Pun et al., (2015). The error quoted is 8.5%, which is equivalent to the uncertainty of the Criegee self-reaction. The blue data points are the results scaled from Chhantyal-Pun et al. (2015), the error quoted are 10%.

Using this information, a simulation of the data from Chhantyal-Pun et al., (2015) could be modelled; a comparison of the modelled data and the experimental data can be seen in Figure 6.15. Unfortunately, it was not possible to directly compare the two datasets; however, the model appears to do a good job at reproducing experimental data (Figure 6.15, Right). By estimating the change in the signal between specific time points it is possible to compare the data, although it is appreciated that this is not the most accurate method of data comparison (Figure 6.15, Right). Moreover, it can be seen that even with the errors included, some of data points shown in Figure 6.15 are thought to be significantly different from each other. It should be noted that this analysis did highlight that the data from Chhantyal-Pun et al. (2015) had more second-order character than the modelled data; this is probably because the value for k_{C1+I} used in the model is the upper limit for this rate coefficient. However, although it is not perfect, the model seemed to do a respectable job at replicating the data from Chhantyal-Pun et al., (2015) so the model was left unchanged and used to simulate the reaction system in the presence of SO_2.

The model was re-run with an initial SO_2 concentration of 1.1×10^{12} molecule cm^{-3} using $k_{C1SO2} = 7.46 \times 10^{-11}$ cm^3 $molecule^{-1}$ s^{-1} for the $CH_2OO + SO_2$ rate constant, this second set of modelled data was then plotted with the data set simulated with no SO_2 present (Figure 6.16).

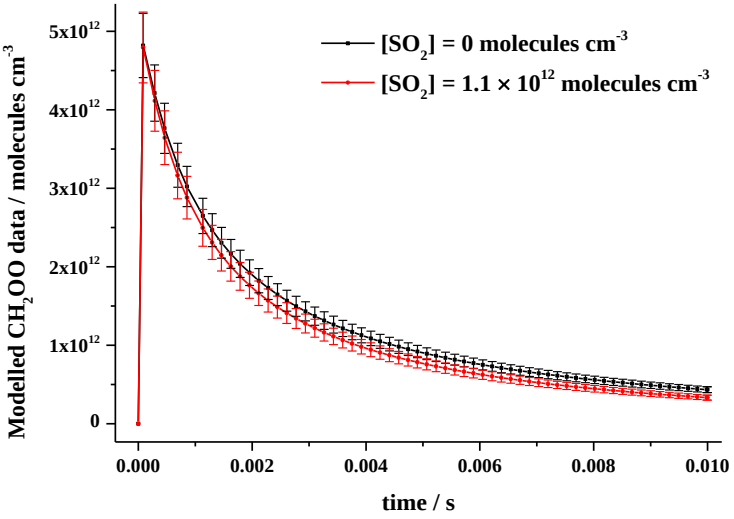

Figure 6.16: A comparison of the reaction system when $[SO_2]$ = 0 molecule cm^{-3} and when $[SO_2] = 1.1 \times 10^{12}$ molecule cm^{-3}. The error quoted for the model run with SO_2 in the system was ~9.5%, this was calculated by propagating the errors associate with k_{C1SR} and k_{C1SO2}.

Interestingly, when the errors associated with the model are included in the analysis, these models are not significantly different from each other until ~5 ms had passed (half the length of the total reaction time). This result suggests that the removal of CH_2OO by SO_2 is only minimal under these reaction conditions. The model was then run using the high $[SO_2]$ evaluation of the rate coefficient, $k_{C1SO2} = (3.80 \pm 0.04) \times 10^{-11}$ cm^3 molecule^{-1} s^{-1}, to see what impact this had on the CH_2OO decays (Figure 6.17).

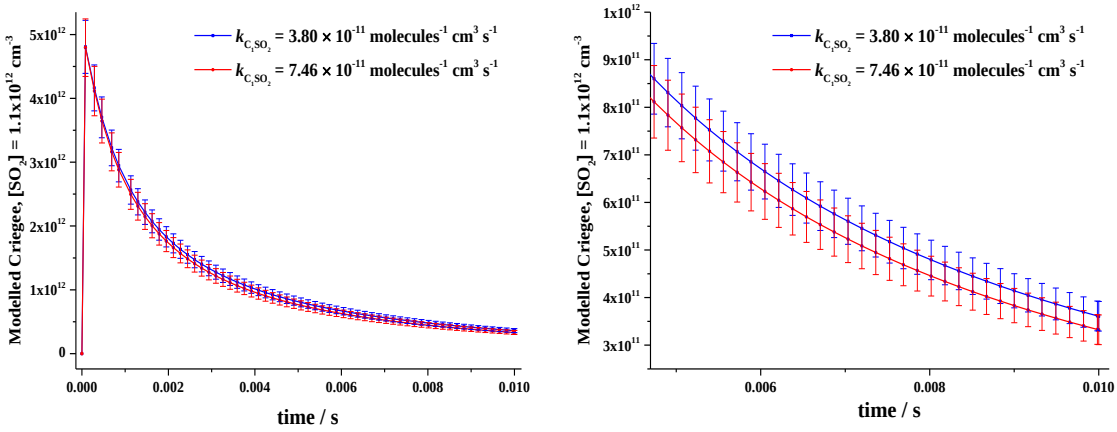

Figure 6.17: (Left) A comparison of the simulated Criegee concentrations using two different reaction models at $[SO_2] = 1.1 \times 10^{12}$ molecule cm^{-3}. These simulations use the two differing values of k_{C1SO2} reported by Chhantyal-Pun et al., (2015): $k_{C1SO2} = 7.46 \times 10^{-11}$ cm^3 molecule^{-1} s^{-1} (red); and $k_{C1SO2} = 3.80 \times 10^{-11}$ cm^3 molecule^{-1} s^{-1} (blue). (Right) Graph displays the same data at $t > 6$ ms, this plot highlights that the datasets are not significantly different from each other, even at long times (~ 10 ms). The error bars quoted for the modelled Criegee concentrations are ~9.5% for k_{C1SO2} = 7.46 $\times 10^{-11}$ cm^3 molecule^{-1} s^{-1} and ~8.5% for $k_{C1SO2} = 3.80 \times 10^{-11}$ cm^3 molecule^{-1} s^{-1}, these were calculated by propagating the errors associated with k_{C1SR} and k_{C1SO2}.

From Figure 6.17 it can be seen that there is no significant difference between these two models at any point during the reaction. Similar results were obtained for models using the two different k_{C1SO2} values at $[SO_2] = 2.2 \times 10^{12}$ molecule cm^{-3}; indeed, at this $[SO_2]$, the simulated Criegee concentrations were not significantly different for at least the first 8 ms of the reaction. These results suggest that, at $[SO_2] < 2.2 \times 10^{12}$ molecules cm^{-3}, the majority of the CH_2OO decay is insensitive to the $CH_2OO + SO_2$ rate coefficient. Of course, this is only a model of the data from Chhantyal-Pun et al., (2015) and therefore does not mean that the same can definitively be said for the experimental data. However, if the model is accurate it certainly implies that the validity of the low $[SO_2]$ experiments may be questionable. At SO_2 concentrations higher than 4×10^{12} molecule cm^{-3} it is believed that the evaluation of k_{C1SO2} becomes significant in the models, therefore it is assumed that there is no question about the validity of these data points (see Figure 6.18). It should be noted that simulations were also run in the presence and the absence of any I atom chemistry; under both sets of conditions the evaluation of k_{C1SO2} did not make any significant difference to the loss of CH_2OO at $[SO_2] < 2.5\times 10^{12}$ molecule cm^{-3} either.

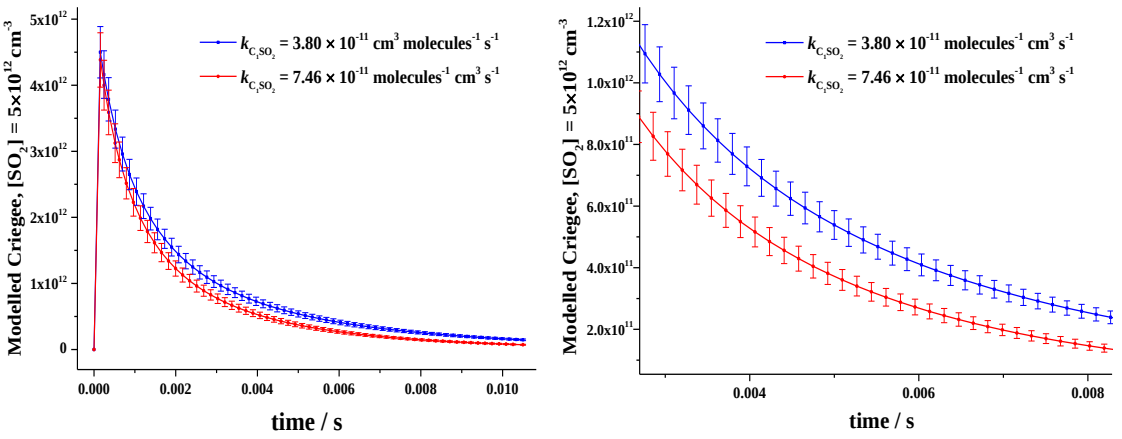

Figure 6.18: (Left) A comparison of the reaction system when $[SO_2] = 5 \times 10^{12}$ molecule cm^{-3}; Note that $k_{C1SO2} = 3.80 \times 10^{-11}$ cm^3 $molecule^{-1}$ s^{-1} (blue) and $k_{C1SO2} = 7.46 \times 10^{-11}$ cm^3 $molecule^{-1}$ s^{-1} (red); (Right) highlights that the datasets are significantly different from each other. The error bars quoted for the model with SO_2 is ~9.5% for $k_{C1SO2} = 7.46 \times 10^{-11}$ cm^3 $molecule^{-1}$ s^{-1} and ~8.5% for $k_{C1SO2} = 3.80 \times 10^{-11}$ cm^3 $molecule^{-1}$ s^{-1}, this was calculated by propagating the errors associated with k_{C1SR} and k_{C1SO2}.

In Chhantyal-Pun et al., (2015) there is some ambiguity as to the actual value of the rate coefficient, k_{C1+I}, and under pseudo first-order conditions this does not matter as the reaction between CH_2OO + I is only a minor channel. However, under the conditions used by Chhantyal-Pun et al., (2015) this reaction may cause interference in the data analysis which may account for the enhanced value of k_{C1SO2} at low $[SO_2]$.

6.1.3.1 C_1 CI+ SO_2 Conclusions

Over the course of this section (6.1.3) a self-consistent body of evidence has been reported concerning the reaction of CH_2OO + SO_2. Initially, some problems were encountered, however, by minimising the $[CH_2OO]_0$ to ~1.5×10^{12} molecule cm^{-3}, the second-order loss of CH_2OO *via* self-reaction were minimised. In this study, a value of k_{C1SO2} was determined, $k_{C1SO2} = (3.8 \pm 0.2) \times 10^{-11}$ cm^3 $molecule^{-1}$ s^{-1}, which is in excellent agreement previous estimations of k_{C1SO2} (Welz et al., 2012, Stone et al., 2014, Liu et al., 2014).

In addition, an in depth analysis of the CH_2OO + SO_2 reaction at low $[SO_2]$ has been completed under pseudo first-order conditions. As a part of the analysis a global fitting was used to fit multiple Criegee traces simultaneously, the results for this analysis indicate that k_{C1SO2} is unchanged at low $[SO_2]$; this result differs from the work of Chhantyal-Pun et al., (2015), however, this is not an wholly unexpected result. Chhantyal-Pun et al., (2015) is the first study to report a bimolecular plot with a positive but decreasing slope. Chhantyal-Pun et al. (2015) make a comparison of this result to the work Sheps (2013). Significantly, unlike the experiments described in Chhantyal-Pun et al. (2015), the work of Sheps (2013) maintains pseudo first-order conditions throughout. According to Chhantyal-Pun et al. (2015), the bimolecular plot from Sheps (2013) could also be interpreted as having a decreasing slope (Figure 6.19); however, it should be noted that no such observation was suggested in the study (Sheps, 2013). Furthermore, there are only a couple of data points taken at low SO_2 concentrations, $[SO_2] < 1.5 \times 10^{13}$ molecule cm^{-3}, in Sheps (2013) and these points also seem to be within the individual error quoted from the line of best fit.

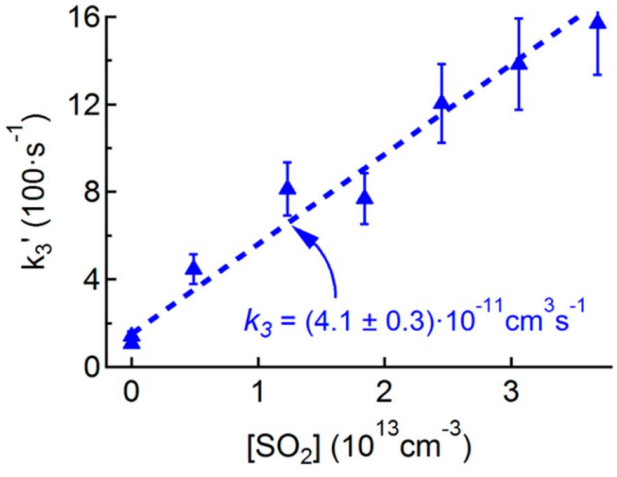

Figure 6.19: Bimolecular plot of the CH_2OO + SO_2 plot reported in Sheps (2013). Note that k_3' and k_3 are the pseudo first-order and first-order rate for the reaction between CH_2OO and SO_2, respectively.

Moreover, in order to explain this behaviour, a complex and novel chemical mechanism is hypothesised by Chhantyal-Pun et al, (2015). To justify their observations a SO_2-catalysed

reversible isomerisation (or ISC) reaction is postulated. However, the potential energy surface of the CH_2OO biradical suggests that all of the isomers of the C_1 Criegee intermediate are considerably more thermodynamically stable (~60 kJ mol^{-1}), meaning that the proposed reversibility of this isomerisation step is highly unlikely to occur (Vereecken et al., 2012).

Conversely, the low [SO_2] results reported in this study contradict the interpretation of Chhantyal-Pun et al., (2015). This work was conducted under more conventional pseudo first-order conditions and shows no evidence of an increased value of k_{C1SO2} at low [SO_2]. Clearly, if it is assumed that k_{C1SO2} remains constant at all concentrations of SO_2 then the reaction can be, once again, described using simple reaction kinetics.

6.1.4 $CH_2OO + NO_2$

In this section of the chapter, results concerning the reaction of the stabilised C_1 Criegee intermediate and NO_2 will be discussed. Different studies have probed this reaction before (Welz et al., 2012, Stone et al., 2014), and, notably, there is still a sizeable discrepancy between the literature results. Welz et al. (2012) report a rate coefficient for this reaction of $k_{C1NO2} = (6.8 \pm 2.0) \times 10^{-12}$ cm^3 $molecule^{-1}$ s^{-1}; as with the reaction between $CH_2OO + SO_2$, this rate coefficient (k_{C1NO2}) was at least three orders of magnitudes faster than previous work had suggested (Calvert, 2000). However, in Stone et al. (2014) the rate coefficient measured was approximately five times smaller, $k_{C1NO2} = (1.5 \pm 0.4) \times 10^{-12}$ cm^3 $molecule^{-1}$ s^{-1}. Notably, the work of Stone et al. (2014) was an indirect study, which utilised LIF to measure HCHO production. Therefore, it is clear that more work is needed to establish which of these recent evaluations is most accurate.

For this study diiodomethane photolysis in the presence of excess oxygen was used for CH_2OO production (R6.1-6.2). The reaction of CH_2OO with NO_2 was then monitored using the PIMS technique, which allows for the direct detection of the stabilised C_1 Criegee intermediate (*m/z* = 46) in the mass spectrometer.

$$CH_2OO + NO_2 \rightarrow \text{Products} \qquad \text{(R6.10)}$$

Problems were encountered using this method of detection as NO_2 and CH_2OO yield the same mass-to-charge ratios (*m/z* = 46). However, it was assumed that the ionization efficiency of NO_2 was low, as the even when large amounts of NO_2 were added to the system, the NO_2 peak was still relatively small. Although, a broad signal was observed at *m/z* = 46 (particularly at high [NO_2]), which was assumed to be caused by NO_2. This made it very difficult to monitor CH_2OO at high [NO_2] as the Criegee signal (S_{CH2OO}) became difficult to see above the background NO_2 signal. The experiments were therefore conducted over a limited range of [NO_2] (0.2 - 1.0×10^{14} molecule cm^{-3}) as the quality of

S_{CH2OO} was significantly compromised at high [NO_2] and signal-to-noise ratios of less than 5 were not uncommon. An example of the data collected in the presence of NO_2 can be seen in Figure 6.20, inset, the bimolecular plot from this data is also shown.

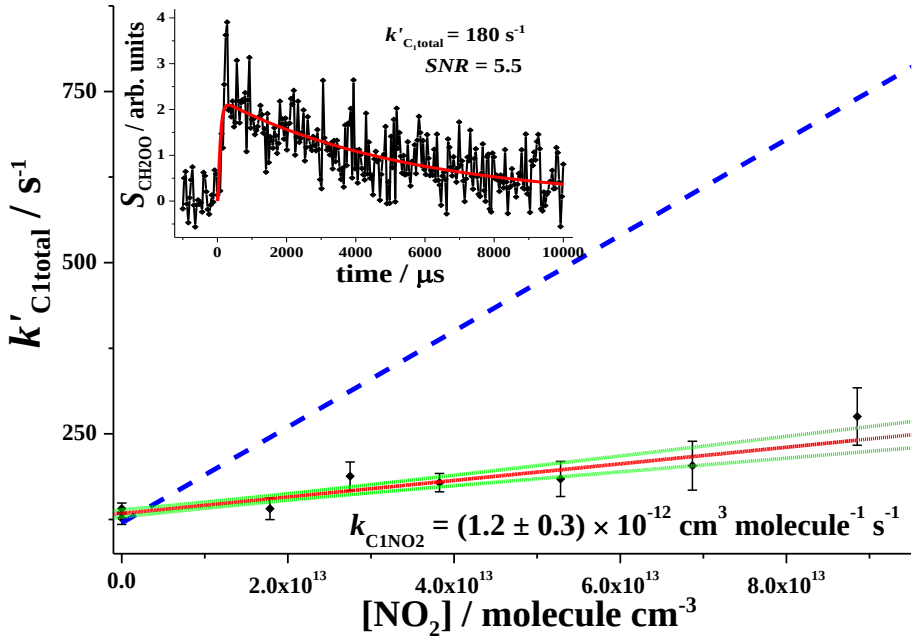

Figure 6.20: A bimolecular plot obtained for the CH_2OO + NO_2 reaction at [NO_2] < 1× 10^{14} molecule cm^{-3}. The blue line is equivalent to $k_{C1NO2} \approx 7 \times 10^{-12}$ cm^3 molecule^{-1} s^{-1}, i.e. the rate coefficient reported in Welz et al. (2012). The error quoted is propagated using the random errors quoted from the experiments (1σ) and a 10% systematic error. (Inset) An example of the Criegee signal measured during the experiments with NO_2. [NO_2] = 3.8 × 10^{13} molecule cm^{-3}; [CH_2OO]$_0$ = 1.5 × 10^{12} molecule cm^{-3}.

From Figure 6.20 it can be seen that the *y*-intercept of the bimolecular plot (i.e. $k'_{C1total}$ in the absence of NO_2) is approximately 150 s^{-1}, this can be used to infer the initial concentration of C_1 CI, [CH_2OO]$_0$. The calculated concentration of CH_2OO present in the system was low, [CH_2OO]$_0$ < 1.5 × 10^{12} molecule cm^{-3}; as the NO_2 concentrations were a kept above [NO_2] > 2× 10^{13} molecule cm^{-3}, all of the experiments were conducted under pseudo first-order conditions. It was also evident that the rate coefficient for the reaction between CH_2OO and NO_2 was relatively small; this was highlighted as only minor changes in the total CH_2OO loss ($k'_{C1total}$) were observed when comparatively large concentrations of NO_2 were added ([NO_2] = 1 × 10^{14} molecule cm^{-3}). From these experiments a rate coefficient of k_{C1NO2} = (1.2 ± 0.3) × 10^{-12} cm^3 molecule^{-1} s^{-1} was determined, and an upper limit of k_{C1NO2} < 2.3 × 10^{-12} cm^3 molecule^{-1} s^{-1}. It was immediately clear from this work that the value of k_{C1NO2} measured is lower from the evaluation in Welz et al. (2012). This is highlighted in Figure 6.20 by the dashed blue line, which is equivalent to the evaluation of the rate coefficient reported in Welz et al. (2012) of $k_{C1NO2} \approx 7 \times 10^{-12}$ cm^3 molecule^{-1} s^{-1}. Both the rate coefficient, k_{C1NO2} = (1.2 ± 0.3) × 10^{-12} cm^3 molecule^{-1} s^{-1}, and the upper limit

determined suggest that rate of the $CH_2OO + NO_2$ reaction is significantly lower than the evaluation by Welz et al. (2012). Conversely, the value of k_{C1NO2} is in good agreement with the indirect rate coefficient reported in Stone et al. (2014) of $k_{C1NO2} = (1.5 \pm 0.4) \times 10^{-12}$ cm^3 molecule^{-1} s^{-1}.

6.1.4.1 C_1 CI + NO_2 Conclusions

The results from this study suggest that any reaction taking place between CH_2OO and NO_2 is relatively slow in comparison to $CH_2OO + SO_2$. That being said, the rate coefficient k_{C1NO2} determined from this study was still several orders of magnitude faster than previously thought (Calvert, 2000). The evaluation of k_{C1NO2} is also significantly smaller than the corresponding rate coefficient reported by Welz et al. (2012), although is of the same order of magnitude. There was some interference evident at high [NO_2] in this study as NO_2 and CH_2OO both have *m/z* = 46; notably, this was not an issue in Welz et al. (2012) as the experiments were conducted using $^{13}CH_2OO$ (*m/z* = 47). It is possible that this NO_2 interference maybe been responsible for the discrepancies in k_{C1NO2} measured. That being said, the bimolecular plot in supporting information of Welz et al. (2012) suggests that the [$^{13}CH_2OO$] used in these experiments was approximately an order of magnitude greater than used in this study. It is therefore feasible that additional reaction channels (possibly I atom chemistry) may lead to the enhanced CH_2OO decay observed. Equally, it should be noted that the experiments reported by Welz et al. (2012) were all completed under pseudo first-order condition so this explanation for the discrepancies is unlikely. However, the results from this study do agree very well with the work of Stone et al. (2014), indicating the lower evaluation of k_{C1NO2} is more reproducible.

6.2 CH_3CHOO Reactivity

6.2.1 Introduction to C_2 Criegee Intermediates

Unlike the C_1 Criegee intermediate, the C_2 CI has two different conformations; they are known as *syn*- and *anti*- conformers. Rotation around the central carbon atom is impeded causing the conformers exhibit distinct chemical properties (see Chapter V, Section 5.1.1 for details). It is understood that the *syn*-conformer is the more stable of the conformations and it is thought to be the formed in greater abundance from CH_3CHI_2 photolysis (~ 90%) (Kuwata et al., 2010, Taatjes, 2013). Work done by Taatjes et al. (2013) established that the stabilized C_2 Criegee biradicals (*syn*-CH_3CHOO and *anti*-CH_3CHOO) both react at a similar rate to the stabilized C_1 Criegee intermediate with both SO_2 and NO_2. Unfortunately, unlike the PIMS set-up used by Taatjes et al. (2013), the Leeds PLP-PIMS system is unable to differentiate between the *syn*- and *anti*- conformers. However, as the *syn*-conformer is

formed more abundantly (~90%) the observed kinetics will be dominated by the reaction of SO_2 with the *syn*-CH_3CHOO, and the rate coefficient determined specific to this reaction. Notably, the reaction between H_2O and *syn*-CH_3CHOO is thought to be orders of magnitude less reactive than the *anti*- conformer and has been estimated to have a rate coefficient between $3 \times 10^{-18} < k_{syn\text{C2H2O}}$ (cm^3 $molecule^{-1}$ s^{-1}) $< 4 \times 10^{-15}$ (Vereecken et al., 2012, Taatjes, 2013). Therefore, if the *syn*-C_2 + H_2O reaction rate is on the lower end of the range given, then the reactions of certain trace gases (such as SO_2 and NO_2) may compete with H_2O as a minor sinks for the C_2 Criegee intermediate in certain environments. Furthermore, as the *syn*-conformer is the more stable conformer and is expected to be formed more abundantly in the atmosphere, understanding the kinetics of this conformer is of greater importance. However, recent work by Newland et al. (2015) suggests that the *syn*-CH_3CHOO may be may undergo significant decomposition within the atmosphere (Newland et al., 2015). Therefore, if the decomposition of the stabilized *syn*-CH_3CHOO is high, the reaction between the C_2 CI and SO_2 may be largely insignificant in the atmosphere.

6.2.2 Experimental

The kinetics of the C_2 Criegee intermediates with SO_2 and NO_2 were, again, studied directly by monitoring the C_2 CI (*m/z* = 60) using time-resolved mass spectrometry. For the C_2 Criegee reactions a CH_3CHI_2/O_2/He/trace gas mixture was used, these experiments were carried out at low pressures (1.0-2.5 Torr) and the gas flows of the helium and oxygen were regulated using mass flow controllers. As with the C_1 Criegee experiments there were problems getting the diiodo-compound to flow through the MFC. To rectify this, the same 'bubbling' procedure was used for the CH_3CHI_2 (Sigma-Aldrich, 98%) as described in Section 6.1.1 (Figure 6.2).

The pathway to the C_2 Criegee intermediate formation can be seen in R6.11-6.13:

$$CH_3CHI_2 + h\nu \rightarrow CH_3CHI + I \quad \text{(R6.11)}$$

$$CH_3CHI + O_2 \rightleftharpoons CH_3CHIO_2^* \rightarrow CH_3CHOO + I \quad \text{(R6.12)}$$

$$CH_3CHI + O_2 \rightleftharpoons CH_3CHIO_2^* + M \rightarrow CH_3CHIO_2 + M \quad \text{(R6.13)}$$

In this section the kinetics of the C_2 Criegee intermediates were investigated with SO_2 and NO_2. Typically 2 - 4% samples of SO_2 and NO_2 (Sigma-Aldrich: 99.9%, 99.5% respectively) were prepared in He and stored in glass bulbs.

For the entirety of this study, diiodo-precursors were initiated by pulsed laser photolysis using an excimer laser (λ = 248 nm, ~50 mJ cm^{-2}) and the gas sampled was photoionized

using λ = 118 nm light (for details see Chapter II). At this photoionization wavelength the kinetics of the *syn*-conformer should be dominant due to its larger concentration, which is estimated to be approximately an order of magnitude greater than the *anti*-conformer (Taatjes, 2013). It should be noted that the photoionization spectra are slightly different for the *syn*- and *anti*- conformers and the *anti*-conformer can be detected at longer ionization wavelengths (~133 nm or ~9.2 eV), meaning the kinetics of both conformers can be measured. However, this was not within the scope of this experiment as the necessary photoionization wavelengths were not attainable.

Again the experiments were controlled using a LabVIEW™ program, designed specifically for data collection and storage from the PIMS apparatus (Baeza-Romero et al., 2012). The data collected was then analysed using OriginPro graphical software to describe the ion signals and was fitted using the equations outlined below (E6.5-6.7). A pseudo-first order bimolecular plot of the data-set was produced by plotting these data points.

$$M_1 = \frac{(S_{\mathrm{C2height}} \times k'_{\mathrm{CH3CHI+O2}} \times k_{\mathrm{samp}})}{(k'_{\mathrm{C2total}} - k'_{\mathrm{CH3CHI+O2}})} \quad \text{(E6.5)}$$

$$M_2 = \frac{e^{-k'_{\mathrm{CH3CHI+O2}} \times t} - e^{-k_{\mathrm{samp}} \times t}}{(k_{\mathrm{samp}} - k'_{\mathrm{CH3CHI+O2}})} - \frac{e^{-k'_{\mathrm{C2total}} \times t} - e^{-k_{\mathrm{samp}} \times t}}{(k_{\mathrm{samp}} - k'_{\mathrm{C2total}})} \quad \text{(E6.6)}$$

$$S_{\mathrm{CH3CHOO}} = M_1 \times M_2 + S_{\mathrm{bg}} \quad \text{(E6.7)}$$

where S_{CH3CHOO} is the time-resolved Criegee signal; S_{C2height} is the maximum height of S_{CH3CHOO}; $k'_{\mathrm{CH3CHI+O2}}$ is the rate of CH_2OO formation; k'_{C2total} is the total loss rate of CH_2OO; k_{samp} is the rate of transportation of the sampled gas to the mass spectrometer (this was held constant during data analysis, k_{samp} = 30000 s^{-1}); t is time; and S_{bg} represents the background signal measured for the individual data traces.

6.2.3 CH_3CHOO Formation

The rate of the $CH_2I + O_2$ reaction, forming the C_1 Criegee intermediate (R6.2), has been previously studied in the literature and a rate coefficient of $k_{\mathrm{CH2I+O2}}$ = (1.28-1.82) × 10^{-12} cm^3 $molecule^{-1}$ s^{-1} has been measured (Enami et al., 2008, Sheps, 2013). The yield of stabilised Criegee intermediates formed from this reaction has also been measured and is estimated to be close to unity at low pressures (Stone et al., 2013). The work by Stone et al. (2013) also highlights the competition between the substitution and association reactions, suggesting that the association reaction (R6.3) is the major channel and the substitution reaction (R6.2), which leads to Criegee formation, is the minor channel (~ 18%) at 760 Torr (Stone et al., 2013):

$$CH_2I + O_2 \rightleftharpoons ICH_2O_2^* \rightarrow CH_2OO + I \quad \text{(R6.2)}$$

$$CH_2I + O_2 \rightleftharpoons ICH_2O_2^* + M \rightarrow ICH_2O_2 + M \qquad \text{(R6.3)}$$

Currently, there is only one published rate coefficient for the reaction between $CH_3CHI + O_2$ (R6.12), where $k_{CH3CHI+O2} = (8.0 \pm 0.8) \times 10^{-12}$ cm^3 molecule^{-1} s^{-1} (Sheps et al., 2014); notably this is approximately 5 times larger than the corresponding reaction for C_1 Criegee formation (R6.2) (Enami et al., 2008). Therefore, it is clear that more work is needed to verify the coefficient for the $CH_3CHI + O_2$ reaction.

Initially, a pseudo first-order study monitoring the I atom (*m/z* =127) was completed, where the concentrations of O_2 were varied from approximately $5 \times 10^{13} - 1 \times 10^{15}$ molecule cm^{-3}, a bimolecular plot of these results was then constructed. However, the analysis of the iodine atom data proved difficult, because the I atom signal was observed to increase at long times in both the presence and the absence of oxygen (Figure 6.21). A possible explanation for this could be poor alignment of the photolysis beam. Consequently, the pseudo first-order rate coefficients determined were highly dependent upon this secondary growth of iodine (Figure 6.22, Left). The data were analysed two different ways: initially, the secondary growth was assumed to be zero and a rate coefficient of $k_{CH3CHI+O2} = (4.7 \pm 0.7) \times 10^{-12}$ cm^3 molecule^{-1} s^{-1} was determined (Figure 6.22, Right). The data were also analysed taking the secondary growth into account, using this approach a larger rate coefficient of $k_{CH3CHI+O2} = (8.6 \pm 1.5) \times 10^{-12}$ cm^3 molecule^{-1} s^{-1} was obtained.

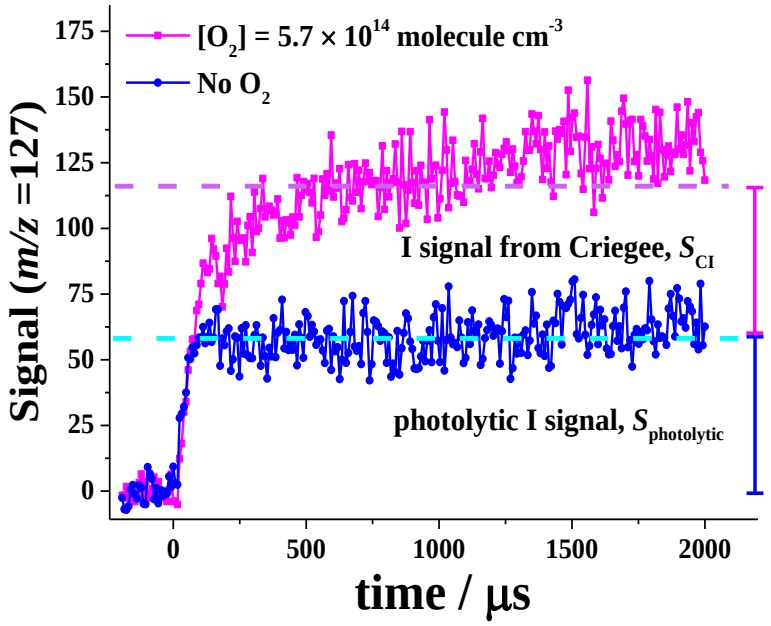

Figure 6.21: A schematic showing diiodoethane photolysis where no oxygen is present (blue line); and in the presence of oxygen (pink), where the addition growth is due to Criegee formation.

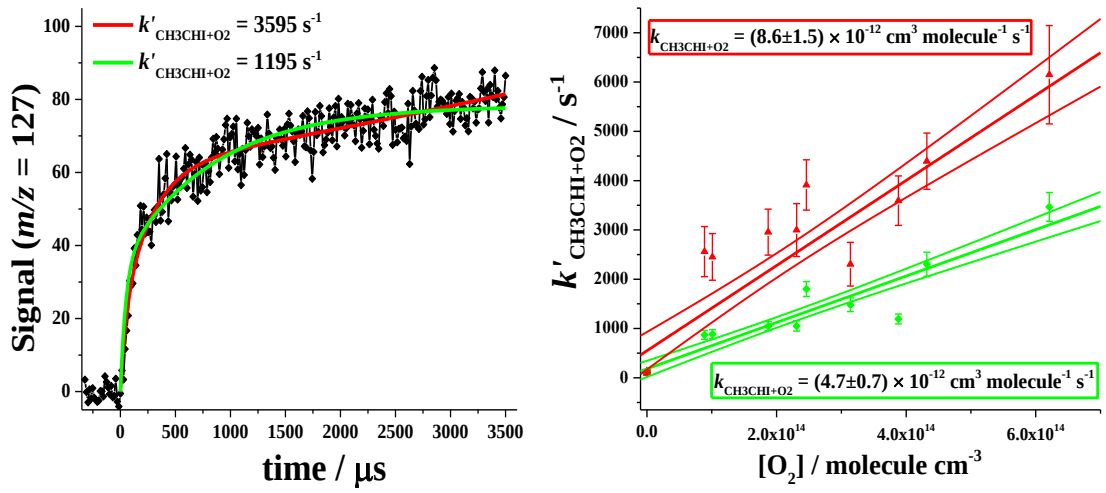

Figure 6.22: (Left) A plot of the I atom signal vs. time, with two different fitting methods used. The red curve takes the secondary growth into account, the green curve does not (Right) The bimolecular plots highlight the differing rate coefficients determined from the different methods of analysis. The linear fittings shown are both unweighted, and the confidence limits are given to 1σ.

To probe the kinetic behaviour of the observed I atom growth at long-times, further experiments were conducted over t = 20 ms. Moreover, higher concentrations of oxygen ($[O_2] \approx 1.5\times 10^{16}$ molecule cm^{-3}) were used simplify analysis; at high oxygen concentrations the pseudo first-order rate coefficient for CI formation will be large ($k'_{CH3CHI+O2} \approx 75000$ s^{-1}) and, therefore, deconvoluted from the kinetics of long-time I atom signal (Figure 6.23).

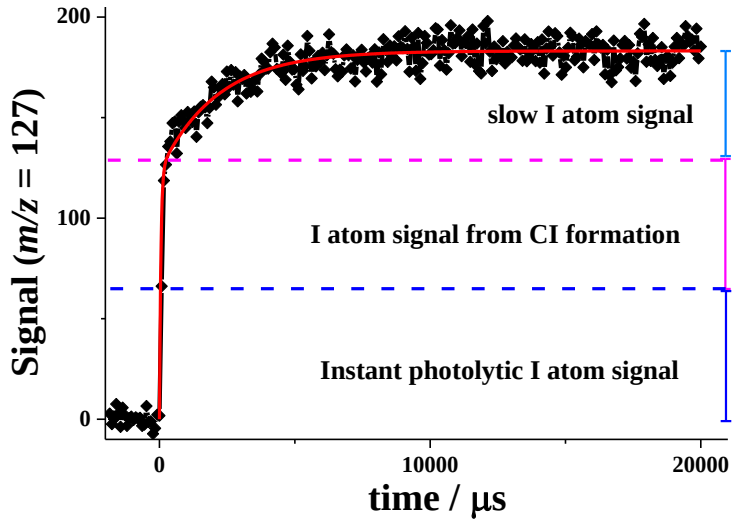

Figure 6.23: A time-profile of the iodine atom signal over 20 ms. At short times (t < 100 μs) the observed I atom signal is cause by both the photolytic and reactive I atom signal. At longer times (t > 100 μs) a slow increase in I atom signals is observed.

From Figure 6.23, it can be seen that the total I atom signal is a combination of three different channels. Analysis of the long-time data sets yields an average rate coefficient for the slow growth of iodine of $k_{slowI} \approx 450$ s^{-1}, this is much larger than the rate of slow iodine

signal observed on the shorter time-scale and suggests the k_{slowI} is dependent upon the oxygen concentration.

One possible explanation for the slow I atom signal is spin-orbit quenching of excited state iodine, I($^2P_{1/2}$) or I*, by oxygen; assuming that the excited state I* has a small ionization efficiency. Notably, the yield of I($^2P_{1/2}$) from CH_2I_2 photolysis (at λ = 248 nm) has been previously determined to be ~45% (Koffend and Leone, 1981). Therefore, assuming CH_3CHI_2 photolyses in a similar manner, the slow growth of iodine observed could be caused by spin-orbit quenching of excited state iodine, I*, by oxygen. However, there were several problems with this hypothesis; firstly, there is no obvious reason why the ionization efficiency of I* would be much smaller than that of I. Secondly, the kinetics of the slow iodine atom signal are far too slow to be caused by O_2 quenching. Note: at this concentration of oxygen, $[O_2] \approx 1.5\times 10^{16}$ molecule cm^{-3}, a pseudo first-order rate coefficient of $k'_{slowI} \approx 500000\ s^{-1}$ would be expected (Derwent et al., 1970), three orders of magnitude larger than was observed from the experiments.

Alternatively, the slow augmentation of the I atom signal may be caused from chemical reaction. During the study it was observed that the diiodoethane precursor had a subtle colour change over time, turning from pale yellow to pale red, suggesting the formation of I_2 in the bubbler. Therefore, the long-time I atom signal could be caused by the reaction of I_2 with the Criegee intermediate (R6.14). This would also explain the possible dependence upon oxygen, as the rate of formation of CIs would also be greater at higher oxygen concentrations.

$$CH_3CHOO + I_2 \rightarrow CH_3CHO + IO + I \qquad \text{(R6.14)}$$

$$IO + IO \rightarrow OIO + I \qquad \text{(R6.15)}$$

It should be highlighted that the CI chemistry cannot account for all of the long-time I atom signal as the pseudo first-order loss rates of CH_3CHOO, $k'_{C2total}$, monitored at *m/z* =46 were consistently at least three times lower, $k'_{C2total} < 150\ s^{-1}$; moreover, some of the CIs are predicted to undergo self-reaction, and wall losses are also possible.

The slow I atom signal could also be from reaction or decomposition of any stabilised ICH_3CHO_2 present in the system (R6.16a-6.16b). However, this cannot be a major channel for slow I atom growth, as the relative ratio of the photolytic signal compared to the combined CI + slow I signal is greater than 1:1 (see Figure 6.23) and theoretically, this is not possible (see R6.11-6.13). However, reactions R6.14-6.16 are examples of reactions that would lead to the formation of iodine atoms at long-times.

$$ICH_3CHO_2 + X \rightarrow I + \text{Products} \qquad \text{(R6.16a)}$$

$$ICH_3CHO_2 \rightarrow I + \text{Products} \quad \text{(R6.16b)}$$

In reaction R6.16a, X represents any radical that could lead to the production of I by reacting with ICH_3CHO_2.

Following the investigation into the long-time I atom signal, a global data analysis was performed to fit both the rate coefficients for C_2 Criegee formation and the long-time I atom signal simultaneously (E6.8-6.13).

$$k'_{\mathrm{CH3CHI+O2}} = (k_{\mathrm{CH3CHI+O2}} \times [O_2]) \quad \text{(E6.8)}$$

$$Y_{\mathrm{SCI}} = \frac{S_{\mathrm{CI}}}{S_{\mathrm{photolytic}}} \quad \text{(E6.9)}$$

$$M_1 = \frac{(S_{\mathrm{CI}} \times k'_{\mathrm{CH3CHI+O2}} \times k_{\mathrm{eff}})}{(k_{\mathrm{slowI}} - k'_{\mathrm{CH3CHI+O2}})} \quad \text{(E6.10)}$$

$$M_2 = \frac{e^{-k'_{\mathrm{CH3CHI+O2}} \times t} - e^{-k_{\mathrm{eff}} \times t}}{(k_{\mathrm{eff}} - k'_{\mathrm{CH3CHI+O2}})} - \frac{e^{-k_{\mathrm{slowI}} \times t} - e^{-k_{\mathrm{eff}} \times t}}{(k_{\mathrm{eff}} - k_{\mathrm{slowI}})} \quad \text{(E6.11)}$$

$$M_3 = \frac{(S_{\mathrm{photolytic}} \times k_{\mathrm{eff}})}{(k_{\mathrm{eff}} - k_{\mathrm{slowI}})} \times \left(e^{-k_{\mathrm{slowI}} \times t} - e^{-k_{\mathrm{eff}} \times t}\right) \quad \text{(E6.12)}$$

$$S_{\mathrm{Iatom}} = M_1 \times M_2 + M_3 + S_{\mathrm{bg}} \quad \text{(E6.13)}$$

Several new parameters have been introduced in E6.8-6.13: S_{Iatom} is the time-resolved iodine signal; $k_{\mathrm{CH3CHI+O2}}$ is the rate coefficient of the Criegee formation; k_{slowI} is the rate coefficient for the slow iodine formation; Y_{SCI} is equivalent to the yield of stabilised CIs formed; S_{CI} represents the I atom signal height caused by Criegee intermediate formation; $S_{\mathrm{photolytic}}$ is equal to the signal height for the photolytic I atom signal observed; and S_{bg} represented the background signal at $m/z = 127$. For the purpose of this analysis the following parameters were shared globally: $k_{\mathrm{CH3CHI+O2}}$, k_{slowI}, k_{samp}, Y_{SCI}; additionally, k_{samp} was held constant at 20000 s^{-1}. Using this methodology a rate coefficient for C_2 CI formation (R6.12) of $k_{\mathrm{CH3CHI+O2}} = (8.4 \pm 1.2) \times 10^{-12}$ cm^3 $molecule^{-1}$ s^{-1} was determined.

Another advantage of using the global analysis is that an estimation of the of the stabilised CI yield, Y_{SCI}, could also be calculated (E6.9). For this analysis the yield of stabilised C2 CIs can be considered as the relative height of the iodine signal from Criegee formation (R6.12) compared to the height of the photolytic I signal formed in R6.11 (see Figure 6.21, E6.9). From the global analysis of these experiments a high stabilised C_2 CI yield of $Y_{\mathrm{SCI}} = (86 \pm 11)$ %, was determined at ~2 Torr.

6.2.3.1 $CH_3CHI + O_2$ Conclusions

From this study a rate coefficient for the formation of the C_2 Criegee intermediate of $k_{CH3CHI+O2}$ = (8.4±1.2) × 10^{-12} cm^3 $molecule^{-1}$ s^{-1} was measured, this is excellent agreement with the rate coefficient previously reported by Sheps et al. (2014) of $k_{CH3CHI+O2}$ = (8.0±0.8) × 10^{-12} cm^3 $molecule^{-1}$ s^{-1}. This work has also determined that the yield of stabilised C_2 Criegee intermediates formed at low pressure is high, Y_{SCI} = (86 ± 11) %. This yield is lower than the equivalent yield of stabilised C_1 CIs, which is close to unity (Stone et al., 2013). However, due to the greater (statistical) distribution of energy within the nascent ICH_3CHO_2*, stabilisation to ICH_3CHO_2 would be more favourable than the corresponding stabilisation of ICH_2O_2*; hence the lower yield of stabilised the C_2 CIs is to be expected. Unfortunately, it was not possible to investigate the pressure dependence of this reaction using the PIMS set-up but it seems likely that the Y_{SCI} will decrease as the pressure increases (R6.13). Reactions R6.11-6.12 contribute only very little to C_2 CI formation within the atmosphere; however, it is possible that in marine environments, where halogenated organic compounds are abundant, reactions similar to this will play a role in CI production (Stone et al., 2013). Therefore it is important that work is done to try to understand the pressure dependence of the yield of stabilised CH_3CHOO formed.

6.2.4 $CH_3CHOO + SO_2$

The reaction between $CH_3CHOO + SO_2$ has been studied closely in recent years (Taatjes, 2013). Similarly to the C_1 Criegee intermediate, the rate coefficient of this reaction has been found to be several orders of magnitude larger than earlier measurements indicated (Taatjes, 2013). Crucially, the reaction between $CH_3CHOO + SO_2$ potentially represents a possible oxidation pathway for sulphur from the $S_{(IV)}$ oxidation state to $S_{(VI)}$, which is a key step in the formation of H_2SO_4 in the atmosphere. However, this is highly dependent on the mechanism of the C_2 CI + SO_2 reaction, over which there is still some ambiguity (R6.17a-6.17b).

$$CH_3CHOO + SO_2 \rightarrow CH_3CHO + SO_3 \quad \text{(R6.17a)}$$

$$CH_3CHOO + SO_2 \rightarrow \text{secondary ozonide / adduct} \quad \text{(R6.17b)}$$

Theoretical studies have predicted that the reaction of larger Criegee intermediates with SO_2 will be pressure dependent (Vereecken et al., 2012). It has also been hypothesised that at atmospheric pressure, and assuming a statistical distribution of energy, the larger Criegee-SO_2 intermediate complexes are likely to stabilise to a secondary ozonide species (SOZ); therefore the production of SO_3 in reactions of larger Criegee intermediates is unlikely. This means the impacts of SO_2 + Criegee intermediate reactions on H_2SO_4 and sulphate aerosol

production will be reduced for larger CIs. That said, field observations from a Finnish boreal forest indicate that larger Criegee intermediates, such as those produced monoterpene ozonolysis, still have some impact on atmospheric concentrations of H_2SO_4 from SO_2 oxidation (Mauldin et al., 2012). However, further work is still required to investigate both the products and pressure dependence of the reactions of larger Criegee intermediates. The aim of this study was to try to better understand the kinetics and the mechanism of this reaction; in particular to identify some of the products of this reaction at the low pressure limit.

Due to its lower volatility, it was difficult to get significant quantities of 1,1-diiodoethane into the reactor. An advantage of this was that the concentration of CH_3CHOO was kept relatively low. The exact initial concentrations for these experiments were unknown, but can be conservatively estimated to be $[CH_3CHOO]_0 < 2.0 \times 10^{12}$ molecule cm^{-3}. It should be noted that this evaluation is based upon a pseudo first order rate coefficient for the C_2 CI self-reaction of k'_{C2SR} = 100 s^{-1}, and a bimolecular rate coefficient of $k_{C2SR} > 5 \times 10^{-11}$ molecule^{-1} cm^{-3} s^{-1}; given that rate of the CH_2OO self-reaction is $k_{C1SR} \approx 7 \times 10^{-11}$ molecule^{-1} cm^{-3} s^{-1}, this estimation does not seem unreasonable.

The disadvantage of working with low concentrations of CH_3CHOO was that the quality of the data collected was poor; signal-to-noise-ratios as low as ~5 were not uncommon (minimum required *SNR* of 3). A range of different concentrations of SO_2 were added to the system and a bimolecular plot was constructed (Figure 6.24). It should be noted that the $[SO_2]$ was kept in excess to ensure pseudo first-order conditions were met.

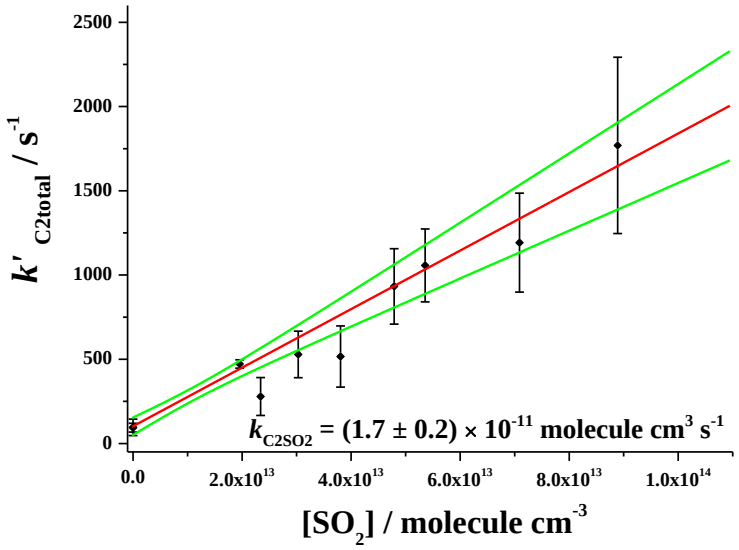

Figure 6.24: A bimolecular plot of the reaction between *syn*-CH_3CHOO and SO_2. The error quoted is propagated using the random errors quoted from the experiments (1σ) and a 10% systematic error.

From Figure 6.24, a bimolecular rate coefficient for the reaction between CH_3CHOO and SO_2 of $k_{C2SO2} = (1.7 \pm 0.2) \times 10^{-11}$ molecule^{-1} cm^{-3} s^{-1} was determined. As previously stated, at the photoionization energies used for the experiment, it is predominantly the reactivity of the *syn*-CH_3CHOO conformer which is probed (Taatjes, 2013). As can be seen from Table 6.9, this evaluation of the rate coefficient compares favourably to other recent studies (Taatjes, 2013, Sheps et al., 2014, Smith et al., 2014). Although the rate coefficient determined from this work is generally lower than the other recommended values, it is within error of the rate coefficient measured by Smith et al. (2014) of $k_{C2SO2} = (2.0 \pm 0.3) \times 10^{-11}$ cm^3 molecule^{-1} s^{-1}.

Table 6.9: Recent evaluations of k_{C2SO2} from literature.

k_{C2SO2} / 10^{-11} cm^3 molecule^{-1} s^{-1}	Reference
2.4 ± 0.3	Taatjes et al. (2013)
2.0 ± 0.3	Smith et al. (2014)
2.9 ± 0.3	Sheps et al. (2014)
1.7 ± 0.2	**This Work**

From Figure 6.24 it can also be seen that the *y*-intercept of the plot is small, $k'_{C2total} = (102 \pm 50)$ s^{-1}; the *y*-intercept of the bimolecular plot (Figure 6.24) is equal to all of the C_2 CI loss processes, which includes wall losses, self-reaction and unimolecular decomposition. Notably, this means the rate of decomposition, k_d, must be below ~100 s^{-1}; this is lower than the evaluation of k_d for the *syn*-conformer made by Newland et al. (2015) of $k_d = (288 \pm 275)$ s^{-1}, although due to the larger uncertainty quoted by Newland et al. (2015) the measurements are not significantly different. Furthermore, the self-reaction and wall losses are thought to contribute to the value of the *y*-intercept, suggesting that the rate of decomposition must be less than $k_d \approx 100$ s^{-1}. Previous experiments indicate that wall losses in the system are $k_{wall} \approx 50$ s^{-1}, meaning a rate coefficient for unimolecular decomposition of $k_d \leq 50$ s^{-1}.

A major advantage of using the PIMS set-up is that multiple species may be monitored simultaneously, meaning that it was possible to investigate the products of the reaction as well. It is understood that at low pressures the primary products of the reaction will be $CH_3CHO + SO_3$ (Figure 6.25); in fact evidence of SO_3 production had previously been observed by Taatjes et al. (2013), however, no study has ever reported acetaldehyde as a product from this reaction.

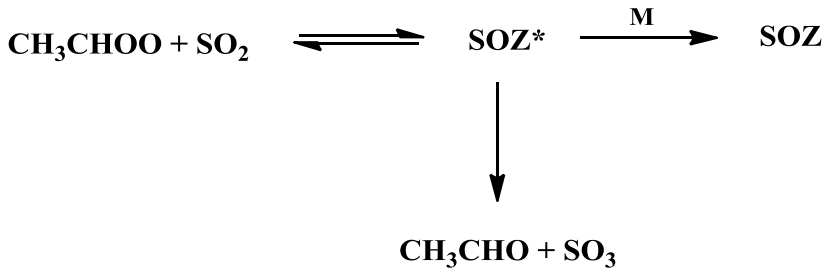

Figure 6.25: A diagram of the proposed reaction scheme of the C_2 CI with SO_2. Note: SOZ refers to secondary ozonide.

In addition to the Criegee signal, $S_{CH3CHOO}$, recorded at *m/z* = 60, a second signal was also observed at *m/z* = 44. Notably, the signal was comprised of a small instant growth and a slower secondary growth (i.e. one formed by chemical reaction). More interestingly still, the kinetics of the *m/z* = 44 signal appeared to be anti-correlated to the observed CH_3CHOO signal (*m/z* = 60), suggesting that the signal at *m/z* = 44 was formed as CH_3CHOO was consumed (Figure 6.26). Due to the mass of the species (*m/z* =44) it was assumed that this signal was caused by acetaldehyde, which was an expected product from the reaction at low pressures (Figure 6.25). Additionally, it was also noted that there was a very slow increase in the CH_3CHO signal at $[SO_2]$ = 0 molecules cm^{-3}. It is suspected that this slow increase in the CH_3CHO signal was due to the self-reaction of the C_2 CI. Upon analysis a rate coefficient of k_g = (51±30) s^{-1} was obtained for the slow growth at *m/z* = 44. This results suggest an upper limit for unimolecular decomposition of $k_d < 79$ s^{-1} (if it is assumed $k_w = 0$) and indicates that k_d for the *syn*-C_2 CI is in agreement with the previous estimation of rate of unimolecular decomposition by Novelli et al. (2014) of $3 < k\ (s^{-1}) < 30$.

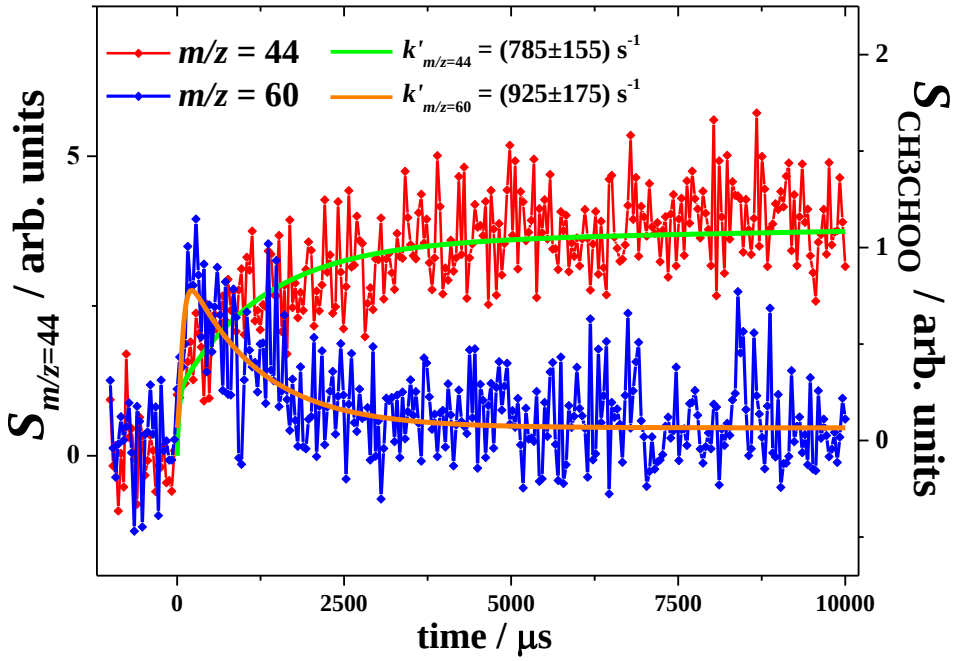

Figure 6.26: A plot showings CH_3CHOO decay, $S_{m/z=60}$, and the simultaneous formation of a species at *m/z* = 44, $S_{m/z=44}$, assumed to be acetaldehyde. The orange and green lines are the fittings to the *m/z*=60 and the *m/z*=44 data respectively.

Following the preliminary analysis, the relationship observed between the two species was compelling. However, to try and verify whether the two species are anti-correlated, a globally fitting function was used. Unlike the previous global fitting methods described (E6.1-6.4), the function must fit both the *m/z* = 60 signal and the *m/z* = 44 signal simultaneously. To fit both data-sets the equations previously used required significant adaptation, including the addition of a second 'z' parameter (*z1*) within the spreadsheet and an if-statement to allow the correct function to be selected for the CH_3CHOO and CH_3CHO data respectively (E6.14-6.23):

If *z1* = 1:

$$k'_{\mathrm{C2total}} = (k_{\mathrm{C2SO2}} \times [\mathrm{SO_2}]) + k_{\mathrm{w}} + k_{\mathrm{X}} \quad \text{(E6.14)}$$

$$M_1 = \frac{(S_{\mathrm{C2height}} \times k'_{\mathrm{C2+O2}} \times k_{\mathrm{eff}})}{(k'_{\mathrm{C2total}} - k'_{\mathrm{C2+O2}})} \quad \text{(E6.15)}$$

$$M_2 = \frac{e^{-k'_{\mathrm{C2+O2}} \times t} - e^{-k_{\mathrm{eff}} \times t}}{(k_{\mathrm{eff}} - k'_{\mathrm{C2+O2}})} - \frac{e^{-k'_{\mathrm{C2total}} \times t} - e^{-k_{\mathrm{eff}} \times t}}{(k_{\mathrm{eff}} - k'_{\mathrm{C2total}})} \quad \text{(E6.16)}$$

$$S_{\mathrm{CH3CHOO}} = M_1 \times M_2 + S_{\mathrm{bg}} \quad \text{(E6.17)}$$

If *z1* = 2:

$$k'_{\mathrm{CH3CHO}} = (k_{\mathrm{C2SO2}} \times [\mathrm{SO_2}]) + k_{\mathrm{w}} + k_{\mathrm{X}} \quad \text{(E6.18)}$$

$$S_{\mathrm{CH3CHOheight}} = S_{\mathrm{C2height}} \times A \times \left(\frac{(k_{\mathrm{C2SO2}} \times [\mathrm{SO_2}]) + k_{\mathrm{X}}}{k'_{\mathrm{CH3CHO}}}\right) \quad \text{(E6.19)}$$

$$N_1 = \frac{(S_{\mathrm{CH3CHOheight}} \times k'_{\mathrm{CH3CHO}} \times k_{\mathrm{eff}})}{(k'_{\mathrm{LossCH3CHO}} - k'_{\mathrm{CH3CHO}})} \quad \text{(E6.20)}$$

$$N_2 = \frac{e^{-k'_{\mathrm{CH3CHO}} \times \mathrm{t}} - e^{-k_{\mathrm{eff}} \times \mathrm{t}}}{(k_{\mathrm{eff}} - k'_{\mathrm{CH3CHO}})} - \frac{e^{-k'_{\mathrm{LossCH3CHO}} \times \mathrm{t}} - e^{-k_{\mathrm{eff}} \times \mathrm{t}}}{(k_{\mathrm{eff}} - k'_{\mathrm{LossCH3CHO}})} \quad \text{(E6.21)}$$

$$N_3 = \frac{(S_{\mathrm{instant}} \times k_{\mathrm{eff}})}{(k_{\mathrm{eff}} - k'_{\mathrm{LossCH3CHO}})} \times \left(e^{-k_{\mathrm{LossCH3CHO}} \times \mathrm{t}} - e^{-k_{\mathrm{eff}} \times \mathrm{t}}\right) \quad \text{(E6.22)}$$

$$S_{\mathrm{CH3CHO}} = N_1 \times N_2 + N_3 + S_{\mathrm{bg2}} \quad \text{(E6.23)}$$

A number of new parameters have been introduced in E6.14-6.23: k'_{CH3CHO} is the rate coefficient of the acetaldehyde formation; k_{X} is the rate coefficient of other reactions which contribute to the production of CH_3CHO (e.g. C_2 CI self-reaction); k_{w} is the non-chemical contributions to CH_3CHOO loss (such as wall reactions); $S_{\mathrm{CH3CHOheight}}$ is height of the CH_3CHO signal; A is a scaling factor; $k_{\mathrm{LossCH3CHO}}$ is equivalent to loss rate of acetaldehyde; S_{instant} is the signal height of any instant CH_3CHO observed; and S_{bg2} represented the background signal at m/z = 44.

Using the equations E6.14-6.23, it was possible to fit the whole data-sets for both CH_3CHOO and CH_3CHO simultaneously, and as many of the parameters as possible were shared in the analysis: k_{C1SO2}, k_{X}, k_{w}, $k_{\mathrm{CH2I+O2}}$, k_{samp}, $k_{\mathrm{LossCH3CHO}}$, A. Some of the parameters were kept constant (k_{samp}, S_{bg} and S_{bg2}) and the rest were allowed to float during the iterations of the fitting until χ^2 was minimised. Using this technique a rate coefficient of $k_{\mathrm{C2SO2}} = (1.8 \pm 0.3) \times 10^{-11}$ cm^3 molecule^{-1} s^{-1} was evaluated. At first, the value of k_{C2SO2} determined was very sensitive to S_{instant}, the precise value of which was unknown; however, an estimate of S_{instant} could be deduced from traces where $[SO_2] = 0$ molecule cm^{-3}. The values of S_{instant} observed in these experiments were then used to constrain the global fitting, reducing the uncertainty of the fitting. The rate coefficient determined using this methodology is in agreement with both the earlier work from this study and with literature values (Taatjes, 2013, Smith et al., 2014).

As mentioned above, it was apparent that there were several channels adding to the signal observed at m/z = 44. To determine if any acetaldehyde was produced from CH_3CHOO + SO_2, alternative equations were used in the global analysis for both the rate of acetaldehyde formation and the yield of acetaldehyde (E6.18b-6.19b). Notably, these equations suggest that acetaldehyde formation is entirely independent of the CH_3CHOO + SO_2 reaction.

$$k'_{\mathrm{CH3CHO}} = k_{\mathrm{w}} + k_{\mathrm{X}} \quad \text{(E6.18b)}$$

$$S_{\mathrm{CH3CHOheight}} = S_{\mathrm{C2height}} \times A \times \left(\frac{k_{\mathrm{X}}}{k'_{\mathrm{CH3CHO}}}\right) \qquad \text{(E6.19b)}$$

Whilst using E6.18b-6.19b to fit the data it became apparent that these equations could not produce a good fit to the data, much worse than equations E6.18-6.19 (Figure 6.27). As the as better fit to the data is yielded from the E6.18-6.19, it suggests the acetaldehyde signal is dependent on the CH_3CHOO + SO_2 reaction. Therefore, this reaction must be partially responsible for the signal at *m/z* = 44, proving that these species are correlated with each other.

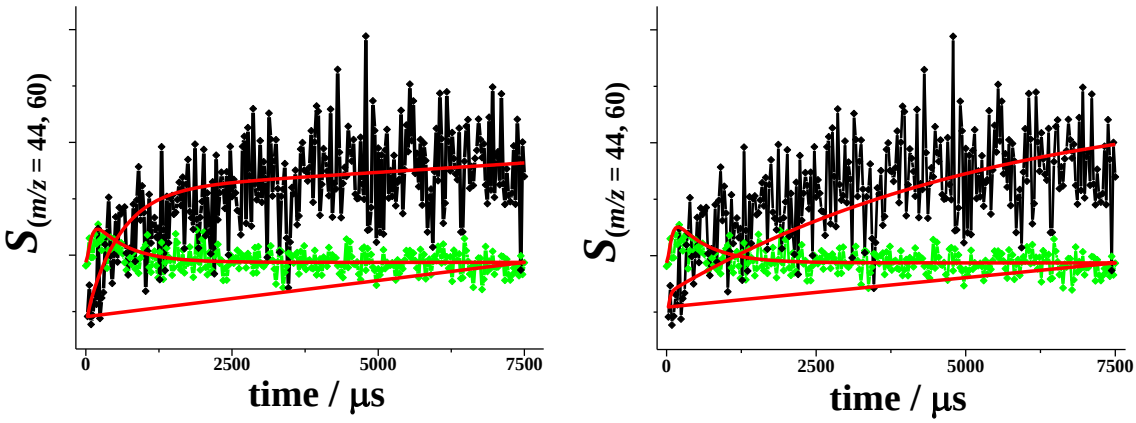

Figure 6.27: (Left) A plot of the data used the Criegee dependent equations (E6.20-6.21); (Right) A plot of the data, here the Criegee independent equations were used to fit the data (E6.20a-6.21a).

It should be noted that other possible products (i.e. SO_3 and the secondary ozonide species) from the reaction were searched for, although none were found. This is not entirely surprising as the ionization potential of SO_3 is ~13 eV (Snow and Thomas, 1990). There was also no sign of the secondary ozonide at *m/z* = 124, this was very close to the I atom signal at *m/z* = 127 (a very large and broad peak); it is therefore plausible that signal from the SOZ may have been masked by this signal. It is also possible that any SOZ formed was fragmented by the photoionization beam. In fact the acetaldehyde observed is actually produced during photoionization rather than by unimolecular decomposition of the SOZ species (see Figure 6.25). That said, as all of the experiments were conducted at low pressures (p < 2.5 Torr) it is thought that decomposition channel will be dominant under these condition. If more time was available, experiments would have been conducted to test whether the CH_3CHO was formed was from photoionization or decomposition; during these experiments a scavenger for CH_3CHO would be added to the system (such as OH radicals). If the CH_3CHO was formed by decomposition, the CH_3CHO would react with the scavenger and the signal at *m/z* = 44 would be depleted. However, if the CH_3CHO was

formed during photoionization, there would be insufficient time for any scavenging to occur and signal at m/z = 44 would persist.

6.2.4.1 C_2 CI + SO_2 Conclusions

The results from this study suggest that the rate coefficient of the reaction between the *syn*-C_2 Criegee and SO_2 is k_{C2SO2} = (1.8 ± 0.3) × 10^{-11} molecule^{-1} cm^{-3} s^{-1}. This value is marginally lower than others found in literature; however it is just within error of the *syn*-C_2 Criegee + SO_2 rate coefficient measured by Taatjes et al. (2013), where k_{C2SO2} = (2.4 ± 0.3) × 10^{-11} molecule^{-1} cm^{-3} s^{-1}. From this study some of the low pressure products of the reaction have been identified. In particular, a strong anti-correlation was observed between the CH_3CHOO and a species at m/z = 44. By using a global fitting it was made clear that the species was formed as the C_2 CI reacts with SO_2, and given the mass, this species is most likely CH_3CHO. This result verifies prior observations made by Taatjes et al. (2013). Significantly, it suggests that (at low pressures) this reaction leads to the formation of SO_3 and the oxidation of sulphur from the $S_{(IV)}$ to the $S_{(VI)}$ is a crucial step to the formation of H_2SO_4 in the atmosphere. However, it is unlikely that this is the major pathway for this reaction at atmospherically relevant pressures, but it could still play minor role.

Additionally, this study also suggests a decomposition rate coefficient for the *syn*-C_2 CI of k_d < 79 s^{-1}, this evaluation is in good agreement with the evaluation made by Novelli et al. (2014) and is not significantly different from the k_d value reported for *syn*-C_2 CI decomposition in Newland et al. (2015).

6.2.5 CH_3CHOO + NO_2

The final reaction explored during this study was that between the C_2 Criegee intermediate and NO_2. This reaction has been previously studied and is thought to react significantly slower than the corresponding C_1 Criegee + NO_2 reaction. The same methodology was used for this study as is described in Section 6.5.2, with CH_3CHOO being monitored directly at m/z = 60. As with the C_1 CI reaction, it was evident that any reaction occurring between these reactants was only very minor. Indeed, even upon adding large concentrations of NO_2, [NO_2] = 2.5 × 10^{14} molecule cm^{-3}, the change in the total Criegee loss rate ($k'_{C2total}$) was only just significantly larger than experiments run in the absence of NO_2; leading to an upper limit of k_{C2NO2} < 1.2 × 10^{-12} molecule^{-1} cm^{-3} s^{-1} for the rate coefficient of the *syn*-C_2 CI + NO_2 reaction.

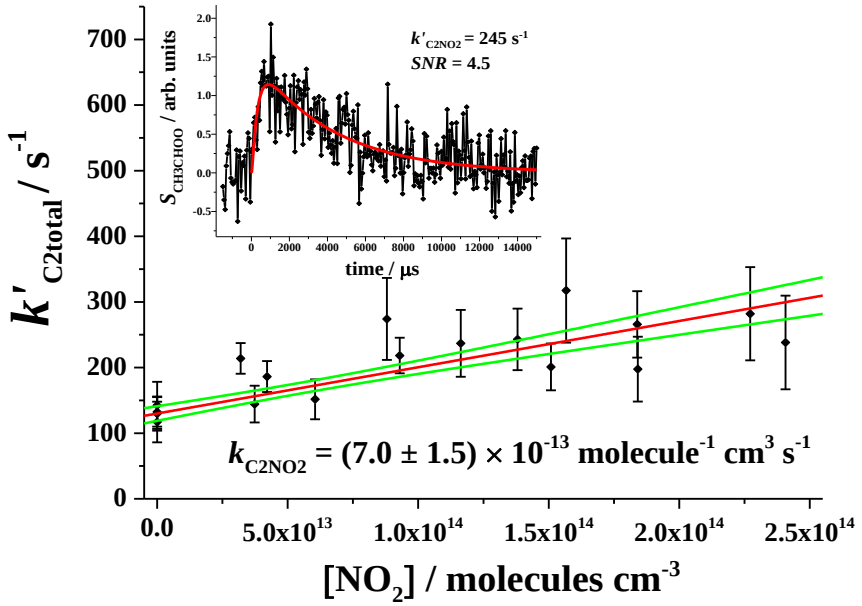

Figure 6.28: A bimolecular plot from the results of the C_2 CI + NO_2 reaction. The confidence limits are at the 1σ level, the error quoted is propagated using the random errors quoted from the plot (1σ) and a 10% systematic experimental error. (Inset) An example of the Criegee signal, $S_{CH3CHOO}$, measured during the experiments with NO_2. $[NO_2] = 1.3 \times 10^{14}$ molecule cm^{-3}.

The results from this study were used to produce a bimolecular plot (Figure 6.28). From Figure 6.28 a C_2 CI concentration of $[CH_3CHOO] \approx 2.5 \times 10^{12}$ molecule cm^{-3} is estimated from the *y*-intercept; however, it is thought that pseudo first-order conditions were upheld due to the large concentrations of NO_2 that were added. From this plot a rate coefficient of $k_{C2NO2} = (7.0 \pm 1.5) \times 10^{-13}$ $molecule^{-1}$ cm^{-3} s^{-1} was determined for the *syn*-CH_3CHOO + NO_2 reaction. The results from these experiments suggest that it is only just possible to say that any significant reactivity was observed, however the rate coefficient retrieved compares relatively well to the other literature evaluations; Taatjes et al. (2013) suggest a value of $k_{C2NO2} = (2 \pm 1) \times 10^{-12}$ $molecule^{-1}$ cm^{-3} s^{-1}. The products of this reaction were also probed. Previous theoretical and experimental work suggests that, unlike the C_2 CI + SO_2 reaction, a CH_3CHOO-NO_2 adduct is formed in this reaction, even at low pressures (Taatjes, 2013). Unfortunately, there was no sign of this species; although there was evidence of CH_3CHO present in the system. However, the quality of the data was low and hence the correlation between Criegee destruction and acetaldehyde formation was not as clear for the C_2 CI + NO_2 reaction; the global fitting procedure was utilised to establish whether acetaldehyde was formed in the CH_3CHOO + NO_2 reaction. The data was fitted using equations (E6.24-6.25) and then using (E6.24b-6.25b):

Scenario 1: Acetaldehyde formation is dependent on k_{C2NO2}

$$k'_{CH3CHO} = (k_{C2NO2} \times [NO_2]) + k_w + k_X \quad \text{(E6.24)}$$

$$S_{\mathrm{CH3CHOheight}} = S_{\mathrm{C2height}} \times A \times \left(\frac{(k_{\mathrm{C2NO2}} \times [\mathrm{NO_2}]) + k_{\mathrm{X}}}{k'_{\mathrm{CH3CHO}}}\right) \quad \text{(E6.25)}$$

Scenario 2: Acetaldehyde formation is independent on k_{C2NO2}

$$k'_{\mathrm{CH3CHO}} = k_{\mathrm{w}} + k_{\mathrm{X}} \quad \text{(E6.24b)}$$

$$S_{\mathrm{CH3CHOheight}} = S_{\mathrm{C2height}} \times A \times \left(\frac{k_{\mathrm{X}}}{k'_{\mathrm{CH3CHO}}}\right) \quad \text{(E6.25b)}$$

For the C_2 Criegee + NO_2 reaction, both equations (E6.24-6.25) and (E6.24b-6.25b) gave equally good fits to the data. Furthermore, both fittings yielded much smaller rate coefficients ($k_{C2NO2} \approx (2 - 5) \times 10^{-13}$ cm^3 molecule^{-1} s^{-1}). This implies that the previous estimate the upper limit for this reaction, $k_{C2NO2} < 1.2 \times 10^{-12}$ molecule^{-1} cm^{-3} s^{-1}, may be an over-estimation for the C_2 CI + NO_2 reaction. It is also evident from these fittings that both set of equations are capable of describing the growth of acetaldehyde. This suggests that the acetaldehyde formation may be independent of the reaction between CH_3CHOO and NO_2; however, the equations E6.24-6.25 also yield a reasonable fit to the data so this cannot be stated conclusively. As the quality of the data was low (*SNR* ≈ 3), it is impossible to say anything definitive about this.

6.2.5.1 C_2 CI + NO_2 Conclusions

For the reaction between the *syn*-C_2 Criegee and NO_2, a rate coefficient of $k_{C2NO2} = (7.0 \pm 1.5) \times 10^{-13}$ cm^3 molecule^{-1} s^{-1} was determined, with an upper limit of $k_{C2NO2} < 1.2 \times 10^{-12}$ molecule^{-1} cm^{-3} s^{-1} recommended. The results of this study compare reasonably well to other literature evaluations, which reported a rate coefficient of $k_{C2NO2} = (2 \pm 1) \times 10^{-12}$ molecule^{-1} cm^{-3} s^{-1} for the *syn*-C_2 Criegee + NO_2 reaction (Taatjes, 2013). An acetaldehyde signal was again observed after $t = 0$ s; little could be said about this signal as the quality of the data was poor. However, unlike the C_2 CI + SO_2 reaction, the acetaldehyde formation is potentially independent of the CH_3CHOO + NO_2 reaction.

6.3 Atmospheric Implications

The atmospheric implications of the reactions studied in this chapter depend largely upon Criegee reactivity towards water and its dimer. However, for the C_1 Criegee intermediate, even when very conservative estimates for the water and water dimer rate coefficients are used, reactions with water dimer + monomer are still predicted to be the overwhelmingly dominant sinks for CH_2OO (Vereecken et al., 2012, Lewis et al., 2015, Anglada and Sole, 2016).

However, the rate coefficient for the *syn*-CH_3CHOO + H_2O is known to be extremely slow and has an estimated rate coefficient of $2.5 \times 10^{-18} < k_{C2H2O} < 4.5 \times 10^{-15}$ cm^3 $molecule^{-1}$ s^{-1} (Taatjes, 2013, Vereecken et al., 2012). This means that potentially the reactions of NO_2 and SO_2 may be minor sinks for the *syn*-C_2 Criegee intermediate. Again, it should be highlighted that, as the *syn*- conformer is expected to be formed more abundantly in marine environments, understanding the kinetics of this conformer is of greater importance for these regions.

Due to its greater atmospheric abundance, the reaction of NO_2 has more potential as a sink for the C_2 Criegee (Brasseur et al., 1999, Vereecken et al., 2012); however, because k_{C2NO2} is so small, this channel is assumed to be almost negligible. It is possible that in dry, but polluted environments, reaction with NO_2 may occur, although any such reactivity would still only be very minor (Vereecken et al., 2012). That being said, using the rate coefficients measured in this work it is estimated that the reaction with NO_2 would be responsible for a maximum of 0.5% of *syn*-CH_3CHOO destruction, even in the most polluted environments (e.g. high [NO_x]). Note: this is using an estimate of the *syn*-C_2 CI + H_2O rate coefficient of $k_{synC2H2O} = 2\times 10^{-17}$ cm^3 $molecule^{-1}$ s^{-1}; this rate coefficient is an approximate average of those reported in Vereecken et al. (2012) and Sheps (2013). The *syn*-C_2 CI + $(H_2O)_2$ rate constant was estimated using a conversion factor from Vereecken et al. (2012) (Anglada et al., 2011, Ryzhkov and Ariya, 2004).

In polluted environments, such as mega cities, it is plausible that the C_2 CI + SO_2 reaction may be a minor channel for the *syn*-CH_3CHOO destruction (Table 6.10). For example, in Beijing, China an average concentration of SO_2 of $[SO_2] > 2.5 \times 10^{11}$ molecule cm^{-3} was recorded (Lin et al., 2012); under these conditions the reaction with SO_2 may be responsible for ~2% of the *syn*-CH_3CHOO loss (T = 283 K). This model may well be a slight over-estimate of the importance of this channel, as the kinetics of other destruction channels (primarily the carboxylic acids) were not taken into account. These results suggest that in certain environments, SO_2 may play a role in C_2 Criegee destruction. In addition to this, the reaction with Criegee intermediates is thought to enhance SO_2 oxidation leading to increased [H_2SO_4]; this will be of particular importance at night when OH concentrations are low (see Chapter I). Note that the reaction between OH + SO_2 is the dominant oxidation reaction leading to sulphate formation in the atmosphere.

Table 6.10: Shows the major loss channels for the C_2 CI. In certain regions SO_2 can compete with the major loss channels and contribute to C_2 CI decay.

Temp. / K	Region	RH / %	$[H_2O]$ / cm^{-3}	$[(H_2O)_2]$ / cm^{-3}	$[SO_2]$ / cm^{-3}	% loss H_2O	% loss $(H_2O)_2$	% loss SO_2
298	Urban	75	5.8×10^{17}	5.5×10^{14}	2.5×10^{11}	0.7	99.1	0.3
298	Urban	50	3.9×10^{17}	2.4×10^{14}	2.5×10^{11}	1.0	98.4	0.6
298	Rural	75	5.8×10^{17}	5.5×10^{14}	2.0×10^{10}	0.7	99.3	0.02
298	Rural	50	3.9×10^{17}	2.4×10^{14}	2.0×10^{10}	1.0	99.0	0.05
283	Urban	75	2.4×10^{17}	9.9×10^{13}	2.5×10^{11}	0.9	98.2	0.9
283	Urban	50	1.6×10^{17}	4.4×10^{13}	2.5×10^{11}	1.3	96.7	2.1
283	Rural	75	2.4×10^{17}	$9.\times10^{13}$	2.0×10^{10}	0.9	99.0	0.1
283	Rural	50	1.6×10^{17}	4.4×10^{13}	2.0×10^{10}	1.3	98.5	0.2

For modelling purposes the following rate coefficients were used: $k_{C2SO2} = 2 \times 10^{-11}$ cm^3 $molecule^{-1}$ s^{-1}; $k_{synC2H2O} = 2 \times 10^{-17}$ cm^3 $molecule^{-1}$ s^{-1}. Values of $k_{synC2H2O2}$ (283 K) = 3.2×10^{-12} cm^3 $molecule^{-1}$ s^{-1} (calculated from (Vereecken et al., 2012)); $k_{synC2H2O2}$ (283 K) = 6×10^{-12} cm^3 $molecule^{-1}$ s^{-1} (Vereecken et al., 2012). Notably, the values for $k_{synC2H2O2}$ were doubled for the calculations at 283 K due to the strong, negative, temperature dependence observed by Smith et al. (2015),

In one recent study, large discrepancies between modelled and measured H_2SO_4 concentrations in a Finnish boreal forest were observed, implying an unexpected increase in SO_2 oxidation. It has been postulated that this oxidation may be caused by CIs produced by monoterpene ozonolysis (Mauldin et al., 2012). Indeed, one recent study suggests that on a regional scale the impact that Criegee chemistry may have on $[H_2SO_4]$ is significant (Percival et al., 2013). In the work of Percival et al. (2013), it is hypothesised that in certain environments the oxidation of SO_2 by Criegee intermediates may compete, and in fact dominate over the other SO_2 oxidation pathways. However, it should be noted that the simulations reported in this study do not account for the reaction between CIs and the water dimer in the steady-state calculations for [CI]. Therefore, it is likely that this study overestimates the steady-state concentration of Criegee intermediates in the atmosphere and hence exaggerates the contribution of CIs to the atmospheric oxidation of SO_2. Note: in Percival et al. (2013) a steady-state concentration of CIs between 4.2×10^4 < [CI] (molecule cm^{-3}) < 3.75×10^5 is calculated. When the contribution of the water dimer reaction is taken into account a steady-state concentration between 2×10^2 < [CI] (molecule cm^{-3}) < 7.5×10^3 is estimated (see Appendix C). Using lower estimations of CI concentration, it is calculated that Criegee intermediates still contribute as minor channels in the SO_2 oxidation process, particularly at night when the hydroxyl radical concentration is low. These calculations suggest that Criegee intermediates may account for up to ~8% of SO_2 removal during the

day and ~45% at night. These calculations support the work of Mauldin et al. (2012), which reported large night time concentrations of H_2SO_4 which could not be explained by OH removal alone.

Table 6.11: Shows the competition between OH and CIs for the removal of SO_2 in the troposphere. The effect of the CI concentration is also highlighted.

Time	k_{OH}/ cm^3 s^{-1}	k_{SO2}/ cm^3 s^{-1}	[OH] / cm^{-3}	[CI] / cm^{-3}	loss OH / %	loss CI / %
Day	1.5×10^{-12}	2.5×10^{-11}	1×10^{6}	5×10^{2}	99.2	0.8
Day	1.5×10^{-12}	2.5×10^{-11}	1×10^{6}	5×10^{3}	92.3	7.7
Night	1.5×10^{-12}	2.5×10^{-11}	1×10^{5}	5×10^{2}	92.3	7.7
Night	1.5×10^{-12}	2.5×10^{-11}	1×10^{5}	5×10^{3}	54.5	45.5

The calculations in Table 6.11 were determined using the following rate coefficients: $k_{SO2} = 2.5\times 10^{-11}$ cm^3 molecule^{-1} s^{-1}, which is an averaged value from the (C_1 and C_2) CI + SO_2 rate coefficients determined from this study; $k_{OH} = 1.5\times 10^{-12}$ cm^3 molecule^{-1} s^{-1} (Atkinson et al., 2004).

6.4 References

ANGLADA, J. M., GONZALEZ, J. & TORRENT-SUCARRAT, M. 2011. Effects of the substituents on the reactivity of carbonyl oxides. A theoretical study on the reaction of substituted carbonyl oxides with water. *Physical Chemistry Chemical Physics,* 13**,** 13034-13045.

ANGLADA, J. M. & SOLE, A. 2016. Impact of water dimer on the atmospheric reactivity of carbonyl oxides. *Physical Chemistry Chemical Physics*.

ATKINSON, R., BAULCH, D. L., COX, R. A., CROWLEY, J. N., HAMPSON, R. F., HYNES, R. G., JENKIN, M. E., ROSSI, M. J. & TROE, J. 2004. Evaluated kinetic and photochemical data for atmospheric chemistry: Volume I - gas phase reactions of O_x, HO_x, NO_x and SO_x species. *Atmos. Chem. Phys.,* 4**,** 1461-1738.

BAEZA-ROMERO, M. T., BLITZ, M. A., GODDARD, A. & SEAKINS, P. W. 2012. Time-of-flight mass spectrometry for time-resolved measurements: Some developments and applications. *International Journal of Chemical Kinetics,* 44**,** 532-545.

BRASSEUR, G. P., ORLANDO, J. J. & TYNDALL, G. S. 1999. *Atmospheric Chemistry and Global Change,* Oxford, Oxford University Press.

BROWN, S. S. & STUTZ, J. 2012. Nighttime radical observations and chemistry. *Chemical Society Reviews,* 41**,** 6405-6447.

BURAS, Z. J., DAMES, E. E., MERCHANT, S. S., LIU, G., ELSAMRA, R. M. I. & GREEN, W. H. 2015. Kinetics and Products of Vinyl + 1,3-Butadiene, a Potential Route to Benzene. *The Journal of Physical Chemistry A,* 119**,** 7325-7338.

CALVERT, J. G. 2000. *The mechanisms of atmospheric oxidation of the alkenes,* New York, Oxford University Press.

CHHANTYAL-PUN, R., DAVEY, A., SHALLCROSS, D. E., PERCIVAL, C. J. & ORR-EWING, A. J. 2015. A kinetic study of the CH_2OO Criegee intermediate self-reaction, reaction with SO_2 and unimolecular reaction using cavity ring-down spectroscopy. *Physical Chemistry Chemical Physics,* 17**,** 3617-3626.

DERWENT, R. G., KEARNS, D. R. & THRUST, B. A. 1970. The excitation of iodine by singlet molecular oxygen. *Chemical Physics Letters,* 6**,** 115-116.

ENAMI, S., SAKAMOTO, Y., YAMANAKA, T., HASHIMOTO, S., KAWASAKI, M., TONOKURA, K. & TACHIKAWA, H. 2008. Reaction Mechanisms of IO Radical Formation from the Reaction of CH_3I with Cl Atom in the Presence of O_2. *Bulletin of the Chemical Society of Japan,* 81**,** 1250-1257.

GRAVESTOCK, T. J., BLITZ, M. A., BLOSS, W. J. & HEARD, D. E. 2010. A Multidimensional Study of the Reaction $CH_2I + O_2$: Products and Atmospheric Implications. *ChemPhysChem,* 11**,** 3928-3941.

IANNI, J. C. 2002. Kintecus , Windows Version 2.80, 2002, www.kintecus.com.

JOHNSON, D., LEWIN, A. G. & MARSTON, G. 2001. The Effect of Criegee-Intermediate Scavengers on the OH Yield from the Reaction of Ozone with 2-methylbut-2-ene. *The Journal of Physical Chemistry A,* 105**,** 2933-2935.

KOFFEND, J. B. & LEONE, S. R. 1981. Tunable laser photodissociation: quantum yield of $I^*(^2P_{1/2})$ from CH_2I_2. *Chemical Physics Letters,* 81**,** 136-141.

KUWATA, K. T., HERMES, M. R., CARLSON, M. J. & ZOGG, C. K. 2010. Computational Studies of the Isomerization and Hydration Reactions of Acetaldehyde Oxide and Methyl Vinyl Carbonyl Oxide. *The Journal of Physical Chemistry A,* 114**,** 9192-9204.

LEWIS, T. R., BLITZ, M. A., HEARD, D. E. & SEAKINS, P. W. 2015. Direct evidence for a substantive reaction between the Criegee intermediate, CH_2OO, and the water vapour dimer. *Physical Chemistry Chemical Physics,* 17**,** 4859-4863.

LIN, W., XU, X., MA, Z., ZHAO, H., LIU, X. & WANG, Y. 2012. Characteristics and recent trends of sulfur dioxide at urban, rural, and background sites in North China: Effectiveness of control measures. *Journal of Environmental Sciences,* 24**,** 34-49.

LIU, Y., BAYES, K. D. & SANDER, S. P. 2014. Measuring Rate Constants for Reactions of the Simplest Criegee Intermediate (CH_2OO) by Monitoring the OH Radical. *The Journal of Physical Chemistry A*.

MAULDIN, R. L., BERNDT, T., SIPILA, M., PAASONEN, P., PETAJA, T., KIM, S., KURTEN, T., STRATMANN, F., KERMINEN, V. M. & KULMALA, M. 2012. A new atmospherically relevant oxidant of sulphur dioxide. *Nature,* 488**,** 193-+.
NEWLAND, M. J., RICKARD, A. R., ALAM, M. S., VEREECKEN, L., MUÑOZ, A., RÓDENAS, M. & BLOSS, W. J. 2015. Kinetics of stabilised Criegee intermediates derived from alkene ozonolysis: reactions with SO_2, H_2O and decomposition under boundary layer conditions. *Physical Chemistry Chemical Physics,* 17**,** 4076-4088.
ORIGINPRO OriginLab. Northampton, MA.
OUYANG, B., MCLEOD, M. W., JONES, R. L. & BLOSS, W. J. 2013. NO_3 radical production from the reaction between the Criegee intermediate CH_2OO and NO_2. *Physical Chemistry Chemical Physics,* 15**,** 17070-17075.
PERCIVAL, C. J., WELZ, O., ESKOLA, A. J., SAVEE, J. D., OSBORN, D. L., TOPPING, D. O., LOWE, D., UTEMBE, S. R., BACAK, A., M C FIGGANS, G., COOKE, M. C., XIAO, P., ARCHIBALD, A. T., JENKIN, M. E., DERWENT, R. G., RIIPINEN, I., MOK, D. W. K., LEE, E. P. F., DYKE, J. M., TAATJES, C. A. & SHALLCROSS, D. E. 2013. Regional and global impacts of Criegee intermediates on atmospheric sulphuric acid concentrations and first steps of aerosol formation. *Faraday Discussions,* 165**,** 45-73.
RYZHKOV, A. B. & ARIYA, P. A. 2004. A theoretical study of the reactions of parent and substituted Criegee intermediates with water and the water dimer. *Physical Chemistry Chemical Physics,* 6**,** 5042-5050.
SHEPS, L. 2013. Absolute Ultraviolet Absorption Spectrum of a Criegee Intermediate CH_2OO. *The Journal of Physical Chemistry Letters,* 4**,** 4201-4205.
SHEPS, L., SCULLY, A. M. & AU, K. 2014. UV absorption probing of the conformer-dependent reactivity of a Criegee intermediate CH_3CHOO. *Physical Chemistry Chemical Physics,* 16**,** 26701-26706.
SMITH, M. C., CHANG, C.-H., CHAO, W., LIN, L.-C., TAKAHASHI, K., BOERING, K. A. & LIN, J. J.-M. 2015. Strong Negative Temperature Dependence of the Simplest Criegee Intermediate CH_2OO Reaction with Water Dimer. *The Journal of Physical Chemistry Letters,* 6**,** 2708-2713.
SMITH, M. C., TING, W.-L., CHANG, C.-H., TAKAHASHI, K., BOERING, K. A. & LIN, J. J.-M. 2014. UV absorption spectrum of the C_2 Criegee intermediate CH_3CHOO. *The Journal of Chemical Physics,* 141**,** 074302.
SNOW, K. B. & THOMAS, T. F. 1990. Mass spectrum, ionization potential, and appearance potentials for fragment ions of sulfuric acid vapor. *International journal of mass spectrometry and ion processes,* 96**,** 49-68.
STONE, D., BLITZ, M., DAUBNEY, L., HOWES, N. U. M. & SEAKINS, P. 2014. Kinetics of CH_2OO reactions with SO_2, NO_2, NO, H_2O and CH_3CHO as a function of pressure. *Physical Chemistry Chemical Physics,* 16**,** 1139-1149.
STONE, D., BLITZ, M., DAUBNEY, L., INGHAM, T. & SEAKINS, P. 2013. CH_2OO Criegee biradical yields following photolysis of CH_2I_2 in O_2. *Physical Chemistry Chemical Physics,* 15**,** 19119-19124.
TAATJES, C. W., O; ESKOLA, A; SAVEE, J; SCHEER, A; SHALLCROSS, D; ROTAVERA, B; LEE, E;DYKE, J; MOK, D; OSBORN, D AND PERCIVAL C 2013. Direct Measurements of Conformer-Dependent Reactivity of the Criegee Intermediate CH_3CHOO. *Science,* 340.
TING, W.-L., CHANG, C.-H., LEE, Y.-F., MATSUI, H., LEE, Y.-P. & LIN, J. J.-M. 2014. Detailed mechanism of the $CH_2I + O_2$ reaction: Yield and self-reaction of the simplest Criegee intermediate CH_2OO. *The Journal of Chemical Physics,* 141**,** 104308.
VEREECKEN, L., HARDER, H. & NOVELLI, A. 2012. The reaction of Criegee intermediates with NO, RO_2, and SO_2, and their fate in the atmosphere. *Physical Chemistry Chemical Physics,* 14**,** 14682-14695.
WELZ, O., SAVEE, J. D., OSBORN, D. L., VASU, S. S., PERCIVAL, C. J., SHALLCROSS, D. E. & TAATJES, C. A. 2012. Direct Kinetic Measurements of Criegee Intermediate (CH_2OO) Formed by Reaction of CH_2I with O_2. *Science,* 335**,** 204-207.

Chapter VII:

Kinetic Studies of Criegee Intermediate with Organic Acids and Alkenes

7. Kinetic Studies of Criegee Intermediate with Organic Acids and Alkenes

Recent work by Welz et al. (2014) has explored the reactivity between both the C_1 and C_2 Criegee intermediates and organic acids. This chapter aims to build on the work of Welz et al. (2014) by measuring both the kinetics and products for the reactions of the C_1 CI with both formic, k_{C1FA}, and acetic acid, k_{C1AA}. From this study rate coefficients of $k_{C1FA} = (3.7 \pm 0.6) \times 10^{-11}$ cm^3 molecule^{-1} s^{-1} and $k_{C1AA} = (7.1 \pm 1.1) \times 10^{-11}$ cm^3 molecule^{-1} s^{-1} for the reactions with formic and acetic acid respectively. Notably, the rate coefficient measured from this study for the reaction between C_1 CI and formic acid is approximately a third of the value reported by Welz et al. (2014), $k_{C1FA} = (1.1 \pm 0.1) \times 10^{-10}$ cm^3 molecule^{-1} s^{-1}. The C_1 CI + acetic acid rate coefficient is approximately half the previous evaluation of $k_{C1AA} = (1.3 \pm 0.1) \times 10^{-10}$ cm^3 molecule^{-1} s^{-1} (Welz et al., 2014).

Additionally, this chapter also contains the results from work investigating the reactivity of the C_1 and C_2 Criegee intermediates with various alkenes (ethene and isoprene). From this work an upper limit of $k_{C1ethene} < 2 \times 10^{-14}$ cm^3 molecule^{-1} s^{-1} was measured for the reaction between the C_1 Criegee intermediate and ethene. For isoprene an upper limit of $k_{C1isoprene} < 3 \times 10^{-13}$ cm^3 molecule^{-1} s^{-1} was measured for the reaction with the C_1 CI, and a rate coefficient of $k_{C2isoprene} = (8.3 \pm 4.1) \times 10^{-13}$ cm^3 molecule^{-1} s^{-1} was measured for the C_2 CI.

7.1 CH_2OO + Organic Acids

7.1.1 Introduction

Following the discovery of the enhanced reactivity of stabilised Criegee intermediates (SCIs) towards atmospheric trace gases (Welz et al., 2012), a number of modelling studies were conducted to determine the impact this additional chemistry had on CI destruction pathways (Vereecken et al., 2012). Previously, it had been assumed that reaction with H_2O and its dimer were the exclusive sinks of CIs; however, Vereecken et al. (2012) showed that for substituted CIs this may not be true in certain environments. In Vereecken et al. (2012), a single rate coefficient of $k_{OrgAcids} = 5 \times 10^{-12}$ cm^3 molecule^{-1} s^{-1} was applied for carboxylic acids; using this evaluation it is predicted that carboxylic acids will be a minor sink for C_1 and *syn*-C_2 CIs (Vereecken et al., 2012). However, recent measurements of CI reactivity with formic and acetic acid suggest that the estimate made by Vereecken et al. (2012) is very conservative (Sipilä et al., 2014, Welz et al., 2014) . Both the work of Welz et al. (2014) and Sipilä et al. (2014) suggest that CIs react extremely rapidly with carboxylic acids (Table 7.1).

Table 7.1: Rate coefficient for CI + carboxylic acids reactions determined from recent studies.

Reaction	k ($\times 10^{-11}$ cm^3 molecule^{-1} s^{-1})	Reference
CH_2OO + HCOOH	11 ± 1	Welz et al. (2014)
CH_2OO + CH_3COOH	13 ± 1	Welz et al. (2014)
anti-CH_3CHOO + HCOOH	50 ± 3	Welz et al. (2014)
syn-CH_3CHOO + HCOOH	25 ± 3	Welz et al. (2014)
anti-CH_3CHOO + CH_3COOH	25 ± 6	Welz et al. (2014)
syn-CH_3CHOO + CH_3COOH	17 ± 5	Welz et al. (2014)
$(CH_3)_2OO$ + HCOOH	5.6 ± 0.6*	Sipilä et al. (2014)
$(CH_3)_2OO$ + CH_3COOH	6.9 ± 0.8*	Sipilä et al. (2014)

***Note: the results from Sipilä et al. (2014) were done using a relative rate method with SO_2, the rate coefficients listed were calculated using a $k_{C2SO2} = 2.0 \times 10^{-11}$ cm^3 molecule^{-1} s^{-1}.**

These results imply that organic acids may be responsible for a significant proportion of CI loss in the atmosphere; in fact, Welz et al. (2014) suggest that carboxylic acids may cause up to ~10% of CH_2OO destruction in boreal forests. The estimation of ~10% is thought to be a slight over-estimation of the CH_2OO + acids loss pathway as this model was executed using, what is now thought to be, a conservative value of $k_{C1H2O} = 9 \times 10^{-17}$ cm^3 molecule^{-1} s^{-1} (Stone et al., 2014). However, it is possible that organic acids may be minor sinks of CH_2OO; moreover, it is likely that carboxylic acids are significant sinks for larger CIs (such as *syn*-CH_3CHOO).

It is hypothesised that the reaction of CH_2OO and formic acid rapidly forms hydroperoxymethyl formate (Figure 7.1); the formation of this HPMF is thought to be barrierless (Long et al., 2009). Hydroperoxymethyl formate (HPMF) is also known to be a key intermediate in the low temperature combustion of dimethyl ether (DME) and was recently positively identified as a product from DME oxidation at 540 K (Moshammer et al., 2015). Furthermore, in a theoretical study conducted by Andersen and Carter (2003) CH_2OO and formic acid have previously been hypothesised as potential products from HPMF decomposition (Figure 7.2). Therefore, having an understanding of the kinetics and products of this reaction may be relevant for both atmospheric and combustion systems.

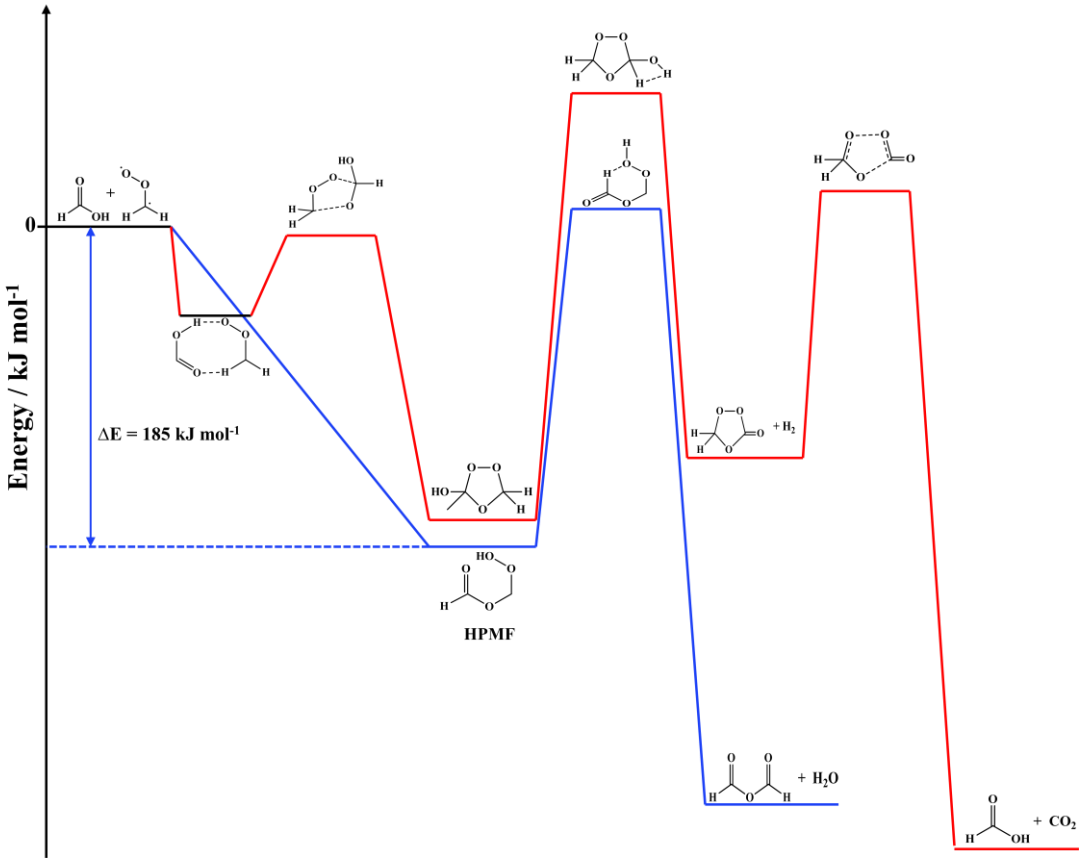

Figure 7.1:A schematic of the potential energy surface of the reaction between CH_2OO and HCOOH. Adapted from Long et al. (2009). The exothermicity of the formation of HPMF is estimated from Long et al. (2009).

The aim of this study is to investigate the kinetics of the C_1 CI with both formic and acetic acid with the hope to corroborate the previous work done exploring these reactions (Welz et al., 2014). In addition to this, information about the products from these reactions will also be monitored using pulsed laser photolysis coupled with photoionization mass spectrometry (PLP-PIMS).

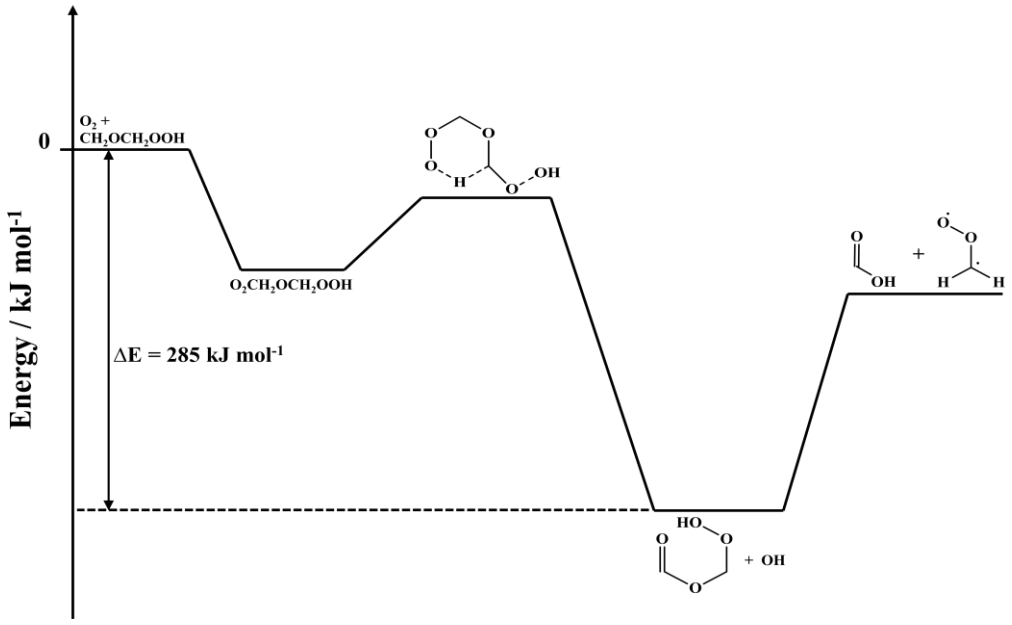

Figure 7.2: A schematic of the potential energy surface showing the HPMF formation in DME oxidation and the hypothesised pathway leading to CH_2OO + HCOOH (Andersen and Carter, 2003). The exothermicity of the formation of HPMF is estimated from Andersen et al. (2003).

7.1.2 Experimental

A similar experimental approach was used for this work as in the previous SCI experiments described in Chapter VI; however, a brief recap of the experimental methodology given be given. For all of the experiments conducted CH_2I_2/O_2/He/HCOOH or CH_3COOH gas mixtures were flowed through the reactor *via* calibrated mass flow controllers (MFCs); all the experiments done using the PIMS technique were conducted at low pressures (1.0-2.5 Torr). To ensure that a reproducible amount of CH_2I_2 was added, a bubbler was used placed after the MFC (see Figure 6.2). Only small amounts of the diiodomethane ($[CH_2I_2] < 1 \times 10^{13\text{-}14}$ cm^{-3}) were added during the experiments as the flow of helium from the MFC and the flow of gases (He and CH_2I_2) out of the bubbler were balanced using a needle valve, which ensured that only the diluted vapours of the diiodo-species were introduced into the reactor. The C_1 CIs were generated by adding large quantities of neat oxygen ($[O_2] = 1 \times 10^{16}$ molecule cm^3) to the CH_2I radicals produced from diiodomethane photolysis (R7.1-7.2).

$$CH_2I_2 + h\nu \rightarrow CH_2I + I \qquad \text{(R7.1)}$$

$$CH_2I + O_2 \rightarrow CH_2OO + I \qquad \text{(R7.2)}$$

For the entirety of this study, diiodo-precursors were initiated by pulsed laser photolysis using an excimer laser (λ = 248 nm, ~50 mJ cm^{-2}) and the gas sampled was photoionized using λ = 118 nm light (for details see Chapter II).

To ensure the experiments were completed under pseudo first-order conditions both the formic and acetic acid added had to be kept in excess of [CH_2OO]. Initially, as with the previous SCI experiments, dilute (~2%) gas bulbs of HCOOH and CH_3COOH (Sigma-Aldrich >98% and Fluka >99.8% respectively) were prepared; however, it became clear that this was a poor method of delivery for the carboxylic acids. It was discovered that in order to get significant (and reproducible) amounts of HCOOH and CH_3COOH through the MFCs, the gases needed to be flowed for a long time prior to the experiments (often overnight). Therefore, it was decided that using a gas bubbler may be a better choice of apparatus; it should be noted that, unlike for the diiodomethane, the bubbler was placed prior to the mass flow controller (Figure 7.3). This added the extra complication that the concentrations of acid had to be determined by calculating the vapour pressure for both formic and acetic acid using Antoine equations described in E7.1 and E7.3 (Speight, 2005). All of the experiments were conducted at 293 K; at this temperature the vapour pressures of the formic and acetic acid are 31.5 Torr and 11.5 Torr respectively (Speight, 2005). Following the calculation of the vapour pressure, the overall concentrations can be calculated using (E7.2 and E7.4).

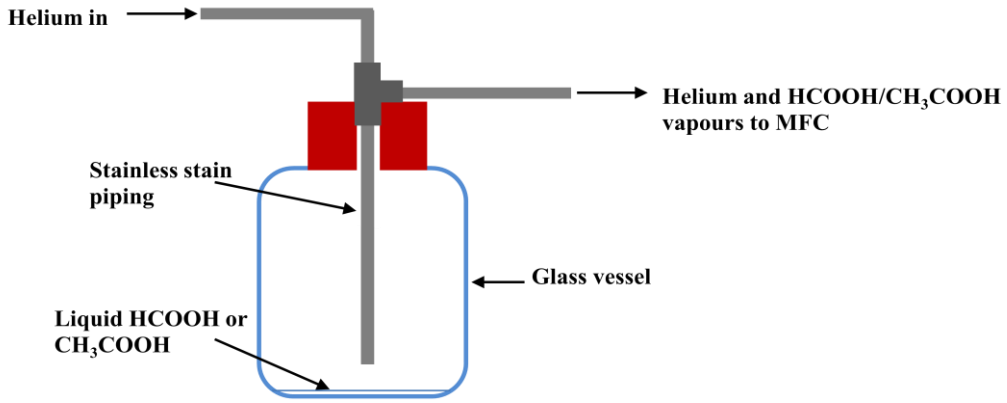

Figure 7.3: A schematic of the bubbling apparatus used to introduce both formic and acetic acid into the reactor.

$$\text{HCOOH vapour pressure (Torr)} = 10^{\left(6.94459 - \frac{1295.26}{218+\text{T(°C)}}\right)} \quad \text{(E7.1)}$$

$$[\text{HCOOH}]\ (\%) = \frac{\text{HCOOH vapour pressure (Torr)}}{\text{total pressure (Torr)}} \times 100\% \quad \text{(E7.2)}$$

$$\text{CH}_3\text{COOH vapour pressure (Torr)} = 10^{\left(7.80307 - \frac{1651.2}{225+\text{T(°C)}}\right)} \quad \text{(E7.3)}$$

$$[CH_3COOH]\ (\%) = \frac{CH_3COOH \text{ vapour pressure (Torr)}}{\text{total pressure (Torr)}} \times 100\% \quad \text{(E7.4)}$$

When using the gas bulbs it is thought that typically the concentrations are accurate to approximately ±5%. Using the vapour pressure method to estimate the concentration is thought to be a less precise technique as there are a number of variables which are assumed to be constant; such as the variations in the backing pressure of helium or possibly small fluctuations in liquid temperature. Both these variables were monitored but may have changed slightly during the course of the experiments. Due to these variables an uncertainty of ±10% is assumed in [carboxylic acid], which when propagated with other systematic uncertainties, led to a total systematic experimental error of ~15%.

It should also be highlighted that both formic and acetic acid have strong intermolecular forces (hydrogen bonds), which lead the formation stable dimer species at high concentrations. In this study the concentrations of both acids (in the reaction mixtures) were kept below 1×10^{14} molecule cm^{-3}, which was low enough to ensure that the monomer was the dominant species ([monomer] > 99% at T = 293 K) (Winkler and Hess, 1994). Moreover, MESMER calculations (completed by D.D.J Medeiros) indicate that the dimer lifetime, τ, is ~25 ms for HCOOH (for CH_3COOH $\tau < 2$ ms), the mixing time prior to the flowtube is at least 0.25 s; this means essentially all of the acid will be in monomer for the reaction. Conversely, the vapour pressures of the acids (i.e. prior to the MFC and further dilution) are much more concentrated ([HCOOH] ≈ 1×10^{18} molecule cm^{-3}), and at these concentrations ~80% of the HCOOH is dimer (82.5% for CH_3COOH). The vapour pressure of the acids are described by the following equations (Khamaganov et al., 2006):

$$P_t = P_D + P_M \quad \text{(E7.5)}$$

Or:

$$N_t = N_D + N_M \quad \text{(E7.6)}$$

$$N_D \rightleftharpoons 2N_M \quad \text{(R7.3)}$$

where: P_t is the total vapour pressure; P_D is the partial pressure of the dimer; and P_M is the partial pressure of the monomer. In equation E7.6: N_t is the total number density; N_D is the number density of the dimer; and N_M is the number density of the monomer.

As every dimer is the system is converted to two monomers in the mixing manifold (R7.3), this means an adjustment is required to calculate the actual concentrations of acid monomer in the gas mixture (E7.7).

$$N_{M^*} = 2N_D + N_M \quad \text{(E7.7)}$$

where N_{M^*} is the corrected monomer number density in the reaction mixture.

The methods of data collection and analysis techniques used in this CH_2OO + organic acid study were analogous to those described in Chapter VI. The experiments were controlled using a LabVIEW™ program, which was designed specifically for data collection and storage using the PIMS setup (Baeza-Romero et al., 2012). The data collected were then analysed used OriginPro graphical software (E7.8-7.10) and used to construct a bimolecular plot.

$$M_1 = \frac{(S_{\mathrm{C1height}} \times k'_{\mathrm{CH2I+O2}} \times k_{\mathrm{samp}})}{(k'_{\mathrm{C1total}} - k'_{\mathrm{CH2I+O2}})} \quad \text{(E7.8)}$$

$$M_2 = \frac{e^{-k'_{\mathrm{CH2I+O2}} \times t} - e^{-k_{\mathrm{samp}} \times t}}{(k_{\mathrm{samp}} - k'_{\mathrm{CH2I+O2}})} - \frac{e^{-k'_{\mathrm{C1total}} \times t} - e^{-k_{\mathrm{samp}} \times t}}{(k_{\mathrm{samp}} - k'_{\mathrm{C1total}})} \quad \text{(E7.9)}$$

$$S_{\mathrm{CH2OO}} = M_1 \times M_2 + S_{\mathrm{bg}} \quad \text{(E7.10)}$$

S_{CH2OO} represents the time-resolved C_1 CI signal; $S_{C1height}$ is the maximum height of S_{CH2OO}; $k'_{CH2I+O2}$ is equivalent to the rate of CH_2OO formation; $k'_{C1total}$ is equal to the total loss rate of CH_2OO; k_{samp} is the rate of transportation of the gas to the mass spectrometer (this was held constant during data analysis, $k_{samp} = 30000\ s^{-1}$); t is time; and S_{bg} represents the background signal measured for the individual data traces.

7.1.3 CH_2OO + HCOOH Reaction

The reaction of the C_1 Criegee intermediate with formic acid is potentially an important reaction not only for atmospheric chemistry, but also for DME combustion as well. Recent studies have identified that the rate coefficient for this reaction, k_{C1FA}, is extremely fast ($k_{C1FA} > 1 \times 10^{-10}$ cm^3 molecule^{-1} s^{-1}) (Welz et al., 2014); this rate coefficient was several orders of magnitude faster than had previously been estimated (Johnson et al., 2001). As yet, there has been little reported about the products from this reaction, although it has been hypothesised that hydroperoxymethyl formate (*m/z* = 92) is a likely product. However, HPMF is yet to be positively identified as a product for the reaction; although the formation of HPMF has been inferred from the detection of formic acid anhydride (FAN, *m/z* = 74), which is thought to be the major product from HPMF decomposition (Neeb et al., 1998). However, the exact mechanism for this reaction is still unknown. Although there have been a number of theoretical studies which have determined the most energetically favourable reaction pathways for the reactions, and the most probable products, of which HPMF is one (Long et al., 2009). The work by Long et al. (2009) identifies two possible channels for the CH_2OO + HCOOH reaction: the first being the attack of the Criegee intermediate on the OH group of the formic acid, leading to the formation of HPMF; and the second being the

formation of a hydroxylated secondary ozonide (Figure 7.1 and Figure 7.4). In addition to the channels reported by Long et al. (2009), an alternative pathway (Figure 7.4, 3) is also shown; in this reaction the Criegee intermediate is inserted into the C-H bond of the acid species.

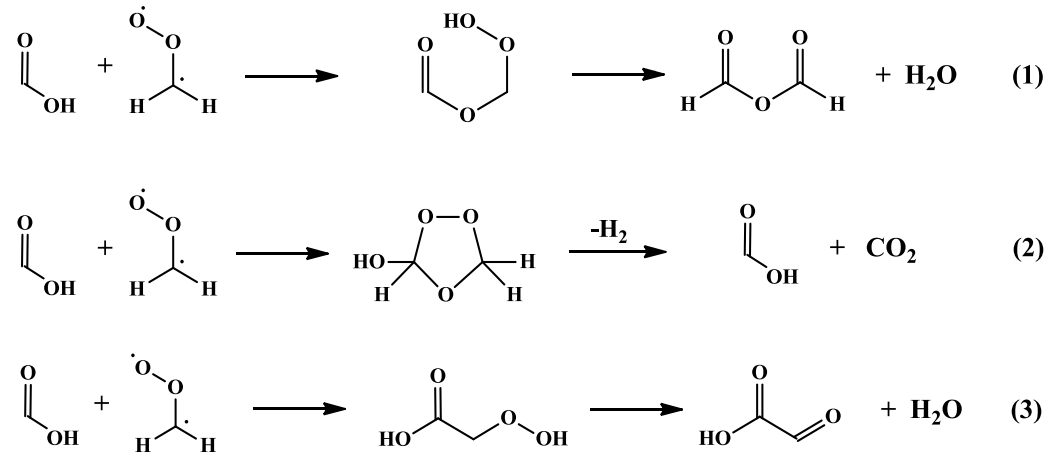

Figure 7.4: A schematic of the possible reaction mechanisms for the reaction between CH_2OO and HCOOH (Long et al., 2009).

Both of these mechanisms reported by Long et al. (2009) were barrierless, with HPMF channel being marginally more thermodynamically favourable. Unlike the work of Andersen and Carter (2003) and Neeb et al. (1998), Long et al. (2009) suggest that there is a significant energy barrier to formic acid anhydride, FAN, formation (Figure 7.1); suggesting that HPMF, rather than FAN, is the kinetically stable product. It should also be noted that Long et al. (2009) predict the hydroxylated secondary ozonide will be the kinetically stable product, even though formic acid and CO_2 are the thermodynamically favoured products from this reaction channel, due to the large barrier for H_2 elimination (Figure 7.1).

Throughout this study it was determined that the concentration of CH_2OO used was $[CH_2OO]_0 \approx 4 \times 10^{12}$ molecule cm^{-3}; under these conditions the quality of the data was high and signal-to-noise ratios between $20 < SNR < 35$ were measured after ~10 traces. Each of the traces collected were analysed using equations E6.1-6.3; the data were then used to create a bimolecular plot (Figure 7.5). It should be noted that the linear regression fit plotted was weighted using the error of the individual data points, meaning the rate coefficient determined put less emphasis of the data with high uncertainties.

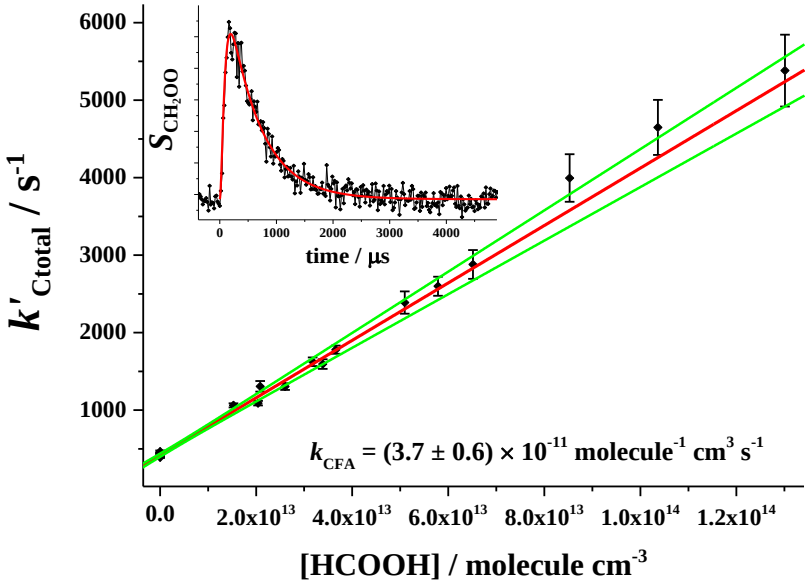

Figure 7.5: An example of the quality of the data collected can be seen in the upper left-hand corner of the bimolecular plot of obtained for the reaction between the C_1 CI + HCOOH. The error quoted is propagated using the random errors quoted from the plot and a 15% systematic experimental error. Uncertainty limits shown are to 2σ.

From Figure 7.5 a rate coefficient of k_{C1FA} = (3.7 ± 0.6) × 10^{-11} cm^3 molecule^{-1} s^{-1} is obtained. This evaluation is approximately a factor of 3 lower than those made by Sipilä et al. (2014) and Welz et al. (2014) (see Table 7.1). Nevertheless, the value of k_{C1FA} from this work is still several orders of magnitude greater than CH_2OO + acetic acid rate coefficients as originally established, where an upper limit of k_{C1AA} < 1 × 10^{-14} cm^3 molecule^{-1} s^{-1} was proposed (Johnson et al., 2001). It should be noted that in Johnson et al. (2001), a rate coefficient for the CH_2OO + formic acid reaction was not reported. However, Welz et al. (2014) do not give details about how they account for dimer to monomer conversion, although they do suggest dimerization is taken into account. It may be possible that acid concentrations were not adjusted for dimer to monomer conversion using the same methodology. If this is the case then it may be prudent to investigate how the adjustment made for dimerization alters the rate coefficient determined from this study, and how the unadjusted rate coefficient compares with the previous literature (Table 7.2).

Table 7.2: Demonstrates the effect that formic acid dimerization has on k_{C1FA} and how our measurements compare to recent literature results.

k_{C1FA} (×10^{-11}) / cm^3 molecule^{-1} s^{-1}	Is dimerization accounted for?	Method used to adjust concentration	Reference
3.7 ± 0.6	Yes	$N_{M^*} = 2N_D + N_M$	This study
6.7 ± 1.1	No	No adjustment	This study
11 ± 1	Yes	Unknown	(Welz et al., 2014)

Adjusting the HCOOH concentration for dimerization has a significant effect on the rate coefficient, k_{C1FA}. As can be seen from Table 7.2, if HCOOH dimerization is not accounted for, a rate coefficient of (6.7 ± 1.1) $\times 10^{-11}$ cm^3 $molecule^{-1}$ s^{-1} was determined. Notably, this evaluation was still approximately half the rate coefficient reported by Welz et al. (2014). However, when acid dimerization is ignored, the rate coefficient calculated from this study are closer to those quoted in Welz et al. (2014). That said, it must be highlighted that the work presented in Table 7.2 is based upon the assumption that neither of the previous studies study took the dimerization of formic acid into account using E7.7; this is doubtful, particularly as Welz et al. (2014) state that dimerization is considered, although, they do not specifically state exactly how this is done.

In addition to the kinetic observations made for the C_1 CI + HCOOH reaction, the aim of this study was to investigate the products from this reaction as well; however, detection of the reaction products proved to be very difficult. Indeed, the expected parent mass signal at *m/z* = 92 from HPMF formation proved to be elusive throughout the entirety of the experiments. In fact there was no conclusive evidence for any product formation. However, a small signal was observed at *m/z* = 64 during some of these experiments (Figure 7.6); although this signal was not always reproducible and was only observed when the quality of data was at its highest.

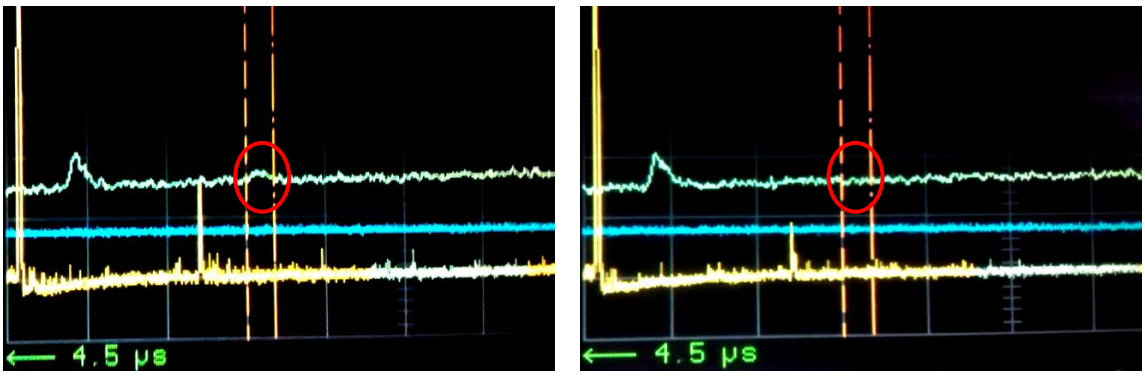

Figure 7.6: Photographs of the mass spectrum observed on the oscilloscope. (Left; green line, peak circled in red) in between the orange markers a small signal is observed (*m/z* = 64) at *t* = 1 ms; (Right; green line, peak circled in red) however, in the absence of 248 nm light no such signal can be seen between the markers.

Notably, the *m/z* = 64 signal observed (at *t* = 1 ms) in the Figure 7.6 was only measurable when the photolysis laser was operative and in the presence of O_2; this implies that the species at *m/z* = 64 is only produced in the presence of CH_2OO. To establish whether this was true, the Criegee signal (*m/z* = 46) and the mass at *m/z* = 64 were monitored simultaneously and the data were plotted on a graph together, Figure 7.7. From this plot it can be seen that the *m/z* =64 signal does seem to be formed on a similar time-scale as the Criegee signal (S_{CH2OO}) is lost: note this was verified upon data analysis. Unfortunately,

there was insufficient data collected with the *m/z* = 64 signal, meaning that a global fitting of the data (as described in Chapter VI, section 6.2.3) could not be used to analyse the data more rigorously than this. However, it should be noted that Welz et al. (2014) also mention the formation of a small mass at *m/z* = 64 in the C_1 + HCOOH reaction. In addition to this, a study exploring low temperature DME oxidation also measures the formation of a mass at *m/z* = 64 (Moshammer et al., 2015) and is attributed as a fragmentation channel of HPMF, $HOOCH_2OH^+$, caused by photoionization. As alluded to, the observation of a mass at *m/z* = 64 implies that the C_1 + HCOOH occurs *via* HPMF formation, as it is difficult to reconcile how a fragment of mass *m/z* = 28 (most likely CO) could be lost by either of the alternative pathways shown in Figure 7.4. Notably, HPMF formation was predicted to be the most thermodynamically stable channel for this reaction (Long et al., 2009).

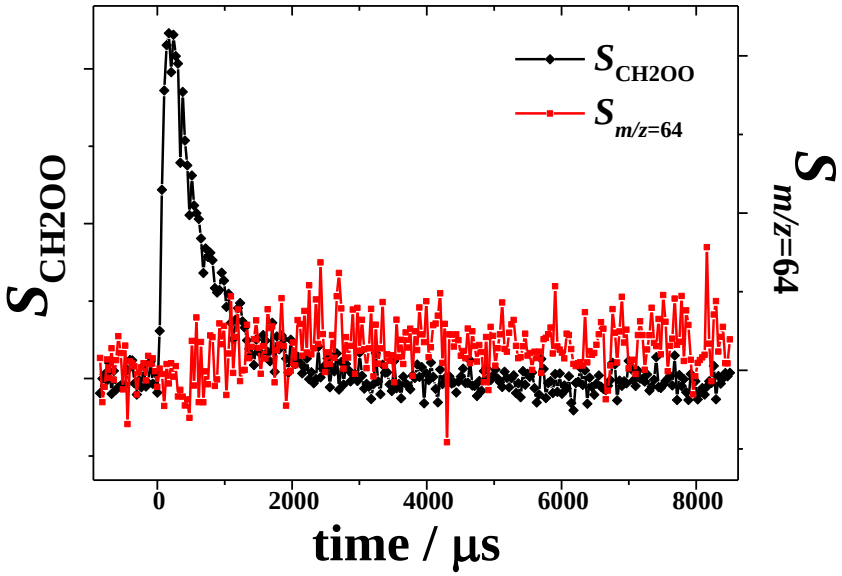

Figure 7.7: A plot showing the correlation between the loss of CH_2OO from the reaction system and the formation of the species at *m/z* = 64.

Additionally, as part of this study hydroxyl radical detection was implemented (see Chapter III, Section 3.1 for details); the OH radical is known to have an ionization potential (IP) significantly greater than photoionization wavelength used in the PIMS technique (~10.49 eV); however, by utilizing a 1 + 1' multiphoton ionization (MPI) scheme OH detection was achieved (Beames et al., 2011). Using this MPI technique a conservative OH detection limit of [OH] < 7×10^{11} molecule cm^{-3} has been established. Therefore, at the concentrations of CH_2OO used throughout these experiments OH detection should be possible, if the yield of hydroxyl radicals from these reactions is substantial ($Y_{OH} > 0.175$). It was decided that the OH detection technique should be used as two of the possible mechanisms for the CH_2OO + HCOOH reaction yield products with hydroperoxy- groups (-

OOH) attached. Notably, the O-O bond is by far the weakest of the bonds in either the HPMF or the hydroperoxy-acetic acid species shown in Figure 7.4. It is likely that OH radicals may be formed from either of these two channels, and so the detection of OH would give some insight as to the mechanism of the reaction.

However, throughout all of the experiments conducted with formic (and acetic) acid, there was no OH was measured. Initially, it was thought that a time-resolved OH signal was observable. However, on closer inspection it was clear that the peak was a consequence of an overloading signal at *m/z* = 14 (attributed as CH_2 formed during diiodomethane photolysis), which caused changing background signal at *m/z* = 17, which in turn led to the pseudo OH signal observed. The signal at *m/z* = 14 was removing by selectively gating the voltages to dispense with this overloading signal; however, even with the gating enabled, no time-resolved OH signal was observed. Moreover, no OH signal even registered on the oscilloscope, this was the best method of detecting smaller signals as the averaging method was faster and 1000 traces could be averaged in 2 minutes, whereas using the Labview™ program data averaging was much slower (see Chapter III, Section 3.1).

This result was slightly unexpected (due to the inherent weakness of the O-O bond in HPMF) and suggests that if any OH is formed from the reaction it is only a minor channel ($Y_{OH} > 0.175$). To verify these results, it was decided that the OH detection technique should be tested to ensure it was sensitive toward hydroxyl radicals. Prior to these experiments, this method of OH detection had only been used for monitoring OH as a reactant; in these experiments the [OH] used was reasonably high $\sim 3.5 \times 10^{12}$ molecule cm^{-3}. From these experiments it was calculated that the technique would be able to detect OH to concentrations at least 50 times lower than this; however, it had never been tested, nor had OH ever been observed as a product from a reaction (and not a reactant). To ensure that this method of OH detection was of practical use, and to verify the results from the C_1 + HCOOH reaction, a complementary study exploring the reaction between acetaldehyde and chlorine (in the presence of O_2) was undertaken. This reaction scheme was selected, not only because it is known to recycle OH (R7.3-7.5), but also because it has been previously investigated using the PIMS set-up (see Chapter IV), so it is known that this technique can be used effectively to probe the CH_3CHO + Cl reaction.

$$CH_3CHO + Cl \rightarrow CH_3CO + HCl \quad \text{(R7.3)}$$

$$CH_3CO + O_2 \rightarrow CH_3(O)O_2^* \quad \text{(R7.4)}$$

$$CH_3(O)O_2^* + M \rightleftharpoons CH_3(O)O_2 + M^* \quad \text{(R7.5a)}$$

$$CH_3(O)O_2^* \rightarrow \textit{cyclo}\text{-}CH_2(O)O + OH \quad \text{(R7.5b)}$$

Through the investigation of the reaction scheme (R7.3-7.5), it was quickly established that the multiphoton ionization technique for OH detection was sensitive to the hydroxyl radicals formed in these experiments. Following this initial discovery, it was decided that the sensitivity of the OH detection method should be explored using this reaction system. Using a Kintecus model of the reaction scheme (R7.3-7.5), the starting conditions of the reaction were investigated to find a mixture of reactants to yield hydroxyl concentration of [OH] ≈ 5×10^{11} molecule cm^{-3}; the purpose of this being to ensure that OH detection was possible at lower hydroxyl radical concentrations. The results of the subsequent experiment can be seen in Figure 7.8.

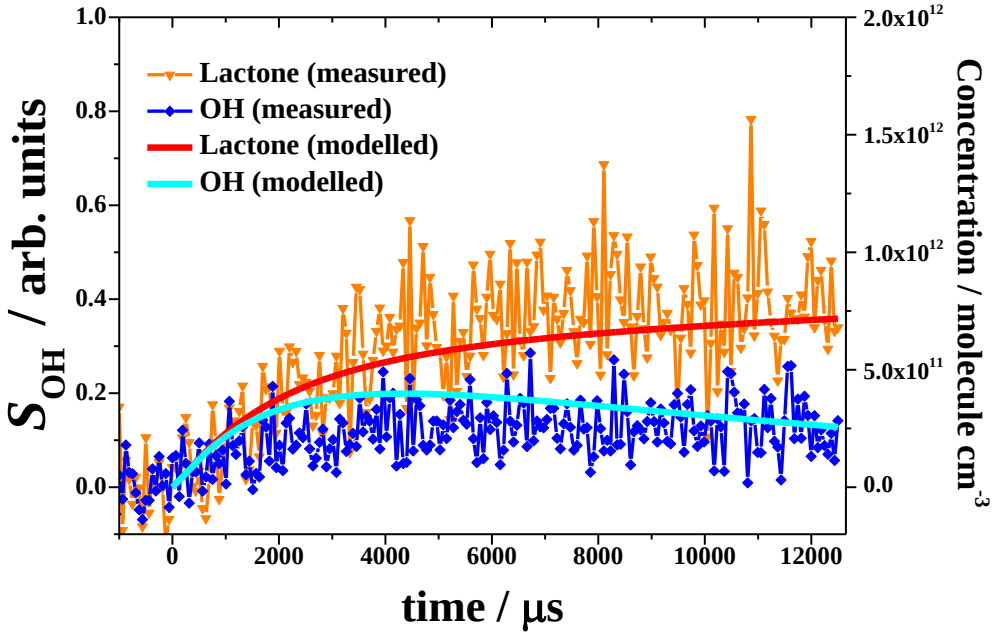

Figure 7.8: A plot highlighting the sensitivity of the MPI technique for OH detection. On the left-hand side *y*-axis the ion signals collected from the experiments are plotted, on the right-hand side the modelled concentrations are plotted.

From Figure 7.8 it is clear that OH detection was possible under these conditions, although the observed signal was small and the data quality low (*SNR* ≈ 3). Nonetheless, OH detection was achieved at low [OH], from the model of the reaction scheme, it is determined that the OH concentration during this experiment was [OH] = (4.0 ± 1.5) × 10^{11} cm^3 $molecule^{-1}$ s^{-1}. This result suggests that OH detection is possible below [OH] < 5 × 10^{11} cm^3 $molecule^{-1}$ s^{-1}; this is significantly lower than the CH_2OO used in the C_1 CI + HCOOH experiments and suggests that any OH formed from this reaction must be minimal. Indeed, through the investigation of the CH_3CHO + Cl + O_2 experiments, a maximum yield of OH can be put on the CH_2OO + HCOOH of Y_{OH} < (0.10 ± 0.04), indicating that if any OH formation is occurring it must only be a minor channel. Although intuitively OH formation

seemed probable from HPMF, it is not entirely surprising that no OH was observed. Even though the O-O bond of the hydroperoxy- group is a weak bond (bond enthalpy, $D_0 \approx 200$ kJ mol^{-1}) (Blanksby and Ellison, 2003), the energy required to break this bond is still larger than the exothermicity of the CH_2OO + HCOOH ($\Delta H \approx 185$ kJ mol^{-1}) (Long et al., 2009). Therefore, there is still a significant energy barrier which must be surpassed before the scission of the O-O bond can occur.

7.1.3.1 CH_2OO + HCOOH Conclusions

From this study of the reaction between CH_2OO + HCOOH a rate coefficient of $k_{C1FA} = (3.7 \pm 0.7) \times 10^{-11}$ cm^3 molecule^{-1} s^{-1} was determined. This evaluation of k_{C1FA} is orders of magnitude greater than earlier determinations of CI + carboxylic acids suggested (Johnson et al., 2001). However, the value of k_{C1FA} from this study is approximately three times smaller than other recent work suggests. Furthermore, unlike the work of Sipila et al. (2014) and Welz et al. (2014) the rate coefficient determined for the C_1 + HCOOH reaction is found to be significantly lower than the reaction of the C_1 + CH_3COOH.

In addition to this kinetic information of the CH_2OO + HCOOH reaction, the products were also investigated. Similarly to the work of Welz et al. (2014), it was not possible to observe any parent mass at *m/z* = 92. It was hoped that this would be possible as work by Moshammer et al. (2015) had proved that HPMF detection was possible using photoionization mass spectrometry (IP ≈ 10.2 eV) from low temperature DME oxidation (540 K). However, the formation of HPMF *via* the pathway shown in Figure 7.2 is estimated to be ~100 kJ mol^{-1} more exothermic than the C_1 + HCOOH reaction, shown in Figure 7.1 (Andersen and Carter, 2003, Long et al., 2009). Therefore, it is possible that increased internal energy stored within the HPMF formed *via* DME oxidation may lead to greater photoionization of this species. There was some evidence of a mass present at *m/* = 64, although this species was not observed during all of the experiments and was right on the limit of detection of the PIMS set-up used. Notably, the observation of a species at *m/z* = 64 is thought to be a fragmentation channel of HPMF photoionization ($HOOCH_2OH^+$) (Moshammer et al., 2015), and hence indicates that this is the mechanism by which the CH_2OO + HCOOH reaction occurs (Figure 7.4).

Finally, in addition to the basic PIMS set-up, a multiphoton ionization technique was also implemented to allow for OH detection (Beames et al., 2011). However, throughout all of the CH_2OO + HCOOH experiments conducted no OH was observed; this suggests that either no OH was formed from this reaction, or the amount of OH formed from the reaction is so small that it was below the detection limit of the MPI technique. From a

complementary study of the $CH_3CHO + Cl + O_2$ reaction system a maximum yield of OH can be put on the CH_2OO + HCOOH of $Y_{OH} < (0.10 \pm 0.04)$, which suggests that if any OH formation is occurring it must only be a minor channel.

7.1.4 $CH_2OO + CH_3COOH$

From Table 7.1 it can be seen that a rate coefficient for the C_1 CI + CH_3COOH in excess of $k_{C1AA} = 1 \times 10^{-10}$ cm^3 molecule^{-1} s^{-1} (Welz et al., 2014), these measurements are at least four orders of magnitude larger than previous evaluations, where an upper limit of $k_{C1AA} > 1\times 10^{-14}$ cm^3 molecule^{-1} s^{-1} was reported (Johnson et al., 2001). However, thus far there have been no studies which have specifically probed the products from this reaction. Additionally, unlike the CH_2OO + HCOOH reaction, there are no theoretical studies which discuss the possible mechanisms or products of the C_1 + CH_3COOH reaction; however, it will likely react in a similar fashion. The three most probable reaction pathways are shown in Figure 7.9. The first possible mechanism involves the CH_2OO attacking the OH group, yielding hydroperoxymethyl acetate (HPMA). It has been hypothesized that the corresponding product from the C_1 + HCOOH reaction (HPMF) may be dehydrated to form formic acid anhydride (Long et al., 2009). The second possible reaction is a cycloaddition to an intermediary hydroxylated secondary ozonide species (Aplincourt and Ruiz-López, 2000); in the final possible reaction the Criegee intermediate is inserted into the C-H bond of the acid species. One of the main objectives of this study is to try and gain some insight as to the mechanism of the reaction.

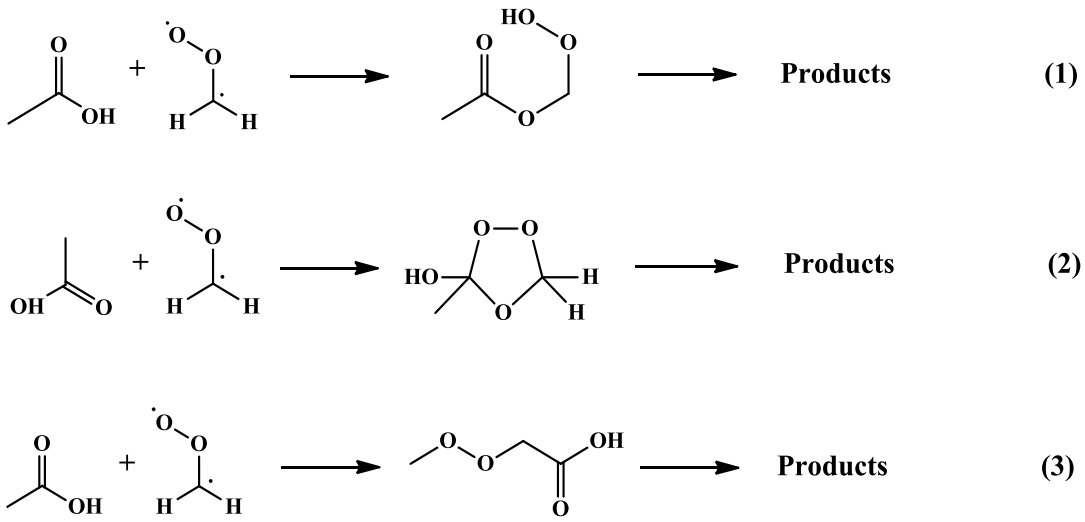

Figure 7.9: A schematic of the most likely reaction mechanisms for the reaction between CH_2OO and CH_3COOH.

Initially, the experiments were conducted at low concentrations of CH_2OO ($1.0 \times 10^{12} < [CH_2OO]_0$/molecule cm^{-3} $< 1.5 \times 10^{12}$). However, due to the low concentration of CH_2OO, the quality of the data was compromised and typically signal-to-noise ratios (*SNR*) below

ten were recorded. That meant that some of the total C_1 CI loss rates ($k'_{C1total}$) determined had sizeable uncertainties (1σ), as large as ~25% for the high [CH_3COOH] data points. After the analysis using equations E7.1-7.3, the data were compiled and a bimolecular plot of the data was constructed (Figure 7.10). The linear regression fit plotted was weighted using the error of the individual data points, meaning the rate coefficient determined put less emphasis of the data with high uncertainties.

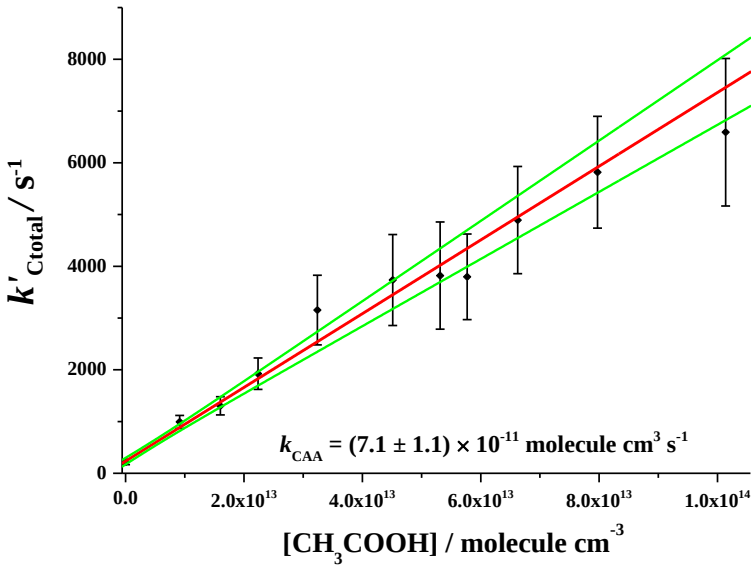

Figure 7.10: A bimolecular plot of obtained for the reaction between the C_1 CI + CH_3COOH. The error quoted is propagated using the random errors quoted from the plot (1σ) and a 15% systematic experimental error. Uncertainty limits shown are to 2σ.

From the bimolecular plot shown in Figure 7.10 a rate coefficient of k_{C1AA} = (7.1 ±1.1) × 10^{-11} cm^3 $molecule^{-1}$ s^{-1} for the reaction between CH_2OO + CH_3COOH was determined, this evaluation is approximately 45% lower than previous literature estimation (see Table 7.3). However, if the dimer to monomer conversion factor that was applied to the [CH_3COOH] prior to analysis is ignored, a different value of k_{C1FA} is obtained (Table 7.3).

Table 7.3: Highlights the effect that acetic acid dimerization has on k_{C1FA} and how our measurements compare to recent literature results.

k_{C1FA} (×10^{-11}) / cm^3 $molecule^{-1}$ s^{-1}	Is dimerization accounted for?	Method used to adjust concentration	Reference
7.1 ± 1.1	Yes	$N_{M^*} = 2N_D + N_M$	This study
12.8 ± 2.0	No	No adjustment	This study
13 ± 1	Yes	Unknown	(Welz et al., 2014)

From Table 7.3, it can be seen that if CH_3COOH dimerization is ignored the measurements made from this study correspond very well with the work of Welz et al. (2014). However, these results are based upon the assumption that neither of the previous studies study took

the dimerization of formic acid into account using E7.7; this is highly unlikely as Welz et al. (2014) state that dimerization is considered, although they do not state how this is done.

The quality from this data was insufficient to yield quantitative information about the products of the reaction, although, there was some evidence for a species with a mass of approximately $m/z \approx 75$. To gain a better understanding of the products from the reaction, time was spent trying to improve sensitivity of the instrumentation; this was achieved by realignment of the photoionization lasers to maximise the signal and also fine tuning of the pinhole position below the mass spectrometer. To further improve the quality of the data collected from this experiment, a new fill was given to the excimer laser; this increased the laser power to approximately 75-100 mJ cm^{-2}. This, in turn, increased the initial concentration of CI to approximately $[CH_2OO]_0 \sim 4 \times 10^{12}$ molecule cm^{-3}. After these alterations the quality of the Criegee signal (S_{CH2OO}) was much improved ($SNR > 30$), and the products of the reactions could be properly investigated. It should be noted that a second bimolecular plot was constructed from the new (higher quality) data and a rate coefficient of $k_{C1AA} = (6.1 \pm 0.9) \times 10^{-11}$ cm^3 $molecule^{-1}$ s^{-1}. However, due to the larger initial concentration of CH_2OO used, it is thought that for some of the low $[CH_3COOH]$ experiments pseudo first-order conditions were not met. Despite this, the rate coefficient retrieved from the bimolecular plot was not significantly different from the previous evaluation made in this study. The emphasis of these experiments was not to obtain kinetic information about the reaction, but instead to try and understand the mechanics of the reaction. Similarly to the C_1 + HCOOH reaction, OH detection was attempted, but no mass was observed at $m/z = 17$. However, with the augmentation in the sensitivity of the detection, it was clear that there was indeed a product forming around $m/z \sim 75$; the exact mass of the species was actually $m/z = 74$ (Figure 7.11).

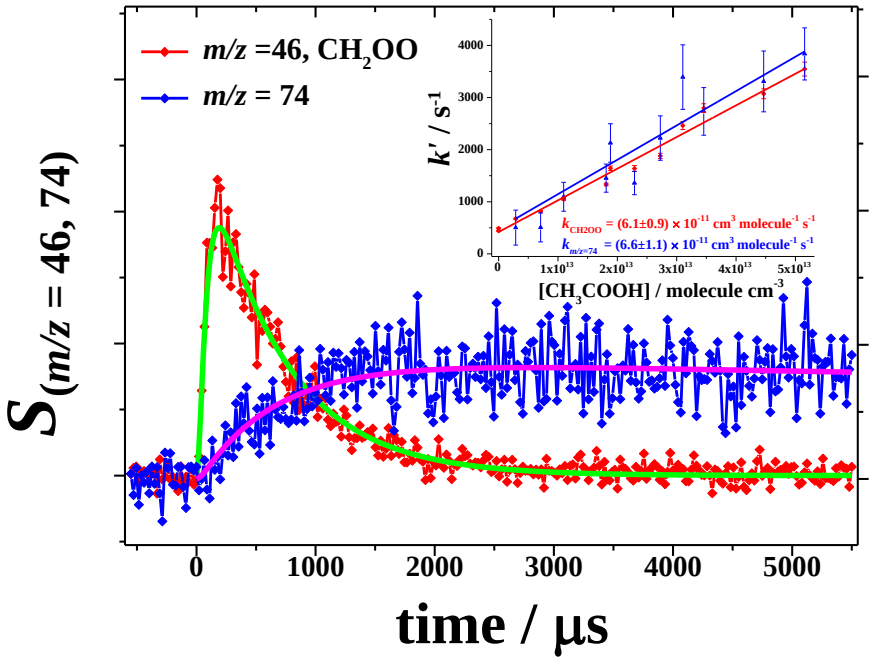

Figure 7.11: A plot showing CH_2OO decay and corresponding formation of a product at *m/z* = 74. Note both the CH_2OO decay rate coefficient and the *m/z* = 74 growth rate coefficient fitted with a pseudo first-order rate coefficients of *k'* = (1560 ± 10) s^{-1}. The inset shows the bimolecular plots produced from analysis of the CH_2OO signal (red) and the signal at *m/z*=74 (blue).

There seems to be a clear correlation between the destruction of the CH_2OO and the formation of a species at *m/z* = 74. To establish whether the species forming at *m/z* = 74 was a product from the reaction between CH_2OO + CH_3COOH, a bimolecular plot of both the CH_2OO and the *m/z* =74 pseudo first-order rate coefficients were plotted together (Figure 7.11, inset). Notably, the rate coefficient obtained from the *m/z* = 74 signal, $k_{m/z=74}$ = (6.6±1.1) × 10^{-11} cm^3 $molecule^{-1}$ s^{-1}, was not significantly larger than rate coefficient determined from the CH_2OO signal, k_{C1AA} = (6.1±0.9) × 10^{-11} cm^3 $molecule^{-1}$ s^{-1}. To verify this result a global fitting, similar to that described in Chapter VI, section 6.3.2., was used. The premise of this type of function is to fit all of the Criegee loss data and *m/z* = 74 growth data simultaneously, meaning that a single evaluation of k_{C1AA} can be calculated for all of the data (a more detailed description of the global fitting procedure can be found in Chapter VI). The data were fitted using two different sets of equations, for two different scenarios; the first set of equations assumes that the formation of the species at *m/z* = 74 is directly dependent upon the loss of CH_2OO from reaction with CH_3COOH (E7.8-7.9). Conversely, the second pair of equations assume that *m/z* = 74 formation is independent of the CH_2OO loss (E7.8a-7.9a). Examples of the fittings produced for both scenarios can be found in Figure 7.11.

$$k'_{m/z74} = (k_{\mathrm{C1AA}} \times [\mathrm{CH_3COOH}]) + k_{\mathrm{w}} + k_{\mathrm{X}} \qquad \text{(E7.8)}$$

$$S_{m/z74\text{height}} = S_{\text{C1height}} \times A \times \left(\frac{(k_{\text{C1AA}} \times [\text{CH}_3\text{COOH}]) + k_{\text{X}}}{k'_{m/z74}} \right) \quad \text{(E7.9)}$$

$$k'_{\text{m/z74}} = k_{\text{w}} + k_{\text{X}} \quad \text{(E7.8a)}$$

$$S_{m/z74\text{height}} = S_{\text{C1height}} \times A \times \left(\frac{k_{\text{X}}}{k'_{\text{m/z74}}} \right) \quad \text{(E7.9a)}$$

In E6.14-6.23: $k'_{m/z74}$ is the rate coefficient for the formation of the species at m/z = 74; S_{C1height} is the height of the Criegee signal (m/z =46); $S_{m/z=74\text{height}}$ represents the height of the signal at m/z = 74; k_{X} is the rate coefficient of other reactions which contribute to the chemical production of m/z = 74 (e.g. C_1 CI self-reaction); k_{w} is the non-chemical contribution to m/z = 74 production; A is a scaling factor.

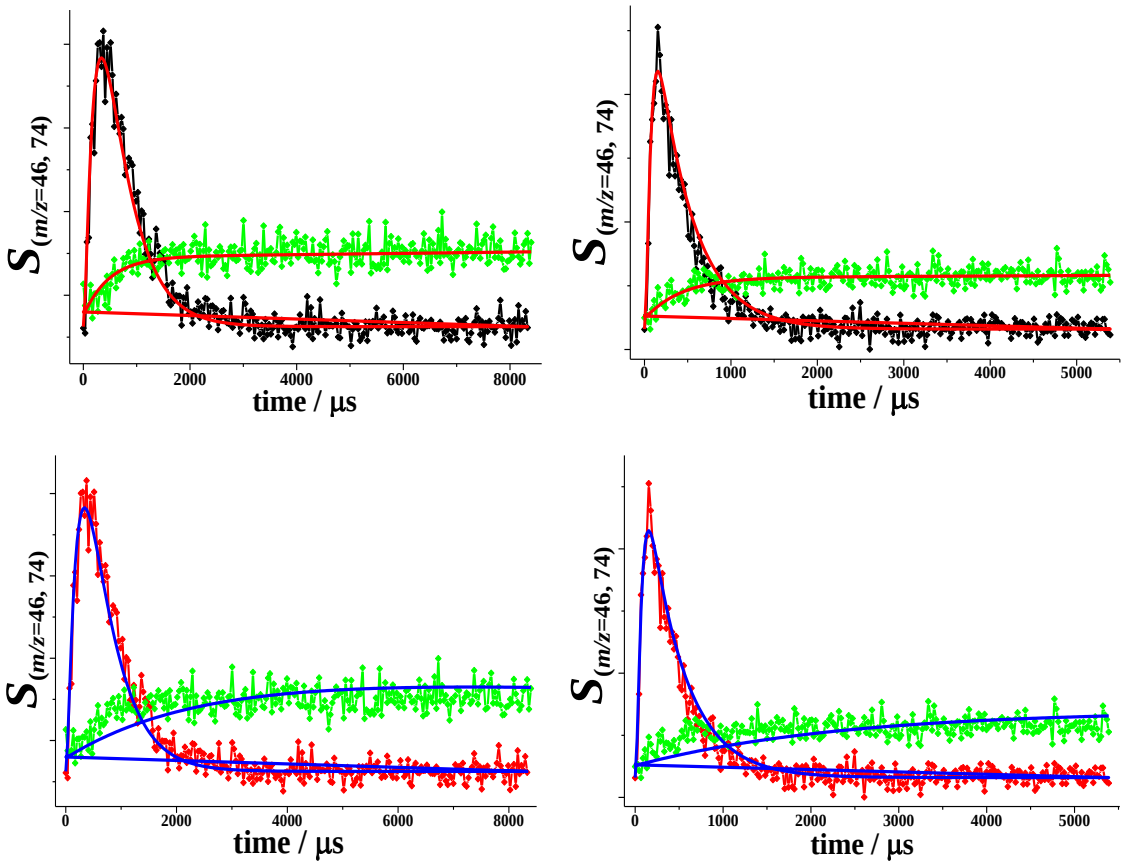

Figure 7.12: (Upper) these graphs are a sample of the globally fitted plots using equations E7.8-7.9, the green points represent the Criegee signal, the black points represent the *m/z* = 74 data and the red line is the fitting through the data. (Lower) these plots are fit using equations E7.8a-7.9a, here the red points represent the Criegee signal, the green points represent the *m/z* = 74 data and the blue line is the fitting through the data. (Left-side) the data shown in both of the plots on the left-hand side were done at [CH_3COOH] = 2.3 × 10^{13} molecule cm^{-3}. (Right-side) the data shown on the right-hand side were done at [CH_3COOH] = 3.4 × 10^{13} molecule cm^{-3}.

From Figure 7.12 it is clear to see the equations E7.8-7.9 give a much better fit to the *m/z* = 74 data, meaning that the species at *m/z* = 74 is dependent upon k_{C1AA} and must be a product the reaction between CH_2OO and CH_3COOH. Furthermore, the rate coefficient determined from the global fitting, $k_{C1AA} = (5.8\pm0.9) \times 10^{-11}$ cm^3 molecule^{-1} s^{-1}, was also in good agreement with the previous analysis.

If it is assumed that the reaction mechanism is similar to the C_1 + HCOOH reaction, there are two possible reaction pathways; the first to be considered is the formation of a hydroxylated secondary ozonide (Long et al., 2009). Once formed it is possible that the secondary ozonide may decompose to O_2 and methyl acetate, *m/z* = 74 (Figure 7.13).

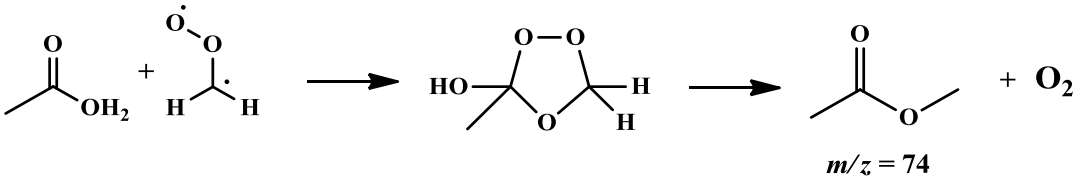

Figure 7.13: Expected products from secondary ozonide species.

Methyl acetate also has an ionization potential of ~10.2 eV (Cannington and Ham, 1985), which is below the threshold of the ionization source (10.5 eV). Conversely, methyl formate has an ionization potential of ~10.8 eV (Watanabe et al., 1962); this would explain why no peak corresponding to methyl formate (*m/z* = 60) was observed in the reaction between CH_2OO + HCOOH. However, the weakest bond in the secondary ozonide species is the O-O bond, making it the most likely to break and it is difficult to justify why reaction would not proceed *via* this mechanism.

The same thought process is applied to the alternative mechanism, where the OH group on the acid attacks the Criegee's central carbon atom to form hydroperoxymethyl acetate. Interestingly, when exploring this mechanism it is possible to reconcile the formation of a species with *m/z* = 74 (Figure 7.14). The species formed is formic acid anhydride (FAN), ionization potential ~ 10.65 eV (Moshammer et al., 2015). However, if this were the mechanism, formic acid anhydride would also be an expected product from the reaction between CH_2OO + HCOOH and no such mass was observed. Although, a small barrier to FAN formation is predicted for the CH_2OO + HCOOH reaction (Long et al., 2009); this may explain no signal was observed at *m/z* = 74 for the C_1 + HCOOH reaction. It is also possible that the signal observed at *m/z* = 74 was from fragmentation of HPMA during photoionization, although if this were the case it would be expected that similar peak would be observed in the formic acid reaction.

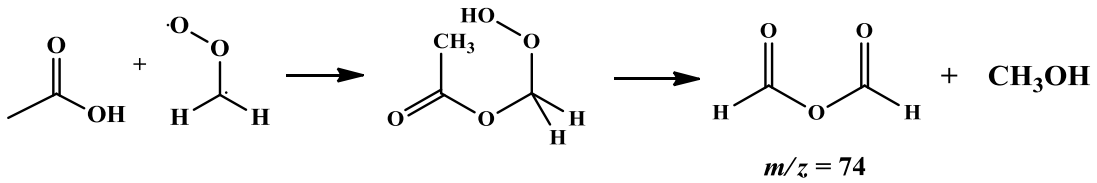

Figure 7.14: Potential products from hydroperoxymethyl acetate decomposition.

7.1.4.1 CH_2OO + CH_3COOH Conclusions

This work describes a comprehensive study of the reaction between C_1 Creigee intermediate and acetic acid, and reports both kinetic and mechanistic information about this channel. The rate coefficient of the reaction was found to be extremely fast, $k_{C1AA} = (7.1 \pm 1.1) \times 10^{-11}$ cm^3 $molecule^{-1}$ s^{-1}, however, this measurement is still approximately 45% lower than other recent studies of the reaction (Sipilä et al., 2014, Welz et al., 2014). Additionally, the products of the reaction were also observed and a small signal at *m/z* = 74 was measured. Upon closer analysis it was apparent that the species at *m/z* = 74 was a product from the CH_2OO + CH_3COOH reaction. This is an interesting result as it gives some mechanistic information about the reaction. Indeed, from only one of the suggested mechanisms will a species with *m/z* = 74 be likely formed; this result therefore implies that the most probable reaction pathway for the reaction is *via* a hydroperoxymethyl acetate species (Figure 7.14). The equivalent pathway for the CH_2OO + HCOOH reaction is hypothesised to be the most thermodynamically stable reaction channel (Aplincourt and Ruiz-López, 2000).

7.1.5 Atmospheric Implications

It is well known that for the C_1 Criegee intermediate the reaction with water and its dimer are the dominant atmospheric sinks; although it is thought that the enhanced kinetics of carboxylic acids may allow these species to compete as a sink for CH_2OO. Indeed, in Welz et al. (2014) it is suggested that the carboxylic acids may be responsible for up to 10% of the CH_2OO removal in boreal forest environments; however, there are some major oversights in these calculations. For instance, the calculations by Welz et al. (2014) do not include $(H_2O)_2$, the dominant sink for CH_2OO in the atmosphere. Another problem is that these calculations do not take any temperature dependency into account for either the carboxylic acids or the water dimer, which is thought to have a strong negative temperature dependence.

However, in the calculations performed as part of this study all of the problems mentioned were taken into account. The concentrations of water used were determined for the different values of the relative humidity (RH) and the water dimer concentrations were calculated using a equilibrium constant of $K_{eqm} = 0.04$ atm^{-1} at 298 K and $K_{eqm} = 0.045$ atm^{-1} at 283 K (Shillings et al., 2011). The concentration of acid (where [acid] = [HCOOH + CH_3COOH])

was estimated using measurements from a paper reviewing atmospheric concentrations of formic and acetic acid (Khare et al., 1999); from this source an [acid] of 2.5 ppbv was used and for the calculations in the rural areas. In Khare et al. (1999) it was also observed that generally much greater concentrations of HCOOH and CH_3COOH were measured in urban environments, for these calculations carboxylic acid concentration of [acid] = 10 ppbv was used. All of this information was then used to calculate the contribution of each sink of the total loss of CH_2OO (Table 7.4). The calculations were done at two different temperatures (298 K and 283 K) to explore the effect of water dimerization, and for rural and urban environments.

Table 7.4: Highlights the major loss channels (including organic acids) for the C_1 CI, these are displayed a percentage loss.

Temp. / K	Region	RH / %	$[H_2O]$ / cm^{-3}	$[(H_2O)_2]$ / cm^{-3}	[Acid] / cm^{-3}	% Loss H_2O	% Loss $(H_2O)_2$	% Loss Acid
298	Rural	75	5.8×10^{17}	5.5×10^{14}	6.3×10^{10}	21.0	78.6	0.4
298	Rural	50	3.9×10^{17}	2.4×10^{14}	6.3×10^{10}	28.6	71.2	0.3
298	Urban	75	5.8×10^{17}	5.5×10^{14}	2.5×10^{11}	21.0	78.5	0.5
298	Urban	50	3.9×10^{17}	2.4×10^{14}	2.5×10^{11}	28.3	70.7	1.0
283	Rural	75	2.3×10^{17}	9.9×10^{13}	6.3×10^{10}	22.8	77.0	0.1
283	Rural	50	1.6×10^{17}	4.4×10^{13}	6.3×10^{10}	30.7	69.0	0.3
283	Urban	75	2.3×10^{17}	9.9×10^{13}	2.5×10^{11}	22.7	76.7	0.6
283	Urban	50	1.6×10^{17}	4.4×10^{13}	2.5×10^{11}	30.4	68.4	1.2

The calculations in Table 7.4 were determined using the following rate coefficients: $k_{C1H2O} = 1\times10^{-15}$ cm^3 $molecule^{-1}$ s^{-1} (Newland et al., 2015); $k_{C2(H2O)2} = 4\times10^{-12}$ cm^3 $molecule^{-1}$ s^{-1} at 298 K (Lewis et al., 2015), to take into account the negative temperature dependence previously observed, this value was doubled for the calculations at 283 K (Smith et al., 2015); finally $k_{C1Acid} = 5.5\times10^{-10}$ cm^3 $molecule^{-1}$ s^{-1}.

From Table 7.4 it can be seen that in rural environments the dominant sinks for CH_2OO are water and its dimer, with the carboxylic acid channel making little impact. However, in urban environments the contribution from the carboxylic acid is greater and this C_1 + acid reaction can be considered a minor channel for CH_2OO destruction. Furthermore, it is thought that in some specific environments the percentage of C_1 CI reaction with carboxylic acids may be greater still. For example, a study was conducted investigating atmospheric carboxylic acids levels in Arizona (Dawson and Farmer, 1988). In Dawson and Farmer (1988) concentrations of HCOOH and CH_3COOH were measured at ~ 3 ppbv and ~ 4 ppbv, respectively. Moreover, the relative humidity in Arizona is generally very low (typically RH = 50% in the morning and 25% in the afternoon) (Osborn, 2016); under these

atmospheric conditions it is calculated that the CH_2OO loss from HCOOH and CH_3COOH will be ~3%.

In addition, CI + acids reactions may have a significant impact upon the oxidation of carboxylic acids in the atmosphere. In fact, calculations suggest that CIs may be a moderate sink for carboxylic acids present in the troposphere, particularly at night when the concentration of OH is low (Table 7.5).

Table 7.5: Highlights the competition between OH and CIs for the removal of carboxylic acid in the troposphere.

Time	k_{OH}/ cm^3 s^{-1}	k_{Acid}/ cm^3 s^{-1}	[OH] / cm^{-3}	[CI] / cm^{-3}	loss OH / %	loss CI / %
Day	7.5×10^{-13}	5.0×10^{-11}	1×10^{6}	1×10^{3}	93.2	6.8
Night	7.5×10^{-13}	5.0×10^{-11}	1×10^{5}	1×10^{3}	57.7	42.3

It should be noted that the calculations in Table 7.5 were determined using the following rate coefficients: $k_{Acid} = 5.5\times 10^{-11}$ cm^3 molecule^{-1} s^{-1}, which is an averaged value from the C_1 CI + carboxylic acid rate coefficients determined from this study; $k_{OH} = 7.5\times 10^{-13}$ cm^3 molecule^{-1} s^{-1}, note this is the rate coefficient of the OH + CH_3COOH reaction (Atkinson et al., 2001).

The calculations presented in Table 7.5 suggest that a significant proportion of atmospheric carboxylic acids (~7% during the day and ~40% at night) are removed by Criegee intermediates. Previously, it has been assumed that the atmospheric oxidation of organic acids was dominated by the reaction with OH (R7.8) (Calvert, 2011).

$$CH_2OO + HCOOH \rightarrow HCOO + H_2O \quad \text{(R7.8)}$$

$$HCOO \rightarrow H + CO_2 \quad \text{(R7.9)}$$

However, if these calculations are accurate and Criegee intermediate also contribute to organic acid removal, the oxidation pathway will clearly be different, with different (initial) products, such as HPMF and HPMA, being formed; this may lead to increased SOA formation in these environments.

7.2 CI + Alkenes

7.2.1 Introduction

Criegee intermediates are predominantly formed from alkene ozonolysis in the atmosphere; notably, CI concentrations are understood to be greatest in regions with high alkene concentrations, such as boreal forests. However, currently there is very little known about Criegee reactivity towards alkenes, and only one previous study has measured any rate

coefficients for this group of reactions (Buras et al., 2014). Originally, it was thought that these species may play an important role as CH_2OO sinks in forest environments where alkene concentrations are high (Stone et al., 2011). However, due to the low reactivity of CIs towards the alkenes, it is predicted that the impact on Criegee loss will be minimal. That said, understanding the rate coefficients for these reactions is still important and in this section the results from experiments of the C_1 CI + ethene (C_2H_4) reaction are reported. In addition to this, the rate coefficients from the reactions of the C_1 + C_2 CIs with isoprene (C_5H_8) are also described; notably, there are no previous measurements of this reaction in the literature.

7.2.2 Experimental

In this section a brief summary of the experimental methodology will be given. For all of the experiments conducted CH_2I_2 (or CH_3CHI_2)/O_2/He/Alkene gas mixture were flowed through the reactor *via* calibrated mass flow controllers (MFCs); these experiments conducted using the PIMS technique were conducted at low pressures (1.0-2.5 Torr). Bubblers were used to ensure a reproducible amount of the diiodo- species were added (see Chapter VI, Figure 6.2). The C_1 + C_2 CIs were generated by adding large quantities of neat oxygen ($[O_2] = 1 \times 10^{16}$ molecule cm^3) to the CH_2I and CH_3CHI radicals, produced from the diiodo- precursors photolysis, respectively (R7.1-7.2 and R6.11-6.12, Chapter VI).

To ensure the experiments were completed under pseudo-first-order conditions both the ethene and isoprene added had to be kept in excess of [CI]. For the purpose of these experiments dilute samples, ~ 5%, of both isoprene (Sigma-Aldrich, ≥ 99%) and ethene (BOC, 99.9%) were prepared in helium and stored in bulbs. This method worked well for isoprene; however, ethene was so unreactive towards CH_2OO that no observed change was measured in the S_{CH2OO}. To rectify this, pure ethene was added directly from the gas cylinder.

Finally, during this study, diiodo-precursors were initiated by pulsed laser photolysis using an excimer laser (λ = 248 nm, typically ~ 50 mJ cm^{-2}) and the gas sampled was photoionised using λ = 118 nm light (for details see Chapter II). The data analysis for the CI + alkene study was done using equations E7.1-7.3 (see Section 7.1.2). Additionally, the data collection and analysis techniques used in this CH_2OO + alkene study have been described previously (Chapter VI).

7.2.3 CH_2OO + Ethene

$$CH_2OO + C_2H_4 \rightarrow \text{Products} \qquad \text{(R7.10)}$$

In this section of the chapter, results concerning the reaction of the stabilised C_1 Criegee intermediate and ethene will be discussed (R7.10). This reaction was chosen because ethene is one of the more abundant alkenes in the atmosphere, $5 < [C_2H_4] < 30$ ppbv (Myers et al., 2015, Na et al., 2001); indeed, in polluted environments atmospheric $[C_2H_4] > 700$ ppbv have been measured in urban environments (Abeles and Heggestad, 1973). It is therefore thought that the potential of ethene as a sink of Criegee intermediates will be greater than for most other alkenes. Only one previous study has probed this reaction (Buras et al., 2014). In the study by Buras et al. (2014) a rate coefficient for this reaction of $k_{C1ethene} = (0.7\pm0.1) \times 10^{-15}$ cm^3 molecule^{-1} s^{-1} was measured.

As mentioned in the experimental section, initially no observable change in S_{CH2OO} was measured, even when relatively high ethene concentrations were added to the system ($[C_2H_4] \approx 2.5 \times 10^{14}$ molecule cm^3). This problem was, somewhat, solved by adding pure ethene into system ($[C_2H_4] > 3.5 \times 10^{15}$ molecule cm^3); although the increase in $k'_{C1total}$ was still only very marginal, implying that the rate coefficient for the reaction, $k_{C1ethene}$, was small. In general the quality of the data collected was low ($5 < SNR < 10$) (Figure 7.14); moreover, it was observed that the quality of the data was significantly worse at the higher concentrations of ethene ($SNR < 5$). It should be noted that throughout these experiments the concentration of the C_1 CI was thought to be $[CH_2OO]_0 \approx 1\times 10^{12}$ molecule cm^3.

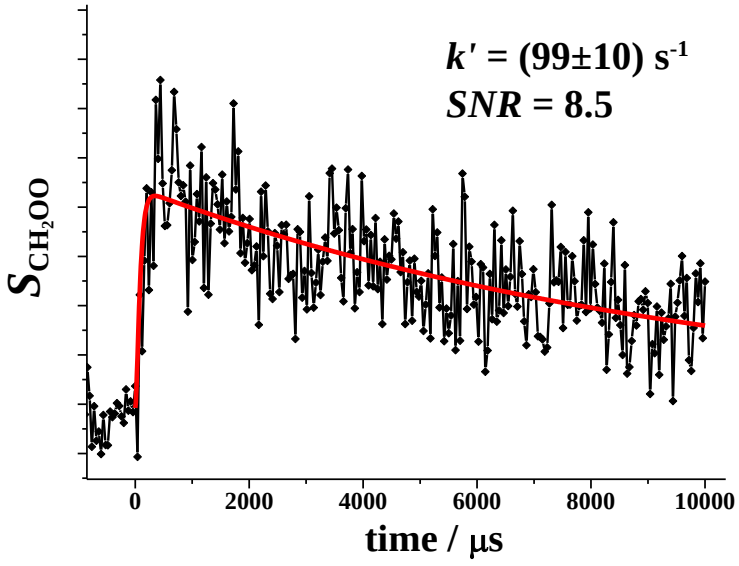

Figure 7.15: An example of the Criegee signal measured during the C_1 + ethene experiments. $[C_2H_4] = 9\times10^{14}$ molecule cm^{-3}, $[CH_2OO]_0 < 1.5\times10^{12}$ molecule cm^{-3}.

The data collected from the C_1 + ethene experiments were collated and a bimolecular plot was assembled (Figure 7.15). From the bimolecular plot of this reaction (Figure 7.15) a rate coefficient for the C_1 + ethene reaction of $k_{C1ethene} = (8 \pm 2) \times 10^{-15}$ cm^3 molecule^{-1} s^{-1} was determined. However, even at high [ethene], the changes in $k'_{C1total}$ are only minor, which suggests that any reaction taking place between CH_2OO and ethene is very slow. Indeed, insufficient ethene could be added to definitively say that any reaction is actually occurring and many of the $k'_{C1total}$ values obtained from the data at high [ethene] (> 2.5×10^{15} molecule cm^3) were not significantly larger than the evaluations of k'_{other} (the value of $k'_{C1total}$ at [ethene] = 0 molecule cm^{-3}). With data of this quality, where no discernible reaction can be seen taking places, it makes little sense quoting a rate coefficient, instead an upper limit of $k_{C1ethene} < 2 \times 10^{-14}$ cm^3 molecule^{-1} s^{-1} is recommended.

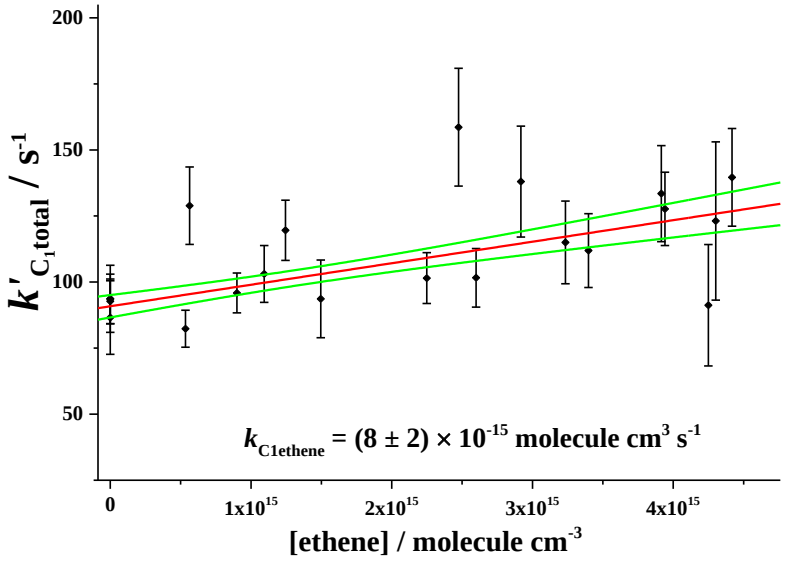

Figure 7.16: A bimolecular plot of the data from the C_1 + ethene study. The error quoted is propagated using the random errors quoted from the plot and a 10% systematic experimental error. Uncertainty limits shown are to 1σ.

The evaluation of $k_{C1ethene}$ using this technique is more than an order of magnitude higher than the rate coefficient by Buras et al. (2014). However, it should be noted that in our experiments the pressure was restricted to approximately 2 Torr, which limited the maximum amount of ethene which could be added to the system ([C_2H_4] < 5×10^{15} molecule cm^3). It is for this reason that the rate coefficient evaluated from this study is described as an upper limit from the reaction. Whereas, the experiments described in Buras et al. (2014) were conducted at higher pressures (10 – 50 Torr), meaning that far greater concentrations of alkene could be added ([C_2H_4] > 2×10^{17} molecule cm^3) and significant changes to $k'_{C1total}$ were observed, $\Delta k'_{C1total} \geq 200$ s^{-1}. Therefore the measurement of $k_{C1ethene} = 0.7 \times 10^{-15}$ cm^3 molecule^{-1} s^{-1} made by Buras et al. (2014) is likely to be the more

accurate evaluation. However, from this study the rate of this reaction shown to be very slow (with an upper limit $k_{C1ethene} < 2 \times 10^{-14}$ cm^3 molecule^{-1} s^{-1}), meaning that the reaction with ethene is not a sink of CH_2OO anywhere in the atmosphere (see section 7.2.6).

7.2.4 C_1 and C_2 CI with Isoprene

The second alkene used as part of this study was isoprene (C_5H_8); unlike the ethene reaction, the reactivity of isoprene towards both the C_1 and *syn*-C_2 Criegee intermediates was investigated. The rate coefficient of CI + isoprene reactions had never previously been recorded in literature, which is surprising given the importance of isoprene within the atmosphere. Isoprene a major biogenic emission (>500 Tg yr^{-1}), is primarily released into the atmosphere from trees and vegetation, and it is thought to play an important role in the HO_x and ozone budgets in certain environments (e.g. rainforests) (Guenther et al., 2006, Stone, 2011). Isoprene has an atmospheric lifetime of only 1- 2 hours (Karl et al., 2006), which is largely due to its reaction with the OH radical. This reaction directly leads to the formation of the isoprene peroxy-radical and HO_2, both of which will further react, and ultimately produce ozone. It should be noted that as part of this reaction cycle both OH and HO_2 are recycled (Peeters et al., 2009); this is important as both these HO_x species are integral to the oxidation within the troposphere (Chapter I). The ozonolysis of isoprene is another important atmospheric reaction contributing largely to the tropospheric production of organic and organic acid compounds, as well as generating OH and HO_2 radicals in yields of approximately 0.26 molecules per molecule of isoprene consumed (Malkin et al., 2010). Due to the reactivity of isoprene in the atmosphere and the volume emitted, isoprene has a key role in determining the oxidising capacity of the atmosphere. It is therefore essential that we understand all the different reactions of isoprene, including its reactivity towards CIs.

Throughout all of the CI + isoprene experiments conducted the quality of the data collected were low (*SNR* < 10). Concentrations of $[CH_2OO]_0 \approx 1.5 \times 10^{12}$ molecule cm^3 and $[CH_3CHOO] < 2.5 \times 10^{12}$ molecule cm^3 are estimated for the C_1 and C_2 Criegee intermediates respectively. An example of the data for the C_1 + isoprene reaction can be seen in Figure 7.16, as with the ethene reaction the rate coefficient was small. In fact, even at high isoprene concentrations, [isoprene] > 2.5×10^{14} molecule cm^{-3}, the value of $k'_{C1total}$ was only just significantly greater than k'_{other}. Therefore, from this data only an upper limit for the C_1 + isoprene reaction could be reliably determined, $k_{C1isoprene} < 3 \times 10^{-13}$ cm^3 molecule^{-1} s^{-1}.

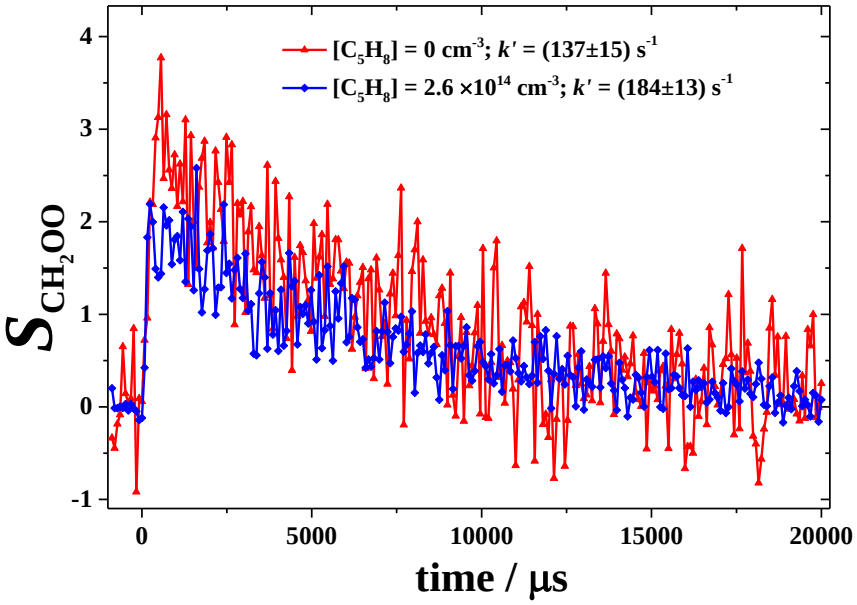

Figure 7.17: A example of the data traces from the C_1 + isoprene reaction. The isoprene concentration for the blue data points is [isoprene] = 0 molecule cm^{-3}. The isoprene concentration for the red data points is [isoprene] = 2.6× 10^{14} molecule cm^{-3}.

Table 7.6: Shows the rate coefficients obtained from the C_1 and C_2 CI reactions with isoprene.

Criegee intermediate	$k_{isoprene}$/ cm^3 molecule^{-1} s^{-1}
CH_2OO	$< 3 \times 10^{-13}$
CH_3CHOO	$(8.3 \pm 4.1) \times 10^{-13}$

In Table 7.6 the rate coefficients measured for both the C_1 and C_2 CIs with isoprene are listed. Notably, the rate for the C_2 reaction, $k_{C2isoprene}$, was significantly greater than the corresponding rate coefficient measured for the C_1 reaction. However, the quality of the data at high [isoprene] was generally poor ($2.5 < SNR < 5$); this led to significant errors associated with $k'_{C2total}$ that were calculated using equations E7.1-7.3. This meant that the majority of the values of $k'_{C2total}$ were not significantly bigger than k'_{other} (Figure 7.17). As the quality of the Criegee signal for the C_2 CI got worse at higher isoprene concentrations, repeating the experiments over a larger range of [isoprene] would have further reduce the quality of the data and so was not attempted.

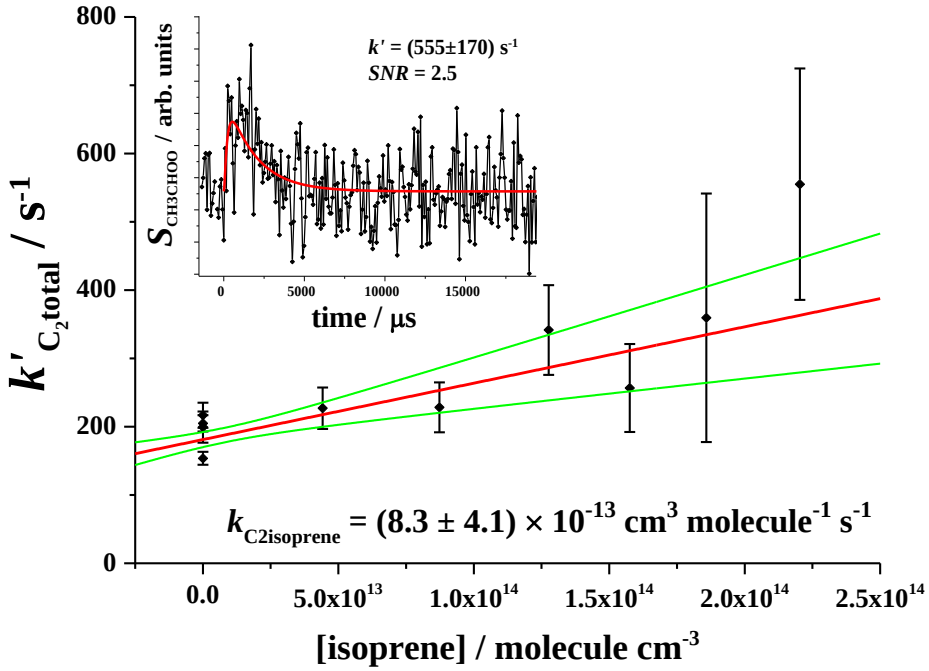

Figure 7.18: A bimolecular plot of the data from the C_2 + isoprene study. The error quoted is propagated using the random errors quoted from the plot and a 10% systematic experimental error. Uncertainty limits shown are to 1σ. The inset is an example of the data quality at

It should be noted that the *syn*- conformer of the C_2 CI is preferentially formed over the *anti*- in the approximate ratio of 9:1, meaning the reaction being predominantly probed is between the *syn*-C_2 CI and isoprene. From these experiments conducted there was some evidence of a reaction occurring between the *syn*-C_2 + isoprene. However, the reaction was clearly slow, with an estimated rate coefficient of $k_{C2isoprene} = (8.3 \pm 4.1) \times 10^{-13}$ cm^3 molecule^{-1} s^{-1}.

7.2.5 Atmospheric and Experimental Implications

From the experiments conducted in the study, both the reactions of ethene and isoprene with the C_1 Criegee intermediate were found to be very slow ($k < 5 \times 10^{-13}$ cm^3 molecule^{-1} s^{-1}). Therefore, even though both of these species are relatively abundant in the atmosphere their contribution to CH_2OO destruction can be considered to be negligible (> 0.05%), even in environments where their concentrations are at their peak.

However, the rate coefficient for the *syn*-C_2 CI with isoprene is significantly faster than either of the C_1 + alkene reactions. Moreover, the rate coefficient of the *syn*-CH_3CHOO with H_2O is thought to be considerably smaller than that of CH_2OO + H_2O. To determine the impact that the reaction with isoprene may have on the loss of the *syn*-C_2 CI, calculations to evaluate the contribution of the C_2 CI + isoprene channel were performed (Table 7.7).

Table 7.7: Shows the loss channels for the C_2 CI, including isoprene (excluding organic acids), these are displayed a percentage loss.

Temp / K	Region	RH / %	$[H_2O]$ / cm^{-3}	$[(H_2O)_2]$ / cm^{-3}	$[C_5H_8]$ / cm^{-3}	% loss H_2O	% loss $(H_2O)_2$	% loss C_5H_8
298	Forested	75	5.8×10^{17}	5.5×10^{14}	6.3×10^{11}	0.7	99.3	0.01
298	Forested	50	3.9×10^{17}	2.4×10^{14}	6.3×10^{11}	1.0	99.0	0.03
298	Urban	75	5.8×10^{17}	5.5×10^{14}	1.3×10^{11}	0.7	99.3	0.01
298	Urban	50	3.9×10^{17}	2.4×10^{14}	1.3×10^{11}	1.0	99.0	0.02
283	Forested	75	2.3×10^{17}	9.9×10^{13}	6.3×10^{11}	0.8	99.2	0.04
283	Forested	50	1.6×10^{17}	4.4×10^{13}	6.3×10^{11}	1.2	98.7	0.09
283	Urban	75	2.3×10^{17}	9.9×10^{13}	1.3×10^{11}	0.8	99.2	0.02
283	Urban	50	1.6×10^{17}	4.4×10^{13}	1.3×10^{11}	1.2	98.8	0.05

In the calculations in Table 7.7, the relative loss rates were determined using the following rate coefficients: $k_{C2isoprene} = 1\times 10^{-12}$ cm^3 molecule^{-1} s^{-1}; $k_{C2H2O} = 1\times 10^{-17}$ cm^3 molecule^{-1} s^{-1}; $k_{C2(H2O)2} = 3 \times 10^{-12}$ cm^3 molecule^{-1} s^{-1} at 298 K (Ryzhkov and Ariya, 2004) and $k_{C2(H2O)2} = 6 \times 10^{-12}$ cm^3 molecule^{-1} s^{-1} at 283 K. Notably, differing values for k_{C1H2O2} were used for the calculation at 298 K and 283 K due to the strong, negative, temperature dependence observed by Smith et al. (2015).

From Table 7.4 it can be seen that, even under the most favourable conditions, the contribution of isoprene to the total loss of the C_2 CI is still minimal (0.14%). It should be noted that these calculations excluded the contribution from any CI + carboxylic acid chemistry, meaning that this will be an overestimation of the isoprene contribution.

All of the results from this study suggest that the reactions between C_1 and C_2 Criegee intermediate and alkenes are likely to contribute only very marginally to the total loss of CIs in the atmosphere. This is an important result, and is of particular interest for isoprene, which as previously mentioned plays an important role in both the HO_x and ozone budgets in certain forest environments. The results from this study not only suggest that isoprene is responsible for only a small amount of CI loss, but they also imply that CIs (which are thought to have an atmospheric concentration of [CI] $\approx 1 \times 10^3$ molecule cm^{-3}) will have only a small impact on atmospheric [isoprene]. Moreover, as the tropospheric removal of isoprene by OH is extremely fast, $k_{OHisoprene} = (10.0 \pm 1.2) \times 10^{-11}$ cm^3 molecule^{-1} s^{-1}, meaning that the reaction with OH will dominate isoprene removal. Therefore, it is likely that the impact of the CI + isoprene reactions will be so small as to be negligible and means that these reactions need not be included in the atmospheric modelling of isoprene.

For chamber studies investigating alkene ozonolysis and Criegee intermediate reactivity with trace gases, higher alkene concentrations (in comparison to tropospheric levels) are often used. However, any interference from the CI + alkene reaction will still likely be

minimal provided sensible starting conditions are used. For example, in the ethene ozonolysis chamber experiments described in Newland et al. (2015), the rate coefficient for the CH_2OO + H_2O reaction was inferred using relative rate experiments. In all of these experiments high concentrations of ethene were used (500 ppbv, $[C_2H_4] \approx 1\times10^{13}$ molecule cm^{-3}) at a range of different relative humidities (1.5 – 20 %). However, even at the lowest water concentrations (RH = 1.5%, $[H_2O] \approx 1\times10^{16}$ molecule cm^{-3}), any CI pseudo first-order loss from the CH_2OO + ethene reaction is calculated to be at least two orders of magnitude smaller than from the CH_2OO + water reaction (when using the value of $k_{C1ethene}$ determined from this study). Furthermore, Newland et al. (2015) also determined the rate of unimolecular decomposition for the C_1 CI from linear plots of $[SO_2]\left(\frac{1}{f} - 1\right)$ vs. $[H_2O]$:

$$[SO_2]\left(\frac{1}{f} - 1\right) = \frac{k_{C1H2O}}{k_{C1SO2}}[H_2O] + \frac{k_d + L}{k_{C1SO2}} \quad \text{(E7.10)}$$

In equation E7.10: f is the fraction of SCIs, which react with the SO_2; k_{C1H2O} is the rate coefficient of the CH_2OO + H_2O reaction; k_{C1SO2} is the rate coefficient of the CH_2OO + SO_2 reaction; k_d is the rate of unimolecular decomposition; L is equal to the other pseudo first-order losses in the system. The generic loss term, L, includes CI + alkene chemistry. Ideally, L should be small, meaning the y-intercept is equal to $\frac{k_d}{k_{C1SO2}}$; conversely, if CI + alkene loss is significant, calculating k_d becomes more difficult. However, modelling of this ethene ozonolysis system again indicates that the CI + alkene pseudo first-order contribution will be small in comparison to the y-intercept, hence verifying the assumption that the y-intercept is equal to $\frac{k_d}{k_{C1SO2}}$.

7.3 References

ABELES, F. B. & HEGGESTAD, H. E. 1973. Ethylene: An Urban Air Pollutant. *Journal of the Air Pollution Control Association,* 23**,** 517-521.

ANDERSEN, A. & CARTER, E. A. 2003. Hybrid density functional theory predictions of low-temperature dimethyl ether combustion pathways. II. Chain-branching energetics and possible role of the Criegee intermediate. *Journal of Physical Chemistry A,* 107**,** 9463-9478.

APLINCOURT, P. & RUIZ-LÓPEZ, M. F. 2000. Theoretical Study of Formic Acid Anhydride Formation from Carbonyl Oxide in the Atmosphere. *The Journal of Physical Chemistry A,* 104**,** 380-388.

ATKINSON, R., BAULCH, D., COX, R., CROWLEY, J., HAMPSON JR, R., KERR, J., ROSSI, M. & TROE, J. 2001. Summary of evaluated kinetic and photochemical data for atmospheric chemistry. *IUPAC***,** 1-56.

BAEZA-ROMERO, M. T., BLITZ, M. A., GODDARD, A. & SEAKINS, P. W. 2012. Time-of-flight mass spectrometry for time-resolved measurements: Some developments and applications. *International Journal of Chemical Kinetics,* 44**,** 532-545.

BEAMES, J. M., LIU, F., LESTER, M. I. & MURRAY, C. 2011. Communication: A new spectroscopic window on hydroxyl radicals using UV + VUV resonant ionization. *The Journal of Chemical Physics,* 134**,** 241102.

BLANKSBY, S. J. & ELLISON, G. B. 2003. Bond Dissociation Energies of Organic Molecules. *Accounts of chemical research,* 36**,** 255-263.

BURAS, Z. J., ELSAMRA, R. M. I., JALAN, A., MIDDAUGH, J. E. & GREEN, W. H. 2014. Direct Kinetic Measurements of Reactions between the Simplest Criegee Intermediate CH_2OO and Alkenes. *The Journal of Physical Chemistry A,* 118**,** 1997-2006.

CALVERT, J. G. M., A; ORLANDO, J. J; PILLING, M. J AND WALLINGTON, T. J 2011. The Mechanisms of Atmospheric Oxidation of the Oxygenates. New York: Oxford University Press.

CANNINGTON, P. H. & HAM, N. S. 1985. He(II) photoelectron spectra of esters. *Journal of Electron Spectroscopy and Related Phenomena,* 36**,** 203-205.

DAWSON, G. A. & FARMER, J. C. 1988. Soluble atmospheric trace gases in the southwestern United States: 2. Organic species HCHO, HCOOH, CH_3COOH. *Journal of Geophysical Research: Atmospheres,* 93**,** 5200-5206.

GUENTHER, A., KARL, T., HARLEY, P., WIEDINMYER, C., PALMER, P. I. & GERON, C. 2006. Estimates of global terrestrial isoprene emissions using MEGAN (Model of Emissions of Gases and Aerosols from Nature). *Atmos. Chem. Phys.,* 6**,** 3181-3210.

JOHNSON, D., LEWIN, A. G. & MARSTON, G. 2001. The Effect of Criegee-Intermediate Scavengers on the OH Yield from the Reaction of Ozone with 2-methylbut-2-ene. *The Journal of Physical Chemistry A,* 105**,** 2933-2935.

KARL, M., DORN, H. P., HOLLAND, F., KOPPMANN, R., POPPE, D., RUPP, L., SCHAUB, A. & WAHNER, A. 2006. Product study of the reaction of OH radicals with isoprene in the atmosphere simulation chamber SAPHIR. *Journal of Atmospheric Chemistry,* 55**,** 167-187.

KHAMAGANOV, V. G., BUI, V. X., CARL, S. A. & PEETERS, J. 2006. Absolute rate coefficient of the OH+ $CH_3C(O)OH$ reaction at T= 287-802 K. The two faces of pre-reactive H-bonding. *The Journal of Physical Chemistry A,* 110**,** 12852-12859.

KHARE, P., KUMAR, N., KUMARI, K. M. & SRIVASTAVA, S. S. 1999. Atmospheric formic and acetic acids: An overview. *Reviews of Geophysics,* 37**,** 227-248.

LEWIS, T. R., BLITZ, M. A., HEARD, D. E. & SEAKINS, P. W. 2015. Direct evidence for a substantive reaction between the Criegee intermediate, CH_2OO, and the water vapour dimer. *Physical Chemistry Chemical Physics,* 17**,** 4859-4863.

LONG, B., CHENG, J.-R., TAN, X.-F. & ZHANG, W.-J. 2009. Theoretical study on the detailed reaction mechanisms of carbonyl oxide with formic acid. *Journal of Molecular Structure: THEOCHEM,* 916**,** 159-167.

MALKIN, T. L., GODDARD, A., HEARD, D. E. & SEAKINS, P. W. 2010. Measurements of OH and HO2 yields from the gas phase ozonolysis of isoprene. *Atmospheric Chemistry and Physics,* 10**,** 1441-1459.

MOSHAMMER, K., JASPER, A. W., POPOLAN-VAIDA, D. M., LUCASSEN, A., DIÉVART, P., SELIM, H., ESKOLA, A. J., TAATJES, C. A., LEONE, S. R., SARATHY, S. M., JU, Y., DAGAUT, P., KOHSE-HÖINGHAUS, K. & HANSEN, N. 2015. Detection and Identification of the Keto-Hydroperoxide ($HOOCH_2OCHO$) and Other Intermediates during Low-Temperature Oxidation of Dimethyl Ether. *The Journal of Physical Chemistry A,* 119**,** 7361-7374.

MYERS, J. L., PHILLIPS, T. & GRANT, R. L. 2015. Emissions and ambient air monitoring trends of lower olefins across Texas from 2002 to 2012. *Chemico-Biological Interactions,* 241**,** 2-9.

NA, K., KIM, Y. P., MOON, K.-C., MOON, I. & FUNG, K. 2001. Concentrations of volatile organic compounds in an industrial area of Korea. *Atmospheric Environment,* 35**,** 2747-2756.

NEEB, P., HORIE, O. & MOORTGAT, G. K. 1998. The Ethene−Ozone Reaction in the Gas Phase. *The Journal of Physical Chemistry A,* 102**,** 6778-6785.

NEWLAND, M. J., RICKARD, A. R., ALAM, M. S., VEREECKEN, L., MUÑOZ, A., RÓDENAS, M. & BLOSS, W. J. 2015. Kinetics of stabilised Criegee intermediates derived from alkene ozonolysis: reactions with SO_2, H_2O and decomposition under boundary layer conditions. *Physical Chemistry Chemical Physics,* 17**,** 4076-4088.

OSBORN, L. 2016. *World Data Center for Meteorology. Climate of the World.* [Online]. Canada.

PEETERS, J., NGUYEN, T. L. & VEREECKEN, L. 2009. HO_x radical regeneration in the oxidation of isoprene. *Physical Chemistry Chemical Physics,* 11**,** 5935-5939.

RYZHKOV, A. B. & ARIYA, P. A. 2004. A theoretical study of the reactions of parent and substituted Criegee intermediates with water and the water dimer. *Physical Chemistry Chemical Physics,* 6**,** 5042-5050.

SHILLINGS, A. J. L., BALL, S. M., BARBER, M. J., TENNYSON, J. & JONES, R. L. 2011. An upper limit for water dimer absorption in the 750 nm spectral region and a revised water line list. *Atmos. Chem. Phys.,* 11**,** 4273-4287.

SIPILÄ, M., JOKINEN, T., BERNDT, T., RICHTERS, S., MAKKONEN, R., DONAHUE, N., MAULDIN III, R., KURTÉN, T., PAASONEN, P. & SARNELA, N. 2014. Reactivity of stabilized Criegee intermediates (sCIs) from isoprene and monoterpene ozonolysis toward SO_2 and organic acids. *Atmospheric Chemistry and Physics,* 14**,** 12143-12153.

SMITH, M. C., CHANG, C.-H., CHAO, W., LIN, L.-C., TAKAHASHI, K., BOERING, K. A. & LIN, J. J.-M. 2015. Strong Negative Temperature Dependence of the Simplest Criegee Intermediate CH_2OO Reaction with Water Dimer. *The Journal of Physical Chemistry Letters,* 6**,** 2708-2713.

SPEIGHT, J. G. 2005. Lange's handbook of chemistry. *The McGraw Hill Companies***,** 395-399.

STONE, D., BLITZ, M., DAUBNEY, L., HOWES, N. U. M. & SEAKINS, P. 2014. Kinetics of CH_2OO reactions with SO_2, NO_2, NO, H_2O and CH_3CHO as a function of pressure. *Physical Chemistry Chemical Physics,* 16**,** 1139-1149.

STONE, D., EVANS, M. J., EDWARDS, P. M., COMMANE, R., INGHAM, T., RICKARD, A. R., BROOKES, D. M., HOPKINS, J., LEIGH, R. J., LEWIS, A. C., MONKS, P. S., ORAM, D., REEVES, C. E., STEWART, D. & HEARD, D. E. 2011. Isoprene oxidation mechanisms: measurements and modelling of OH and HO_2 over a South-East Asian tropical rainforest during the OP3 field campaign. *Atmos. Chem. Phys.,* 11**,** 6749-6771.

STONE, D., EVANS, M. J., EDWARDS, P. M., COMMANE, R., INGHAM, T., RICKARD, A. R., BROOKES, D. M., HOPKINS, J., LEIGH, R. J., LEWIS, A. C., MONKS, P. S., ORAM, D., REEVES, C. E., STEWART, D., AND HEARD, D. E. 2011. Isoprene oxidation mechanisms: measurements and modelling of OH and HO_2 over a South-East Asian tropical rainforest during the OP3 field campaign. *Atmos. Chem. Phys.,* 11.

VEREECKEN, L., HARDER, H. & NOVELLI, A. 2012. The reaction of Criegee intermediates with NO, RO_2, and SO_2, and their fate in the atmosphere. *Physical Chemistry Chemical Physics,* 14**,** 14682-14695.

WATANABE, K., NAKAYAMA, T. & MOTTL, J. 1962. Ionization potentials of some molecules. *Journal of Quantitative Spectroscopy and Radiative Transfer,* 2**,** 369-382.

WELZ, O., ESKOLA, A. J., SHEPS, L., ROTAVERA, B., SAVEE, J. D., SCHEER, A. M., OSBORN, D. L., LOWE, D., MURRAY BOOTH, A., XIAO, P., ANWAR H KHAN, M.,

PERCIVAL, C. J., SHALLCROSS, D. E. & TAATJES, C. A. 2014. Rate Coefficients of C_1 and C_2 Criegee Intermediate Reactions with Formic and Acetic Acid Near the Collision Limit: Direct Kinetics Measurements and Atmospheric Implications. *Angewandte Chemie (International Ed. in English),* 53**,** 4547-4550.
WELZ, O., SAVEE, J. D., OSBORN, D. L., VASU, S. S., PERCIVAL, C. J., SHALLCROSS, D. E. & TAATJES, C. A. 2012. Direct Kinetic Measurements of Criegee Intermediate (CH_2OO) Formed by Reaction of CH_2I with O_2. *Science,* 335**,** 204-207.
WINKLER, A. & HESS, P. 1994. Study of the Energetics and Dynamics of Hydrogen Bond Formation in Aliphatic Carboxylic Acid Vapors by Resonant Photoacoustic Spectroscopy. *Journal of the American Chemical Society,* 116**,** 9233-9240.

Chapter VIII: Concluding Remarks and Future Work

Chapter VIII:

Concluding Remarks and Future Work

8. Concluding Remarks and Future Work

8.1 Summary of Work and Atmospheric Implications

In the first chapter of this thesis the tropospheric oxidation of both anthropogenic and biogenic organic species to CO_2 were outlined, as were the potential impacts these species have on the Earth's climate. In particular, the importance of the species involved with atmospheric oxidation is highlighted. Furthermore, all of the work presented in chapters IV, VI and VII has a direct impact on oxidation within the lower atmosphere; in particular, how small changes in the understanding of the tropospheric chemistry can influence the oxidation of different atmospheric pollutants (such as VOCs, SO_2 and NO_2) in both polluted (Chapter IV) and remote forested environments (Chapters VI + VII).

In Chapter IV the mechanism of the reaction between CH_3CHO + OH was probed in detail, from this study all of the evidence suggests that the reaction does not proceed by a simple abstraction reaction (Butkovskaya et al., 2004), although in the proposed mechanism, hydrogen abstraction from the acyl carbon is the first step. During this study, the products of the reaction were monitored directly using time-resolved mass spectrometry. Using this technique it was observed that methyl radicals were generated from this reaction; moreover, these radicals had identical time profiles to the acetyl radicals. Therefore it is proposed that due to the exothermicity of the abstraction reaction, a significant fraction (~15%) of the nascent acetyl radicals formed have sufficient energy to dissociate, forming CH_3 and CO radicals (D'Anna et al., 2003). It should be noted that experiments were conducted to prove that the methyl radicals were not formed during acetyl photoionization.

$$CH_3CHO + OH \rightarrow CH_3CO + H_2O \quad \text{(R8.1a)}$$

$$\rightarrow CH_3 + CO + H_2O \quad \text{(R8.1b)}$$

All of the experiments in this study were conducted at low pressures (1 – 60 Torr); however, MESMER calculations suggest that even at atmospherically relevant pressures approximately 10% of the nascent acetyl radicals will still undergo the chemically activated dissociation to methyl radicals. Although reaction R8.1b is only a minor channel, it will still have an impact on both tropospheric concentrations of PAN, which will be reduced, and formaldehyde, a stable product from methyl radical oxidation (Brasseur et al., 1999).

Chapters VI and VII are focussed around a different family of tropospheric oxidants, Criegee intermediates. Generally, atmospheric concentrations of CIs are so low they can be considered as only minor (or negligible) oxidants within the atmosphere. However, in certain forested environments (where BVOC emissions are high) it has been suggested that

CIs may be a small sink for trace gas pollutants such as SO_2 and NO_2 (Mauldin et al., 2012, Welz et al., 2012). Notably, the focus of Chapter VI was to investigate the reaction of both the C_1 and C_2 Criegee intermediates with SO_2 and NO_2. From this study, the rate coefficients of all of the reactions were found to be orders of magnitude larger than previous, indirect measurements had reported (Johnson et al., 2001). Furthermore, the work reported in this chapter is the first to identify acetaldehyde as a product from the C_2 CI + SO_2, indirectly implying that the reaction oxidises SO_2 to SO_3. This is understood to be a crucial step in the formation of H_2SO_4 within the atmosphere. The results from this study support the findings from previous laboratory work (Welz et al., 2012, Taatjes, 2013); they also support field measurements from Finland where an extra night time source of H_2SO_4 is observed, which they attribute to the oxidation of SO_2 to SO_3 by CIs (Mauldin et al., 2012). Moreover, although the C_2 Criegee intermediate is only a minor sink of SO_2 in the atmosphere, larger CIs may prove to be more significant as their reactivity towards water and the water dimer, are thought to be much smaller (Anglada and Sole, 2016).

The aim of Chapter VII was to further investigate the reactions of Criegee intermediates with carboxylic acids reactions, and in particular to elucidate on the products of these reactions. Notably, the C_1 CI and formic acid have previously been suggested as an intermediate in the decomposition of hydroperoxy methyl formate, which itself is an intermediate the oxidation of DME (Andersen and Carter, 2003). It was hoped that HPMF would be observed as a product from the C_1 + HCOOH reaction, however, this was not possible using the PLP-PIMS set-up. From the results of these experiments nothing quantitative could be said about the products, although product analysis has made it possible to hypothesise potential pathways for the reactions. Moreover, the products observed from both of the reactions, m/z = 64 and m/z = 74, for the formic and acetic acid reactions respectively, were consistent with the study by Welz et al. (2014), where the same mass peaks were also observed. Lastly, the significance of CIs as atmospheric oxidants of carboxylic acids was determined. From these calculations it was apparent that CIs may contribute considerably to the removal of organic acids from the atmosphere, particularly at night. This is of substantial interest as the products from CI + carboxylic acid reactions will be very different from the products of OH + carboxylic acid reactions it is in competition with (Long et al., 2009, Calvert, 2011).

8.2 Other Possible Implications

As alluded to above, the atmospheric impact of the chemistry discussed in this thesis is likely to be relatively small, however, their impact may be more significant when discussing the low temperature (T < 800 K) combustion of oxyfuels such as ethanol and dimethyl ether

(DME). There are a number of similarities atmospheric oxidation and combustion chemistry, indeed, the atmosphere is often considered as a low temperature combustion system. Therefore, it is unsurprising that, often, similar oxidation pathways for specific species (i.e. ethanol) can be used to describe both systems. A theoretical study completed by Lee et al. (2002), focussed on the formation of acetyl peroxy in low temperature combustion systems; in this study it was predicted that a significant proportion (43.1%) of the nascent acetyl radicals reacted to form acetyl peroxy (p = 1 atm and T < 550 K) (Lee et al., 2002). However, it is likely that this does not take into account the existence of the post reaction complex predicted in Chapter IV, and hence may underestimate the fraction of acetyl radicals which undergo dissociation (D'Anna et al., 2003).

Similarly, the C_1 Criegee intermediate, CH_2OO, is also hypothesised to be implicated in the low temperature combustion of DME (Andersen and Carter, 2003); this work highlights all of the possible loss channels of hydroperoxymethyl formate (HPMF). Notably, in Andersen and Carter (2003) the unimolecular decomposition of the hydroperoxymethyl formate to form formic acid and a Creigee intermediate is presented, a pathway which had not previously been considered (Andersen and Carter, 2003). Furthermore, it is predicted that this channel has a reasonably low activation energy, making it competitive with the other reaction pathways hypothesised (Figure 8.1). A study by Gutbrod et al. (1997) has shown the decomposition of the Creigee intermediate can lead to the recycling of a second hydroxyl radical, and hence chain-branching. However, this is not the most favourable path (Gutbrod et al., 1997).

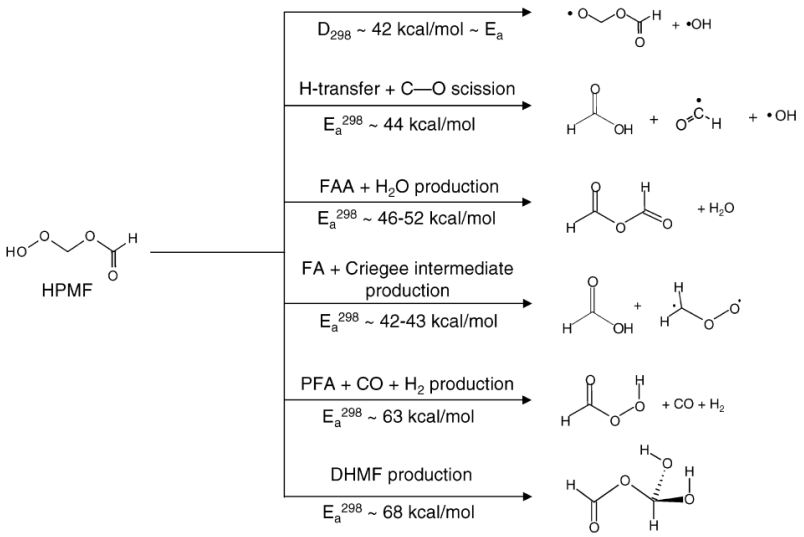

Figure 8.1: Schematic summary of the theoretical loss reactions of HPMF (Andersen and Carter, 2003).

8.3 Future Work

There are several different avenues in which the work presented in this thesis could be taken in the future: firstly, more work is still needed to expand the functionality of the PLP-PIMS set-up, discussed in Chapter III. Additionally, more work still needed to fully understand the some of the atmospheric species examined, in particular the atmospheric fate of Criegee intermediates and their products.

8.3.1 Future Work: Instrument Development

The results from Chapter III suggest that the configuration changes made to adapt for a high pressure set-up were largely ineffective and the sensitivity was found much lower than expected; this suggests that there is little point continuing with the development of this configuration. However, there is potential in the OH detection technique described (Beames et al., 2011), although the reliability and sensitivity must be improved. For example, one way to increase the sensitivity of the technique would be to optimise the length of the delay line of the photoionization pulse, to ensure it overlaps in time with the 282.5 nm laser pulse. It should be noted that some testing has been done to improve the synchronisation of the laser pulses, however further optimisation would undoubtedly improve the sensitivity of the technique. Thus far, the technique has also relied upon the Nd:YAG laser to produce both the 355 nm light necessary for photoionization and the 532 nm light (required for 282.5 nm generation) simultaneously. Currently, to achieve the required output power of the 532 nm, light was detuned on the doubling crystal to reduce its power. A consequence of the detuning the 532 nm light output is that the laser power decreased over time and constant retuning is necessary. However, it is believed this could be rectified by the use of an additional laser, such that the 532 nm and 355 nm light could be generated separately.

As mentioned above, all of the reaction systems investigated in this thesis have implications for the Earth's atmosphere (and combustion chemistry). To increase the relevance of the results from this work, especially their relevance for combustion systems, the temperature dependences must be fully understood. Therefore, a reconfiguration of the PLP-PIMS set-up to include some level of temperature control would be useful. In recent years a high temperature and pressure LIF set-up has been under development at the University of Leeds (Stone et al., 2016). In the LIF system the temperature of the gas in the reactor tube is controlled by varying the voltage applied to a heating coil (Watlow, WATROD tubular heater) surrounding the reactor (Figure 8.2a).

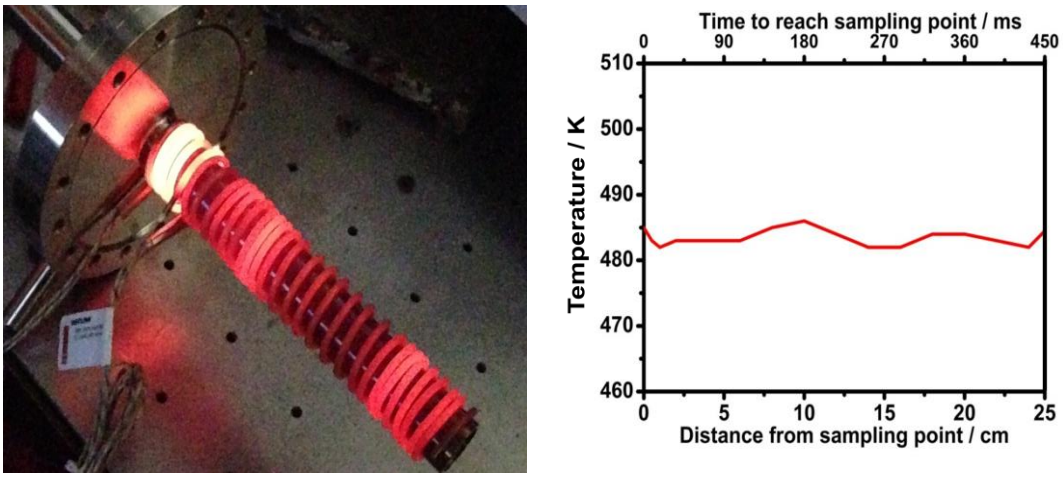

Figure 8.2: (a) A photograph on the left shows the tubular heating coil used in the high temperature and pressure LIF set-up; (b) A plot on the right shows the temperature profile of the heated gases along the length of the reactor tube (Stone et al., 2016).

Using this technique it is possible to heat the gas to approximately 750 K, moreover, once heated temperature of the gas remained constant for the length of the flowtube (Figure 8.2b). It is thought that a similar temperature control system could be implemented for the PLP-PIMS set-up.

8.3.2 Future Work: Criegee Intermediates

Over the past five years there have been a number of important discoveries which have greatly improved our understanding of the role Criegee intermediates in the atmosphere. Initially, the enhanced kinetics shown from the direct measurement of the C_1 and C_2 CIs with SO_2 and NO_2 created a renewed interest in Criegee chemistry and it was proposed that the reactions with these trace gases may be a significant sink for CIs (Percival et al., 2013). However, recent kinetic measurements of the CI + H_2O suggest that the dominant sink for Criegee intermediates is the reaction with the water dimer (Lewis et al., 2015); making SO_2 and NO_2 only very minor sinks for Criegee intermediates. Although there is now a general consensus that the water dimer is the dominant sink for C_1 and C_2 Criegee intermediates, there is much which is still unknown about the Criegee intermediate chemistry within the atmosphere. For example, even though theoretical studies investigating the mechanism of the C_1 CI + water dimer reaction (Anglada and Sole, 2016), there is still very little experimental evidence of the products (or the mechanism) for this reaction.

Furthermore, while the reactivity of the C_1 CI is relatively well understood, our current understanding of the larger Criegee intermediate is more uncertain. For example, there is still ambiguity as the rate of the *syn*-C_2 CI with H_2O. Moreover, there are currently no direct measurements of the C_2 CI with the water dimer. Another area where there still appears to be some debate is decomposition rate of the C_2 Criegee intermediate, where currently

values ranging between 3 s^{-1} and 563 s^{-1} are estimated (Novelli et al., 2014, Newland et al., 2015). It should be highlighted that using the PLP-PIMS set-up a decomposition rate coefficient of between $20 < k_d\ (s^{-1}) < 80$. However, due to the large variation between these measurements, more work is still needed to verify this. Notably, having a clear understanding of both the reactivity and decomposition of the C_2 Criegee intermediate is imperative for accurate atmospheric modelling.

8.4 References

ANDERSEN, A. & CARTER, E. A. 2003. Hybrid density functional theory predictions of low-temperature dimethyl ether combustion pathways. II. Chain-branching energetics and possible role of the Criegee intermediate. *Journal of Physical Chemistry A,* 107**,** 9463-9478.

ANGLADA, J. M. & SOLE, A. 2016. Impact of water dimer on the atmospheric reactivity of carbonyl oxides. *Physical Chemistry Chemical Physics*.

BEAMES, J. M., LIU, F., LESTER, M. I. & MURRAY, C. 2011. Communication: A new spectroscopic window on hydroxyl radicals using UV + VUV resonant ionization. *The Journal of Chemical Physics,* 134**,** 241102.

BRASSEUR, G. P., ORLANDO, J. J. & TYNDALL, G. S. 1999. *Atmospheric Chemistry and Global Change,* Oxford, Oxford University Press.

BUTKOVSKAYA, N. I., KUKUI, A. & LE BRAS, G. 2004. Branching fractions for H_2O forming channels of the reaction of OH radicals with acetaldehyde. *Journal of Physical Chemistry A,* 108**,** 1160-1168.

CALVERT, J. G. M., A; ORLANDO, J. J; PILLING, M. J AND WALLINGTON, T. J 2011. The Mechanisms of Atmospheric Oxidation of the Oxygenates. New York: Oxford University Press.

D'ANNA, B., BAKKEN, V., BEUKES, J. A., NIELSEN, C. J., BRUDNIK, K. & JODKOWSKI, J. T. 2003. Experimental and theoretical studies of gas phase NO_3 and OH radical reactions with formaldehyde, acetaldehyde and their isotopomers. *Physical Chemistry Chemical Physics,* 5**,** 1790-1805.

GUTBROD, R., KRAKA, E., SCHINDLER, R. N. & CREMER, D. 1997. Kinetic and theoretical investigation of the gas-phase ozonolysis of isoprene: Carbonyl oxides as an important source for OH radicals in the atmosphere. *Journal of the American Chemical Society,* 119**,** 7330-7342.

JOHNSON, D., LEWIN, A. G. & MARSTON, G. 2001. The Effect of Criegee-Intermediate Scavengers on the OH Yield from the Reaction of Ozone with 2-methylbut-2-ene. *The Journal of Physical Chemistry A,* 105**,** 2933-2935.

LEE, J., CHEN, C.-J. & BOZZELLI, J. W. 2002. Thermochemical and Kinetic Analysis of the Acetyl Radical (CH_3CO) + O_2 Reaction System. *The Journal of Physical Chemistry A,* 106**,** 7155-7170.

LEWIS, T. R., BLITZ, M. A., HEARD, D. E. & SEAKINS, P. W. 2015. Direct evidence for a substantive reaction between the Criegee intermediate, CH_2OO, and the water vapour dimer. *Physical Chemistry Chemical Physics,* 17**,** 4859-4863.

LONG, B., CHENG, J.-R., TAN, X.-F. & ZHANG, W.-J. 2009. Theoretical study on the detailed reaction mechanisms of carbonyl oxide with formic acid. *Journal of Molecular Structure: THEOCHEM,* 916**,** 159-167.

MAULDIN, R. L., BERNDT, T., SIPILA, M., PAASONEN, P., PETAJA, T., KIM, S., KURTEN, T., STRATMANN, F., KERMINEN, V. M. & KULMALA, M. 2012. A new atmospherically relevant oxidant of sulphur dioxide. *Nature,* 488**,** 193-+.

NEWLAND, M. J., RICKARD, A. R., ALAM, M. S., VEREECKEN, L., MUÑOZ, A., RÓDENAS, M. & BLOSS, W. J. 2015. Kinetics of stabilised Criegee intermediates derived from alkene ozonolysis: reactions with SO_2, H_2O and decomposition under boundary layer conditions. *Physical Chemistry Chemical Physics,* 17**,** 4076-4088.

NOVELLI, A., VEREECKEN, L., LELIEVELD, J. & HARDER, H. 2014. Direct observation of OH formation from stabilised Criegee intermediates. *Physical Chemistry Chemical Physics,* 16**,** 19941-19951.

PERCIVAL, C. J., WELZ, O., ESKOLA, A. J., SAVEE, J. D., OSBORN, D. L., TOPPING, D. O., LOWE, D., UTEMBE, S. R., BACAK, A., M C FIGGANS, G., COOKE, M. C., XIAO, P., ARCHIBALD, A. T., JENKIN, M. E., DERWENT, R. G., RIIPINEN, I., MOK, D. W. K., LEE, E. P. F., DYKE, J. M., TAATJES, C. A. & SHALLCROSS, D. E. 2013. Regional and global impacts of Criegee intermediates on atmospheric sulphuric acid concentrations and first steps of aerosol formation. *Faraday Discussions,* 165**,** 45-73.

STONE, D., BLITZ, M., INGHAM, T., ONEL, L., MEDEIROS, D. J. & SEAKINS, P. W. 2016. An instrument to measure fast gas phase radical kinetics at high temperatures and pressures. *Review of Scientific Instruments,* 87**,** 054102.

TAATJES, C. W., O; ESKOLA, A; SAVEE, J; SCHEER, A; SHALLCROSS, D; ROTAVERA, B; LEE, E;DYKE, J; MOK, D; OSBORN, D AND PERCIVAL C 2013. Direct Measurements of Conformer-Dependent Reactivity of the Criegee Intermediate CH_3CHOO. *Science,* 340.

WELZ, O., SAVEE, J. D., OSBORN, D. L., VASU, S. S., PERCIVAL, C. J., SHALLCROSS, D. E. & TAATJES, C. A. 2012. Direct Kinetic Measurements of Criegee Intermediate (CH_2OO) Formed by Reaction of CH_2I with O_2. *Science,* 335**,** 204-207.

Appendices

Appendix A – Steady State Approximation of Ozone

In Chapter 1, Section 1.3.2, the steady state for O_3 in polluted environments was shown, the derivation of this is given below (Seinfeld and Pandis, 2012).

$$NO_2 + h\nu\ (\lambda < 430\ nm) \rightarrow NO + O(^3P) \quad \text{(RA.1)}$$

$$O(^3P) + O_2 + M \rightarrow O_3 + M \quad \text{(RA.2)}$$

$$NO + O_3 \rightarrow NO_2 + O_2 \quad \text{(RA.3)}$$

Before the steady state approximation for O_3 can be determined, the rate equations for $O[^3P]$ and O_3 must first be determined:

$$\frac{d[O(^3P)]}{dt} = J_{A1}[NO_2] - k_{A2}[O(^3P)][O_2][M] \quad \text{(EA.1)}$$

$$\frac{d[O_3]}{dt} = k_{A2}[O(^3P)][O_2][M] - k_{A3}[O_3][NO] \quad \text{(EA.2)}$$

Following this a steady state approximations were sequentially applied to $[O(^3P)]$ and $[O_3]$:

$$\frac{d[O(^3P)]}{dt} = 0$$

$$[O(^3P)] = \frac{J_{10}[NO_2]}{k_2[O_2][M]} \quad \text{(EA.3)}$$

$$\frac{d[O_3]}{dt} = 0$$

$$[O_3] = \frac{k_{A2}[O(^3P)][O_2][M]}{k_{A3}[NO]} \quad \text{(EA.4)}$$

A final substitution gives the steady state approximation for O_3:

$$[O_3] = \frac{J_{10}[NO_2]}{k_{12}[NO]} \quad \text{(EA.5)}$$

Appendix A – References

SEINFELD, J. H. & PANDIS, S. N. 2012. *Atmospheric chemistry and physics: from air pollution to climate change*, John Wiley & Sons.

Appendix B – Further Details of Stimulated Emission

In Chapter II, Section 2.3.1, the principles behind stimulated emission are discussed and a simplified version of the relationship between population inversion and the Beer-Lambert is shown in E2.2. In Appendix B this relationship will be discussed in more detail.

Lasing will only commence if there is a sufficient net increase in photon density in a single orientation. This can be a challenge as stimulated emission generally reaches an equilibrium where absorption and emission occur at the same rate. This was first suggested by Albert Einstein and can be explained by the following equation (Einstein, 1917):

$$N_1.B_{12}.\rho(\nu) = N_2.B_{21}.\rho(\nu) + N_2.A_{21} \quad \text{(EB.1)}$$

In equation EB.1: N_1 equals the number of species in lower state (ground state), N_2 is number of species in the upper state, B_{12} is the Einstein transition probability coefficient from state 1 to 2, and B_{21} is the Einstein transition probability from state 2 to 1, $\rho(\nu)$ is the photon energy density at frequency υ, and finally A_{21} the Einstein coefficient for spontaneous emission (Einstein, 1917).

The equation above can be split into the three processes associated with absorption and emission: the first component of the equation $N_1.B_{12}.\rho(\nu)$ refers to the transition rate of stimulated absorption. The second element $N_2.B_{21}.\rho(\nu)$ describes the rate of stimulated emission, finally the rate of spontaneous emission is equal to $N_2.A_{21}$. It should be noted that as part of his 1917 paper Einstein proved that the probability of a transition is independent of direction *i.e.* $B_{12} = B_{21}$.

Equation EB.1 highlights a challenge in lasing, as under normal conditions N_1 is far greater the N_2, meaning the system will reach an equilibrium where stimulated absorption and emission occur at similar rates and emission is limited by absorption. In order for lasing to commence, this equilibrium must be disrupted and the rate of stimulated emission must be greater than the rate of stimulated absorption; for this to occur N_2 must be greater than N_1 and the population of the states should be inverted. If N_2 is greater than N_1 then there will be an exponential increase in light transmission which leads to the amplification of light of the associated wavelength – this can be explained with the Beer-Lambert law (EB.2):

$$I_t = I_0 e^{(-\sigma n l)} = I_0 e^{(-\alpha l)} \quad \text{(EB.2)}$$

I_t represents the intensity of transmitted light, I_0 is the intensity of the incident light, σ is the absorption cross section, n is the number density, α is the extinction coefficient (note: $\alpha = \sigma \times n$), and l is the path length of the laser medium.

$$\alpha = B_{12}\left(\frac{h\nu}{c}\right)(N_1 - N_2) \quad \text{(EB.3)}$$

The above equation (EB.3) is known as the extinction coefficient equation. In this equation: c represents the speed of light, 2.99792458×10^8 m s^{-1} (Penrose, 2005). Note all the other terms in EB.3have previously been described.

From these equations (EB.2 and EB.3) we can see that the intensity of transmitted light is proportional to a negative exponent of the absorption cross-section, which itself is directly dependent on $N_1 - N_2$. Therefore if $N_2 > N_1$ the intensity of transmitted light will increase exponentially, and hence lasing can occur.

Appendix B – References

EINSTEIN, A. 1917. Quantum theory of radiation. Physikalische Zeitschrift, 18, 121-128.
PENROSE, R. 2005. The road to reality: a complete guide to the laws of the universe. New York: Alfred A. Knopf.

Appendix C – Estimation of Steady-state concentration for Criegee intermediates

The steady-state concentration of Criegee intermediates can be determined using the following equation:

$$[\mathrm{CI}] = \frac{k_{\mathrm{CI}} f_{\mathrm{SCI}} [\mathrm{O_3}][\mathrm{alkene}]}{k_{(\mathrm{H2O})2}[(\mathrm{H_2O})_2] + k_{\mathrm{H2O}}[\mathrm{H_2O}] + k_{\mathrm{SO2}}[\mathrm{SO_2}] + k_{\mathrm{acid}}[\mathrm{acid}] + k_{\mathrm{uni}}} \qquad \text{(EC.1)}$$

In equation EC.1: [CI] is the steady-state concentration of Criegee intermediates; k_{CI} is the rate coefficient of CI formation; f_{SCI} is the fraction of SCI formed; $k_{(H2O)2}$ is the rate coefficient of CI + $(H_2O)_2$ reaction; k_{H2O} is the rate coefficient of CI + H_2O reaction; k_{SO2} is the rate coefficient of CI + SO_2 reaction; k_{acid} is the rate coefficient of CI + carboxylic acid reactions; and k_{uni} is the rate coefficient of unimolecular decomposition.

A range of [CI] concentrations were estimated using the following parameters: f_{SCI} =0.3; k_{CI} = 5×10^{-18} cm^3 $molecule^{-1}$ s^{-1}; 5×10^{11} < [O_3] (molecule cm^{-3}) < 7.5×10^{11} (Percival et al., 2013); 5×10^{10} < [alkene] (molecule cm^{-3}) < 7.5×10^{11} (Percival et al., 2013, Newland et al., 2015); $k_{(H2O)2}$ = 4×10^{-12} cm^3 $molecule^{-1}$ s^{-1} (Lewis et al., 2015); 2.5×10^{14} < [$(H_2O)_2$] (molecule cm^{-3}) < 5.5×10^{14}; k_{H2O} = 1×10^{-16} cm^3 $molecule^{-1}$ s^{-1} (Welz et al., 2014); 4×10^{17} < [$(H_2O)_2$] (molecule cm^{-3}) < 6×10^{17}; k_{SO2} = 2.5×10^{-11} cm^3 $molecule^{-1}$ s^{-1}; 1×10^{10} < [SO_2] (molecule cm^{-3}) < 2.5×10^{11} (Vereecken et al., 2012, Lin et al., 2012); k_{acid}= 5×10^{-11} cm^3 $molecule^{-1}$ s^{-1}; 6×10^{10} < [acid] (molecule cm^{-3}) < 2.5×10^{11} (Vereecken et al., 2012, Souza et al., 1999); and k_{uni} = 100 s^{-1}.

Using this information above a range for the steady-state CI concentration can be estimated at 2.0×10^2 < [CI] (molecule cm^{-3}) < 7.5×10^3. This leads to a conservative estimation of [CI] ≈ 1×10^3 molecule cm^{-3}; a value, which when necessary, will be used in subsequent calculations.

Appendix C – References

LEWIS, T. R., BLITZ, M. A., HEARD, D. E. & SEAKINS, P. W. 2015. Direct evidence for a substantive reaction between the Criegee intermediate, CH_2OO, and the water vapour dimer. *Physical Chemistry Chemical Physics,* 17**,** 4859-4863.

LIN, W., XU, X., MA, Z., ZHAO, H., LIU, X. & WANG, Y. 2012. Characteristics and recent trends of sulfur dioxide at urban, rural, and background sites in North China: Effectiveness of control measures. *Journal of Environmental Sciences,* 24**,** 34-49.

NEWLAND, M. J., RICKARD, A. R., ALAM, M. S., VEREECKEN, L., MUÑOZ, A., RÓDENAS, M. & BLOSS, W. J. 2015. Kinetics of stabilised Criegee intermediates derived

from alkene ozonolysis: reactions with SO_2, H_2O and decomposition under boundary layer conditions. *Physical Chemistry Chemical Physics,* 17**,** 4076-4088.
PERCIVAL, C. J., WELZ, O., ESKOLA, A. J., SAVEE, J. D., OSBORN, D. L., TOPPING, D. O., LOWE, D., UTEMBE, S. R., BACAK, A., M C FIGGANS, G., COOKE, M. C., XIAO, P., ARCHIBALD, A. T., JENKIN, M. E., DERWENT, R. G., RIIPINEN, I., MOK, D. W. K., LEE, E. P. F., DYKE, J. M., TAATJES, C. A. & SHALLCROSS, D. E. 2013. Regional and global impacts of Criegee intermediates on atmospheric sulphuric acid concentrations and first steps of aerosol formation. *Faraday Discussions,* 165**,** 45-73.
SOUZA, S. R., VASCONCELLOS, P. C. & CARVALHO, L. R. F. 1999. Low molecular weight carboxylic acids in an urban atmosphere: Winter measurements in São Paulo City, Brazil. *Atmospheric Environment,* 33**,** 2563-2574.
VEREECKEN, L., HARDER, H. & NOVELLI, A. 2012. The reaction of Criegee intermediates with NO, RO_2, and SO_2, and their fate in the atmosphere. *Physical Chemistry Chemical Physics,* 14**,** 14682-14695.
WELZ, O., ESKOLA, A. J., SHEPS, L., ROTAVERA, B., SAVEE, J. D., SCHEER, A. M., OSBORN, D. L., LOWE, D., MURRAY BOOTH, A., XIAO, P., ANWAR H. KHAN, M., PERCIVAL, C. J., SHALLCROSS, D. E. & TAATJES, C. A. 2014. Rate Coefficients of C_1 and C_2 Criegee Intermediate Reactions with Formic and Acetic Acid Near the Collision Limit: Direct Kinetics Measurements and Atmospheric Implications. *Angewandte Chemie International Edition,* 53**,** 4547-4550.

Appendix D – List of Publications

As required by the regulations for thesis submission, this appendix shows the papers in which work from this thesis has been published:

STONE, D., BLITZ, M., DAUBNEY, L., HOWES, N. U. M. & SEAKINS, P. 2014. Kinetics of CH_2OO reactions with SO_2, NO_2, NO, H_2O and CH_3CHO as a function of pressure. *Physical Chemistry Chemical Physics,* 16**,** 1139-1149.

HOWES, N.U.M., LOCKHART, J. P. A., BLITZ, M. A., CARR, S. A., VARGA, T., BAEZA-ROMERO, M. T., HEARD, D.E., SHANNON, R. J., SEAKINS, P. W. 2016.

For both publications I performed all the experiments described using the PLP-PIMS set-up. Notably, both publications contain other complementary work, which was performed by other member of the P. W. Seakins group. My work from the publications are, respectively, the basis for Chapters VI and IV of this thesis.